

Development and application of oxygen nanosensors for the assessment of molecular oxygen in 2D and 3D cell culture

Reem Mohammed Abohujel, BSc, MSc

Thesis submitted to the University of Nottingham for the

Degree of Doctor of Philosophy

School of Pharmacy

March 2022

Abstract

Nanoparticle science is a rapidly developing field within a variety of scientific disciplines. Developing nanosensor-based nanoparticles for measuring intracellular oxygen is of great interest as a diagnostic tool. It helps to understand and investigate biological responses that affect health, the status of the disease, and the mechanisms of curative therapies. The measurements are based on changes in luminescence intensity quenched by the increase in oxygen concentration. This approach provides information on cellular spatial and temporal measurement and the assessment of kinetics in multiple biological samples for different applications.

This study describes the development and characterisation of ratiometric oxygen nanosensors to improve the monitoring of oxygen in a biological system. Moreover, in order to obtain biological insights that would help to expand the knowledge of nanosensor trafficking, pH nanosensors were used to investigate intracellular pH responses. Thus, oxygen and pH nanosensors were tracked in *situ* to provide the intracellular fate that correlates with physiological relevant mechanisms. The ratiometric approaches were used in both oxygen and pH nanosensors. Oxygen nanosensors designed by conjugating a platinum porphyrin to the surface of the polyacrylamide matrix and entrapping 5-(and-6) - carboxytetramethylrhodamine (TAMRA) in polyacrylamide nanoparticles. Ratiometric nanosensors for pH sensing were prepared by entrapping the OG (Oregon green) and (FAM) Fluorophores 5- and 6-carboxyfluorescein sensitive fluorophores to pH and TAMRA insensitive fluorophore to pH in a polyacrylamide matrix.

Nanosensors were developed and fluorophores conjugating to polyacrylamide nanoparticles optimised and calibrated using fluorescence microscopy imaging. Both oxygen and pH nanosensors were investigated in terms of their co-localisation with lysosome and mitochondria in the cells. This was done to overcome the limitations of oxygen monitoring problems. Intracellular monitoring of oxygen by nanosensors brings hope for cellular responses to micro-environmental change especially responses that report cellular vital signs activity. Oxygen nanosensors have been applied to the biological systems of immune cells (THP-1 differentiated macrophage) and hepatic cells (HepG2 cells), resulting in five major findings:

1) Nanosensors were successfully delivered to macrophage and HepG2 cells without affecting cell viability and metabolic activity. In addition, calibration of sensors was conducted in fixed cells within a controllable oxygen chamber connected to a fluorescence microscope.
2) In studying nanosensors application, oxygen nanosensors were delivered to macrophages in order to control phenotype modulation by monitoring oxygen. However further investigation has revealed that Pt porphyrin modulates macrophage phenotype with continuous imaging. This is caused by enhancing ROS generation which leads to unreliable metabolic endpoint measurements. Therefore, application of nanosensors in biological system in this thesis focuses on studying oxygen monitoring in hepatic cells.
3) Nanosensors location were determined in hepatic cells with respect to lysosomes and mitochondria in order to help correlate oxygen consumption with cellular metabolic activity. It has been found that oxygen nanosensors are most likely to be distributed in the cytoplasm.

4) Endpoint measurement of oxygen has been assessed in hepatic cells exposed to different insults using imaging microscopy. Reported oxygen concentrations were supported with an apoptotic assay to understand the effect of cellular functionality.
5) Oxygen nanosensors were applied on 3D cellular model of spheroids to evaluate oxygen nanosensors in tumour model. Spheroid is a multicellular aggregate which is a complex architecture model of tumour. These characteristics limit the detection capability of oxygen sensing probe and failure of oxygen detection. With these challenges, oxygen sensors are becoming extremely useful for screening drugs by detecting oxygen gradients in spheroids. The kinetic of oxygen concentration was monitored to assess the effect of environmental reactions.

Acknowledgements

I would like to express my sincere gratitude to my supervisor Prof Jonathan Aylott, for providing me with such a great opportunity to be a student in Nottingham University under his guidance. In my study project, I am appreciative for his encouragement, support, and guidance. Special thanks for the universal support I received in all my time at Nottingham and at Saudi Arabia. Also, I would like to thank Prof Amir Ghaemmaghami for his guidance and advice through my work in the biological part of my research. I gratefully appreciate Dr. Veeren Chauhan's guidance, patience, advice, support, encouragement, and being a friendly supervisor. Also, a special thanks goes to Dr. Francesca Giuntini for her help in synthesizing metalloporphyrin.

I would like to thank my sponsor, King Saud University in Saudi Arabia, for providing me with this opportunity to grow as a research scientist, expand my knowledge and return to campus with the new blood of experience.

Additionally, thanks to all members of the Aylott group, Tom Booth for his training, accepting, and answering continuous questions about microscopy. I owe much gratitude to Dr Amjad Selo for his electron microscopy training and help. Also Dr Constantin Tanase for helping me in preparing spheroids. Thanks to SLIM centre members Robert Markus, Seema Bagia for technical help and training.

Thanks to my colleagues in life science, Arsalan Latif, Lisa Kämmerling for stimulating discussions and making a lab a great environment to work in. A special debt of thanks is reserved for Dr Suha Alharbi and Dr Asmaa Alghamdi for being great friends and being there when I need help and guidance. Thank you to all my friends who have always been there to talk through everything. Last but not least, I would like to give great thanks to my family, my mum, dad, brothers, and sisters for their continual support and prayers through my Ph.D. I would not have made it to this stage without their encouragement. You are always there whenever I have needed help with anything and always looked out for me. Special thanks to my husband Suliman for his support to reach my goals and to achieve my PhD.

Table of Contents

ABSTRACT ..... **I**

ACKNOWLEDGEMENTS ..... **IV**

LIST OF FIGURES ..... **X**

LIST OF TABLES ..... **XV**

LIST OF ABBREVIATIONS ..... **XVI**

CHAPTER 1 . INTRODUCTION **1**

1.1 PREFACE 1

1.2 HISTORY AND TYPES OF NANOSENSORS 2

1.2.1 Electrochemical nanosensors 4

1.2.2 Mechanical/vibrational nanosensors 5

1.2.3 Optical nanosensors 7

1.2.3.1 Principle of luminescence 8

1.2.3.2 Principle of phosphorescence 9

Quantum Yield 11

1.3 EXPLORING FLUORESCENT NANOSENSORS POTENTIAL FOR BIOLOGICAL APPLICATION 12

1.3.1 Versatility of chemical tailoring of nanosensors 13

1.3.2 Dye loading strategies 15

1.3.3 Examples of nanosensors used for biological applications: 16

1.3.3.1 State of the art of the pH nanosensor 16

1.3.3.2 State of the art of oxygen nanosensors 21

1.4 APPLICATION OF NANOSENSORS IN BIOLOGICAL SYSTEM 29

1.4.1 Application of nanosensors in immune system 29

1.4.2 Monitoring of respiration in cancer model 31

1.5 THESIS OUTLINE 34

CHAPTER 2 . MATERIALS AND METHODS **37**

2.1 MATERIALS POLYACRYLAMIDE NANOSENSORS 37

2.1.1 Cell culture 39

2.2 METHODS 41

2.2.1 Preparation of polyacrylamide nanoparticles and conjugation to sensing indicators 41
2.2.2. Nanosensor characterisation 44
2.2.2.1. Particle size and zeta potential 44
2.2.2.2. Fluorescence response 44
2.2.2.3. Field emission gun scanning electron microscope (FEG-SEM) 45
2.2.2.4. Evaluation of oxygen nanosensors' sensitivity in response to oxygen depletion 45
2.3 CELL CULTURE 46
2.3.1 Differentiation of THP-1 to macrophage 46
2.3.2 Characterisation of M1 and M2 phenotypes 46
2.3.2.1 Immunostaining 46
2.3.2.2 Characterisation of polarised macrophages to M1 and M2 phenotypes 46
2.3.2.3 Calibration of oxygen nanosensors using THP-1 differentiated macrophage 47
2.3.2.4 Impact of nanosensors on macrophages 48
2.3.2.5 Stability monitoring of ratiometric fluorescence intensity 48
2.3.2.6 2',7'-dichlorodihydrofluorescein diacetate (H_2DCFDA) assay for detecting ROS 49
2.3.2.7 Modulation of oxygen and pH concentration in macrophage cells 49
2.3.3 Hepatic cells (HepaG2 cell line) 50
2.3.3.1 Viability assay using Toxilight® Kit 50
2.3.3.2 Respiration assay (ratiometric imaging of hypoxia) 50
2.3.3.3 Use of imaging flow cytometer platform to test changes in oxygen intracellularly 52
2.3.4 Influence of O_2/pH flux in 3D hepatic cancer cell models measured using fluorescent nanosensors 52
2.3.5 Intracellular fate of nanosensors 53
2.4 DEVELOPMENT AND OPTIMIZATION METHODOLOGY FOR RATIOMETRIC MEASUREMENTS 53
2.4.1 Methodology of image analysis 54

2.4.2 Methodology for analysing co-localisation of nanosensors with lysosome and mitochondria 58
2.5 STATISTICAL ANALYSIS 59
CHAPTER 3 . DESIGN, SYNTHESIS AND CHARACTERISATION OF OXYGEN NANOSENSORS 60
3.1 INTRODUCTION 60
3.1.1 Synthesis of oxygen nanosensors 60
3.1.1.1 Polyacrylamide nanosensors 61
3.1.1.2 Porphyrin utilisation for measurement of intracellular oxygen 62
3.2 NANOSENSOR CHARACTERISATION 65
3.2.1 Dynamic light scattering 66
3.2.2 Zeta potential 68
3.2.3 Fluorescence response 69
3.2.3.1 Fluorescence spectrophotometer 69
3.2.3.2 Fluorescence microscope 70
3.3 DEVELOPMENT AND OPTIMISATION OF METHODOLOGY FOR FLUORESCENCE RATIOMETRIC MEASUREMENTS 74
3.3.1 Technical consideration of ratiometric measurements 74
3.3.1.1 Nanosensor calibration 74
3.3.1.2 Image acquisition 74
3.3.1.3 Microscope alignment 75
3.3.1.4 Exposure and gain 75
3.3.1.5 Image analysis 75
3.3.1.5.1 Determination of the measurement region (thresholding): 76
3.3.1.5.2 Background removal: 76
3.3.1.5.3 Automation of image analysis: 76
3.4 RESULTS AND DISCUSSION 77
3.4.1 Reproducibility of nanosensor fabrication technique 77
3.4.2 Optimisation of fluorophores concentration incorporated in nanosensors 81
3.4.3 Characterization and re-evaluated of optimal concentration of oxygen nanosensors' fluorophores 85

3.4.4 Calibration of oxygen nanosensors using fluorescence microscope 86
3.4.5 Temperature effect on nanosensors fluorescence response 88
3.4.6 Evaluation of oxygen nanosensor sensitivity 89
3.5 CONCLUSION 91

CHAPTER 4 . INTRACELLULAR EVALUATION OF OXYGEN IN MACROPHAGE 93

4.1 INTRODUCTION 93
4.1.1 Response of macrophage to nanosensors based nanoparticles 93
4.1.1.1 Surface chemistry of polymeric matrix 94
4.1.1.2 Charge 95
4.1.1.3 Size 95
4.1.2 Utilisation of nanosensors based nanoparticles for live cell measurement 96
4.1.3 Assays used for modulating intracellular oxygen 98
4.2 RESULTS AND DISCUSSION 100
4.2.1 Characterization of THP-1 differentiated macrophage 100
4.2.2 Macrophage polarisation 101
4.2.2.1 Cytokines productions 101
4.2.2.2 Immuno-fluorescent staining 102
4.2.3 Co-localisation of porphyrin and TAMRA of oxygen nanosensors, in THP-1 differentiated macrophage 104
4.2.4 Stability monitoring of ratiometric fluorescence intensity 105
4.2.5 Impact of oxygen nanosensors on cell metabolic activity 108
4.2.6 Impact of polyacrylamide nanosensors on phenotypic modulation of macrophage 109
4.2.7 ROS detection with oxygen and pH nanosensors using 2',7'-dichlorodihydrofluorescein diacetate (H_2DCFDA) 111
4.2.8 Applying oxygen nanosensors in immune cells 113
4.2.8.1 Calibration of oxygen nanosensors in fixed cells 113
4.2.8.2 Modulation of oxygen concentration in macrophage 115
4.2.8.3 Modulation of pH in macrophage 117

4.2.9 Heat map of oxygen distribution in macrophage within co-culture model (MRC-5/ macrophage) 119
4.3 CONCLUSION 125
CHAPTER 5 . STUDYING OXYGEN FLUX IN HEPATIC CELLS 127
5.1 INTRODUCTION 127
5.2 RESULTS AND DISCUSSION 129
5.2.1 Toxicity assay 129
5.2.2 Intracellular fate of nanosensors 129
5.2.3 Respiration assay (ratiometric imaging of hypoxia) 134
5.2.4 Apoptosis assay 143
5.2.5 Use of imaging flow cytometry platform to test change of oxygen intracellularly 145
5.2.6 Study of pH / O_2 flux in 3D hepatic cancer cell models using fluorescent nanosensors 148
5.3 CONCLUSION 156
CHAPTER 6 . CONCLUSION 158
CHAPTER 7 . REFERENCE 165
CHAPTER 8 . APPENDICES 188
8.1 APPENDIX A 188
8.2 APPENDIX B 189

List of Figures

Figure 1-1: Diagram showing the steps involved in making thread-based oxygen sensors. (A) A picture of a wire sensor, with just one thread electrode. (B) Image of a tip sensor taken at the tip. (C) Photograph of a sensor with a curved tip. (D) Image of a finger with a tip sensor coiled around it, adapted from Junfei *et al.* [17]. 5
Figure 1-2: Schematic of a microcantilever biosensor and (b) an image of the cantilever taken with a scanning electron microscope (SEM), adapted from Liu *et al.* [21]. 6
Figure 1-3: Design of the PI/Si/SiO2 microcantilever as rectangle, The Wheatstone bridge produced a voltage output voltage when an input voltage was applied to it, adapted from Tian *et al*.[20]..... 7
Figure 1-4: Jablonski energy diagrams, adapted from Lakowicz *et al* [30]. 9
Figure 1-5: Phosphorescence representative scheme of spin conversion from singlet (excited state) to (triplet) excited state adapted from Pandey [33]..... 10
Figure 1-6: A) Carboxylic acid of biomolecules (blue) conjugation to amino-functionalised nanoparticles (green) by carbodiimide-NHS mediated coupling. B) Conjugation of azido- and alkynyl-functionalized polymeric nanoparticles using Cu as a catalyst. C) Electrostatic reaction..... 14
Figure 1-7: Schematic of the fibre-optic probe with a sensing membrane [62]. 17
Figure 1-8: Design of nanosensors A) nanosensors with single indicator fluorophore B) nanosensors with ratiometric design indicator and reference fluorophores. . 18
Figure 1-9: fluorescein derivatives structure equilibrium that change with pKa [68]. 20
Figure 1-10: Luminescence of indicator dyes quenching by oxygen. 23
Figure 1-11: Reversible response of oxygen nanosensors to deoxygenated air by nitrogen gas and oxygenated air by oxygen. X axis (time of response), Y axis (ratio measurement of indicator dye porphine (PtTFPP) / Coumarin 6 (C6)) [90]. 24
Figure 1-12: Classification of oxygen nano-sensing probes. 26
Figure 1-13: A) Chemical structure backbone of major oxygen sensing probes (tetraphenyl pyrol) based on metallo-porphyrin. B) 5,10,15,20 tetrakis pentafluorophenyl porphyrinatoplatinum (Pt TFPP). C) The spectrum of absorption and emission of porphyrin..... 28
Figure 1-14: Mitochondrial inner membrane complexes structure, generation of electron leaks and proton leaks in the electron transport chain, adapted from Lin Li *et al.* [121]..... 32
Figure 2-1: Structure of 5,10,15,20 tetrakis pentafluorophenyl porphyrinatoplatinum (Pt TFPP) [45]..... 38
Figure 2-2: Polyacrylamide nanoparticle synthesis scheme. 1) Acrylamide 2) N,N methylenebis (acrylamide) 3) N-(3-aminopropyl) methacrylamide (APMA) 4) (3-acryamidopropyl) trimethylammonium (ACTA)..... 41
Figure 2-3: A) Round bottom flasks with nanosensors during polymerisation. The flask covered by aluminium foil to avoid photo-degradation of fluorophores. Balloons

filled were filled with argon to complete the polymerisation reaction on deoxygenated environment. B) Rotary evaporator of remaining solvent after final wash of nanoparticles produces a dry powder. 43
Figure 2-4: Schematic diagram differentiation of THP-1 to macrophages. Then schematic of calibration with oxygen nanosensors using imaging with microscope. 48
Figure 2-5:Schematic representation of cellular distribution of healthy, apoptotic and necrotic cells in dot plot analysis using Annexin /PI kit [132]. 51
Figure 2-6: HepaG$_2$ cells seeded in Aggrewell ^{TM} plates. A) Control spheroid. B) Spheroid pre-treated with O_2 nanosensor. C) Spheroid pre-treated with a pH nanosensor..... 52
Figure 2-7: A) Schematic representation of image analysis for oxygen nanosensor calibration. 55
Figure 2-8: Fiji Code and algorithm of used for image analysis to provide a measurement a histogram of nanosensors intracellularly. 57
Figure 2-9: Calculation of Co-localisation Pearson's coefficient from coloc2 in image J 59
Figure 3-1: Schematic of dynamic light scattering principle, adapted from HORIBA Co. [145] 66
Figure 3-2: Theory of Zeta potential, adapted from Tengku Mohd *et al* [147]. 68
Figure 3-3: Schematic representation of based components of fluorescence spectrophotometer, adapted from Gomes *et al* [150]. 70
Figure 3-4: Labelled parts of fluorescence microscope. A) Microscope [43]. The colour green denotes light that is focused on the specimen, red denotes the emitted light from the sample, and yellow denotes light that has been transferred. B) Filter block [43] (Where the lenses and filters arranged). 72
Figure 3-5: Characterization of size by using DLS A) pre-conjugation and B) post-conjugation to Pt porphyrin. C) Zeta potential values (mV) of polyacrylamide nanoparticles pre and post- conjugation of Pt porphyrin. 78
Figure 3-6: A) Transmission electron microscope (TEM) images, B) Field Emission Gun Scanning Electron microscopy (FEG-SEM) at magnification 110,000x and 50,000x..... 80
Figure 3-7: Spectrum of A) excitation and emission of Porphyrin and B) excitation and emission of TAMR. 81
Figure 3-8: A) Oxygen nanosensor suspension. B) Immersed oxygen meter in oxygen nanosensor suspension in a tight oxygen environment. C) Balloons with oxygen and argon had been bubbled in suspension. 82
Figure 3-9: A) Fluorescence spectrum of oxygen nanosensors (0.5mg/ml), Oxygen sensitivity of sensor is measured by fluorimeter. Increase in fluorescence response of porphyrin (at 0.05mg/ml) to decrease in oxygen concentration and constant response of TAMRA to change in oxygen concentration B) Linear response of normalised fluorescence intensity versus% of normalised oxygen concentrations by Stern-Volmer equation..... 83

Figure 3-10: A) Fluorescence spectrum properties of porphyrin and TAMRA and B) improved the linear response of normalised fluorescence intensity versus% of normalised oxygen concentrations by Stern-Volmer equation..... 85
Figure 3-11: 1) humidity column. 2) Ibid gas controller. 3) Ibid chamber [166]. 86
Figure 3-12: Visualise brightness change of porphyrin and TAMRA in oxygen nanosensors suspended in PBS using hypoxia chamber connected to wild field microscope (oxygen concentration 0 – 20 %). The graph illustrates linear response of oxygen concentration in chamber and oxygen nanosensors. 87
Figure 3-13 : Effect of incubation temperature (37°C) on oxygen nanosensors intensity. Error bars represent (SD for n=3). 88
Figure 3-14: A) Spectrum of increasing Pt porphyrin intensity by consumption of dissolved oxygen by glucose oxidase in deionized water. B) Kinetic analysis of oxygen consumption by glucose oxidase enzyme. Error bars represent (SD for n=3). 89
Figure 3-15: Monitoring of pH during oxygen consumption using pH meter Error bars represent (SD for n=3) (P <0.0001). 90
Figure 4-1 : THP-1 differentiated macrophage (M0) treated with oxygen nanosensors. M0 tagged by Alexa flour480 CD68 marker of M0. 100
Figure 4-2: ELISA assay of A) TNF-α expression of M1 polarised macrophage. B) IL-10 expression of M2 polarised macrophage. Data showed mean optical density at 450nm which representative for n=3, (level of significant ****p<0.0001, ***p<0.001, **p<0.01). 102
Figure 4-3: Visualised images of characterisation of M1 and M2 polarized macrophage that expressed calprotectin and mannose receptor, respectively. Scale = 10 µm. 103
Figure 4-4: Macrophage treated with A) TAMRA and B) Porphyrin nanosensors. C) 2D histogram of fluorophores (porphyrin and TAMRA channels) conjugated nanoparticles in THP-1 differentiated macrophage. Scale = 50 µm. 104
Figure 4-5: Monitoring of ratiometric fluorescence intensity at D1, D4 and D7. Error bars represent SD, n= 3, P= <0.05. 105
Figure 4-6: Visualisation images of intracellular oxygen nanosensors at maximum and minimum of oxygen concentration in chamber. 106
Figure 4-7: Reversibility response of intracellular oxygen nanosensors to change of micro-environmental oxygen. Ratiometric Mean fluorescence Intensities (MFI) when cycled between 0 and 100 % dissolved oxygen concentration (Oxygen determined by Neofox Oceanoptic). 107
Figure 4-8: A) Alamar blue ® (metabolic activity). B) Cytotox glu® for (cell viability) Data is representative for n=3, (P= <0.05). 108
Figure 4-9: Cytokines in the supernatants of THP-1 differentiated macrophages cultured with 100ng/ml LPS, 100 µg/ml oxygen and 250 µg/ml pH nanosensor were measured by means of ELISA for (A)TNF-α and B) IL-10. Data presented are the mean ± SD of at 3 independent experiments, each experiment with one

passage number (9-11), n=4, = ±SD (level of significant ****p<0.0001, ***p<0.001, **p<0.01, *p<0.05) 110
Figure 4-10: A) Detection of ROS by H2DCFDA dyes. Data represent for n=3, (level value of significant ****p<0.0001, ***p<0.001, **p<0.01,*p<0.05). B) Corresponding images of cells that were treated with Menadione, pH NS, oxygen NS compared with control. Scale = 100 µm. 112
Figure 5-1: Toxicity assay of oxygen nanosensors in HepaG2 cells. Cells were treated with 100 µg/ml of nanosensors. Data showed mean luminescence intensity which representative for n=3, (level value of significant ****p<0.0001, ***p<0.001, **p<0.01). 129
Figure 5-3: Histogram of oxygen distribution in cells. Oxygen concentration in response to 1, 5 and 25µM acetaminophen, statistics based two experimental repeats (n = 5 ROI). Corresponding colour oxygen maps are shown under the histograms. 136
Figure 5-4: Histogram of oxygen distribution in cells A) control in response to B) 5µM propranolol, C) 250µM methotrexate and D) 5µM antimycin, statistics based two experimental repeats (n = 5 ROI). Corresponding colour oxygen maps are shown next to the histograms 139
Figure 5-5: Histogram of pH distribution in A) control of $HepG_2$cells in response to B) 1mM, C) 5 mM, D)25 mM acetaminophen. (n=5 ROI). 142
Figure 5-6: Histogram of pH distribution in A) control of HepG2cells in response to 5mM propranolol, 250µM methotrexate, and 5 µM antimycin. (n=5 ROI). 142
Figure 5-8: Maximum intensity of Ch:11 (porphyrin) and Ch:03 (TAMRA) images of HepaG2 cells using image stream instrument 147
Figure 5-9: A) HepG2 spheroids mean size is 136, B) distribution of nanosensors in spheroid treated with pH nanosensors Brightfield, Red is TAMRA channel, Green is OG&FAM. 149
Figure 5-10: Image histogram of average z stack HepG2 cell spheroids treated with pH nanosensors exposed to pharmacological drugs acetaminophen 5mM, acetaminophen 25mM, 16uM antimycin. (± SD = 3 ROI) for above corresponding images 150

Figure 5-11: Fluorescence intensities distribution heat map of ratiometric spheroid images (fixed spheroid) when exposed to glucose/glucose oxidase at different time point. 0, 10, 20 and 30 minutes. Image J used for map analysis. 152
153
Figure 5-12: Oxygen distribution map of ratiometric spheroid images (live spheroid) when exposed to glucose/glucose oxidase at different time point 0, 10, 20 and 30 minutes..... 153
Figure 5-13: Live spheroid images of oxygen mapping, spheroid exposed to 25mM acetaminophen and 16 uM antimycin at different time point 30 minutes. 154
Figure 5-14: Plot profile of oxygen concentration change within different Z stack image of spheroids, Z stack is slice of spheroid in mm 155
Figure A.1: A) Flow cytometry dot plot of untreated cells, B) treated cells with absolute TAMRA dye, C) treated cells with absolute porphyrin dye D,E ,F, G) 50, 100, 250, 500 µg/mL oxygen nanosensors. 188
Figure A-2: Example of signal enhancement after removing background in image analysis 189
Figure B-1: Reduction of ABMA intensity with presence of porphyrin nanosensors which indicate H2O2 production. 189
Figure B-2: Monitoring effect of LPS and interferon ɣ on oxygen consumption in macrophage cells Data represents n =3 repeat and error bars =SD. 190
Figure B-4: Morphological change of macrophage as a result of continuous imaging of nanosensors that prove Pt porphyrin generation of ROS. 192
Figure B-5: Effect of different pH range (3 - 7.5) on the intensity of porphyrin (used for sensing oxygen) in dual oxygen and pH nanosensor 192

List of Tables

Table 1.1: Most common commercial available fluorophores 34

Table 3.1: Luminescent metalloporphyrin-based probes for oxygen, the polymer support used and the purpose of using oxygen nanosensors, type of cells used in study, reference..... 78

Table 4.1: list of compounds has mitochondrial membrane complex un-coupler and inhibitors .....**Error! Bookmark not defined.**

Table 5.1: Co-localisation of Pearson's Correlation Coefficients (PCC) for TAMRA nanoparticles and oxygen nanosensors with mitochondria and lysosomes, calculated from five microscopic images of two experiments. 130

List of abbreviations

ACTA	(3-acrylamidopropyl) trimethylammonium
AKDR	Adenylate kinase detection reagent
AOT	Dioctyl sulfosuccinate sodium
APMA	N-(3 Aminopropyl)methacrylamide hydrochloride
APS	Ammonium persulfate
ATCC	American Type Culture Collection
BSA	bovine serum albumin
Coloc 2	Co-localisation
COVID-19	Coronavirus disease
d.nm	Diameter
DABI	4,6 Diamidine-2'-phenylindole dihydrochloride
DLS	Dynamic light scattering
DLS	Dynamic Light Scattering
ECAR	Extracellular acidification rate
ELISA	Enzyme-linked immunosorbent assay
ETC	Electron transport chain
FAM-SE	Fluorophores 5- and 6-carboxyfluorescein succinimidyl ester
FBS	Foetal bovine serum
FEG-SEM	Field emission gun electron microscopy
Glu	Glucose
GO	Glucose oxidase
H_2DCFDA	Hydroxychlorofluorescine diacetate
ISC	intersystem crossing
LPS	Lipopolysaccharide
LUT	Look up table
M1 and M2	Macrophage phenotypes 1 and 2
NA	Numerical aperture
NADH	Nicotinamide adenine dinucleotide
NAPQI	N-acetyl benzoquinone imine
NMRC	Nanoscale and Microscale Research Centre
NPs	Nanoparticles
OCR	Oxygen consumption rate
OG-SE	Oregon Green® 488 carboxylic acid acid succinimidyl ester

PBS	Phosphate buffered saline
PCC	Pearson’s Correlation Coefficient
Pd(II)	Palladium
PDHF	Polyfluorene derivatives poly(9,9-dihexylfluorene)
PDI	Polydispersity index
PFA	Paraformaldehyde
PFO	Poly(9,9-dioctylfluorene
PLA	Polylactic acid
PMA	Phorbol-12-myristate acetate
Pt porphyrin	Platinum porphyrin
PtOEP	Platinum(II) octaethylporphine
PtOEPK	Platinum octaethylporphine ketone
PtPFPP	Pt(II)-tetrakis(pentafluorophenyl) porphyrin
rcf	Relative centrifugal force
Ru.(III)	Ruthenium
ROI	Region of interest
ROS	Reactive oxygen species
SNR	Signal to noise ratio
TAMRA-SE	5- and 6 carboxytetramethylrhodamine succinimidyl ester
TEM	Transmission electron microscopy
TEMED	N,N,N,N tetra methyl ethylene diamine
V-ATPase	Vacuolar-type ATPase
W/V	Weight/Volume
°C	Degree Celsius

Chapter 1 . Introduction

1.1 Preface

The main focus in this thesis is fabrication and development of oxygen nanosensors and their application. This is to improve existing methods for the monitoring of oxygen in cellular monolayers and 3D cultures of different biological systems. The design of oxygen nanosensors has been developed in our group in collaboration with Dr. Francesca Giuntini at Liverpool John Moores University, who synthesised the indicator dye.

Oxygen nanosensors are composed of a polymer matrix coupled to a synthetic dye which report oxygen concentrations with a quantifiable phosphorescence signal. In the development process of oxygen nanosensors, the indicator dye concentration is critical and needs to be optimised in order to provide high phosphorescence signal and while being non-invasive to for the cells undergoing measurement.

From the perspective of biological applications, as well as measuring the oxygen concentration, it is important to track nanosensors location so that the spatial location of the measurement is known too. Using nanosensors enables researchers to both, make measurements of the analyte of interest and to spatially localise these measurements. This is beneficial when attempting to target monitoring of specific organelles in cells and to determine the exact site of measurements and link to physiological activity of the cells.

Another interesting approach when using nanoparticle- based nanosensors is to observe how the chemistry of coupling fluorophores might affecting cellular trafficking.

For example, in this study, the Pt porphyrin molecule coupled to the surface of the polyacrylamide matrix of oxygen nanosensors was compared to pH sensitive nanosensors, which have different indicator and reference dyes encapsulated in polyacrylamide nanoparticles. Studying the cellular fate of oxygen and pH nanosensors as a result of their different surface chemistries can help gain an understanding of nanoparticle trafficking and movement.

In this thesis, oxygen nanosensors were used in two biological systems which were models for the immune system and for hepatic cancer. This chapter will provide an overview of the nanosensors used, as well as the biological systems they were applied to.

1.2 History and types of nanosensors

German physician Paul Ehrlich won a Nobel Prize over 100 years ago on how cells interact with chemical dyes. His study generated a theory of interaction between chemical compounds and cells, influenced by their chemical composition [1]. In 1959, the concept of nanotechnology was introduced by the Nobel laureate Richard Feynman, at an American Physical Society meeting at the California Institute of Technology, in a talk entitled ‘There’s Plenty of Room at the Bottom’. This was an encouragement for the development of nano-medicine [2]. Consequently, the revolution continues, as optics and chemistry combine to develop nanotechnology and invent new advanced analytical techniques, able to visualise and measure events at the nanoscale. The majority of the adaptations in biological systems, leading to healthy or diseased status, take place in microenvironments at the sub-cellular level, which is the current limit of our knowledge

There are conventional diagnostic techniques that can effectively screen for/or identify markers of interest. For example, polymerase chain reaction (PCR) sequencing, enzyme linked immunosorbent assay (ELISA) and blotting methods are common on molecular which is based on molecular biology techniques. However, all these techniques have some disadvantages whether that be time taken to carry out the analysis, the inability to carry out *in situ* measurements or the cost per test [3]. Ideally, new analytical methods would require little sample preparation, be quick, cost-effective and provide results that were specific, sensitive and reproducible [4]. Nanotechnology can provide potential solutions, implementing strategies that overcome some of the limitations demonstrated by other techniques, for example the small sizes of nanosensors can lead to fast response times.

A nanosensor is defined by a device or tool with maximum dimensions of 100 nm that has sensing characteristics [5]. It is used to provide information on the nanoscale and convert it into analysable data [6]. Nanosensors used for detecting biological biomarkers can be easy to prepare, sensitive, cheap, and can be used to monitor multiple analytes [3]. Further, they have the capability to monitor physical or chemical phenomena such as temperature, light, potential transmitted by cells and to then convert this to measurable signals [7]. Further, nanosensors can be considered as analytical devices that allow monitoring of important biological analytes which afford insights into cellular activity [8]. Generally, bio-sensing procedures are composed of three main steps: 1) detecting of the stimuli by a detector, 2) generating the output signal, 3) processing the output signal and presenting the results. In 2020, Abdel-Karim *et al*. reviewed different categories of nanosensors and their compositions [7]. They classified the nanosensors according to transducer structure into: 1) optical

nanosensors, 2) electrochemical nanosensors, 3) mechanical/vibrational nanosensors. Each of these nanosensor classifications is discussed below in more detail:

1.2.1 Electrochemical nanosensors

The basic concept of electrochemical nanosensors is the interaction of an analyte of interest with the nanosensor produces an electrical signal proportionally related to the analyte concentration. There are different types of electrical signal that can be induced or monitored, including: 1) amperometric, 2) potentiometric, 3) conductometric which detect varieties of analytes [9]. Typical electrochemical nanosensors consist of a working electrode (to detect the analyte) and reference electrode (insensitive to analyte) separated by electrolytes [9]. Electrochemical nanosensors provide many advantages: short response times that carry out real-time monitoring of biological processes possible. Simplicity of use, inexpensive, cost and the possibility of miniaturisation [10]. Their primary disadvantage is that they are prone to fouling and need replacing when applied for long-term use [11].

The Clark electrode, first reported in 1959 [12] was developed to facilitate biological oxygen measurements [13, 14]. However, accurate spatial measurements are limited with this type of electrode due to its oxygen consumption and results in cellular measurements being restricted to single point oxygen measurement [15].

Recently, micro/ nano-electrode array sensors have evolved particularly as a result of the rapid advancement in micro/nano meter scale machining technology. However, challenges are still present due to difficulties in miniaturisation and fabrication of sensors, particularly with regards to electronics integration with [16].

An example of electrochemical nanosensors is use of an extremely flexible electrochemical oxygen sensor that detects dissolved oxygen content with great sensitivity and uses threads as sensing electrodes. Specifically, threads which act as sensing electrodes are composed of two silver-coated threads as the cathode and anode for measuring dissolved oxygen over a large or small area, Figure 1-1Figure 1-1 [17]. However, while thread nanosensors showed good repeatability and stability; further studies need to be carried out to test sensing selectivity to oxygen not to other gases [17].

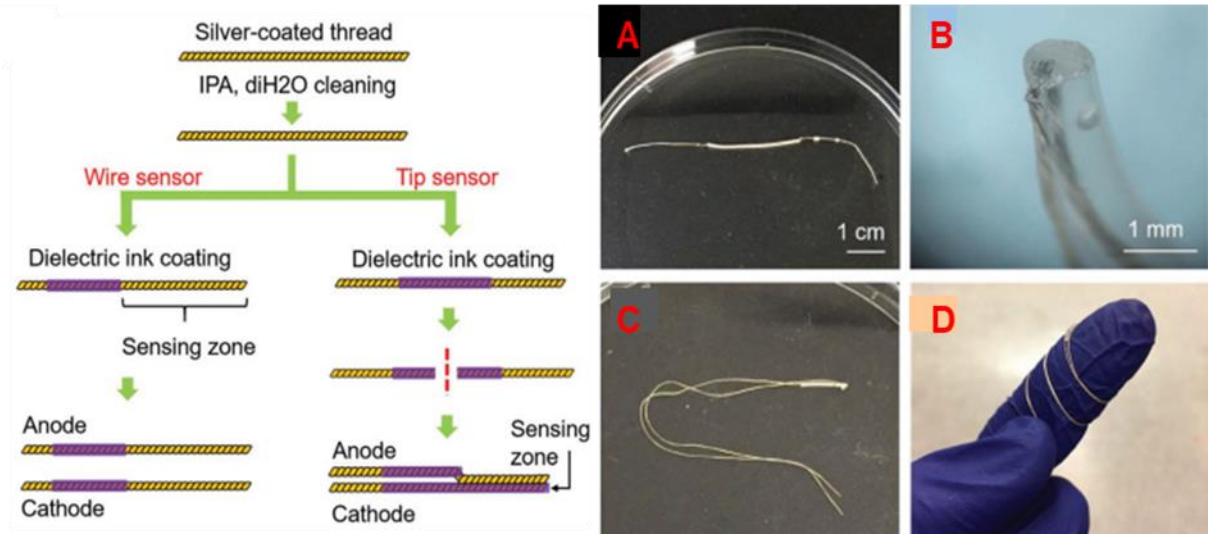


Figure 1-1: Diagram showing the steps involved in making thread-based oxygen sensors. (A) A picture of a wire sensor, with just one thread electrode. (B) Image of a tip sensor taken at the tip. (C) Photograph of a sensor with a curved tip. (D) Image of a finger with a tip sensor coiled around it, adapted from Junfei *et al.* [17].

1.2.2 Mechanical/vibrational nanosensors

Mechanical nanosensors are based on measuring the forces at the molecular level. The main advantage of this type of nanosensors is that they are sensitive to mass. Therefore, detection of mass is enhanced when the mass of mechanical sensors

decreases to nanoscale. However, fluid detection by mechanical nanosensors might be affected by viscosity due to decrease of sensitivity [3]. To solve issues of sensitivity in fluid detection, a technique has been developed based on a sensing array of resonant microcantilevers. Resonance-based sensors can continue to function with good sensitivity in a variety of liquid physiological conditions [18]. However, the sensitivity is an advantage of this technique, it considered as the main issue. Since almost anything has mass, a wide range of compounds in a sample might theoretically create a signal and hence impair selectivity [19]. Therefore, to advance these biosensors an integration of different techniques, electrochemistry and microcantilevers Figure 1-2, were used to enhance sensitivity and selectivity [20].

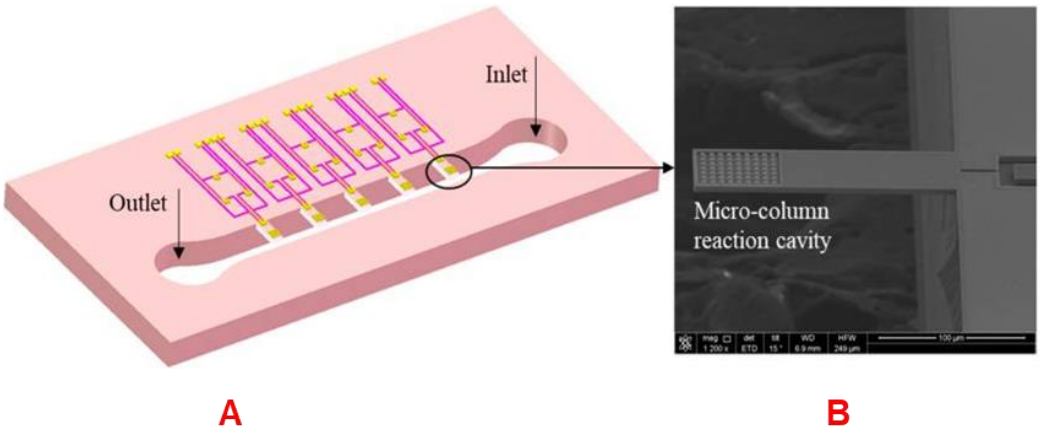


Figure 1-2: Schematic of a microcantilever biosensor and (b) an image of the cantilever taken with a scanning electron microscope (SEM), adapted from Liu *et al.* [21].

This was demonstrated in a study carried out by Tian *et al*. in a study that used an electrochemical microcantilever biosensor for detection of Aflatoxin B1 pollutant of food. It has been shown that the prepared PI/Si/SiO2 microcantilever demonstrated excellent mechanical characteristics coupled with a maintained electrical voltage output, Figure 1-3 [20].

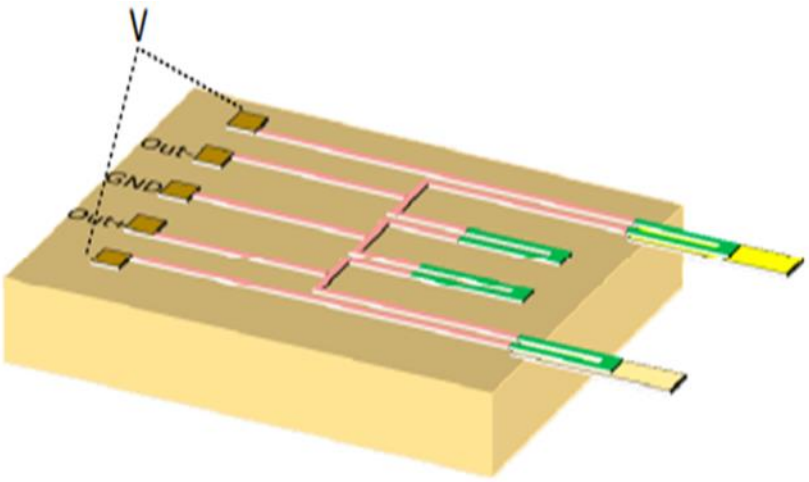


Figure 1-3: Design of the PI/Si/SiO2 microcantilever as rectangle, The Wheatstone bridge produced a voltage output voltage when an input voltage was applied to it, adapted from Tian *et al*.[20].

1.2.3 Optical nanosensors

Optical signal detection by nanosensors offers excellent sensitivity due to the specificity imparted by molecular recognition centres conjugated to nanomaterials. However, the sensitivity significantly depends on how the optical phenomena are detected. Optical sensors are categorised to several detection modes, e.g., absorption, fluorescence, Raman and refraction [3]. They have been applied in different research areas such as biotechnology, medical application, environmental science and chemical industries [7].

One of the many promising optical nanosensors are fluorescent nanosensors [22-27]. This is due to the high sensitivity to the analytes gained from fluorescence as compared with ultraviolet (UV) absorption, the range of photoactive molecules which can be combined in a single particle for different analytical purposes, and the ability to

make qualitative (detection) and quantitative measurements. Simplistically, fluorescence nanosensors are comprised of nanoparticles conjugated to at least one type of photoactive units [7]. These photoactive units use fluorescence and/or phosphorescence to emit their signal, the basis of these techniques are explained below.

1.2.3.1 Principle of luminescence

Luminescence is the emission of light from a substance resulting from a transition from an excited electronic state to the ground state. Luminescence is categorised into two forms; fluorescence and phosphorescence, depending on the type of excited state transition [28]. Spectroscopic changes can be explained using the Jablonski energy diagram Figure 1-4 that show the processes that occur during the absorption and emission of light by a molecule. The electronic ground state and first and second excited singlet states are represented by S_0, S_1 and S_2 respectively.

Most molecules reside in the lowest vibrational level of the ground electronic state at room temperature, and when light is absorbed, they are raised to produce excited states. The molecule absorbs light to create either the first, S_1, or second, S_2, excited state, as shown in the simplified the diagram below. The molecule then relaxes and transits from the S_2 to the S_1 in a vibrational state which is termed as (internal conversion). As relaxation occurs, the electron relaxes from S_1 to S_0, through radiative emission, which is termed as fluorescence, or non-radiative emission via heat or vibrations. A fluorescent photon is usually captured at longer wavelengths and lower energy levels than an excited photon due to loss of energy during the internal conversion which occurs within 10^{-12} s or less [29, 30]. Fluorescence emission rates

are approximately 10^8 s^{-1}, meaning that a typical fluorescence lifetime is close to 10 ns (10 x 10^{-9} s). Life time is the average amount of time elapsed between a fluorophore's excitation and return to the ground state is known as lifetime [30].

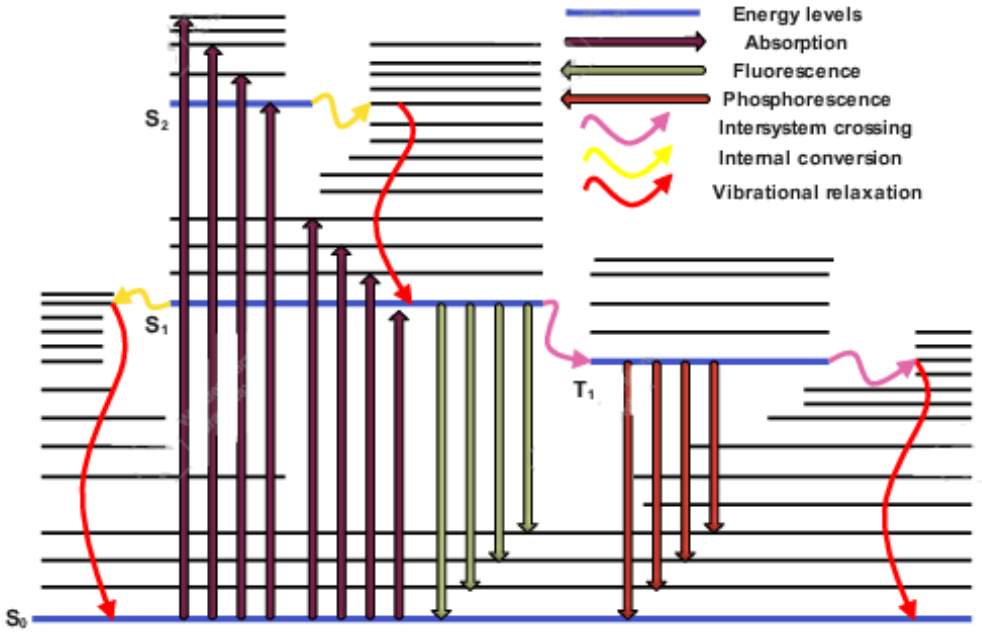


Figure 1-4: Jablonski energy diagrams, adapted from Lakowicz *et al* [30].

1.2.3.2 Principle of phosphorescence

Phosphorescence is the process where electrons relax from the excited triple state (T_1) to the ground state (S_0). For the electron to transfer from the excited single state (S_1) to the excited triplet state (T_1) they undergo a process known as intersystem crossing [31]. The emission rates are slow (10^3 to 100 s^{-1}), so that phosphorescence lifetimes are typically milliseconds to second. The fluorescent and phosphorescent lifetimes of a molecule are an intrinsic property of that molecule [30, 32]. In some cases, however, fluorescent intensity is quenched by a different mechanism, the use

of a quencher molecule and these systems can be developed to indicate the presence of a quencher (analyte). Quenching mechanisms can be generated as a result of interactions between the excited states of a neighbouring molecules, energy transfer, complex-formation and collisional quenching [15]. They are highly dependent on the period of time an electron or molecule stays in the excited state [31],Figure 1-5.

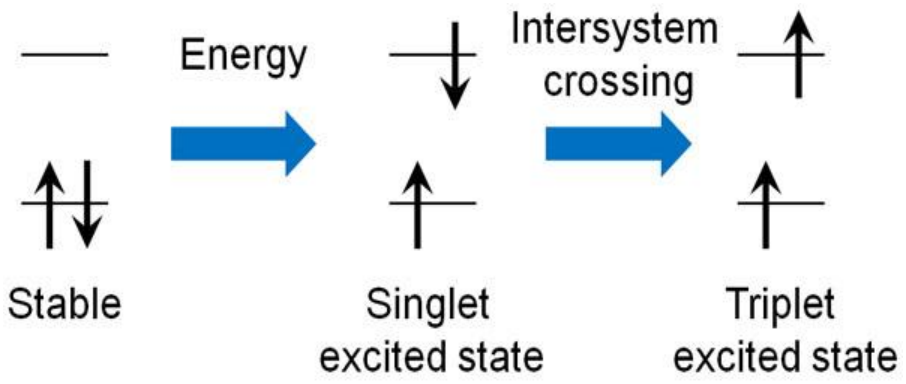


Figure 1-5: Phosphorescence representative scheme of spin conversion from singlet (excited state) to (triplet) excited state adapted from Pandey [33].

Fluorescence emission efficiency is measured by quantum yield, yields (φ). The fluorescence quantum yield measures the amount of photons that are emitted versus those that are absorbed. This can be calculated by dividing the rate of radiative fluorophores (Γ) by the sum of rate of radiative (Γ) and non-radiative deactivation (Knr) of the excited electronic state [30] [34].

$$(\varphi) = \frac{(\Gamma)}{(\Gamma) + (Knr)}$$

Quantum Yield

If the rate of radiationless decay (knr) is significantly lower than the rate of radiative decay (Γ), then the quantum yield can be very close to unity. Quantum yield can be measured relative to a standard with known fluorescent quantum yield. These compounds' quantum yields are often independent of excitation wavelength, the standards can be applied anywhere they exhibit useful absorption [35].

The most common method for determining the quantum yield is to compare the wave length integrated intensity of the unknown with the standard. To prevent of inner filters effects, the optical density is kept below 0.05, or the optical densities of the sample and reference (r) are equal at the excitation wavelength. The quantum yield of the unidentified molecule is determined by

$$Q = Q_R \frac{I}{I_R} \quad \frac{OD_R}{OD} \quad \frac{n^2}{n_R^2}$$

Where Q is quantum yield, *I* is the integrated intensity, OD is the optical density and n is the refractive index. The reference fluorophore of known quantum yield is denoted by the subscript R. It is not essential to adjust for the various excitation intensities of various wavelengths because it is assumed in this expression that the sample and reference are excited at the same wavelength. This ratio was calculated by taking into account the intensity that a detector in a medium with refractive index n_0 observed from a point source in a medium with refractive index n_i. So the ratio $(ni /n_0)^2$ influences the observed intensity [36]. And this highly present the importance of sensitivity of fluorophores used in fluorescent nanosensors [36].

1.3 Exploring fluorescent nanosensors potential for biological application

Nanoparticle based optical sensor technology has been developed over the past quarter of a century, with first particle based sensor reported by Sasaki *et al* in 1996 and the first nano-sized particle sensors named PEBBLE (Probes Encapsulated by biologically Localized Embedding) for measurement of pH [37].

Fluorescent nanosensors are an exciting tool used in multidisciplinary research [38]. They have several advantages: i) reversible response, ii) non-invasive when used for biological measurement, iii) reliable sensitivity and specificity, iv) capability of using ratiometric measurements [26]. To make ratiometric measurements, two different fluorophores are incorporated into the nanoparticle matrix, one of them is an indicator for the analyte and the other acts as a reference (not sensitive to the analyte) and the intensity ratio is obtained, rather than an absolute intensity. The goal of using this approach is to overcome the drawbacks that affect using single intensity measurements such as fluctuations of excitation light source, detector sensitivity and sensor concentration [39]. Chauhan *et al* utilised a combination of fluorophores; Oregon green and carboxy fluorescein, as indicators to measure pH and platinum porphyrin as an indicator dye to measure and molecular oxygen [15]. There are various sensing modes based on fluorescence, including intensity, lifetime, energy transfer and quenching efficiency, that can be correlated with detection and quantitation data of the analyte [40].

1.3.1 Versatility of chemical tailoring of nanosensors

Several studies have recently been conducted with the use of nanomaterials, especially nanoparticles, such as silica [6, 7], polylactic acid nanoparticles (PLA) [8], poly (lactic-co-glycolic acid) nanoparticles (PLGA) [9], and polyacrylamide [10]. NPs have properties that can be addressed to meet the requirements for implementation in the body [22, 41, 42]. The key properties that allow NPs synthesised from these materials to act as nanosensors are summarised as follows:

- Matrix of polymeric NPs can be prepared by standard and cheap chemicals.
- Monomers are polymerised to form inert material that shields sensing fluorophores from interference cell components [43].
- The polymeric materials have the capacity to be functionalised to facilitate the incorporation or conjugation of sensing moieties [22].

The chemical versatility of the nanosensors allows for surface-functionalisation where the surfaces present a chemical reactive group, which may be amino, carboxyl or thiol [44]. This group can then be included in a variety of conjugation strategies to link sensing or targeting moieties to the NP, these interactions can be facilitated via covalent, non-covalent and electrostatic mechanisms as detailed below:

1) In the form of a carbodiimide-mediated reaction between the amino and carboxylic group, to form an amide group using 1-ethyl-3-(3-(dimethylamino) propyl) carbodiimide hydrochloride (EDC) chemistry. The typical procedure involves activation of the carboxylic acid (-COOH) group by EDC and the N-hydroxysulfosuccinimide sodium salt (sulfo-NHS) in a buffer to produce an active O-acylisourea intermediate, which can then react with the amino ($-NH_2$) group contained in nanoparticles to yield a stable amide bond Figure 1-6 A [45].

2. The azide–alkyne cycloaddition reaction catalysing by influence of copper, Figure 1-6 B**.**

   Noncovalent linkage, which includes electrostatic interactions between cationic NP with anionic biomolecules Figure 1-6 C [46].

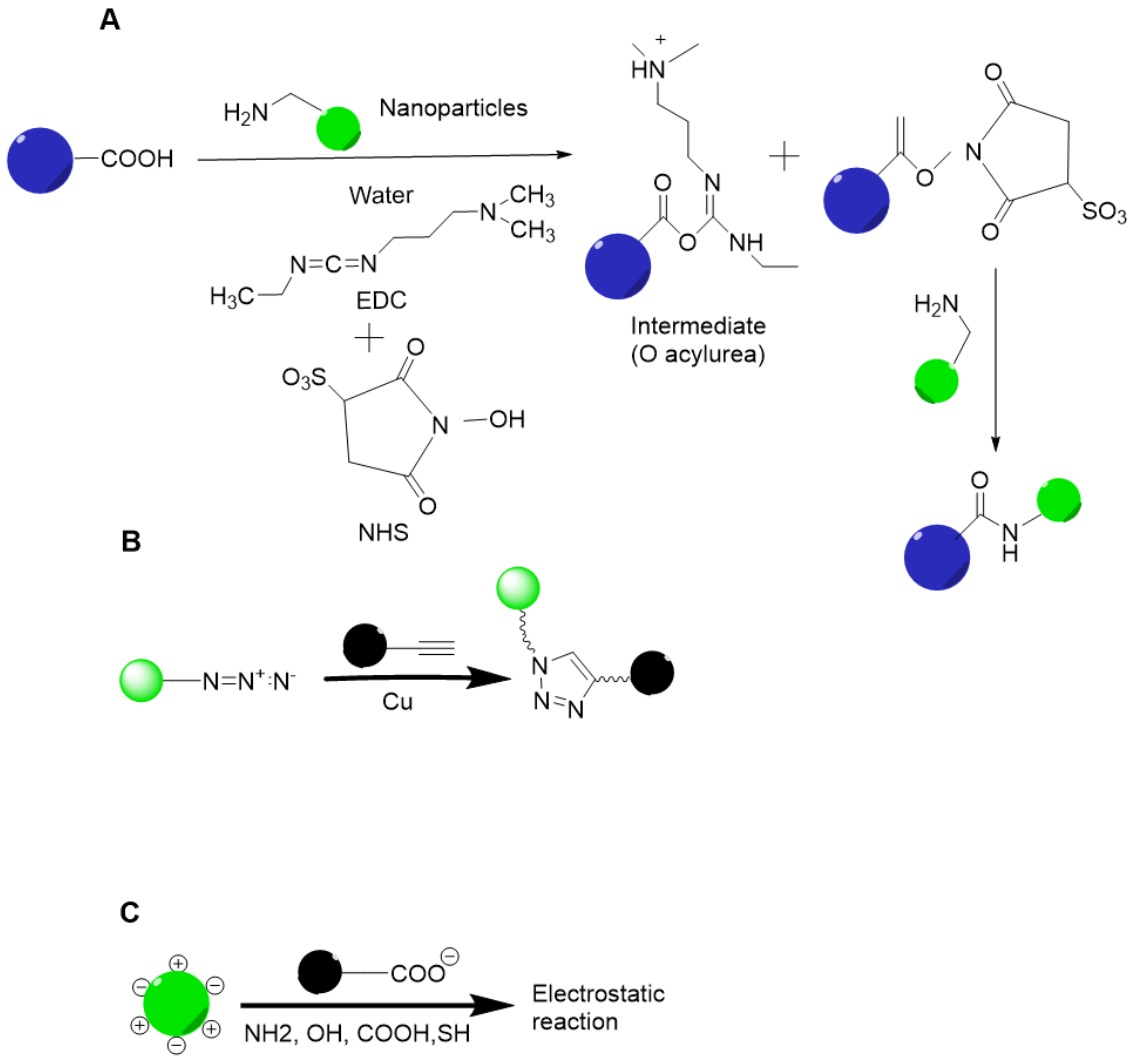


Figure 1-6: A) Carboxylic acid of biomolecules (blue) conjugation to amino-functionalised nanoparticles (green) by carbodiimide-NHS mediated coupling. B) Conjugation of azido- and alkynyl-functionalized polymeric nanoparticles using Cu as a catalyst. C) Electrostatic reaction.

1.3.2 Dye loading strategies

The mechanism of loading fluorophores into polymer NPs is important for the efficiency of sensing properties. The most common limitation of NPs with entrapped fluorophores is leaching of the fluorophores from the particles into the environment (e.g cytosol of cells) which decreases brightness of nanosensors, increases the background signal and can cause negative effects to the sample [47]. Therefore, a range of different approaches are used for loading fluorophores into particles. These include covalent, non-covalent and electrostatic, as mentioned above. Non-covalent methods are largely performed by physical entrapment, which can be through linking a fluorophore to a larger molecule such as dextran [22] or through polymer through swelling [48]. This process is simple, however it suffers a major limitation of dye leaching. This leaching can be resolved to some extent by selecting of hydrophobic or hydrophilic dyes which are better retained in the polymer matrix [49].

Another problematic aspect of loading dyes in polymer NPs is that aggregation can cause a quenching effect, which in turn reduces quantum yield and brightness of the fluorescent NP. Therefore design of fluorescence dyes and conjugation method to NPs are the key aspects to reduce aggregation [50]. This problem can be overcome by using covalent attachment of dyes to NP matrices, to prevent π – π interactions which is called pi-stacking [51], and optimise signal generation.

The requirements of dye-loaded NPs for photo-stability, brightness, and rapid response are suitable for bio-imaging applications [52]. To date, fluorescent NPs have been used for labelling biological targets or tracking the behavioural change of cells

[53, 54]. In this thesis, research will focus on oxygen and pH nanosensors that will be detailed in the next sections.

1.3.3 Examples of nanosensors used for biological applications:

1.3.3.1 State of the art of the pH nanosensor

Determination of pH is one of the key markers for monitoring biochemical and metabolic pathways of intracellular processes [43]. Additionally, pH changes have an extracellular effect on medicinal compounds penetrating to the therapeutic target [55, 56]. In early works, sensors had been developed to be used at the micro-scale such as fibre optics [57, 58]. The first fibre optic sensor was introduced in the early eighties by Peterson et al. It was introduced to monitor blood pH based on the absorbance change of phenol red, which is a pH indicator [59].

Fibre optics are composed of a hair-thin fibre which is made of plastic or glass. It is surrounded by cladding which acts as the outer reflecting layer [60]. Optical fibre sensors are often characterised by the presence of a distal tip containing the sensing fluorophores. They have has a small tip dimension, which has the capability for cellular insertion [61], Figure 1-7. Such systems can be coupled with microscopy techniques to characterise local changes in fluorescence within a biological system.

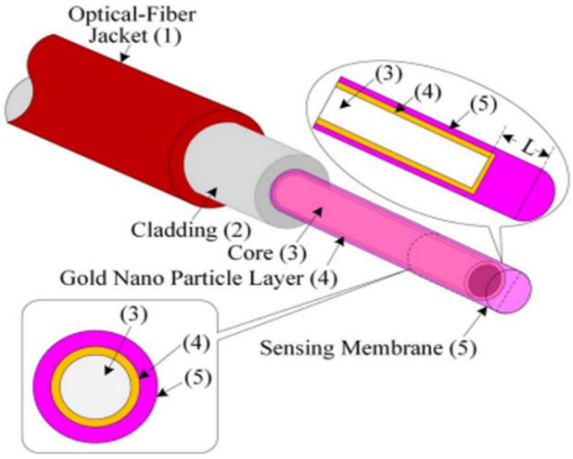


Figure 1-7: Schematic of the fibre-optic probe with a sensing membrane [62].

The advantages of this approach are fast response, low cost, ease of fabrication and detection range is often ideal for measurements in biological systems [63]. However, fibre optics are limited for biological measurements due to cell perturbation as a result of membrane puncture. Therefore, there is a desire for alternative methods that are non-invasive and offer more reliability [64].

Among the several methods for monitoring pH, fluorescence nanosensors are widely used. One such example is an optical pH nanosensor composed of an indicator dye which is entrapped or adsorbed by covalent linking in a proton permeable polymer matrix, Figure 1-8 A [22]. Another approach of nanosensor which is encapsulate indicator and reference dyes in polymeric matrix, Figure 1-8 B.

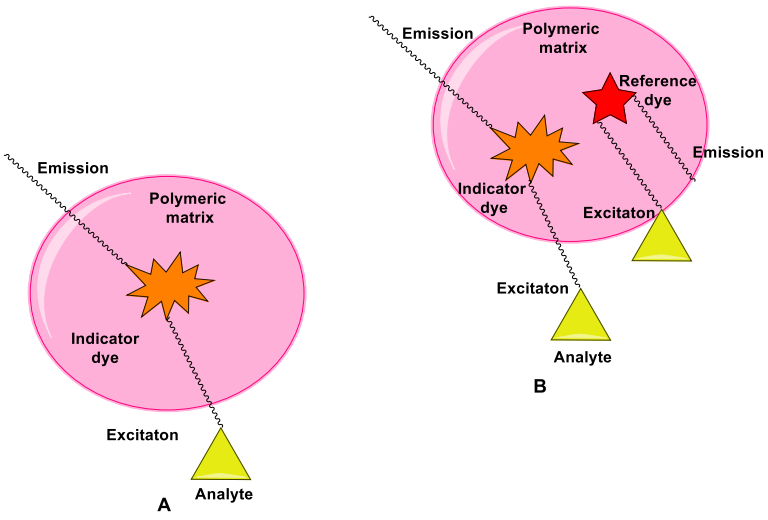


Figure 1-8: Design of nanosensors A) nanosensors with single indicator fluorophore B) nanosensors with ratiometric design indicator and reference fluorophores.

There are many commercially available fluorophores that are pH sensitive and used as free dyes for the measurement of pH, such as fluorescein derivatives, naphthalimide derivatives, rhodamines and boron-dipyrromethene (BODIPY) dyes, presented in Table 1.1. However, free dyes have been shown to be unreliable when measuring biological systems, affecting cellular organelles by causing photo-toxicity or binding to cell components such as proteins [65]. Therefore, the idea of coupling or entrapping fluorophores within biomaterials was developed [66].

Fluorescein derivatives are the predominant fluorophores used for cellular measurements, both as free dyes and within nanosensors. This is due to its versatile chemistry and near-neutral response of fluorescein and its derivatives. The equilibrium between the carboxylic functionality and the lactone group which is highly dependent on surrounding pH, and leads to changes in photo-physical properties, is shown in Figure 1-9. At a neutral pH under excitation 490nm, the most fluorescent di-anionic form dominates over other forms. Mono-anionic fluorescein exhibits a blue-shifted

absorption below pH 6.4, followed by a sharp decline in fluorescence. Neutral and further cationic versions of fluorescein become non-fluorescent when exposed to radiation at even lower pH levels [67, 68].

To obtain maximum sensitivity of pH measurements, especially when attempting to extend the dynamic range, a careful selection of the fluorophores ratios with tuned pKa should be considered [69].

Table 1.1: Most common commercial available fluorophores

Fluorophores	pKa	Excitation/Emission	Reference
2′,7′-Bis-(2-carboxyethyl)-5-(and-6) carboxyfluorescein (BCECF)	6.97	508/530	[70]
Carboxyfluorescein (5(6)-FAM)	6.4	490/520	[22]
Oregon green	4.7	490/520	[22]
PHRodo	6.6	561/585	[71]
CypHer 5E	6.3	644/633	[72]
Chromenoquinoline	2.32	352/414	[73]

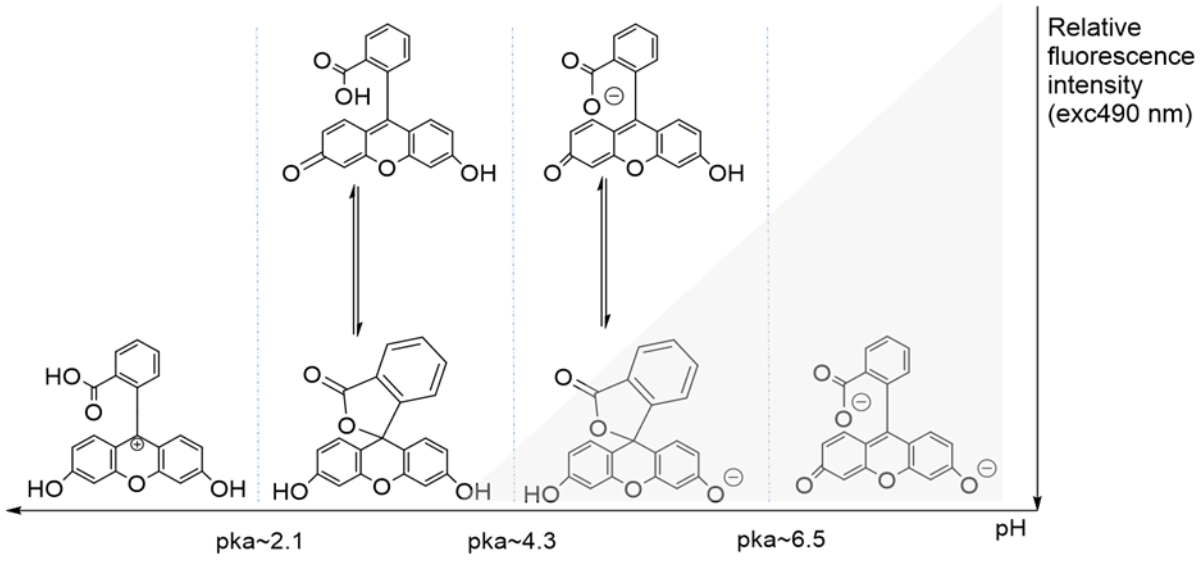


Figure 1-9: fluorescein derivatives structure equilibrium that change with pKa [68].

1.3.3.2 State of the art of oxygen nanosensors

Gauging oxygen tension by measuring dissolved oxygen (DO) has considerable importance as an indicator for the cellular environment, particularly to detect defective metabolism [74] and to study tumour respiration [75], and has additional importance in diagnosing disease and cancer associated with excessive reactive oxygen species (ROS), which is a by-product of the metabolic reactions of DO [76].

Although extensive research has been carried out on measuring oxygen by describing the consumption rate or measuring extracellular environmental oxygen, no adequate studies explain cellular dynamic oxygen change. Therefore, finding a technique for the real-time measurement of oxygen is extremely important. Measuring oxygen would provide a diagnostic sign of respiration dysfunction of cells which would consequently causes the disruption of physiological activity.

Historically, there are several methods proposed for the determination of DO. The first method for the determination of oxygen in water was the Winkler titration in 1888, which was devised by Lajos Winkler [77]. The basic concept of this method is that the oxygen quantified in the sample oxidizes iodine ions to iodine quantitatively; the amount of iodine is then determined by titrating with a standard thiosulfate solution. To assign the end point, there are two methods: 1) automated method by reading the absorption of ultraviolet light and 2) a manual method by using starch indicator [78].

Another significant method for measuring dissolved oxygen was initiated with the invention of the Clark electrode and is still applied today. The sensing concept is based on polarography, where a platinum oxygen-sensitive electrode and silver reference electrode are combined and immersed in a KCl solution. The principle is based on measurement of the potential of the electric current between electrodes, which is proportional to the oxygen partial pressure in aqueous solution. The main disadvantage of this approach is the oxygen consumption by the system, which leads to incorrect measurements at low pO_2 levels [79].

Being aware of the limitations of the above techniques, fluorescent nanosensors have been developed for oxygen measurement. They have a powerful advantage comparing to other approaches, in that the miniaturisation can be simply performed, and they are not limited to point-to-point measurement. The majority of oxygen optical sensors are based on the collisional quenching of the excited state of a luminescent indicator dye by oxygen [39, 80-82].

The most commonly utilised indicators used for oxygen sensing are ruthenium complexes, porphyrin complexes, iridium (III) complexes, osmium and rhenium complexes and lanthanide complexes. The luminescent dyes such as ruthenium polypyridyl complexes and palladium/platinum have been attractive in the field of oxygen sensing due to their tuneable spectroscopic and chemical modification [83], high quenching efficiency, photo-stability, long lifetimes, solubility in the polymer matrix and ability to be excited by low-price sources such as an LED or diode laser [84].

Among all of the luminescence oxygen nanosensors reported in literature, the probes that utilise the principle of detection by the quenching of oxygen show great promise as, firstly, they can be fabricated to be non-invasive and sensitive to oxygen [39], and secondly, they exhibit high spatial and temporal resolution that can be obtained when imaged with optical microscopy [85]. The concept of quenching involves a dynamic collision between the molecular oxygen and the (triplet) excited electronic state of oxygen sensing probes, Figure 1-10 [40]. This is interaction considered as photo-physical and not a photo-chemical process [47].

Investigations have been carried out to challenge oxygen sensors to test their reversibility response which is crucial for monitoring of cell kinetic of oxygen depletion and cell recovery [86-89]. Studies have been conducted by exposing intracellular sensors to oxygenated and deoxygenated environment by controlling oxygen concentration, these studies have been shown a reversible response of deoxygenated and oxygenated cellular environment, Figure 1-11.

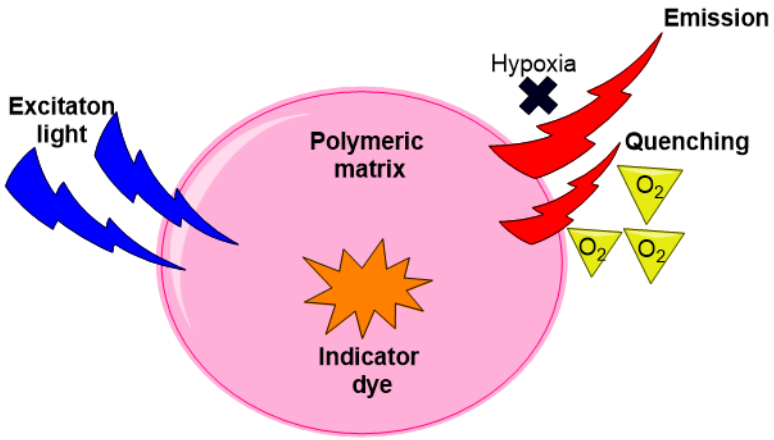


Figure 1-10: Luminescence of indicator dyes quenching by oxygen.

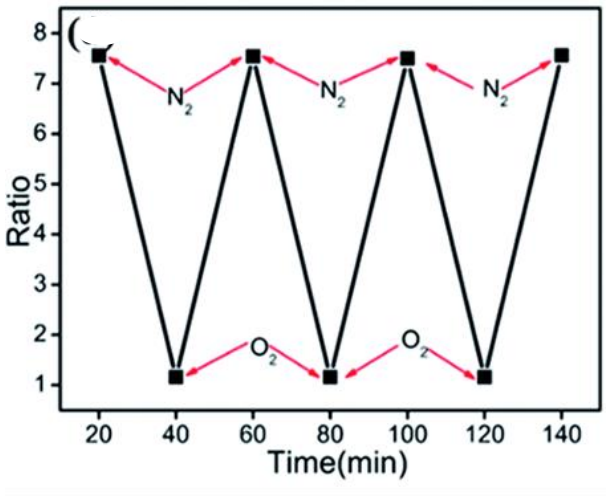


Figure 1-11: Reversible response of oxygen nanosensors to deoxygenated air by nitrogen gas and oxygenated air by oxygen. X axis (time of response), Y axis (ratio measurement of indicator dye porphine (PtTFPP) / Coumarin 6 (C6)) [90].

With regard to the correlation between the concentration of oxygen [O_2] and intensity (or decay time), it can be explained by the Stern-Volmer equation:

$$F_0/F = t_0/t = 1 + K_{SV}\,[O_2]$$

In this equation, F_0 and F are the fluorescence (luminescence) intensities of a probe in the absence and presence of oxygen, respectively; K_{SV} is the Stern–Volmer constant, which is a constant of the lifetime of the probe and the (polymeric) solvent, and [O_2] is the concentration of oxygen in the sample. The dissolved oxygen [O_2] may be replaced by the partial pressure of oxygen (pO_2).

A sensor limit of detection (LOD) can be determined by the Stern-Volmer constant. The LOD can be derived from the initial slope (K_{SV}) of the quenching plot and by the resolution of the instrument.

Fluorescent nanosensors have lower K_{SV} values in comparison with phosphorescence-based nanosensors, and therefore they have higher LODs [91]. Therefore, phosphorescence probes with long lifetimes are required, in order to obtain sensitive measurements at low oxygen concentrations. In this regard, Wang *et al*. mentioned numerous oxygen sensing dyes in their review [91]. Comparing K_{sv} between fluorescence polycyclic aromatic hydrocarbons (PAHs) dyes with metal–ligand complexes dyes, data has been found that shows the enhancement of sensitivity metal–ligand complex dyes, data has shown the enhancement of sensitivity with metal-ligand complexes due to phosphorescence properties. That was specifically revealed with metalloporphyrin which exhibits a sensitivity of K_{sv} equal to approximately 83% [92].

Metal-Ligand complex dyes

Luminescent oxygen-sensing probes are classified into four groups: 1) organic sensing probes (mainly polycyclic aromatic hydrocarbons and fullerenes), 2) metal-ligand complexes (transition metal-ligand complexes and metalloporphyrins), 3) intrinsically luminescent nanomaterials [91], 4) multiple emitters and related species [93], Figure 1-12.

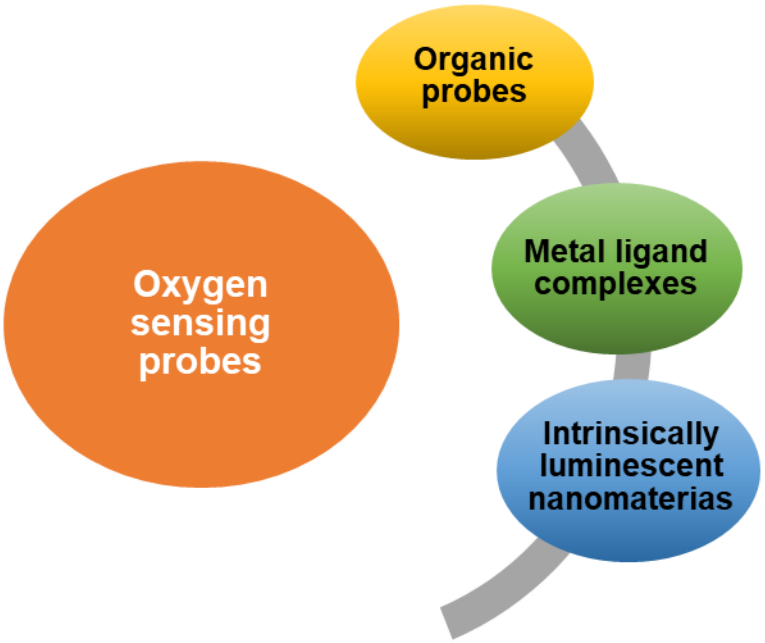


Figure 1-12: Classification of oxygen nano-sensing probes.

Metal-ligand complex probes, Figure 1-13 A, are considered to be one of the most relevant probes for sensing of oxygen. They have the advantages of long decay times and thus a long-lived excited state, which makes collisional quenching by oxygen statistically efficient, they also exhibit large Stokes shifts which enhance their photostablity.

Their structure can be modified to some extent to adjust their chemical and spectroscopic properties, as well as to be capable of conjugation for biomedical applications. A useful example of oxygen sensing dyes are platinum Pt- and palladium Pd porphyrin Figure 1-13 B which have been extensively applied to optical oxygen measurement [15].

Generally, porphyrins have strong absorptions bands between 390 and 420 nm (*Soret* bands). Therefore, the indicator gives a strong brightness when photoexcited via this band in the visible regions (400–550 nm), and bright, well-resolved emissions via the 630–700 nm regions, Figure 1-13 C [94]. Intensity signals from the fluorophore-based sensor can be affected by many factors including dye concentration, optical properties of the sample or photo-bleaching. Therefore, stable and precise calibration is difficult to achieve. To overcome this issue, use of an oxygen insensitive reference and ratiometric measurements are applied to compensate factors that might influence these instabilities [95].

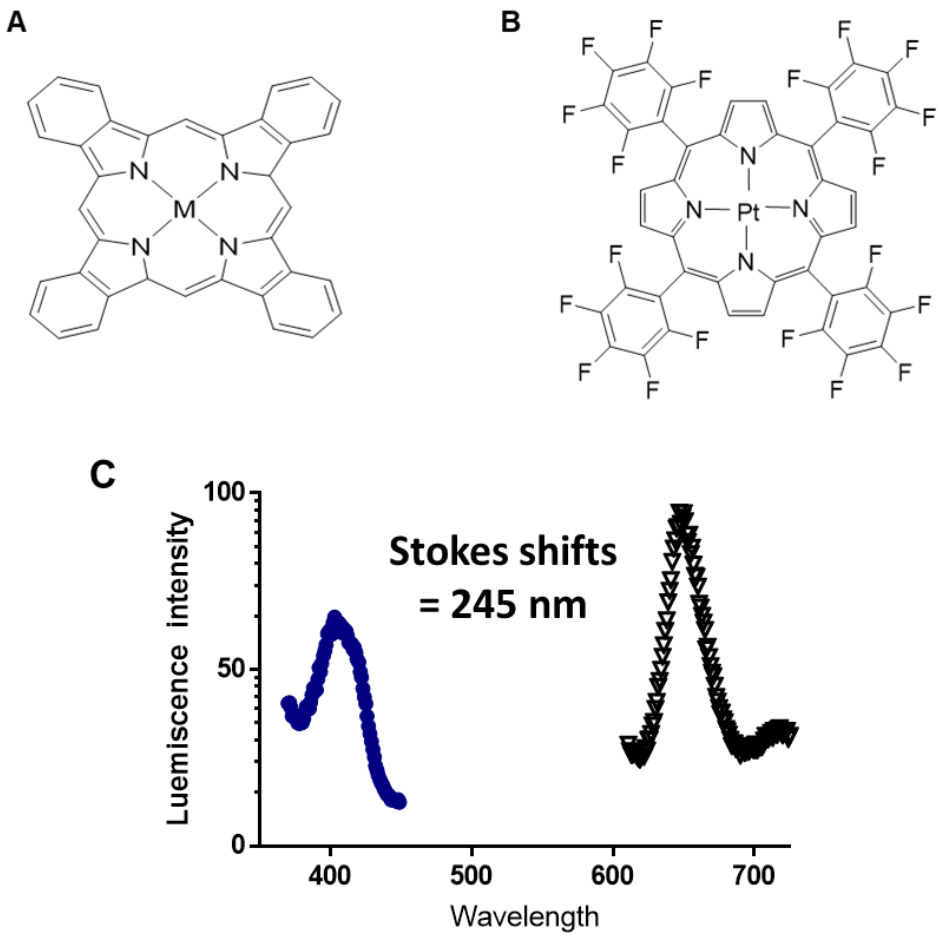


Figure 1-13: A) Chemical structure backbone of major oxygen sensing probes (tetraphenyl pyrol) based on metallo-porphyrin. B) 5,10,15,20 tetrakis pentafluorophenyl porphyrinatoplatinum (Pt TFPP). C) The spectrum of absorption and emission of porphyrin.

In addition to Pt and Pd porphyrins, there are other metal centres incorporated into porphyrin compounds and used for biomedical applications. For example zinc for generating reactive oxygen species in photodynamic therapy [96]. Interestingly, it has been shown that metal free-forms of porphyrins are strongly quenched by oxygen. This distinction of oxygen quenching is further exemplified in studies using tetraphenylporphyrin which have show oxygen quenched fluorescence reduced by 60%. However, it has been reported that its utilisation for sensing oxygen is limited due to inadequate photo-stability [91].

No doubt that metalloporphyrin probes have been used successfully for measuring oxygen intracellularly [94] and extracellularly using cell cultures, and were shown to be suitable for many conventional imaging techniques. Furthermore, modifying the structure was shown to result in the enhancement of their solubility in aqueous biological environments [45]. Such modifications could be achieved by introducing either positive or negative charged moieties by introducing the charged functional group to improve water solubility such as a single carboxylic group for selective conjugation in mild biocompatible conditions [45, 87].

Although extensive research has been carried out on the development of oxygen nanosensors for improving sensing properties and targeting specific measurement purposes [97-99], there is a lack of research into how the nanosensors are trafficked within cells and the effects of surface-conjugated sensing species of measurement response and intracellular fate.

1.4 Application of nanosensors in biological system

1.4.1 Application of nanosensors in immune system

The immune system exerts a fundamental mechanism in protecting the body from the continuous exposure to pathogens. It is composed of a group of different cells that originate, develop and mature from bone marrow and the thymus. These cells produce molecules, such as cytokines and antibodies, which have a principal role in the immune defence system [100]. The immune system works via two main concepts in protecting the body, relying on the activities of the involved cells: innate immunity and

adaptive immunity. Both innate and adaptive immune responses work synergistically to eradicate external stimuli [101].

Interaction of nanoparticles with the immune system can cause its suppression or its overstimulation, and therefore investigations are required to be conducted before using nanoparticles in biological systems [102]. Additionally, macrophage phenotypes can be reversed by reprogramming the polarised macrophage [103]. Thus, macrophage reprogramming plays a crucial role in maintaining immune system homeostasis. Further, macrophage reprogramming explains immune pathways for evaluating the mechanism and treatment of disease [104]. Polarised macrophage status is usually characterised using multiple approaches. These methods include quantification of cell surface markers, transcription factors and cytokines, often using flow cytometry. The method of characterisation was developed to be rapid and does not require a large number of cells using a fast imaging-based approach, which distinguishes cell size and morphology using a fluorescence microscope [105].

Nanoparticles are often used intracellularly for cell imaging and tracking of organelles or for therapeutic delivery purposes, but there are inadequate studies for cell tracking and assessment of its phenotype status and metabolic functionality [106]. Interestingly, immune responses are dynamic reactions, and to check the overall reactions, evaluation of cell responses at different times are needed [107]. Indeed, dynamic monitoring of biomarkers has been investigated and controlled using nanosensors interacting with the immune system [108], which can produce answers for important research questions seeking to understand receptor-mediated pathways [109].

It has been proven that nanosensors are actively phagocytosed by macrophages [110]. This provides opportunities for real-time monitoring inside and outside the cells due to different features between phenotypic metabolic modulation [105]. It is important to note that measurement of acidification and respiration are powerful for assessing glycolysis and oxidative phosphorylation [111, 112]. Additionally, abnormality in oxygen and pH concentrations could be a sign of a disease state or inflammation [113].

1.4.2 Monitoring of respiration in cancer model

It is understood that cancer cells maintain their metabolism by reprograming strategies to meet their energetic needs [114]. Cancer cells have their own metabolic features. That means cancer cells take up the glucose and glutamine at a high degree for aerobic glycolysis [115]. It is well known that mitochondria play a key role in energy metabolism and regulation of the cell cycle and have a powerful function of producing ATP through oxidative phosphorylation [116]. In addition, mitochondria play a role in macromolecule metabolism, e.g. lipid, protein DNA and RNA, by producing metabolic precursors and by-products, such as reactive oxygen species and ammonia [117]. Indeed, mitochondria are dynamic and because of this, they have a powerful role in cellular communication through signalling pathways and contact with other organelles, such as endoplasmic reticulum, lysosomes and nucleolus [118]. Therefore, it is well understood that mitochondria coordinate responses and signalling pathways to cellular stressors, e.g. oxidative stress, decrease in cellular nutrients and genetic alteration [117].

Mitochondria are composed of an inner mitochondrial membrane (IMM) and an outer mitochondrial membrane (OMM). The OMM has pores to diffuse large molecules through [119], whereas IMM is a tight membrane for diffusing ions and small molecules. In the inner membrane, oxidative phosphorylation takes place in protein complexes that create an electrochemical gradient across the membrane [120]. The electron transport chain (ETC) is composed of five types of transmembrane protein complexes (I – V).

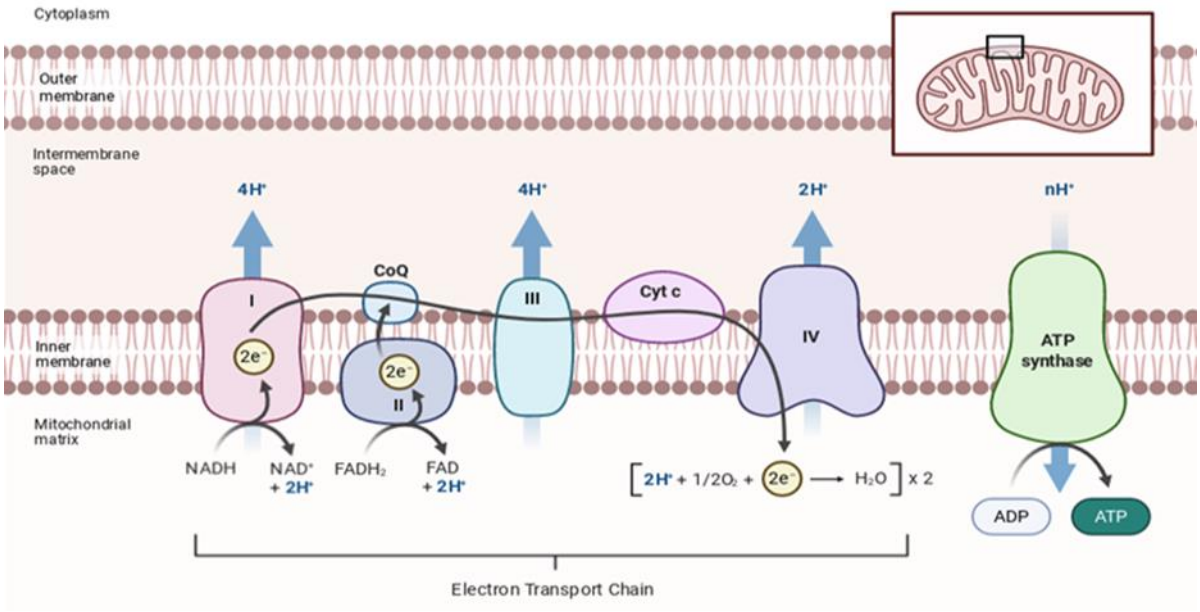


Figure 1-14: Mitochondrial inner membrane complexes structure, generation of electron leaks and proton leaks in the electron transport chain, adapted from Lin Li *et al.* [121].

The electron and proton gradients across the inner mitochondrial membrane are used in the synthesis of ATP in the oxidative phosphorylation process [122]. This process takes place through a sequence of acceptor cytochromes. Oxygen is the final electron acceptor, resulting in the production of water; this process is catalysed by cytochrome c oxidase (COX) (complex IV) [119]. Respiration is considered an important parameter in vitro to study compound toxicity, which is one of the major challenges facing the pharmaceutical industry [123]. For the dynamic determination of a cell response to a drug, several assays are conducted to test compounds in vitro in cell culture [124, 125]. Studies in the literature reported that approach which relies on the light quenching of nanosensors could be applied by obtaining an intensity readout from different instrumentation, such as a fluorimeter and plate reader [126]. Nonetheless, hypoxia imaging provides oxygen concentration, cell morphology, biological insights and dynamic pathways [127, 128]. Hypoxia imaging is a very useful technology for cellular mapping [129].

1.5 Thesis outline

As described in the preface, the focus of this work is the development of fluorescent ratiometric oxygen nanosensors for intracellular measurements using an immune cells and cancer spheroids as models. Additionally, the research will enhance a knowledge of oxygen nanosensors and their behaviour. Moreover, tracking cellular fate of oxygen nanosensors in comparison to pH nanosensors.

Aims and objectives:

1- Optimise oxygen nanosensor response by the selection of fluorophores for ratiometric measurement and conjugating indicator dye (Pt porphyrin) to the surface of polyacrylamide nanoparticle and incorporating reference dye (TAMRA) into nanoparticles, enabling nanosensors to accurately sense micro-environmental oxygen.

2- Calibration of oxygen nanosensors intracellularly using THP-1 differentiated macrophage using imaging microscopy techniques, as well as monitoring oxygen concentration changes using pharmacological compounds (oxygen modulators).

3- Investigate effect of oxygen nanosensors on macrophage phenotypic modulation to M1 or M2 phenotypes. This is to compare the presence of Pt porphyrin conjugated to the nanoparticle surface with the positively charged pH nanosensors.

4- Determine oxygen nanosensors intracellular localisation with regards to lysosomes and mitochondria and compare with cellular uptake of pH nanosensors.

5- Utilise oxygen nanosensors in HepG2 cells and monitor metabolic activity when stressed by insults that disturb electron transport chain (ETC) and consequently change oxygen distribution and link this with biological activity of early apoptosis and necrosis.

The following contents of this thesis attempt to build on research in the nanosensors field to influence their use for real time diagnostic tools of disease state.

Chapter 1: Introduction describes the research development of nanosensors as an advanced tool to explore physiological activity. Consideration of the parameters is required to affect the overall measurement such as nanosensor fabrication, selection of indicators, dye concentrations and loading to the nanoparticles and tracking cellular location. Satisfactory optimisation of these factors could result in successful biological measurements and a better understanding of cellular activity.

Thus, the overall aim of this thesis is to develop oxygen nanosensors for biological research and use analytical techniques such as fluorescence microscopy for ratiometric measurements, with the motive of using of oxygen nanosensors as a tool for the rational study of drug metabolic mechanism and disease progression.

Chapter 2 includes general materials and methods, methodology used making nanosensors, as well as the conditions for cell culture. There is also discussion of the microscopy parameters and methodologies used for calibration and image analysis. While **Chapter 3** elucidates the preparation of nanosensors, including optimisation of fluorophores (Pt porphyrin) and (TAMRA) to achieve measurement of oxygen. The nanosensors were characterised in terms of dynamic range, optical activity, size and

physical characteristics using a range analytical approaches. Further, oxygen nanosensors were calibrated in fixed cells under controlled oxygen conditions, with measurement performed using a fluorescent microscope.

In Chapter 4, oxygen nanosensors were investigated with respect to phenotype modulation in macrophage cells. Sensitivity was studied in fixed and live cells by using enzymatic reaction and oxygen modulators, respectively. **In Chapter 5,** tracking of oxygen nanosensors is performed using super-resolution microscopy. In addition, fluorescence microscopy-based oxygen mapping demonstrate the end point measurement of oxygen in 2D and 3D hepatic cells exposed to different conditions. The conclusions are summarised for each chapter in **Chapter 6.** In **Chapter 7**, the references and appendices of the work in this thesis are presented.

Chapter 2 . Materials and Methods

2.1 Materials Polyacrylamide nanosensors

(Acrylamide, N,N methylene bisacrylamide) monomers, N-(3 Aminopropyl)methacrylamide hydrochloride (APMA), (3-acrylamidopropyl) trimethylammonium (ACTA), hexane and absolute ethanol (analytical grade) were obtained from Fisher Scientific, Ammonium persulfate (APS), N,N,N,N tetra methyl ethylene diamine (TEMED) (initiator), Polyoxyethylene (4) lauryl ether (Brij30®) and dioctyl sulfosuccinate sodium (AOT) (surfactants). Sodium borate decahydrate, glucose (Glu) and glucose oxidase (GO) were obtained from Sigma Aldrich.

Fluorophores: Fluorophores 5- and 6-carboxyfluorescein succinimidyl ester (FAM-SE), Oregon Green® 488 carboxylic acid acid succinimidyl ester (OG-ES) and 5- and 6-carboxytetramethylrhodamine succinimidyl ester (TAMRA-SE) were purchased from Invetrogen™. Porphyrin dye, (Figure 2-1) was donated by Dr Francesca Giuntini from Liverpool University.

Gases: O2 (99.99%, extra dry grade), argon (99.99%, extra dry grade)

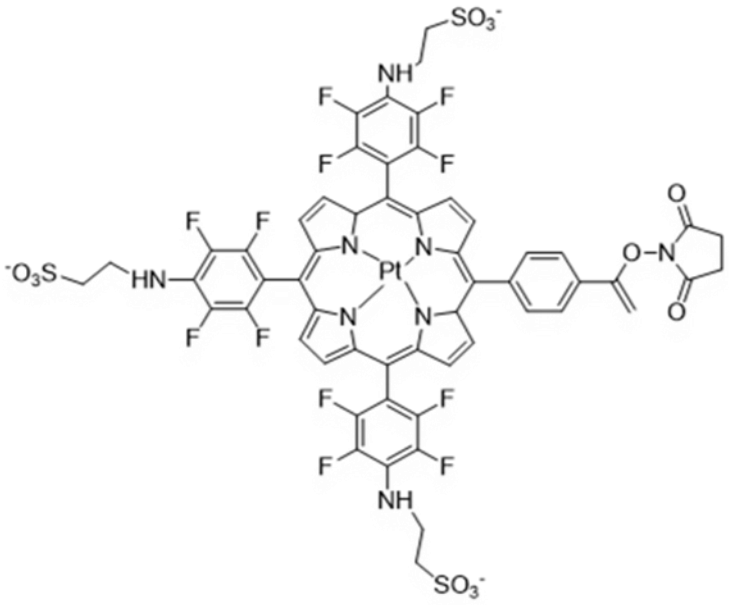


Figure 2-1: Structure of 5,10,15,20 tetrakis pentafluorophenyl porphyrinatoplatinum (Pt TFPP) [45].

Instruments: Centrifuge (Hermle z300), rotary evaporator (Buchi Rotavapor R-200). Fluorescence spectrophotometer (Cary Eclipse Agilent, UK). Ocean Optics NeoFox (NFB0181). Fluorescence microscope**:** *Nikon* Eclipse TS100 Fluorescence Inverted Microscope. Transmission electron microscopy (TEM) (FEI Technai 12, Biotwin). Field emission gun electron microscopy (FEG-SEM), numerical aperture (NA) (20x and 40x), (JEOL 7100F, UK). Fluorescence plate reader (TECAN® SPARK 10M).

2.1.1 Cell culture

THP-1 cell line (with passage number in the range of 3–20) and HepG5 hepatic cells were purchased from American Type Culture Collection (ATCC).

Medium of THP-1 cells: RPMI medium 1640, foetal bovine serum, penicillin/streptomycin solution, HEPES buffer and sodium pyruvate were purchased from Sigma Aldrich. Glutamax® solution was purchased from Gibco.

Medium of Hepatic cells (HepaG2 cell line): Williams' medium E with Glutamax I was supplemented with 10% foetal bovine serum, 100 IU/mL penicillin, 100 µg/mL streptomycin, 5 µg/mL bovine insulin and 50 µM hydrocortisone hemisuccinate.

Plates: Ibid 8-well plates were purchased from Thistle Scientific. 24 well black- glass bottom plate obtained from Greiner.

Alexa Fluor® 488 Anti-CD68 antibody was purchased from Abcam. Mouse anti-human 27E10 primary antibody from Thermo Scientific, rabbit anti-human CD206 primary antibody Abcam. Secondary antibody Rhodamine-X goat anti-mouse IgG (H+L) for mouse 27E10 primary antibody. Alexa Fluor® 488 goat anti-rabbit IgG (H+L) for rabbit anti-CD206 primary antibody from Thermo Scientific. 4,6 Diamidine-2'-phenylindole dihydrochloride (DABI) from Thermo Scientific. TrypLE from Gibco. Goat serum, Trypan blue and Paraformaldehyde (PFA) 4% from Sigma Aldrich. Cell light® lysotracker® was obtained from Invitrogen, phosphate buffered saline (PBS) from Sigma. Human TNF-α ELISA Duoset® DY210-05, Human IL-10 ELISA Duoset® DY2107B.

For metabolic activity: *Alamar Blue*® assay (Invitrogen DAL1025).

Insults (pharmacological compounds): Antimycin and Bafilomycin (Sigma Aldrich), Acetaminophen BioXtra (A7085) and Methotrexate hydrate powder, BioReagent (M8407).

Cell viability: Toxilight® cytotoxic Bioassay Kit by Lonza Bioscience

Apoptosis assay: Annexin V-Biotin Assay Kit eBioscience™

Spheroid preparation: Aggrewell™400 (StemCell Technologies) plates

Cell co-localisation study: Cell light lysosomes – GFP (Invitrogen), cell light mitochondria – GFP (Invitrogen).

2.2 Methods

2.2.1 Preparation of polyacrylamide nanoparticles and conjugation to sensing indicators

The polyacrylamide nanoparticle preparation method used was classified as reverse micro-emulsion polymerization, Figure 2-2. Hexane solvent was deoxygenated by purging a flask with argon for 30 min. In another 100 ml round-bottom flask, 1.59 g of AOT was weighed; 3.08 g of Brij30® was then added and the flask placed on a magnetic stirrer. The flask was sealed with a rubber bung. Argon was then added to the flask through a needle connected to an argon line, while another outlet needle was used to remove gas.

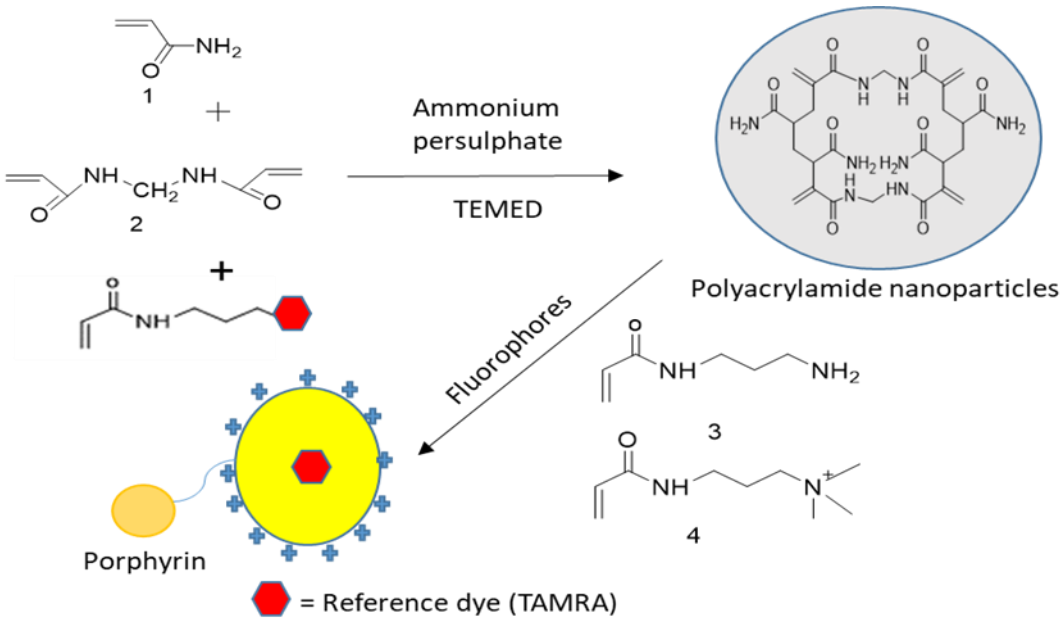


Figure 2-2: Polyacrylamide nanoparticle synthesis scheme. 1) Acrylamide 2) N,N methylenebis (acrylamide) 3) N-(3-aminopropyl) methacrylamide (APMA) 4) (3-acryamidopropyl) trimethylammonium (ACTA).

The monomer solution was prepared by weighing 540 mg of acrylamide and 160 mg of N, N methylene bisacrylamide into a 20 mL glass vial. The mixture was dissolved in 1.5 mL of water by sonication, for the synthesis of ratiometric oxygen nanosensors, 90 µL of TAMRA fluorophore was added to the solution. After that, 42 mL of deoxygenated hexane was added to the mixture of surfactants, and argon was then allowed to purge for 5 minutes, during which a balloon was attached to the outlet needle to maintain an inert environment. The needle connected to the argon line was removed after the balloon was inflated. The monomer solution with fluorophore was added to the oil system using a syringe and needle after which the mixture was left for 10 minutes to allow a micro-emulsion to form.

To initiate polymerization in the same flask, 100 mg of APS was weighed and then dissolved in 1 mL of deionized water to form 10% w/v. solution. The balloon was removed, and 30 µL of APS (10% w/v) and 15 µL of TEMED were quickly added to the flask. The flask was then resealed, and the inlet was reattached to the argon line for 5 minutes until the balloon was inflated again. The reaction was left for two hours to allow the process of polymerization to take place, Figure 2-3.

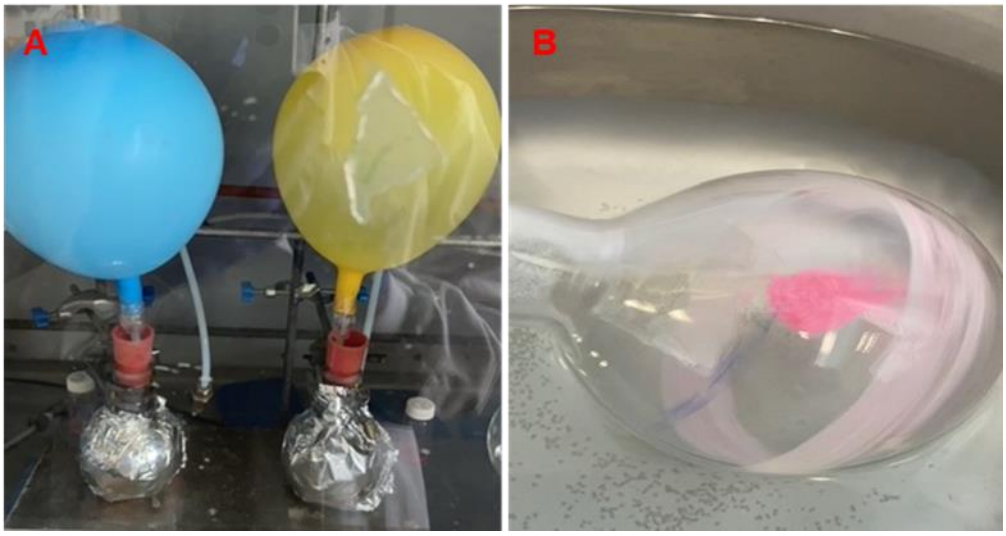


Figure 2-3: A) Round bottom flasks with nanosensors during polymerisation. The flask covered by aluminium foil to avoid photo-degradation of fluorophores. Balloons filled were filled with argon to complete the polymerisation reaction on deoxygenated environment. B) Rotary evaporator of remaining solvent after final wash of nanoparticles produces a dry powder.

Once finished, the stopper was removed, and the hexane was evaporated using rotary evaporation at room temperature until the solution became viscous and cloudy. The viscous solution was reconstituted in 30 mL ethanol, and the solution was poured into a falcon tube and centrifuged at 6000 relative centrifugal force (rcf). The supernatant was discarded, and the pellet was re-suspended in ethanol and centrifuged again at 6000 rcf (g). Washing was repeated five times to ensure purification from surfactants. In the final wash, the pellets were re-suspended in 10 mL ethanol and then evaporated using rotatory evaporation. The dry solid was collected in a light-protected vial and then sealed and stored at -20°C.

.

To prepare the oxygen nanosensors, 100 mg of polyacrylamide nanoparticles containing TAMRA were weighed and mixed with 4 mg Pt porphyrin in 5 mL of deionized water. The suspension was sonicated until dissolved and then left on the stirrer overnight to complete the reaction. The purification step, was performed to remove unconjugated Pt porphyrin from the nanosensors. Dried washed samples were stored at 4°C.

2.2.2. Nanosensor characterisation

2.2.2.1. Particle size and zeta potential

The nanoparticle size was determined using dynamic light scattering (DLS) (Zetasizer nano Zs, Malvern Instruments Ltd., UK) for the mean diameter (d.nm) and polydispersity index (PDI). The analysis was performed at a temperature of 25°C. All samples were diluted for these measurements. The results were recorded after 13 runs for Zetasizer. Surface charge measurements were taken using Zetasizer nano Zs (Malvern Instruments Ltd., UK). Polyacrylamide nanosensors of 0.5 mg/mL were suspended in de-ionised water and loaded into the disposable capillary cells.

2.2.2.2. Fluorescence response

Fluorescence intensities were measured by fluorescence spectrophotometer (Cary Eclipse Agilent, UK) for metalloporphyrin (excitation max. 405 nm, emission max. 650 nm) and TAMRA (excitation max. 400 nm, emission max. 590 nm). Phosphorescence was evaluated by taking a 1 mg/mL dilution of nanosensors in water and purging the suspension with O_2 for increased O_2 concentration, followed by purging with argon for decreased O_2 concentration, using oxygen and argon gas, respectively. The phosphorescence of metalloporphyrin in response to the change in oxygen concentration was measured by fluorimeter. Known oxygen concentrations were

determined using an Ocean Optics NeoFox (NFB0181) phosphorescence-based optical sensor probe and recorded.

2.2.2.3. Field emission gun scanning electron microscope (FEG-SEM)

A polyacrylamide nanoparticle suspension of 0.5mg/mL was diluted in water, and 10 µL of the suspension was distributed on a stub and dried overnight. The suspension was placed on metal, sticky with carbon to render it conductive. Then, the stub was introduced to the field emission gun scanning electron microscope (FEG-SEM), (JEOL 7100F, UK) at the Nanoscale and Microscale Research Centre (NMRC) (Nottingham university).

2.2.2.4. Evaluation of oxygen nanosensors' sensitivity in response to oxygen depletion

A 1 mg/mL oxygen nanosensor suspension was mixed with 6 mM glucose and 1 mg/mL glucose oxidase in a sealed quartz cuvette. The fluorescence intensity was measured using a fluorescence spectrophotometer. In parallel experimental condition in a beaker, the pH was monitored using a pH meter (Jenway model 3510) during the experiment. This was performed to ensure the selectivity of Pt porphyrin for oxygen and monitor formation of gluconic acid as a result of glucose and glucose oxidase reaction.

2.3 Cell culture

2.3.1 Differentiation of THP-1 to macrophage

THP-1 cells were differentiated into macrophages by incubating them with Phorbol-12-myristate acetate (PMA). Two thousands cells were seeded in an Ibidi 8-well plate with 50 ng/mL of PMA-containing medium for 6 hours [130].

2.3.2 Characterisation of M1 and M2 phenotypes

2.3.2.1 Immunostaining

For immunostaining, THP- 1 cell were differentiated as described above in section 2.3.1. Then, the cells were washed with PBS and fixed using 4% PFA for 10 minutes. The cells were incubated for 30 minutes with 1% (bovine serum albumin) BSA as a blocking agent. The cells were then incubated overnight with CD68 antibodies at 4°C. Then, microscopy was used for imaging in the ZOE^{TM} fluorescent cell imager.

2.3.2.2 Characterisation of polarised macrophages to M1 and M2 phenotypes

Characterisation was conducted by immunostaining naïve THP-1 differentiated macrophages, which were seeded with a mixture of 50ng/mL GM-CSF, 20ng/mL IFN-ɣ or 100ng/mL LPS for M1 polarisation or a mixture of 50ng/mL M-CSF or 20 ng/mL IL-4 for M2 polarisation. Usually, M0 macrophages are exposed to a mixture of cytokines for up to 72 hours. The polarised macrophages were stained with antibodies, calprotectin and mannose surface marker receptors, which have been associated with M1 and M2 cells, respectively [105, 131]. The cells were imaged using ZOE^{TM} fluorescent cell imager at red channel (excitation: 556/20 nm, emission: 615/61 nm) and green channel (excitation: 480/17 nm, emission: 517/23 nm) for calprotectin and mannose receptors, respectively. The second method of characterisation was by ELISA. The supernatants of M1 and M2 polarised macrophages were collected, and

the ELISA technique was conducted to quantify TNF-ɣ and IL-10 cytokine production according to the manufacturer's instructions.

2.3.2.3 Calibration of oxygen nanosensors using THP-1 differentiated macrophage

The previously described method in section 2.3.1 for differentiation of THP-1 to macrophage was used. Differentiated macrophages were treated with 100 µg/mL of oxygen nanosensors for 24 hours. Treated cells were washed with PBS three times then fixed with 4% PFA for 15 minutes, followed by permeabilising cell membrane by Triton X 10 (0.5% v/v).

Finally, to calibrate oxygen nanosesnors using the microscope, the cells were placed in an ibidi chamber coupled with a fluorescence microscope. This Ibidi chamber was supplied with oxygen, nitrogen and carbon dioxide gases. The percentage of oxygen was controlled using the Ibidi gas controller, and the cells were imaged at each oxygen concentration.

The fluorescent images of the cells were collected and processed using Image J which will be explained in section 2.4. Figure 2-4 is a schematic of the process from cell differentiation to image analysis.

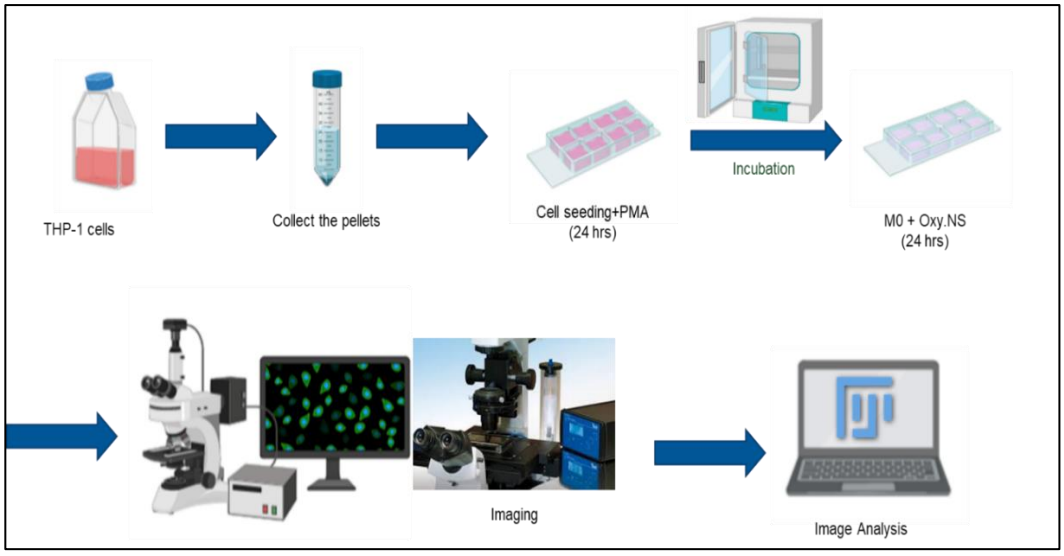


Figure 2-4: Schematic diagram differentiation of THP-1 to macrophages. Then schematic of calibration with oxygen nanosensors using imaging with microscope.

2.3.2.4 Impact of nanosensors on macrophages

Nanosensors impact on macrophage modulation was investigated by collecting the supernatants of naïve THP-1 differentiated macrophages, which were treated with oxygen and pH nanosensors with 100 ng/mL LPS as a positive control. Cytokine production was quantified using Dueset® ELISA kit for pro-inflammatory and anti-inflammatory phenotypes, TNF-ɣ and IL-10, respectively. The protocol was applied as instructed by manufacturer.

2.3.2.5 Stability monitoring of ratiometric fluorescence intensity

A stability test of the nanosensor emission was performed by monitoring the intracellular fluorescence intensity in fixed cells over one week. Macrophage cells after differentiation by PMA as prescribed in (Section 2.3.1); they were treated with 100 µg/mL of nanosensors overnight. The cells were then washed with PBS three times and fixed with 4% v/v PFA for 15 minutes. The cells' fluorescence was monitored

by a plate reader over one week. The fixed cells were preserved at 4°C for 7 days for each experiment.

2.3.2.6 2',7'-dichlorodihydrofluorescein diacetate (H_2DCFDA) assay for detecting ROS

The following protocol was provided by the Invitrogen Company and modified to fit the experimental conditions. The experiment was conducted on THP-1 differentiated macrophages, so the cells adhered tightly to the plate. Macrophages were treated with nanosensors overnight. Then, the cells were washed with PBS three times.

Briefly, H_2DCFDA was dissolved in DMSO to make a stock solution of 2 mM shortly before use. Then, the growth medium was removed from culture plate and attached cells were re-suspended in pre-warmed medium without phenol red. H_2DCFDA was added to the medium at a final concentration of 5 µM as a probe. The plate cells of cells containing H_2DCFDA probe were then incubated at 37°C for 1 hour. Finally, the cells were imaged using fluorescence microscopy of green channel (excitation 495/ emission 527 nm). Image intensities were processed and analysed using Image J.

2.3.2.7 Modulation of oxygen and pH concentration in macrophage cells

THP-1 were seeded at density of 20 x 10^3 /cm^3 in 8-well plate in each well and treated with PMA for 24 hours. After that, the cells were washed and kept in fresh media for 6 hours. For 24 hours, the cells were exposed to 100 µg/mL oxygen nanosensors. In the final step cells were washed with PBS three times then treated with bafilomycin at concentrations 0.25 µM and 10 µM of antimycin for 30 minutes. Untreated macrophage cells were used as a control. Cells were imaged using Nikon wide field microscope.

For modulation of pH, the macrophage cells were prepared as the steps mentioned above. Then cells were treated with 50 µg/mL of pH nanosensors for 24 hours. Then cells were imaged by the same manner.

2.3.3 Hepatic cells (HepaG2 cell line)

Terminally differentiated hepatic cells, HepaG2™ (ThermoFisher), were maintained by continuous passaging.

2.3.3.1 Viability assay using Toxilight® Kit

HepaG2 cell density of 250 x10^3 were seeded on a 24-well plate, with concentrations of oxygen nanosensors ranging from 50–1000 µg/mL overnight. Non-treated cells with oxygen nanosensors were considered as a control. Then, the cells were washed with 1000 µL PBS three times and lysed with lysis buffer, according to the protocol of the assay kit. All reagents were brought up to room temperature before use. Then, 20 µL of cell supernatant was transferred to a luminescence-compatible 96-well plate, and 100 µL of Adenylate kinase detection reagent (AKDR) were added to each well and left for 5 minutes. Finally, the plate was placed in a plate reader (TECAN® SPARK 10M) to initiate recording of luminescence signal of Adenylate kinase.

2.3.3.2 Respiration assay (ratiometric imaging of hypoxia)

HepG2 cells (9–15 passages), were seeded on a 24-well plate at 51 x 10^3cells/cm^2 per well and allowed to adhere overnight. After that, the cells were treated with 100 µg/mL oxygen nanosensors for 24 hours. The treated cells were washed with PBS three times and then treated with 1, 5 or 25 mM acetaminophen for 24 hours.

The same experimental setup was used with 5 mM propranolol, 5 µM antimycin and 250 µM methotrexate for 24-hour treatments. Finally, the cells were imaged with a fluorescence microscope using 20x magnification, 0.4 numerical aperture NA (air objective). Images were processed and analysed by Image J.

Apoptosis assay: The apoptosis assay was carried out for the cells treated with pharmacological compounds which are mentioned in previous (section 2.3.3.2). Cells were exposed to pharmacological compounds for 24 hours. After that, the cells were detached from the plate using 100 µL of Tryple E for 5 minutes. Cell suspensions were collected in 500 µL tubes.

The cell suspensions were then mixed with annexin V/ propidium iodide reagents, as explained in a manufacturer protocol. Finally, data was recorded using a flow cytometer and analysed using Kaluza software. The concept of interpreting the result is based on distribution of cells within the dot plot as in Figure 2-5.

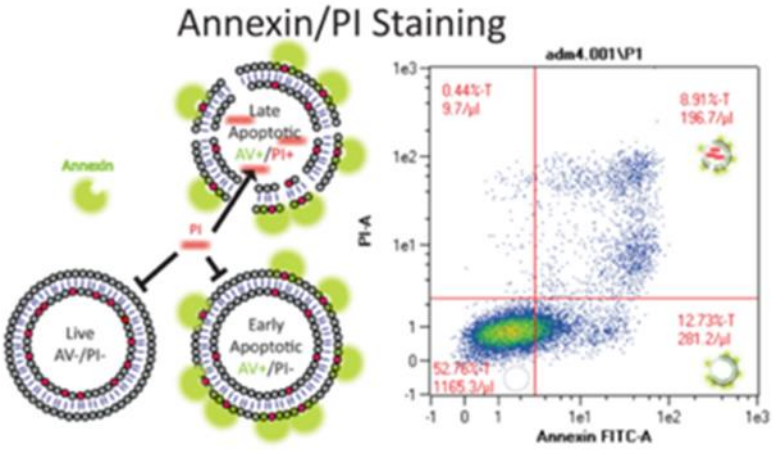


Figure 2-5:Schematic representation of cellular distribution of healthy, apoptotic and necrotic cells in dot plot analysis using Annexin /PI kit [132].

2.3.3.3 Use of imaging flow cytometer platform to test changes in oxygen intracellularly

HepaG2 cells were prepared, as mentioned in section 2.3.3.2, and treated with oxygen nanosensors. Then, cells were treated with the same prescribed pharmacological compounds. After that, cells were detached from the plate for 5 minutes using 100 µL of TrypleE after two time points: 1 and 24 hours. The cell suspension was collected in 1000 µL eppendorf. Finally, cells were imaged using image stream (ImageStreamX MkII, UK) and IDIEA software used for data analysis.

2.3.4 Influence of O_2/pH flux in 3D hepatic cancer cell models measured using fluorescent nanosensors

The study of 3D hepatic cancer cells was performed by preparing spheroids from $HepG_2$ cells.

Spheroid preparation: At confluence, $HepaG_2$™ were harvested with TrypLE Express and seeded into Aggrewell™400 (StemCell Technologies) plates at a density of 1.2×10^5 cells per well. Following the manufacturer's protocol, the plate was centrifuged at 100 g for 3 min, followed by incubation at 37°C with 5% CO_2 for 96 h, Figure 2-6.

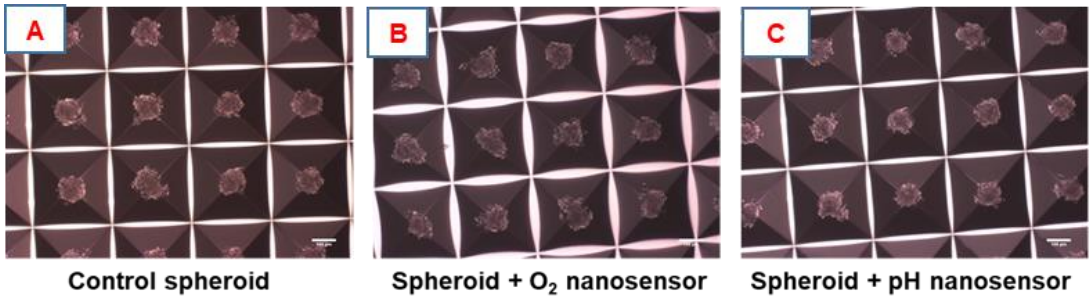


Figure 2-6: $HepaG_2$ cells seeded in Aggrewell ™ plates. A) Control spheroid. B) Spheroid pre-treated with O_2 nanosensor. C) Spheroid pre-treated with a pH nanosensor.

2.3.5 Intracellular fate of nanosensors

Intracellular fate measured with lysotracker®: To label cells with CellLight® specific to lysosome, they were incubated with growth medium containing lysotracker® at concentrations of 10 and 50 particles per cell (PPC)/mL.

The desired concentration was calculated based on the following formula:

$$\text{Volume of CellLight® Reagent (mL)} = \frac{\text{Number of cells} \times \text{desired PPC}}{1 \times 10^8 \text{ CellLight® particles/mL.}}$$

Then, the cells were incubated overnight, washed with PBS three times and fixed with 4% v/v PFA. Nucleus was stained with DAPI for 5 minutes.

The cells were imaged using a super-resolution microscope (ELYRA PS.1 super resolution system from a Zeiss 780), water immersion lens 63x magnification/1.2 NA.

Intracellular fate measured with mitochondria: The same method used with CellLight® lysosomes was applied to label mitochondria using CellLight® specific to mitochondria.

2.4 Development and optimization methodology for ratiometric measurements

The methodology of ratiometric measurements were conducted using fluorescence imaging techniques where the data of intensities was processed from images obtained from wide field microscopy. The methodology tool used to analyse the data was Image J software. In this section, the schematic methodology of image analysis will be explained in detail.

2.4.1 Methodology of image analysis

Image analysis relied on extrapolating the intensities of nanosensors from images, considering that porphyrin intensities changed with oxygen concentrations and that TAMRA intensities remained constant. For pH nanosensors, OG and FAM intensities were changed with pH and TAMRA remained constant.

A chart in Figure 2-7 explains the order of steps used to calibrate oxygen nanosensors in images taken using Nikon Microscope. The steps presented in Figure 2-7 A describe how to deal with raw data in ImageJ software. In the first step, the data was opened in image J software and split in the brightfield green and red channels. Step two states that it is important to remove pixels not related to the real signal. The third step is to mask the signal. Then, ratiometric measurements are taken by dividing porphyrin intensity by TAMRA intensity. The final step is to fit the intensity to the Stern-Volmer equation, which uses the known oxygen concentration to calculate the intensity from experimental images. This equation, which is specifically used to calculate oxygen concentrations, is described in Chapter 1**.** Figure 2-7 B shows a schematic method used to represent oxygen distribution intracellularly. Oxygen distribution or mapping was conducted after calculating the ratio intensities from indicator dye and reference dye and generating the resulted Look up table (LUT) image with multicolour. The important step here is to apply the calibration in calibrate plugins in the software and extract image with calibration bar within calibrated range. Macros of Image J analysis were explained in Figure 2-8.

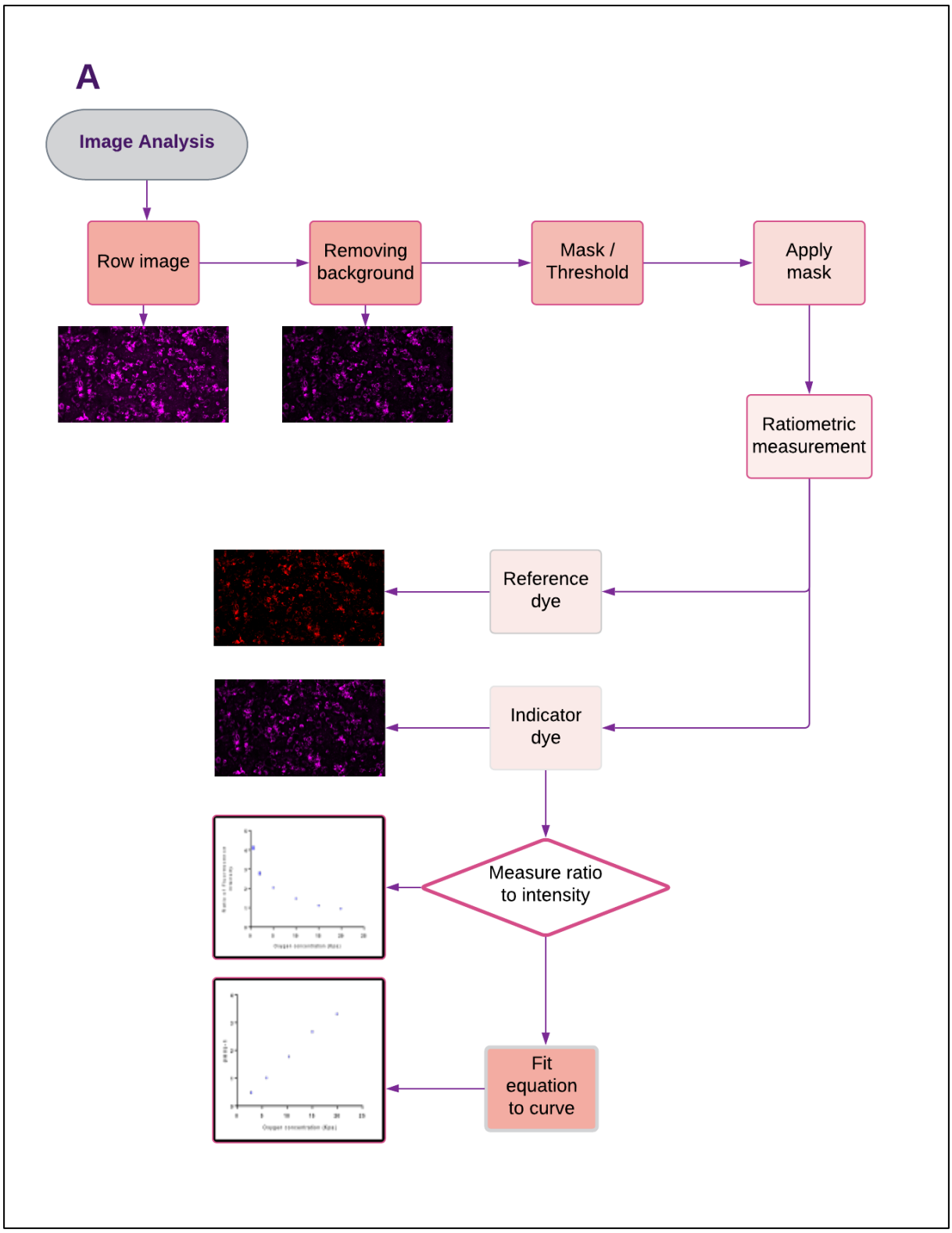


Figure 2-7: A) Schematic representation of image analysis for oxygen nanosensor calibration.

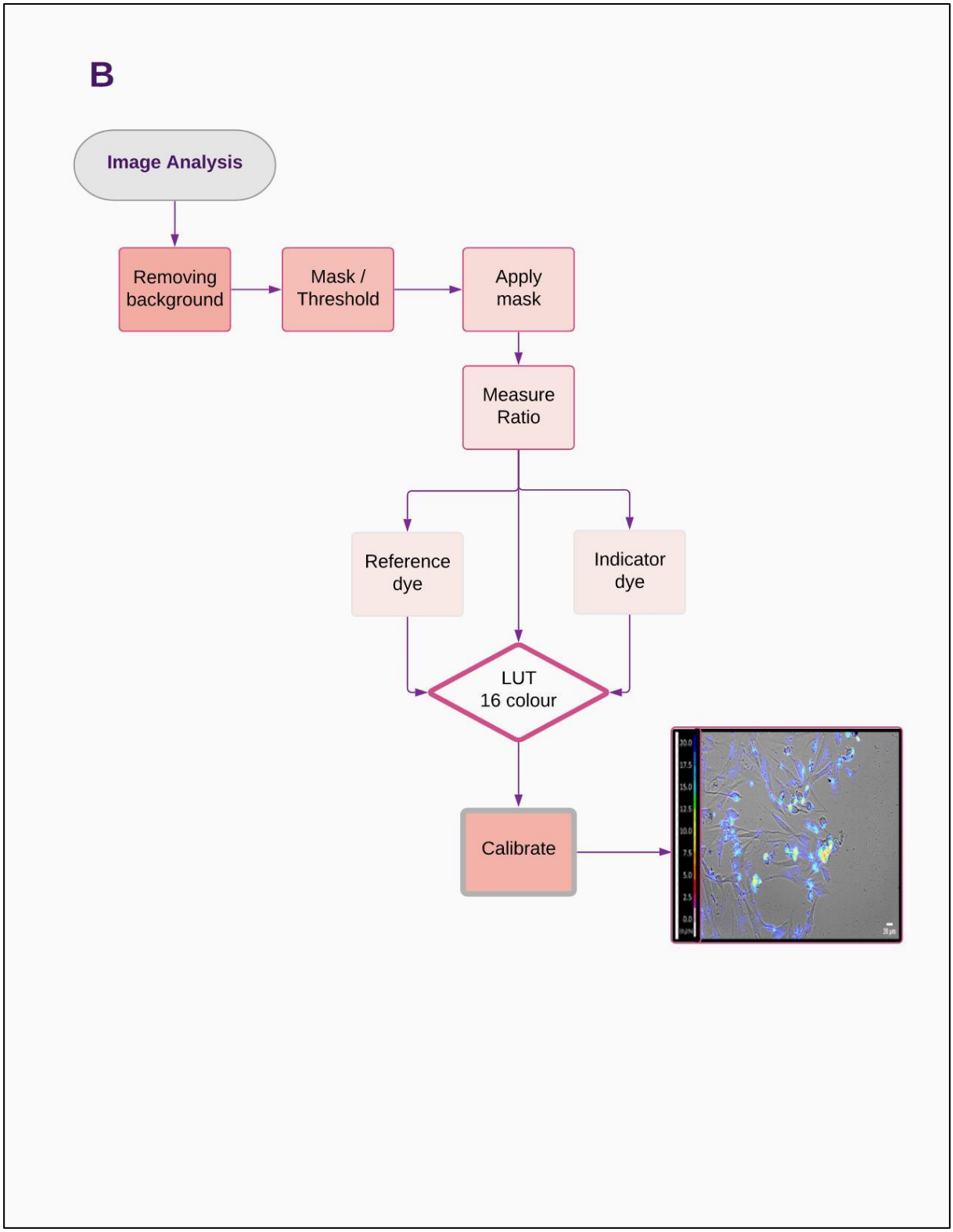


Figure 2-7: B) Schematic representation of intracellular oxygen heat mapping.

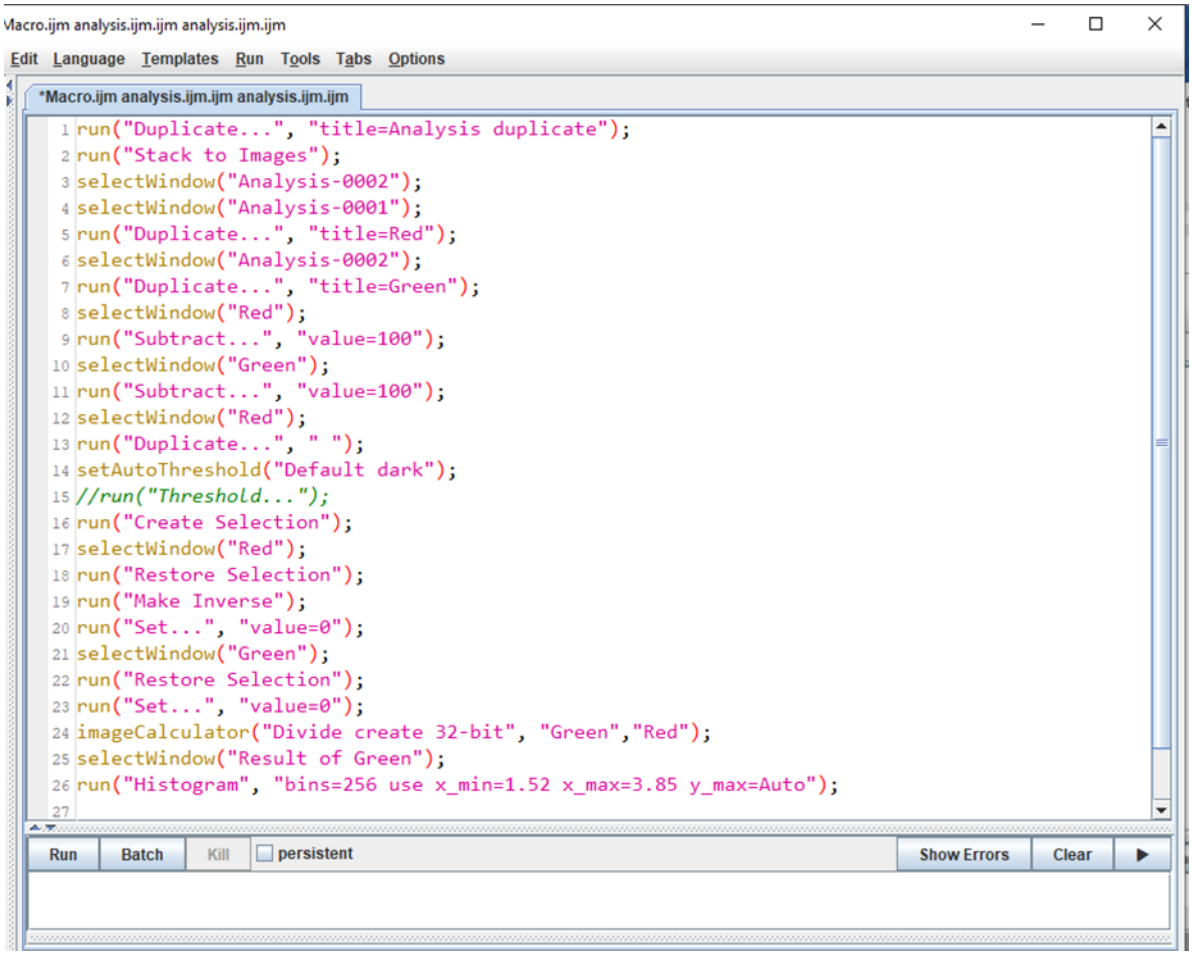


Figure 2-8: Fiji Code and algorithm of used for image analysis to provide a measurement a histogram of nanosensors intracellularly.

2.4.2 Methodology for analysing co-localisation of nanosensors with lysosome and mitochondria

The co-localisation of pH and oxygen nanosensors in the cells was determined by staining lysosome and mitochondria with green CellLight®. To represent co-localisation of pH nanosensors, TAMRA was encapsulated within polyacrylamide nanoparticles, and OG and FAM were not used because of the interference of their colour with green CellLight®. The co-localisation of oxygen nanosensors was represented by TAMRA (red) and porphyrin (magenta), with mitochondria represented by CellLight® (green).

Both methodologies of co-localisation analysis using lysosomes and mitochondria followed the same steps: raw data were opened by ImageJ, and background images were removed. For co-localisation (Coloc 2), shown in ImageJ, channels of the colour under study were chosen, region of interest (ROI), and the co-localisation was measured using Pearson's Correlation Coefficient (PCC), Figure 2-9. The association of two colour variables was considered to be strong when R = 0.5–1, medium when R = 0.3–0.5 and small when R< 0.3 [133].

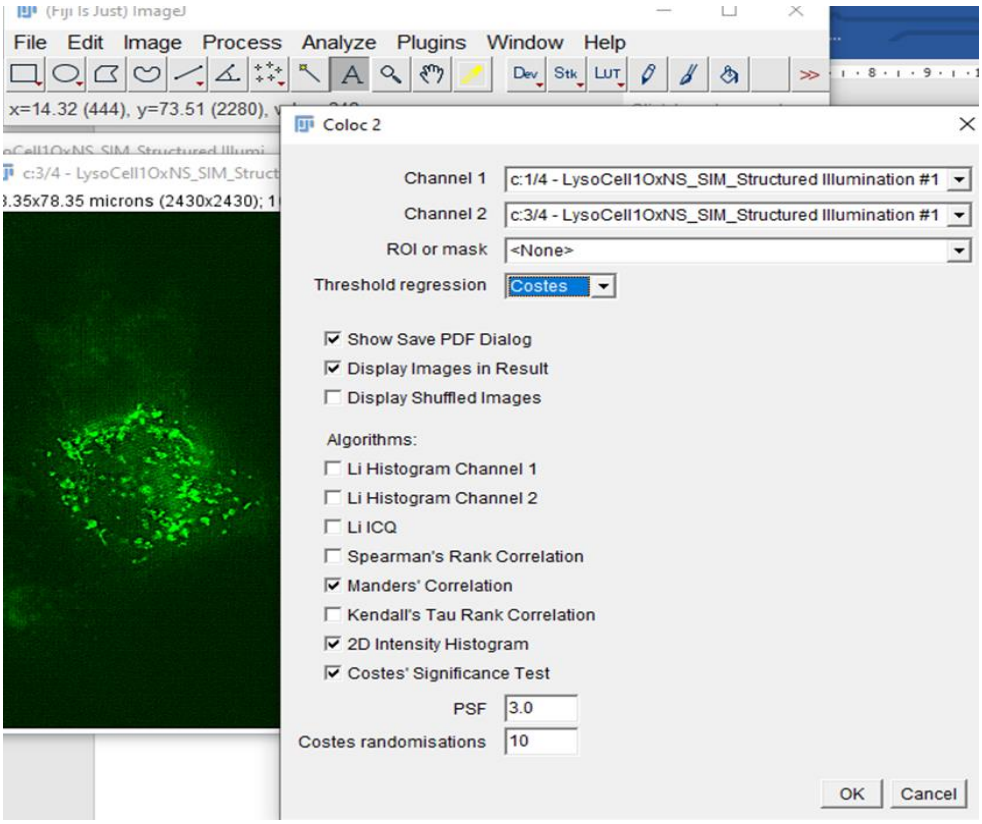


Figure 2-9: Calculation of Co-localisation Pearson's coefficient from coloc2 in image J

2.5 Statistical analysis

The data was generated by multiple experiments to obtain the mean. To test the significance data, one way and two way ANOVA were used depends on variables used. It was performed by GraphPad Prism software. Additionally, comparison between data set was based on P value. ANOVA test: the results of an ANOVA show if there are statistical differences in the group means within a data set, but they do not show which groups are statistically distinct. A set of multiple comparison tests, such as Tukey's and Dunnett's multiple comparison tests, can be used to determine whether groups are statistically distinct. Dunnett's test compares all means to a control mean, whereas Tukey's multiple comparison test compares all means of all study groups to one another. One-way ANOVA analysis and Dunnett's multi-comparison test were carried out for the aim of this thesis.

Chapter 3 .Design, synthesis and characterisation of oxygen nanosensors

3.1 Introduction

The aim of this chapter is to develop optical oxygen nanosensors with optimised conditions to make intracellular oxygen measurements. This was performed in three stages:

- Synthesis of polyacrylamide nanoparticles
- Optimisation of fluorophore conjugation
- Evaluation the sensitivity of oxygen nanosensors

To produce nanosensors for intracellular monitoring, there are two primary design issues. Firstly, the sensor must have features that allow it to be taken up by cells. Second, the sensor must have appropriate optical properties, such as fast response time, high signal-to-noise ratio and sensitivity to gradient oxygen concentration. To ensure accuracy, and be compatible with widely available fluorescence microscopes it is preferred to use ratiometric measurements, which as described in Chapter 1 requires both indicator and reference dyes to be entrapped in the sensor matrix. This can be achieved by optimising both the fluorophores and their conjugation to nanoparticles. Design and optimisation of the fluorophores, and synthesis of the sensors are critical considerations for optimisation and are addressed in this chapter.

3.1.1 Synthesis of oxygen nanosensors

As described in Chapter 1, dye loading or conjugation is crucial for nanosensor efficiency. Covalent conjugation of fluorophores to polyacrylamide was investigated in

this work with the aim of optimising nanosensor response in terms of brightness of dyes and prevention of photo-bleaching.

The methods used in this study, were described in detail in Chapter 2. Nanosensors were fabricated to perform ratiometric measurements by incorporating TAMRA dye into nanoparticles and conjugating Pt porphyrin to the surface of nanoparticles.

3.1.1.1 Polyacrylamide nanosensors

Polyacrylamide is a common type of matrix used for nanoparticle synthesis. It is inert, hydrophilic, porous and inexpensive to produce with standard laboratory equipment [134]. It is a hydrogel copolymer cross-linked to form a polymeric network, which is produced by the reaction of two monomers. These NPs are synthetic polymers and have a well-defined structure that can be modified to yield tailorable functionality. It is synthesised by a method of free-radical cross-linking polymerisation of acrylamide and N, N-methylene-bisacrylamide [66].

Furthermore, robust fabrication techniques for controlling the size, charge, and shape of polyacrylamide nanoparticles are available [22]. It has been shown that a long plasma circulation lifetime (~24 h) rendered them suitable as nano-devices medically capable for imaging and photodynamic therapy [135].

Nanoparticles of 10-100 nm in diameter are considered to offer optimal tumour accumulation as they avoid fast renal elimination and recognition by the immune system (e.g., phagocytes) when applied *in vivo* [89].

Polyacrylamide NPs have a wide variety of applications and have successfully been used as nanosensors, for example measuring pH *in vivo* and in real-time [24], and measuring dissolved oxygen in the physiological environment [15] as well as the monitoring of glucose [66].

Chemical tailoring of polyacrylamide NPs has been shown to be an appropriate method to increase their functionality. Amine functionalisation of polyacrylamide NPs is achieved by introducing of N-(3-aminopropyl) methacrylamide (APMA) into the polyacrylamide matrix. The amine group can be considered as a bridge to bond with the fluorophores via a covalent bond. By covalently linking the fluorophores to the NP matrix leaching is prevented [136].

Additionally, surface modification of polyacrylamide NPs can facilitate the intracellular delivery of nanosensors by introducing nett positive charge to the NP which enables then to cross cellular membranes. This has been demonstrated by incorporating the monomer (3-acrylamidopropyl) trimethylammonium chloride (ACTA) into the polymeric NP [22]. This results in a positive surface charge that is known to facilitate cellular uptake via endocytosis. Accordingly, sensors with charged groups have been functionalised as a method for controlling cellular delivery [45].

3.1.1.2 Porphyrin utilisation for measurement of intracellular oxygen

In the general introduction optical probes were described, particularly luminescence probes that have extensive application in oxygen measurement. Oxygen sensing by luminescence quenching is an analytically powerful tool [137]. Of the number of

luminescence oxygen nanosensors reported in the literature, the probes that utilise the principle of detection by quenching of oxygen show great promise because: (1) they can be fabricated to be non-invasive to the sample and sensitive to oxygen [39] and (2) high spatial and temporal resolution can be obtained when imaged with optical microscopy [95].

As mentioned previously, an important advantage of this type of phosphorescent probes is the spectroscopic and chemical properties that can be modified to some extent via structural modifications. For example, biocompatible attachments of the oxygen-sensitive probes to support materials of interest (polymers, fibres, etc.) would need to be water soluble and provide covalent conjugation to the desired support. Vasil'ev and Borisov fabricated water-soluble cationic complexes of Pt (II), Pd (II) and Rh(III) porphyrins. The synthesised cationic metalloporphyrins were conjugated to an (anionic) ion-exchange matrix to produce sensitive, stable and fast-responding sensor films [37]. Some examples of porphyrins conjugated to nanoparticles are summarised in Table 3.1.

Table 3.1**:** Luminescent metalloporphyrin-based probes for oxygen, the polymer support used and the purpose of using oxygen nanosensors, type of cells used in study, reference.

Type of porphyrin	Materials (conjugated or encapsulated)	Applications	Type of cells used	References
Pt-porphyrin	Polylactic acid (PLA)nanoparticles, PLA alginate nano-microparticles	For oxygen and glucose biosensing	L929 mouse fibroblast cell lines	[87]
Pt-porphyrin	Organically modified silicate (ormosil) nanoparticles	Intracellular oxygen sensing	rat C6 glioma cells	[80]
Platinum octaethylporphine ketone (PtOEPK)	Poly(decyl methacrylate) (PDMA)	Oxygen sensing	Human plasma	[138]
Platinum(II) octaethylporphine ketone or PtOEPK	The ormosil PEBBLE	Cellular respiration	C6-glioma cells	[139]
Pd-tetra- (4-carboxyphenyl) tetrabenzoporphyrin dendrimer (G2)	Polyacrylamide (PAA) hydrogel nanoparticles	Oxygen measurement	A549 human lung adenocarcinoma cells and C6 glioma cells	[89]
Pt(II)-5,10,15,20-tetrakis-(2,3,4,5,6-pentafl uorophenyl)-porphyrin	Eudragit RL-100	Intracellular oxygen	Mouse embryonic fibroblasts MEF cells, Cortices from embryonic age (E)18 rat embryos	[140]
Pt(II)-tetrakis(pentafluorophenyl) porphyrin (PtPFPP)	Eudragit RL-100	Intracellular oxygen	MEF cells	[141]
Palladium meso-tetraphenylporphyrine	Polystyrene nanoparticles	Intracellular oxygen	Murine alveolar macrophages	[142]
Platinum(II) octaethylporphine (PtOEP)	polyfluorene derivatives poly(9,9-dihexylfluorene) (PDHF) and poly(9,9-dioctylfluorene) (PFO)	Oxygen sensing	J774 A1 macrophages	[95]

Ratiometric measurements require two emission bands: one sensitive to oxygen and the other not. Ratiometric measurements allow the determination of concentration while eliminating the effect of nanoparticle concentration, light fluctuations and cellular location of the nanosensors [142]. Reference dyes need to be non-responsive oxygen, and photostable [143]. The emission of the reference dye should not overlap with the indicator dye emission and there should not be any energy transfer. Furthermore, both dyes have to have the similar solubility to ensure their compatibility with the matrix; this will prevent leaching from the matrix [138]. There are several dyes which have been used as reference dyes – some of them are porphyrins [87] and others are commercially available dyes such as TAMRA-SE [15]. Following our interest in using oxygen nanosensors for biological applications, water-soluble Pt-porphyrin sensitive oxygen was conjugated to the surface of polyacrylamide matrix and commercially available TAMRA (reference dye) was incorporated into the matrix.

3.2 Nanosensor characterisation

Nanosensor characterisation involves optical and physical methods to determine the nanosensor properties so that different batches of nanosensors can be compared. Different instrumental techniques are utilised for optical characterization (fluorescence response, brightness and stability). While Field Emission Gun-Scanning Electron Microscope (FEG-SEM), Dynamic Light Scattering (DLS) and Zetasizer are used for physical characteristics (size, charge and shape). All these characterisation methods are discussed in the following sections.

3.2.1 Dynamic light scattering

DLS is a technique used for measurement of a particle size. Its principle depends on the amount of light (intensity) scattered by particles which move in a solution through the effect of Brownian motion. Brownian motion is the random movement of particles in a solution as a result of a collision with molecules in solvents that are moving due to their thermal energy [144], Figure 3-1.

Therefore, when laser light interacts with the particles, light scatters in all directions, leading to the fluctuation of light intensity. This fluctuation depends on the size of particles in solution; larger particles cause the light to fluctuate more than the smaller particles do.

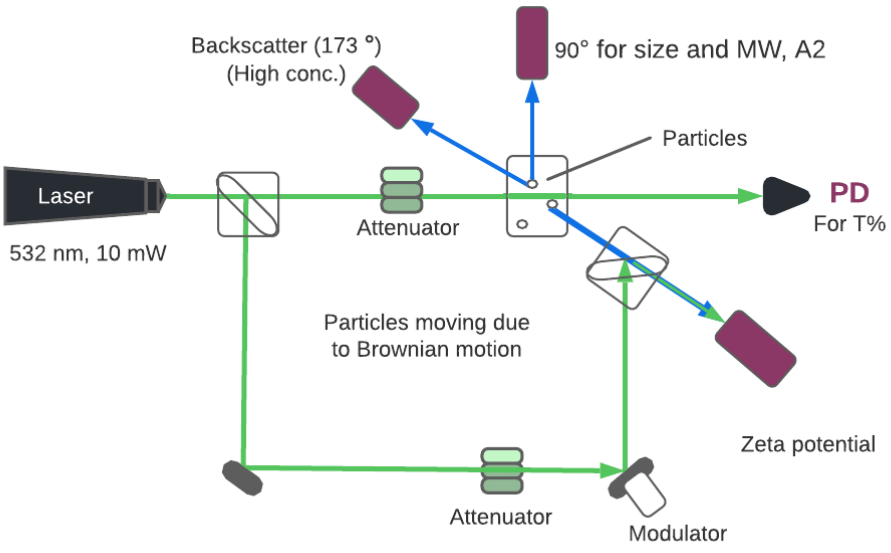


Figure 3-1: Schematic of dynamic light scattering principle, adapted from HORIBA Co. [145]

The size of the particles can be defined by the hydrodynamic diameter, which is the diameter of particles measured in dynamic light scattering in suspension, thus representing the diffusion of particles in the fluid. It can be calculated using the Stokes-Einstein equation by knowing the time-dependent fluctuation in light scattering intensity by calculating the translational diffusion coefficient [146]

$$d(H) = \frac{kT}{6\pi\eta D}$$

Where: d(H) = hydrodynamic diameter

k = Boltzmann's constant (1.38×10^{-23}) J

T = absolute temperature

η= viscosity of solvent

D= translational diffusion coefficient ($m^2.S^{-1}$)

3.2.2 Zeta potential

Zeta potential is the difference in potential between the stationary ions surrounding the nanoparticle and ions in the suspending medium. It is a nett charge developed at the surface of particles which is affected by the distribution of ions in surrounding interfacial region. Therefore, the concentration of counter ions (ions of opposite charge to that of the particle) increased close to the surface, Figure 3-2.

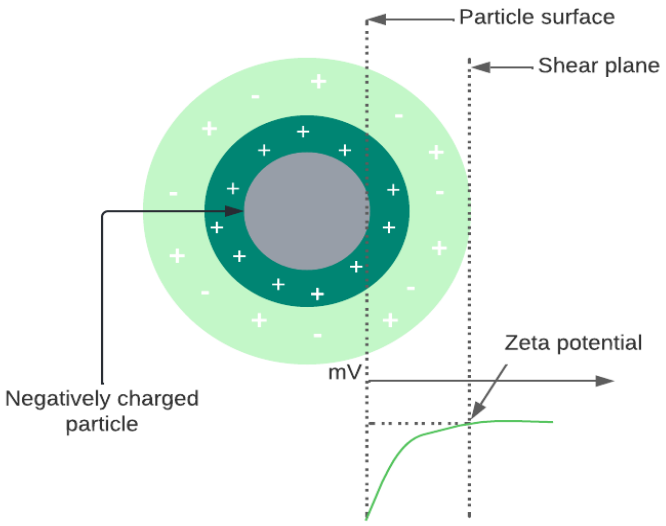


Figure 3-2: Theory of Zeta potential, adapted from Tengku Mohd *et al* [147].

Thus, each particle is surrounded by the electrical double layer. The liquid layer surrounding the particle has two parts; an inner region, where the ions are strongly bound and an outer region where ions are less firmly held. When the particle moves due to gravity, ions within the boundary move with it. The boundary, which is called the surface of hydrodynamic shear or slipping plane, and the boundary potential is known as Zeta potential [148].

3.2.3 Fluorescence response

Fluorescence is a well-established technique and often the method of choice for intracellular measurements. It is non-invasive, inexpensive and versatile for detecting analytes. Detection of fluorophores can be achieved using different instrumentation depending on the application and sensitivity required. This instrumentation involved can be a; standard fluorimeter, fluorescence plate reader, flow-cytometer for detecting fluorescence markers in cells and fluorescence microscopies (wide-field, confocal or super-resolution).

3.2.3.1 Fluorescence spectrophotometer

Fluorescence spectroscopy uses a spectrophotometer that can record both excitation and emission spectra. That is, it has the ability to determine the emission maxima by determining the emission spectrum measured at single excitation wavelength. Conversely, it is able to determine the excitation maxima by scanning the excitation spectrum at a single emission wavelength [30, 36].

A schematic representation of the fluorescence spectrometer is shown in Figure 3-3 which includes: light source which is usually a xenon arc lamp; monochromators to pick the excitation and emission wavelengths; photomultiplier detector. The result is presented as a spectrum showing fluorescent intensity against wavelength. The advantages of fluorescence spectroscopy are that it is a rapid, accessible and precise technique to perform analysis of fluorescent molecules [36].

The conventional fluorescence spectrometer has a single cuvette holder for measuring a sample. However, in order to get higher throughput with a multisampling approach, measurements can be carried out using a plate reader [149].

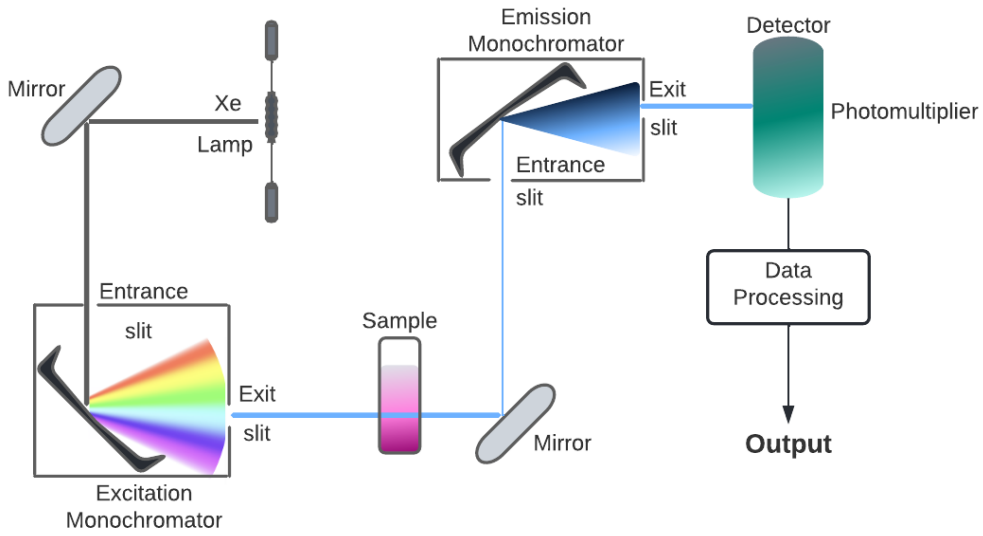


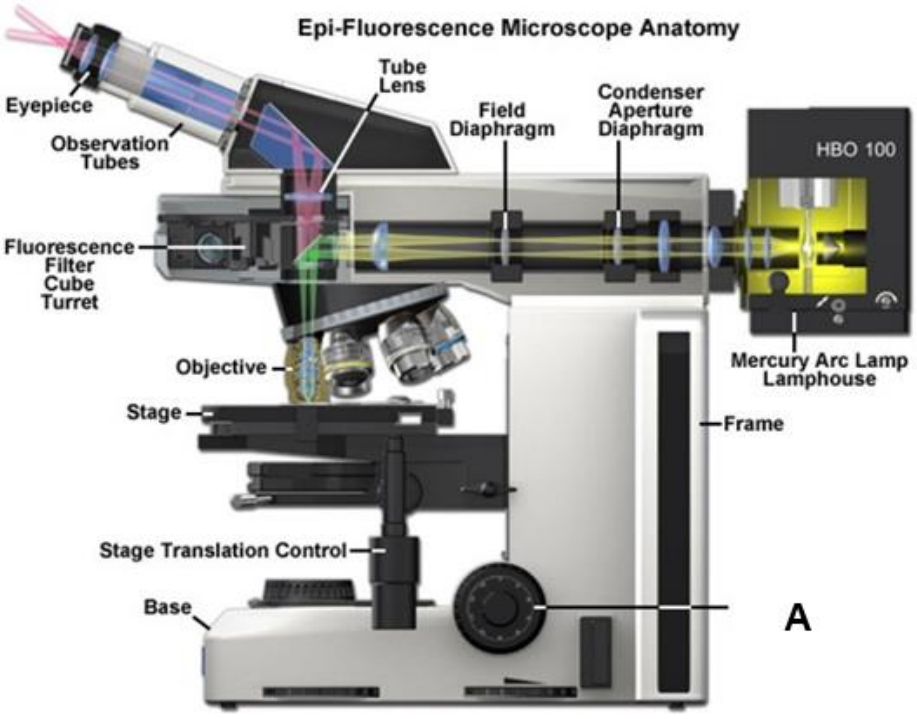
Figure 3-3: Schematic representation of based components of fluorescence spectrophotometer, adapted from Gomes *et al* [150].

3.2.3.2 Fluorescence microscope

Fluorescence microscopes are instruments that can be used to visualise physiological process in cells and tissues [151]. They provide highly specific images that can quantify the amount, cellular location of metabolites and ions. However, to make non-fluorescent entities visible they are offer required to be labelled with fluorescent dyes [152]. For example, DAPI dye is used to label nuclear DNA.

A fluorescence microscope functions by exciting the fluorophores in a specimen with a desired and specific wavelengths of light from a powerful light source e.g. LED or laser. Light is reflected by a dichroic mirror in a filter cube to illuminate the sample. After light hits the sample, it excites the fluorophores, which then emit fluorescent light at a longer wavelength. The emitted light is captured by the objective and then filtered before being sent to the detector for image digitalisation Figure 3-4 A [42]. The excitation, emission filters and dichromatic mirror are contained in a filter block as shown in Figure 3-4 B.

Only the emission should reach the detector, so that the resulting fluorescent structures are superimposed with high contrast against a very dark (ideally black) background. The limits of detection are generally governed by the darkness of the background and by the ability to eliminate excitation light since it is typically much brighter than the emitted fluorescence [40].



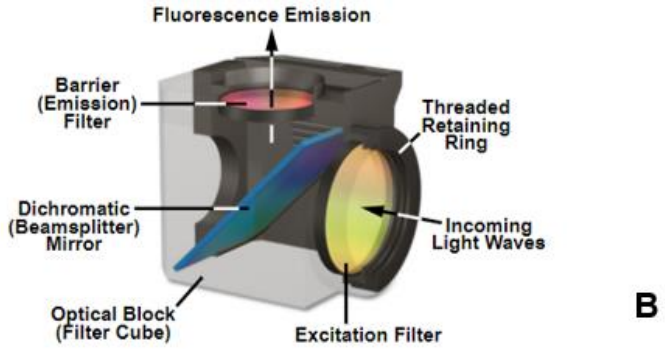


Figure 3-4: Labelled parts of fluorescence microscope. A) Microscope [43]. The colour green denotes light that is focused on the specimen, red denotes the emitted light from the sample, and yellow denotes light that has been transferred. B) Filter block [43] (Where the lenses and filters arranged).

Fluorescence microscopy is often the method of choice for studying dynamic behaviour intracellularly. Different molecules can be stained with different colours allowing for the multiple tracking of molecules simultaneously. Wide field microscopy is the most widely used method for measuring intracellular analytes because the instruments are most widely available and the technique is less likely to cause phototoxicity and photobleaching. This is because the illumination is less intense than the laser light is used in confocal microscope [41]. Although the trade-off is that conventional wide-field microscopy does not offer as high resolution as confocal microscopy or multiphoton microscopies. It does, however, allow for the capturing of images of the entire object field simultaneously in a parallel processing system, as compared to the scanning-based confocal microscopy and multiphoton microscopy. The whole-field nature of this approach can provide a very high data acquisition rate, making it attractive for imaging transient biological processes [44].

3.3 Development and optimisation of methodology for fluorescence ratiometric measurements

3.3.1 Technical consideration of ratiometric measurements

There are general factors that should be optimised to enhance reliability of the measurement. These factors should be kept standardised throughout the experiments

3.3.1.1 Nanosensor calibration

Generally, calibration is required for accurate measurements. It is critical to match the experimental settings with that in calibration conditions to ensure reliable measurements. The most straightforward technique for calibration is to simulate real environmental conditions using predetermined standard analyte concentration [39], [153], [154].

3.3.1.2 Image acquisition

Image acquisition means the process of capturing the image. It is important to acquire the image with suitable camera with known dynamic range [155]. The process of image acquisition is highly dependent on the hardware system used in the camera, which is composed of sensor that converts light (photons) into electrical charges so that an image can be reconstructed [155]. When using the image to extract data, there are number of factors should be considered: 1) lighting of illumination, 2) camera settings for the lens, 3) data which is stored as binary bits in a computer [156]. As regards the number of bits used to store a number limits the range of values, it can take for example 8 bit data, 2^8 =256 possible values can be stored. This represents grey levels from 0 (black) to 255 (white). 4) File format: There are different formats with different properties. Some formats compress the data which make the size smaller. Example of formats are JPEG, PNG and TIFF.

3.3.1.3 Microscope alignment

Microscope alignment means acquiring the image at specific wavelengths. In a perfectly aligned microscope, a point of fluorescence signal is co-localised at the exact same point in different (colour) channels [157]. Ratiometric measurement involves dividing the indicator intensities by reference intensities taken from different channels, therefore it is essential to have precise alignment between the channels.

3.3.1.4 Exposure and gain

The amount of light required to excite the sample is determined by the length of time the sample is exposed to the excitation light [158]. The highest exposure time will result in increased SNR ratios, but also leads to an increased risk of photo-bleaching and photo-toxicity. Gain, on the other hand, refers to the detector's sensitivity settings. The gain settings can be increased to the maximum. However, this can lead to an increase in background signal, as well as that of the signal. Saturation of pixels should be avoided as this means changes in signal can no longer be detected, though these pixels can be eliminated during image analysis in some cases [159].

3.3.1.5 Image analysis

Image analysis for ratiometric measurements is detailed in work published for pH nanosensors [22]. The fundamental considerations for image analysis include:

1- Thresholding
2- Background removal
3- Automation of image analysis

3.3.1.5.1 Determination of the measurement region (thresholding):

Image thresholding means selecting pixels above (or below) an intensity value. With colour images, each colour channel might have a separate threshold or it could be associated with the dimensions of a colour space [160].

3.3.1.5.2 Background removal:

Images acquired by fluorescence microscopy methods usually contain background. The reasons for the background could be from plate auto-fluorescence, media fluorescence or noise from the detector. Different methods for subtracting background have been proposed for image analysis. One approach is to take an image of the cell without nanosensors and calculate the mean value; this mean value is then subtracted from the images [22]. In a similar method, this value could be obtained from identifying an ROI outside the cells [161]. It should be noted that the majority of published research studies do not offer a specific procedure for removing the background from images [98].

3.3.1.5.3 Automation of image analysis:

Tools that can consistently extract data from images in a short amount of time are necessary for data analysis of multiple images. There are commercially available software packages with facilities (plug-ins) for operating ratiometric measurements. FIJI (open source) and MATLAB are extensively used software for image analysis.

3.4 Results and Discussion

Polyacrylamide nanoparticle preparation is simple and cost effective as a platform for conjugating dyes to fabricate nanosensors. Therefore, polyacrylamide-based nanosensors were chosen for oxygen responsive nanosensors. Fabrication of polyacrylamide nanosensors has been reported previously in our group [15, 22, 45] for measuring pH and oxygen intracellularly.

3.4.1 Reproducibility of nanosensor fabrication technique

Synthesized polyacrylamide nanoparticles were evaluated in terms of reproducibility by measuring the hydrodynamic diameter (d.nm) and the polydispersity index (PDI). Size and charge were measured before and after of conjugation to Pt porphyrin dye on the polyacrylamide surface. It has been shown that the average hydrodynamic diameter of polyacrylamide nanoparticles was centred at 40.7 nm, Figure 3-5Figure 3-5 A with polydispersity of 0.24. While the size of nanoparticles after conjugating with Pt porphyrin was 53nm, Figure 3-5 B with polydispersity of 0.30. Zeta potential was also measured and gave values of 14.96 mV and 3.15 mV for pre- and post-conjugated polyacrylamide nanoparticles, respectively. The type of functional groups on the nanoparticles surface is thought to be the cause of this variation in zeta potential levels [162]. Amine functionalisation by APMA is a useful method to facilitate conjugation to fluorophores and the reason for a high positively charge zeta potential as shown in Figure 3-5 C. Post-conjugation, Pt porphyrin occupied polyacrylamide nanoparticles surface leading to decrease of zeta potentials to 3.15 mV.

Small values of standard deviation of size and charge indicate a good reproducibility of nanosensor production. Previously reported polyacrylamide nanoparticles have been synthesised between 40 and 100 d.nm [22, 96], which were comparable to our results.

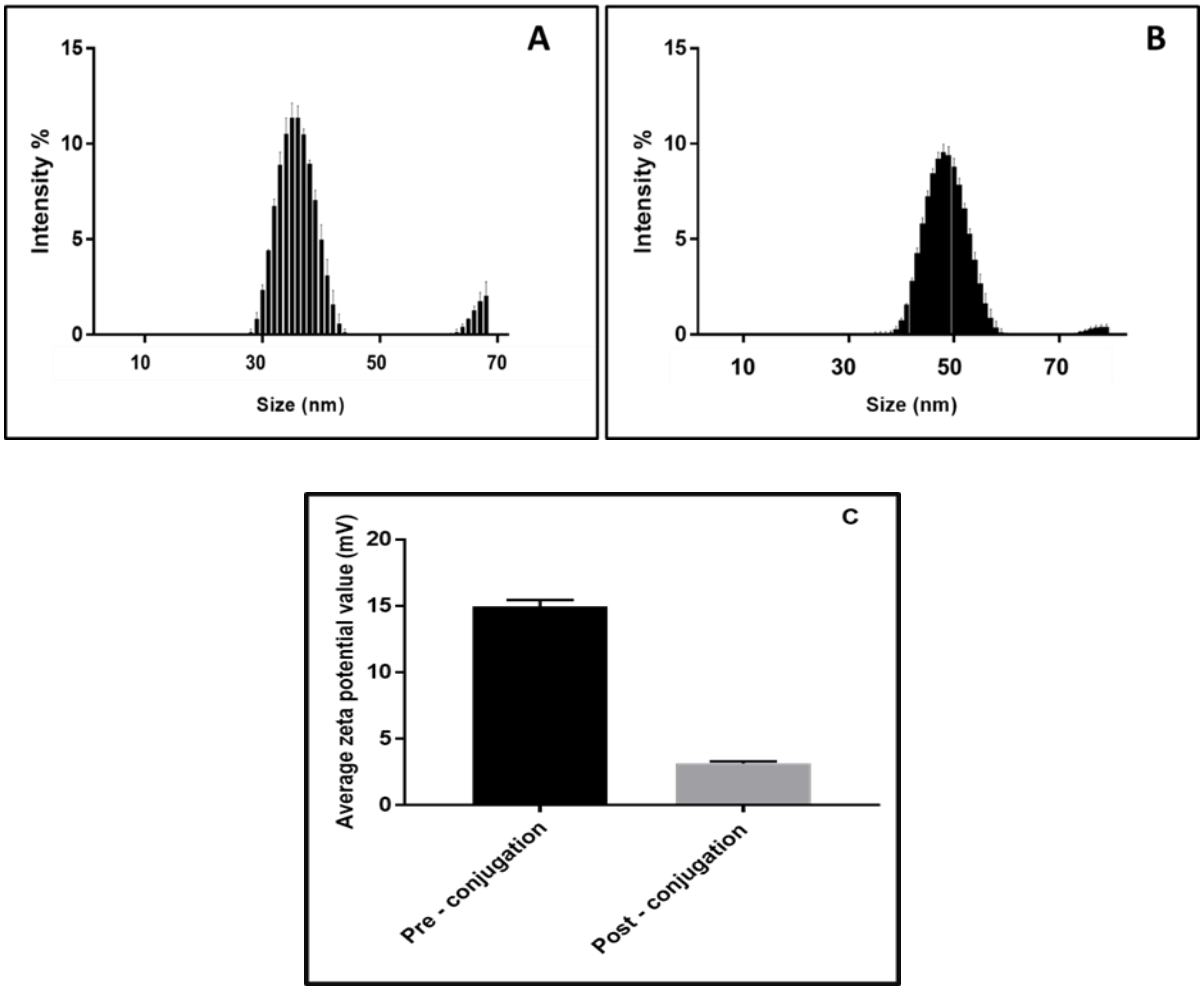


Figure 3-5: Characterization of size by using DLS A) pre-conjugation and B) post-conjugation to Pt porphyrin. C) Zeta potential values (mV) of polyacrylamide nanoparticles pre and post-conjugation of Pt porphyrin.

There are additional methods to characterise the size and shape of nanosensors which rely on electron microscopy imaging. However, in some previously reported cases, electron microscopy imaging is challenging due to the requirement for a conductive layer to be deposited on the surface of particles which affected the morphology of the nanoparticles [163]. Particles were mainly measured by DLS and different electron microscopy techniques which used by other research group [164],[163],[24]. They noticed an aggregation with electron microscopy in the main, although an advance technique was applied to show morphology and the size of particles.

In our work, particles were also imaged using transmission electron microscopy, TEM, Figure 3-6 A. The images appear to show large particles and flat sheet layers that we speculate resulted from aggregation due to high voltages used to achieve better resolution. To overcome this problem, Field Emission Gun Scanning Electron Microscope (FEG-SEM) was used to image the oxygen nanosensors. These conditions help to image nanoparticles successfully as a smaller electron beam diameter coupled with lower voltages could be used. The resulting image with spherical particles in the size range from 30 to 80 nm is shown in Figure 3-6 B.

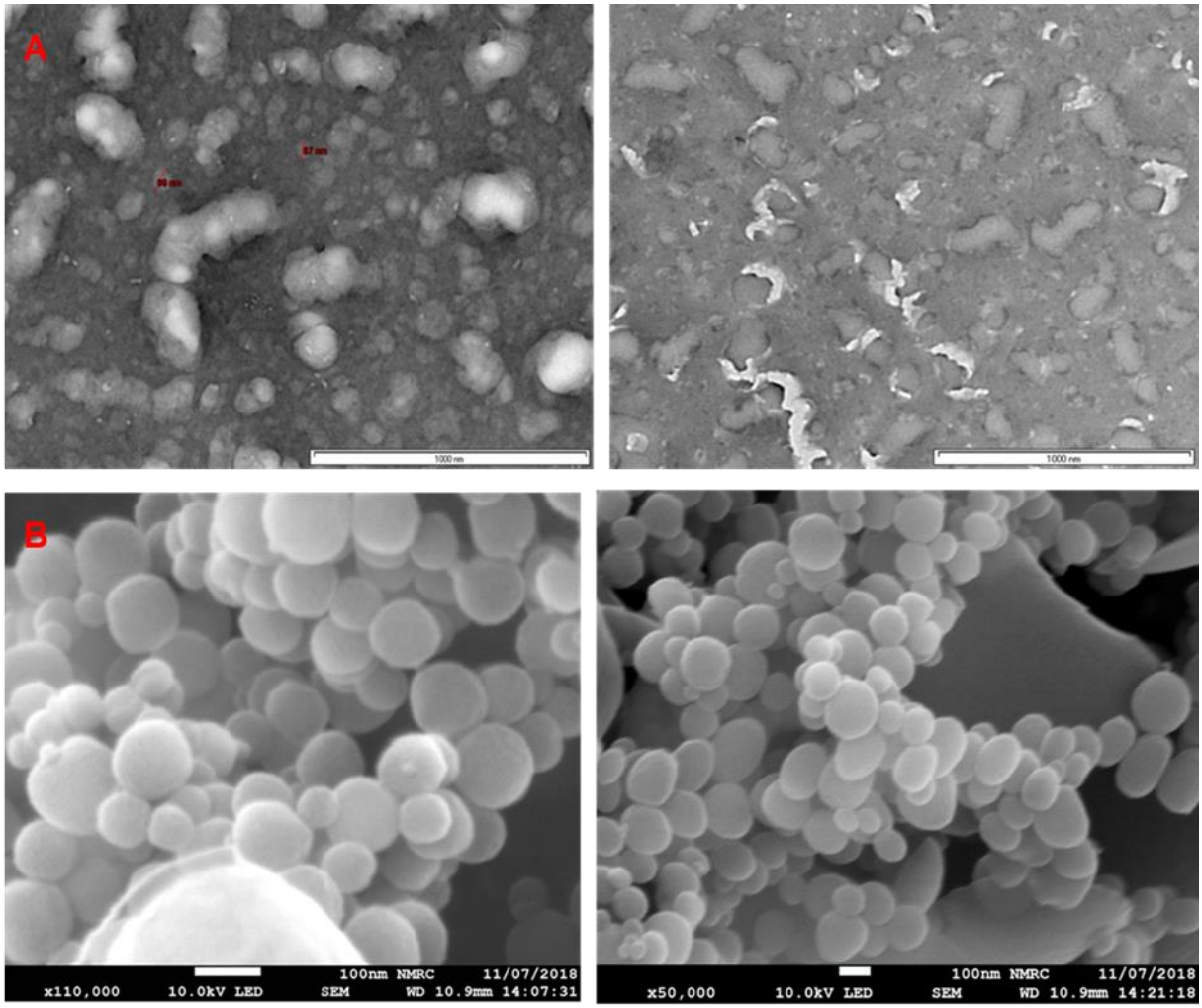


Figure 3-6: A) Transmission electron microscope (TEM) images, B) Field Emission Gun Scanning Electron microscopy (FEG-SEM) at magnification 110,000x and 50,000x.

Characterisation of nanosensors size and morphology were followed by finding out the optimal concentration of fluorophores, in the next section, that produce response for sensing oxygen concentration.

3.4.2 Optimisation of fluorophores concentration incorporated in nanosensors

The development of ideal chemical probes for imaging and sensing of hypoxia remains elusive. Porphyrin dyes are promising components of advanced sensing systems because of their photochemistry and stability [165]. To perform accurate measurements, it is important to conduct ratiometric measurements, and this requires optimisation of both fluorophore concentrations, Pt porphyrin indicator and TAMRA reference, in terms of their response and sensitivity to oxygen. The methods for making the porphyrin-TAMRA nanoparticles was described in Chapter 2 section (2.2.1), where the porphyrin, which is sensitive to oxygen, was covalently conjugated to the amine functionalised polyacrylamide nanoparticles once the polymerisation had been carried out.

The initial concentration of porphyrin used was 0.05 mg/mL. This concentration was explored in terms of its fluorescence response, sensitivity to *in situ* oxygen. TAMRA (reference dye) was incorporated in polyacrylamide nanoparticle during polymerization process in a concentration of 0.02 mg/mL. Initially, the fluorophores were tested for a maximum excitation and emission.

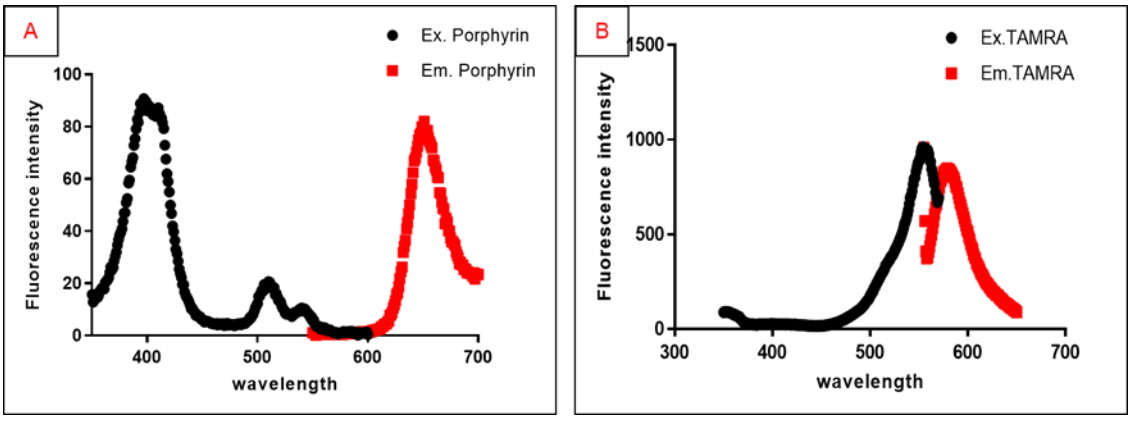


Figure 3-7: Spectrum of A) excitation and emission of Porphyrin and B) excitation and emission of TAMR.

As shown in Figure 3-7 A, the maxima excitation and emission wavelengths of Pt porphyrin are 398 and 648 nm, respectively. In Figure 3-7 B, the maxima excitation and emission wavelengths of TAMRA are 552 and 577 nm, respectively. The calculated Stokes shift for porphyrin is 250 nm. The pictures in Figure 3-8 A show three different batches of oxygen nanosensors. The clear suspension indicated that the NPs are small size compared to cloudy suspension which indicated the larger size. As shown in Figure 3-8 B nanosensors in a 5 mL tube were placed on the stirrer and analysed using an Ocean Optics oxygen meter to measure response to oxygen. This was done by exposing nanosensors to pre-determined oxygen concentrations as illustrated in Figure 3-8 C.

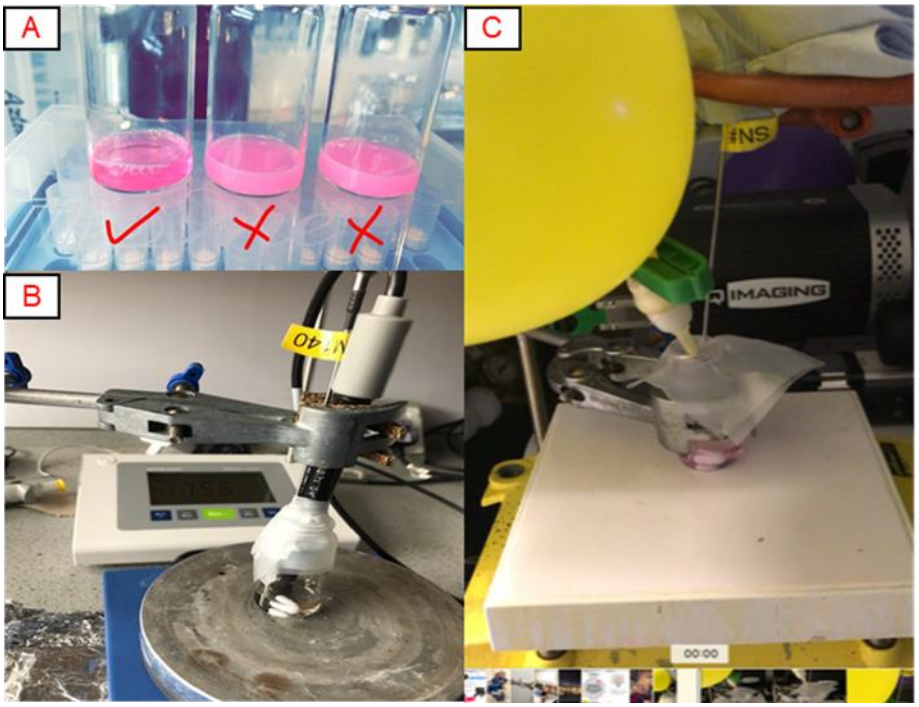


Figure 3-8: A) Oxygen nanosensor suspension. B) Immersed oxygen meter in oxygen nanosensor suspension in a tight oxygen environment. C) Balloons with oxygen and argon had been bubbled in suspension.

Different dissolved oxygen concentrations were prepared by bubbling with pre-determined oxygen concentrations. The results in

Figure 3-9Figure 3-9 A show the fluorescence intensity of TAMRA (577 nm) remains constant in response to changes in oxygen concentrations, while the intensity of Pt porphyrin (650 nm) increased with a decrease in oxygen concentration. The graph in Figure 3-9 B was generated by taking a ratio of signal at 650/577 nm and plotted against oxygen concentration (Stern-Volmer plot). Figure 3-9 B shows a good response to oxygen concentrations from 0–100%, with R^2 = 0.972 demonstrating a good fit of linearity.

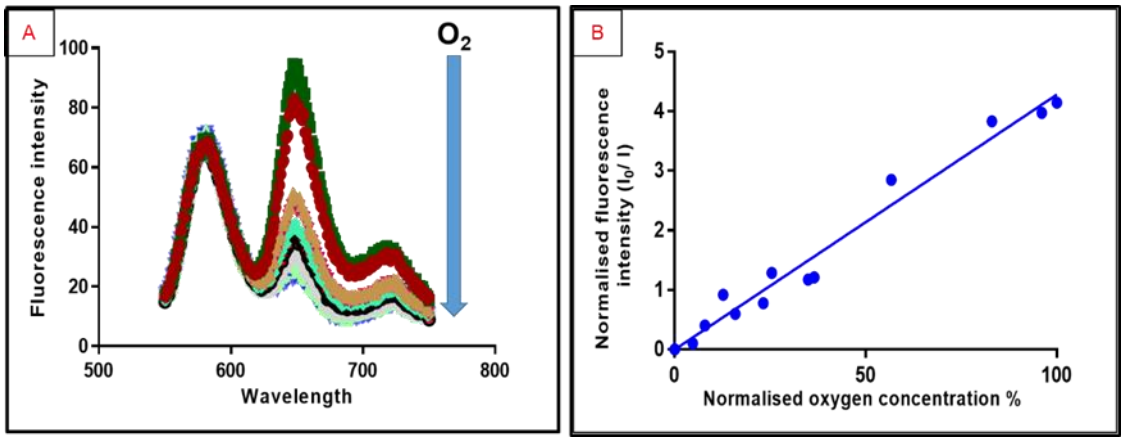


Figure 3-9: A) Fluorescence spectrum of oxygen nanosensors (0.5mg/ml), Oxygen sensitivity of sensor is measured by fluorimeter. Increase in fluorescence response of porphyrin (at 0.05mg/ml) to decrease in oxygen concentration and constant response of TAMRA to change in oxygen concentration B) Linear response of normalised fluorescence intensity versus% of normalised oxygen concentrations by Stern-Volmer equation.

From the results shown in Figure 3-9, it can be seen that the nanosensor emission is low (fluorescent intensity, 100 au). Preliminary testing of oxygen nanosensors deployed intracellularly showed a weak signal when measured using flow cytometry (Appendix Figure A.1). Cells which were treated with 50, 100, 250 µg/mL (Figure D, E, F respectively) of oxygen nanosensors exhibited TAMRA emission but no porphyrin signal was observable. Increasing concentration of oxygen nanosensors to 500 µg/mL (Figure G) did show signal from both Pt porphyrin and TAMRA but also demonstrated a highly toxic effect on the cells. Therefore, the initial Pt-porphyrin and TAMRA fluorophore concentrations in the nanosensor matrix were re-evaluated and optimised with monitoring by fluorescence spectrophotometer.

The challenge of low signal can be overcome by: conjugating and loading more indicator in the nanosensors, finding the optimal concentration of reference dye during the preparation of nanosensors, or increasing the light power used in the fluorescence analysis (spectrometer, microscope or flow cytometer).

3.4.3 Characterization and re-evaluated of optimal concentration of oxygen nanosensors' fluorophores

The optimal amount of the fluorophores to be loaded into the nanosensors was found to be 4mg and 1 mg for Pt porphyrin and TAMRA, respectively. These were in agreement with those reported previously by Chauhan [15]. The sensitivity of the optimised fluorophores was studied using 0.5 mg/mL of nanosensors using fluorescence spectrometer (c.f. 3.3.2) and wide-field microscope (3.3.4). Figure 3-10 A shows the fluorescence response of the optimised oxygen nanosensors in aqueous suspension measured using a fluorescence spectrophotometer. The optimised oxygen nanosensors showed that the emission from both fluorophores was amplified when compared to the emission from the initial oxygen nanosensors (Figure 3-9). The normalised ratiometric fluorescence intensities have shown an excellent linearity by applying Stern-Volmer equation R^2 =0.998**,** Figure 3-10 B

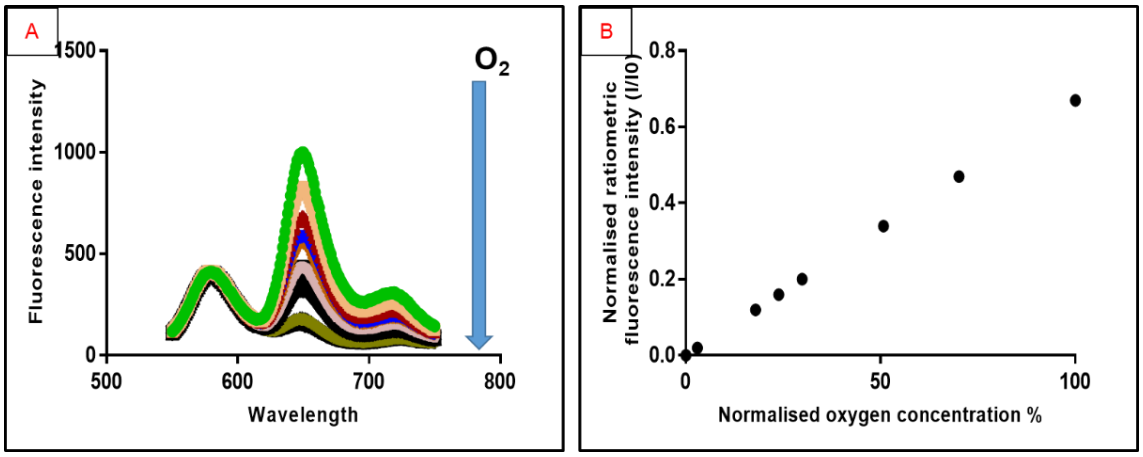


Figure 3-10: A) Fluorescence spectrum properties of porphyrin and TAMRA and B) improved the linear response of normalised fluorescence intensity versus% of normalised oxygen concentrations by Stern-Volmer equation.

3.4.4 Calibration of oxygen nanosensors using fluorescence microscope

In order to use oxygen nanosensors for biological applications, it is important to calibrate nanosensors containing different dissolved oxygen concentrations using a fluorescence microscope as fluorescent microscopy is widely used within biological research. The straightforward approach to calibrate nanosensors is to add some nanosensor suspension to an Ibidi slide in closed system, which is an Ibidi stage incubation system connected to the microscope Figure 3-11. The oxygen concentration will be monitored using an Ibidi controller of nitrogen/oxygen/carbon dioxide gas mixture using a guidance method by the manufacturer. The main advantage of the Ibidi incubation system is that it provides an efficient and precise physiological environment of gas, temperature and humidity for cellular imaging. However, controlling of gas is considered a sensitive technique and time consuming because of the time needed for medium saturation with a specific gas concentration.



Figure 3-11: 1) humidity column. 2) Ibid gas controller. 3) Ibid chamber [166].

By taking different images of oxygen nanosensors in porphyrin and TAMRA channels at different oxygen concentrations, images show a change in brightness in porphyrin channel images with an increase of oxygen diffusing into the suspension while TAMRA channel images show approximately the same brightness, Figure 3-12 (images). The data was extracted from images as an average intensity and then fitted to a Stern-Volmer plot of the intensity ratio of oxygen nanosensors against oxygen concentration which showed a linear response R^2=0.995, Figure 3-12.

A difficulty encountered in this experiment was to determine the concentration of oxygen diffused into suspension of nanosensors as the time required for the suspension to reach equilibrium in the chamber is extremely important. In our experiments, the optimal time for oxygen saturation was found 30 minutes. Generally, the microscope calibration approach helps to identify the factors that might affect image analysis when applying the method to cellular investigations, such as image acquisition, gain and exposure time [22]. However, standardising the microscopic conditions is crucial to obtain consistent results.

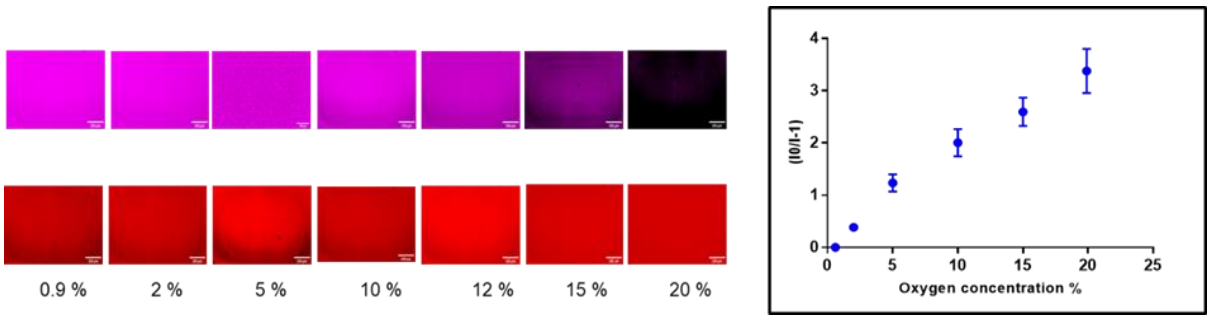


Figure 3-12: Visualise brightness change of porphyrin and TAMRA in oxygen nanosensors suspended in PBS using hypoxia chamber connected to wild field microscope (oxygen concentration 0 – 20 %). The graph illustrates linear response of oxygen concentration in chamber and oxygen nanosensors.

3.4.5 Temperature effect on nanosensors fluorescence response

In order to use oxygen nanosensors intracellularly, the incubation temperature (37°C) must be considered as a factor that might affect the nanosensor response. Therefore, an experiment was designed to measure the intensity of oxygen nanosensors during period of time (3, 6, 18 and 24 hours) using a fluorescence spectrophotometer. The result in Figure 3-13 shows no significant reduction in fluorescence intensity during incubation time.

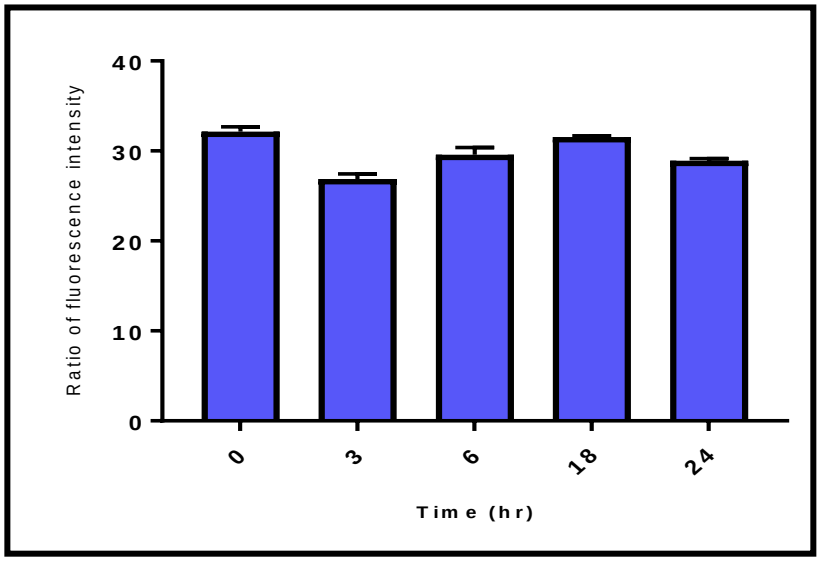


Figure 3-13 : Effect of incubation temperature (37°C) on oxygen nanosensors intensity. Error bars represent (SD for n=3).

3.4.6 Evaluation of oxygen nanosensor sensitivity

It is important to study the sensitivity and reversibility of the prepared oxygen nanosensors. As described in Chapter 2, a suspension of oxygen nanosensors (1 mg/mL) and glucose (6 mM) was mixed and exposed to 1 mg/mL glucose oxidase enzyme solution in an air-tight cuvette. After the reaction started, oxygen localised in the cuvette was consumed over time, leading to an increase in the fluorescence intensity of the Pt porphyrin. The fluorescence intensities of both Pt porphyrin and TAMRA were recorded and the ratiometric measurements were calculated and then plotted versus time and oxygen concentration (mM/mL).

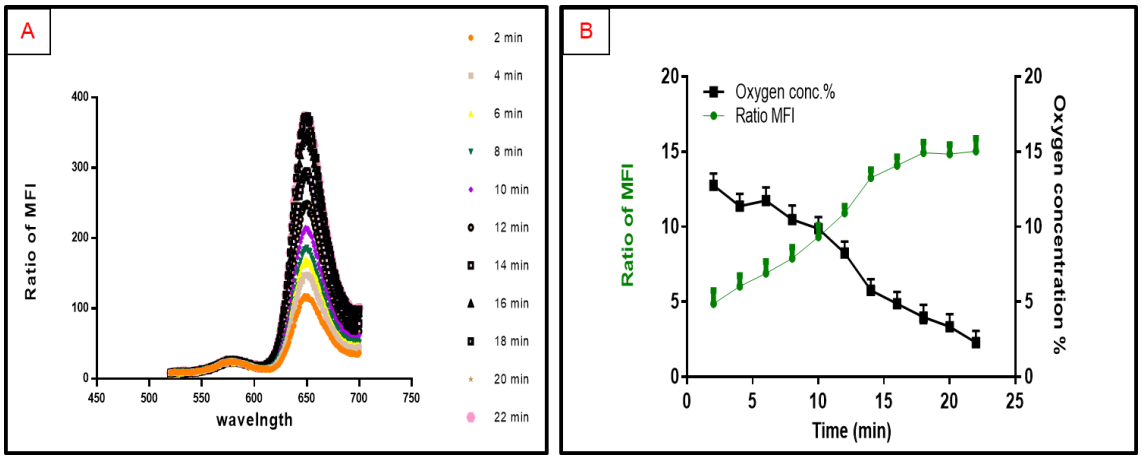


Figure 3-14: A) Spectrum of increasing Pt porphyrin intensity by consumption of dissolved oxygen by glucose oxidase in deionized water. B) Kinetic analysis of oxygen consumption by glucose oxidase enzyme. Error bars represent (SD for n=3).

As shown in Figure 3-14 A, Pt porphyrin emission increases with time until the oxygen has been consumed; the intensity increased until is showed a plateau after about 20 minutes, see Figure 3-14 B. There was a concern that the consumption of oxygen by glucose oxidase may also result in a change in the pH of the medium. By monitoring the pH of system using simple pH meter, it was shown that there was no change in pH across the timescale of the experiment, Figure 3-15.

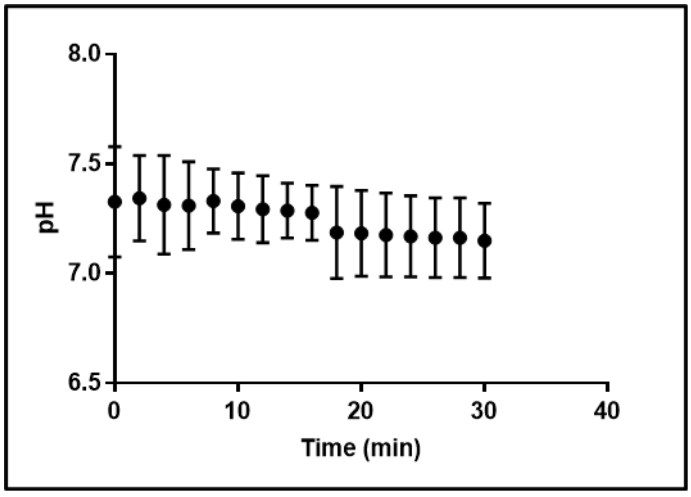


Figure 3-15: Monitoring of pH during oxygen consumption using pH meter Error bars represent (SD for n=3) (P <0.0001).

The nanosensors have the capability to monitor the oxygen concentration under induced hypoxia. This bring to light the use of oxygen nanosensors approaches intracellularly and the monitoring of physiological reactions by oxygen and glucose monitoring, with merits of good sensitivity. However, the cellular oxygen concentration might be affected by the complexity of cell components and cellular pH. Thus, investigation of Pt-oxygen nanosensors will be explored intracellularly.

3.5 Conclusion

The work that has been done in this chapter shows that oxygen-sensitive nanosensors could be fabricated using a robust methodology. Polyacrylamide nanosensors containing Pt porphyrin and TAMRA fabricated using this technique were spherical and sized between approximately 40 - 55 nm in diameter, as determined using dynamic light scattering and FEG-SEM. The morphology of the nanosensors was assessed using FEG-SEM which gave high resolution images.

The TAMRA and Pt porphyrin fluorophores were assessed and directly conjugated to the polyacrylamide matrix via amine-functionalised polymer. Post-polymerisation conjugation of Pt porphyrin dye was preferential due to dye degradation observed during free-radical polymerisation of the acrylamide to from the polyacrylamide nanoparticle matrix.

The ratiometric nanosensors were sensitive to dissolved oxygen with excellent linearity (R^2 = 0.997) when analysed using a Stern-Volmer plot. The overall quenching response reaches approximately 97% which is measured by using the equation (I_0/I) x100. The small size and hydrophilic nature of the polyacrylamide nanoparticles, as well as the use of ratiometric measurement, results in a good overall quenching response and good linearity to dissolve oxygen from 0 to 100% saturation. The nanosensors have good reversibility and a good response to trace amounts of oxygen. For the present study, a wide field microscope as well as a fluorescence spectrophotometer was used for ratiometric measurements. In the optical nanosensors field, there has been a focus on fabrication of oxygen nanosensors designed for biological applications. This chapter presented the fabrication, characterisation and calibration of polyacrylamide oxygen-sensitive nanosensors as a

prelude to cellular investigations to be presented in Chapters 4 and 5. The establishment of a standardised procedure for performing calibrations and measurements of intracellular oxygen has received comparatively little attention and is important because the ability to perform ratiometric measurements is highly dependent on the experimental setup.

Chapter 4 . Intracellular evaluation of oxygen in macrophage

4.1 Introduction

The aim of this chapter is first to examine the immune response of macrophages to nanosensors. Second aim is to study the impact of Pt porphyrin as ROS generator on macrophage phenotype modulation. The third aim is to implement oxygen nanosensors within live cells and validate the optimised methodologies described in Chapter 2 and Chapter 3 by exposing the cells to pharmacological compounds that affect intracellular oxygen levels. Each of these aims will be explained as follows:

4.1.1 Response of macrophage to nanosensors based nanoparticles

In the previous chapter, optimal oxygen nanosensors fabrication was discussed for intracellular measurements. In this chapter, the use of oxygen nanosensors intracellularly will be presented using a macrophage immune cell model. Macrophages are an integral part of immune response. Their cumulative heterogeneity is involved in the progress or prevention of diseases. The heterogeneous phenotype properties of macrophage correlates with different metabolic activity [167]. In addition, extensive studies have been conducted on macrophage response to analytical devices based on biomaterials such as nanoparticles [168, 169]. The data available revealed that the chemical composition of the polymer, size, surface chemistry, as well as hydrophobicity, can polarise the macrophage differently [170]. This alteration of macrophage polarisation results in changes of macrophage phenotype and initiates metabolic cascade along different pathways [171].

Ideally, biomaterial physicochemical factors could be tuned to control macrophage response and to an extent is possible [172]. The following section reviews the effects

of physicochemical properties of biomaterials on phenotype modulation of macrophage.

4.1.1.1 Surface chemistry of polymeric matrix

Altering the surface chemistry of nanoparticles has a strong impact on macrophage phenotype modulation [168]. Modification of nanoparticles surface by adding or removing functional groups such as amine group (-NH_2) or carboxylic group (–COOH) changes the hydrophobicity, pH and charge of nanoparticles [173]. Moreover, conjugation of nanoparticles to compounds such as carbohydrates modulates macrophages to pro-inflammatory phenotype [104]. In addition, some surfaces such as hydrophobic polyurethane induces the production of anti-inflammatory cytokines (IL-10) and decrease the production of anti-inflammatory cytokines (TNF-α, IL-1β) [174].

In the context of switching from pro-inflammatory to anti-inflammatory lineages to promote wound healing, surfaces of biomaterials can be modified to create a favourable cytokine microenvironment (increased levels of IL-10 and TFG-β) [175]. Additionally, *Jones et al.* studied effect of hydrophilic surfaces compared with hydrophobic surfaces of polyacrylamide on macrophage. It was shown that macrophages switch their phenotype from pro-inflammatory to anti-inflammatory with modified surfaces from hydrophilic to hydrophobic [176]. Interestingly, these results also suggested the effect of charge modification on hydrophilicity and hydrophobicity.

4.1.1.2 Charge

The overall charge of macrophage cell membrane is negative [177]. Thus, biomaterials with surface charge can modulate macrophage response. Generally, cationic charged surfaces are prone to cause pro-inflammatory response and increased internalisation than anionic and neutral charged materials [178].

The response of macrophage to polyacrylamide has been studied previously by different groups [176, 179]. One of the study has shown that the neutral surface charge of polyacrylamide modulates naïve macrophage to pro-inflammatory phenotype in human macrophage *in vitro* [176]. Moreover, a study conducted by Chen *et al* has shown that hyper-branched polymers conjugated with fluorescent dyes, changed the polymer surface charge and consequently the macrophage response was observed to differ [180].

It is important to consider the chemistry of dyes that have impact on overall nanoparticle charge and consequently physical characteristics, such nanoparticle size. Recently, it has been reported that protein aggregated on the surface of nanoparticles forming a corona can significantly increase the effective particle size [181]. The explanation of how corona forms rely on the surface chemistry as well as surface charge [182].

4.1.1.3 Size

Size of nanoparticles can be tuned for different biological applications [183]. Tuneable size of nanoparticles has an impact on immune responses [184]. This is through changing its phenotype. Therefore, uptake and clearance of particles are different by exposing them to different range of sizes [185].

This is exemplified in the work undertaken by Yue *et al.* which highlighted that nano-sized particles could influence (TNF-α) pro-inflammatory cytokine production in J774A.1 macrophage cell line. On the other hand, no noticeable (TNF-α) level was determined for micro-particles. Indicating that further studies should be focused on large particles that might be less immunogenic [186]. In a similar study, the author suggested the inflammatory response of macrophage to the small size of nanoparticle is due to exposure of cells to the large surface area of small nanoparticle size [187].

It is challenging to balance cumulative factors such as nanoparticle surface chemistries, charge and size that can enhance or suppress macrophage activity and which can subsequently affect macrophage polarisation [188]. However these factors can be controlled by tuning method of nanoparticle fabrication for development of non-destructive analytical tool such as nanosensors for cell measurement.

4.1.2 Utilisation of nanosensors based nanoparticles for live cell measurement

Development of a non-invasive tool such as nanosensors for metabolic dynamic profiling of macrophage is important [189, 190]. This can help correlate metabolic activity and molecular expression for potential use in diagnostic and therapeutic applications [3]. Nanosensor based nanoparticles have been previously used as a diagnostic tool for measurement of biomarkers such as pH [113], oxygen [167] and ROS [230] in macrophages.

For the purpose of using nanosensors for dynamic measurement of biomarkers such as oxygen measurement in live cells, response of macrophages to the nanosensors is required to be investigated. As discussed in Chapter 2, nanosensors have been synthesised that are composed of polyacrylamide matrix functionalised by amine group to facilitate conjugation to Pt porphyrin as indicator dye on the surface and encapsulated TAMRA as reference dye.

There are a several published studies showing effect of surface chemistry on macrophage phenotypic modulation. However, it is important to note that there is a lack of data available showing the effect of Pt porphyrin on phenotype change. Nevertheless, different types of porphyrin have been used for photodynamic therapy to generate ROS to induce phenotype modulation [191, 192].

4.1.3 Assays used for modulating intracellular oxygen

The current methods utilised for monitoring oxygen involve use of pharmacological compounds that have an effect on cell function to cause measurable response. It was reported that pharmacological compounds that affect cellular respiration rely on a mechanism of action targeting cellular metabolic activity [193-195]. These compounds act mainly on mitochondria, Table 4.1.

Table 4.1: list of compounds has mitochondrial membrane complex un-coupler and inhibitors

Pharmacological agent	**Type**	**Cell types**	**References**
FCCP,(Carbonylcyanide-p trifluoromethoxyphenylhydrazone) CCCP,(carbonylcyanidem-chlorophenylhydrazone)	Potent mitochondrial oxidative phosphorylation uncoupler	Mouse embryonic fibroblasts (MEF), Pheochromocytoma(PC12)	[194], [195], [190], [196]
Antimycin A	Complex III inhibitor (An inhibitor of cellular respiration).	HeLa G cell lines, PC12 cells, SH-SY5Y cells, HepG2	[197], [194], [198] [193]
Bafilomycin	VTP-ase inhibitor and it has mitochondrial respiration effect	PC12 cells, SH-SY5Y cells	[194], [199],
Rotenone	Complex I inhibitor	Glial cell	[200], [201]

There are different strategies to manipulate pathways that alter mitochondrial activity such as targeting electron transport chain (ETC), which involve complexes I-IV of mitochondrial membrane [202-204]. FCCP, act as un-coupler which deplete membrane potential lead to enhancement of oxygen consumption. Further, it disrupts proton across the inner membrane which alter the proton gradients [205].

This effect can be clearly seen in previous work that rotenone and antimycin can inhibit complex I and complex III, respectively [200, 206]. Leading to inhibition of two main origins of ROS production as a result of a blockade of electron transfer. Incomplete electron transfer to oxygen could lead to accumulation of ROS and that inhibit cell proliferation [200]. Additionally, bafilomycin has been shown to have transient alteration of mitochondrial complex which affect oxygen concentration [194].

In a number of studies, cells are pre-incubated with inhibitor or un-coupler compounds for a period of time [207]. The duration of treatment is dependent on the experimental protocol. Theoretically, mitochondrial transient effect are most likely to be detected in short period of time. Therefore, it should be considered that treatment time could alter cellular pathways and imbalance of electron transport resulting in loss of cell viability [208].

4.2 Results and discussion

4.2.1 Characterization of THP-1 differentiated macrophage

THP-1 cells differentiated macrophage were used as a model for dynamic transition of oxygen. THP-1 cell line are commonly used cell line for differentiating to macrophages. A considerable amount of literature has been described the differentiation of human THP-1 cells into naïve macrophage by culturing the cells with phorbol-12-myristate13-acetate (PMA) [209], [131]. To confirm differentiation of THP-1 cells to macrophage, CD68 surface marker was evaluated by visualisation under a microscope [210]. CD68 was shown to be expressed in differentiated macrophage and treated with oxygen nanosensors which include porphyrin and TAMRA dyes, confirming that no effect of nanosensors on CD68 expression, Figure 4-1**.**

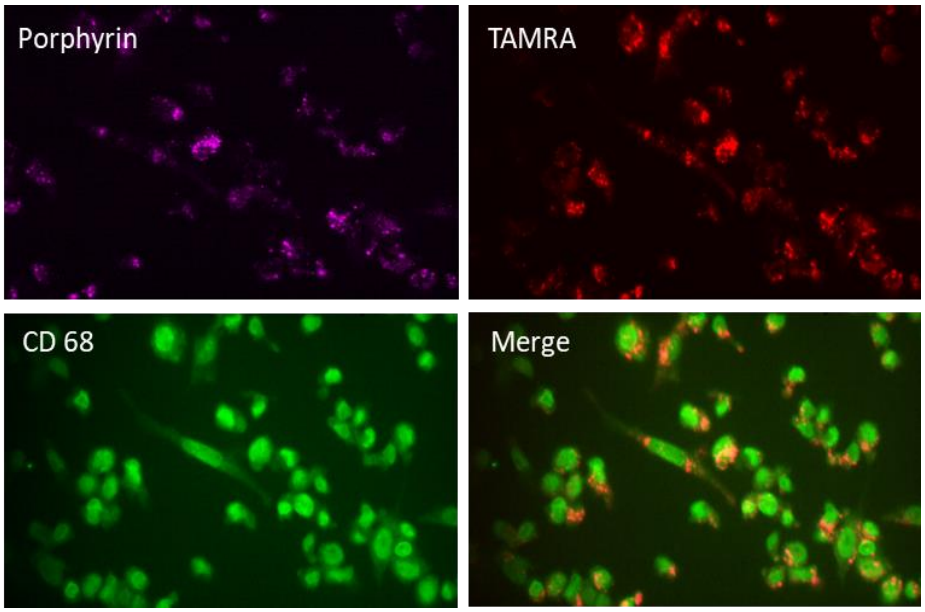


Figure 4-1 : THP-1 differentiated macrophage (M0) treated with oxygen nanosensors. M0 tagged by Alexa flour480 CD68 marker of M0.

4.2.2 Macrophage polarisation

4.2.2.1 Cytokines productions

Numerous studies have associated macrophage response to different micro-environmental stimuli which is responsible to develop a range of phenotypes [104]. Each of phenotypes has a signature characteristic of metabolism [211]. Thus, differentiated macrophages characterised in response to different stimuli extensively in different works to investigate its phenotype M1 and M2 subsets [212]. To polarize naïve macrophage to M1 cells, M0 macrophages were treated with 50 ng/mL GM-CSF, 100 ng/mL LPS and 20 ng/mL IFN-ɣ. Additionally, M2 cells were also generated by using 50 ng/mL M-CSF and 20 ng/mL IL-4 [131]. These biomolecules have been shown to stimulate macrophage polarisation to pro-inflammatory or anti-inflammatory phenotypes. Macrophage phenotypes were tested by examining cytokines production, TNF-ɣ and IL-10, to detect pro-inflammatory and anti-inflammatory, respectively. Supernatants were obtained from M1 and M2 cells then analysed by ELISA technique. Figure 4-2 show high significant expression of TNF-ɣ when polarise to M1 while high level of IL-10 significantly expressed when polarised to M2.

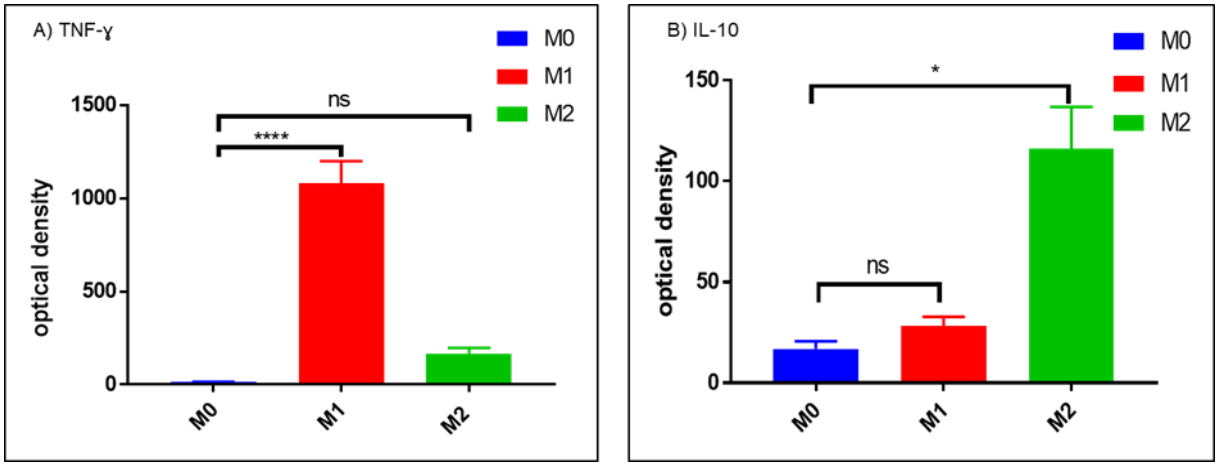


Figure 4-2: ELISA assay of A) TNF-α expression of M1 polarised macrophage. B) IL-10 expression of M2 polarised macrophage. Data showed mean optical density at 450nm which representative for n=3, (level of significant ****p<0.0001, ***p<0.001, **p<0.01).

4.2.2.2 Immuno-fluorescent staining

In addition to measuring the cytokine production, visualisation immunostaining of naïve macrophage was characterised using fluorescence microscopy. Therefore, activated macrophages were analysed by using marker staining of calprotectin and mannose receptor (CD206) for M1 macrophages and M2 macrophages, respectively. The results interpreted by visualising images of M1 and M2. The images have shown that mannose receptor of green M2 higher than that expressed in M1. On the other hand, calprotectin in red have expressed in M1 compared to that in M2, Figure 4-3**.**

Characterisation of macrophage helps to prior treatment of cells with nanosensors helps to identify cell morphology in each phenotype. As well as, helps to recognise nanosensors behaviour on macrophage cells. The next section will explore study oxygen nanosensor intracellular delivery with co-localisation analyses.

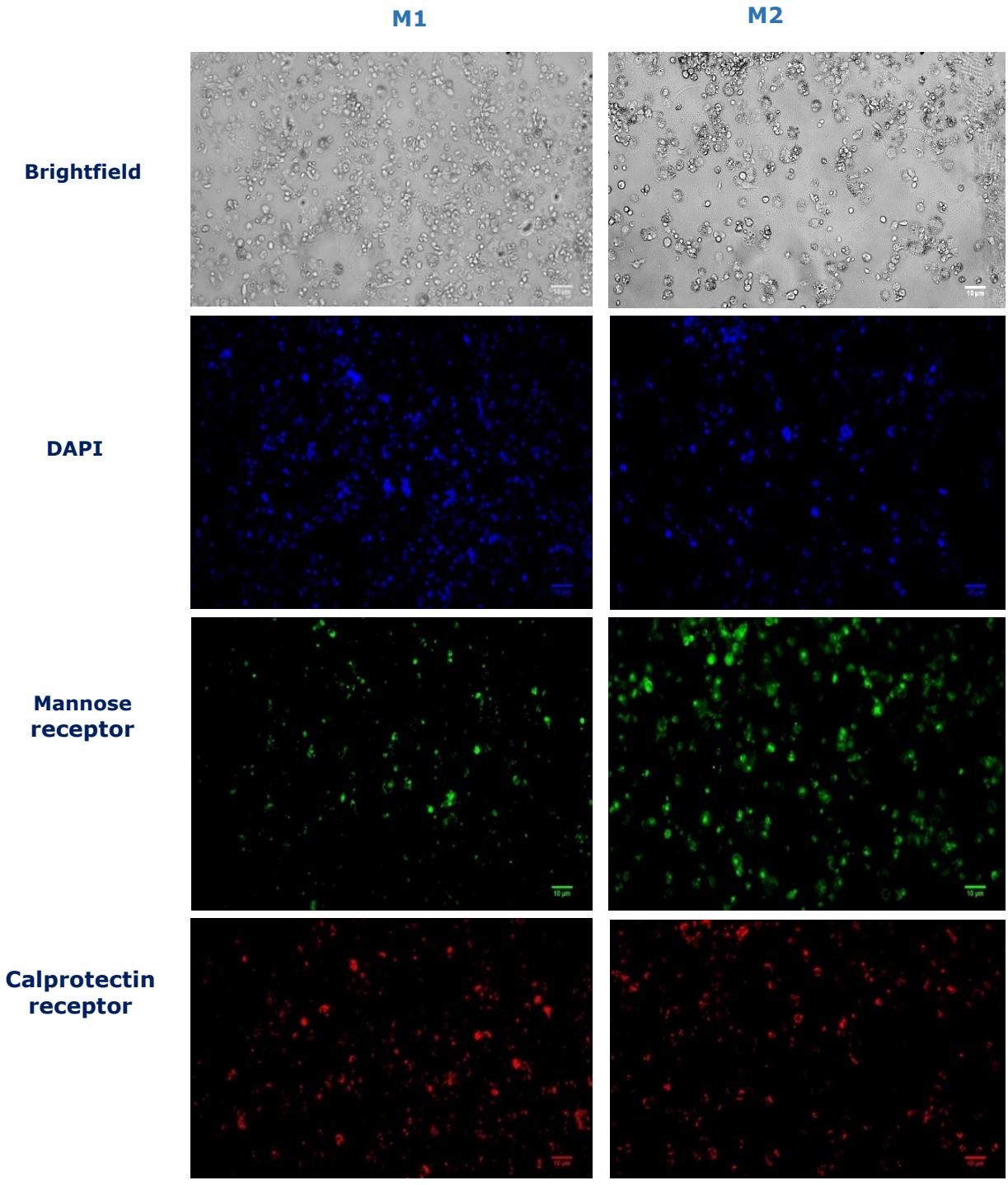


Figure 4-3: Visualised images of characterisation of M1 and M2 polarized macrophage that expressed calprotectin and mannose receptor, respectively. Scale = 10 µm.

4.2.3 Co-localisation of porphyrin and TAMRA of oxygen nanosensors, in THP-1 differentiated macrophage

Naked dyes that used for detection of oxygen are toxic for the cells and once internalised may leach from sample or can be metabolised [213] .Therefore, dyes are conjugated to nanoparticles as a matrix support to prevent leaching. In order to confirm the presence of both TAMRA and porphyrin which conjugated to the same nanoparticle location and not leached or degraded, the study of co-localisation was conducted. The result in Figure 4-4 shows the high (PCC) of = 0.92 which confirm strong co-localisation of nanosensor dyes in the same place. Figure 4-4 also shows that the dyes associated with the nanoparticles do not exhibit leaching into extracellular spaces.

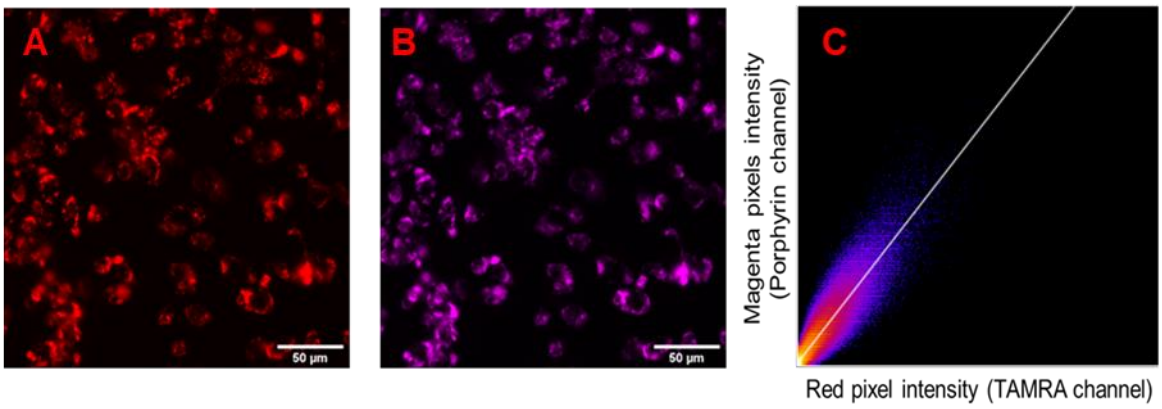


Figure 4-4: Macrophage treated with A) TAMRA and B) Porphyrin nanosensors. C) 2D histogram of fluorophores (porphyrin and TAMRA channels) conjugated nanoparticles in THP-1 differentiated macrophage. Scale = 50 µm.

4.2.4 Stability monitoring of ratiometric fluorescence intensity

The reported nanosensors stability vary in available liturature, Stability is typically monitored by monitoring the dyes leaching from nanosensor suspension [189, 199]. In this study, intracellular fluorescence intensity of oxygen nanosensors has been monitored over one week. Monitoring of fluorescence intensity is to confirm the duration of fluorescence oxygen nanosensor stability. The intensity was measured at day 1 , day 4 and day 7. Figure 4-5 shows a reduction in fluorescence inteinsity by approximetly 50 % after 24 hours of treating cells. While the ratiometric intensity reduced by 70 % after a week. It is important to note that there is a limited window in which amino-functionalized polyacrylamide particles can be utilized to conjugate secondary precursors because it has been demonstrated that they form aggregates. Aizde and alkyne linkers can be used in place of amino groups to extend the shelf life of nanoparticles [22].

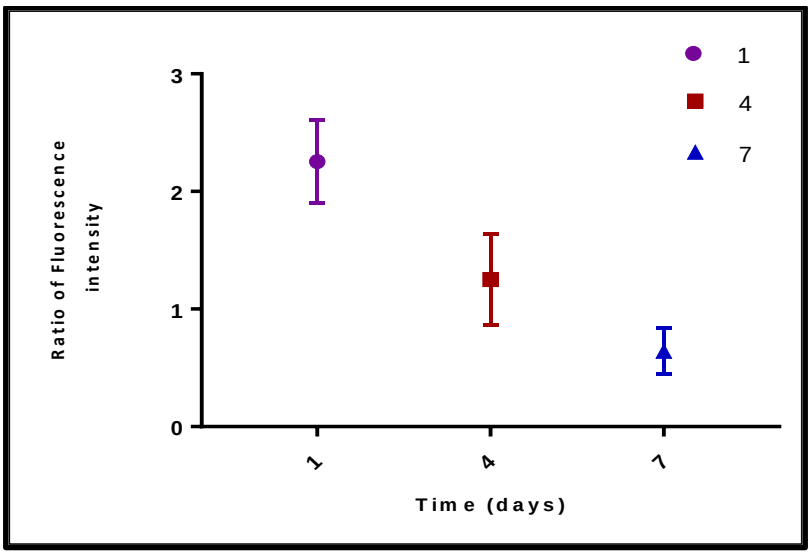


Figure 4-5: Monitoring of ratiometric fluorescence intensity at D1, D4 and D7. Error bars represent SD, n= 3, P= <0.05.

As part of nanosensor sensitivity study to oxygen, intracellular macrophage of oxygen nanosensors in fixed cells were tested to show the reversibility response. Using fluorescence microscopy chamber to monitor hypoxia environment, cells were exposed to high and low oxygen and allowed the gas diffused to the cells. Visual images of intracellular nanosensors in Figure 4-6 have shown that Pt porphyrin quenched by oxygen concentration at the maximum oxygen saturation in chamber. This was compared by minimum oxygen concentration that shows bright images.

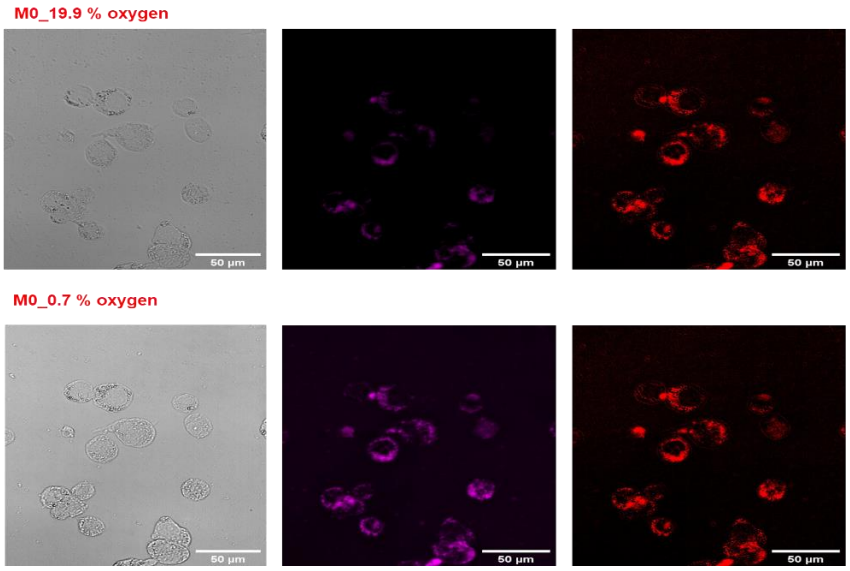


Figure 4-6: Visualisation images of intracellular oxygen nanosensors at maximum and minimum of oxygen concentration in chamber.

The fluorescence intensity was evaluated in fixed cells using a plate reader. Figure 4-7 shows by bubbling the oxygen and argon in the plate, the reversibility of oxygen nanosensor response to change in oxygen concentration can be demonstrated.

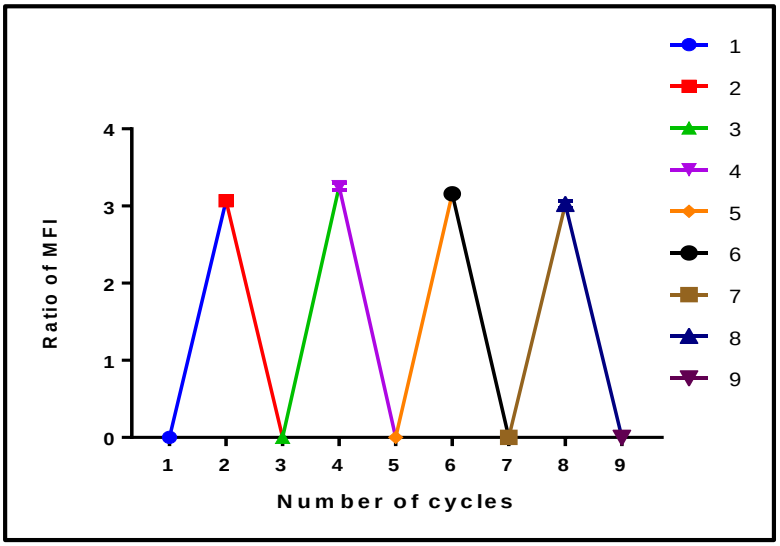


Figure 4-7: Reversibility response of intracellular oxygen nanosensors to change of micro-environmental oxygen. Ratiometric Mean fluorescence Intensities (MFI) when cycled between 0 and 100 % dissolved oxygen concentration (Oxygen determined by Neofox Oceanoptic).

Previous sections in this chapter focus on intracellular nanosensor from its sensitivity perspective. Nevertheless, macrophage cells react to nanosensors as discussed in the introduction of this chapter. The following sections of this chapter, cover cellular interactions from a biological perspective starting with toxicity assay.

4.2.5 Impact of oxygen nanosensors on cell metabolic activity

It is important to determine a safe concentration of oxygen nanosensors for the cells that would not affect cellular physiological activity, this is because need of use nanosensors as an inert reporter for accurate oxygen measurement in the absence particle related artefacts. However, it is important to note the oxygen nanosensor concentrations should not be lower than their limit of detection, to make meaningful measurements. This study examines metabolic activity using Alamar blue® assay by methods described in Chapter 2.

Figure 4-8 A shows that treatment of macrophage with less than or equal 250 µg/mL of oxygen nanosensors resulted no significant impact on cellular activity. To validate Alamar blue ® assay result, cytotox glu® assay was conducted to test cell membrane integrity and cell viability by measuring luciferase luminescence of dead cells. Figure 4-8 B illustrates that oxygen nanosensors can be used up to approximately 200 µg/mL without affecting cell viability. It has been seen that these safe concentrations produce adequate signal for measurements which will be detailed in section 4.2.8 and 4.2.9.

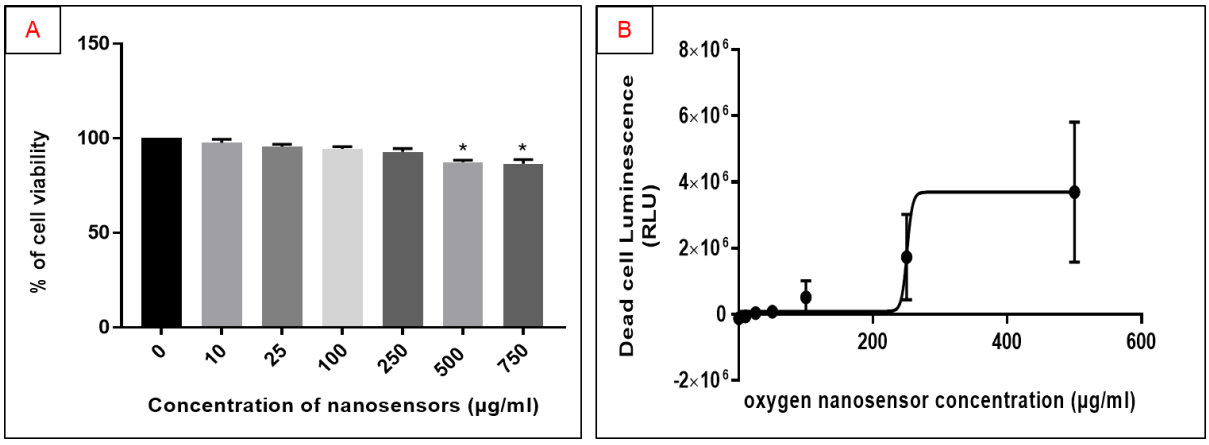


Figure 4-8: A) Alamar blue ® (metabolic activity). B) Cytotox glu® for (cell viability) Data is representative for n=3, (P= <0.05).

4.2.6 Impact of polyacrylamide nanosensors on phenotypic modulation of macrophage

Generally, macrophage as an immune cells respond to external stimuli by expressing cytokines that determine phenotype modulation. For the purpose of utilising nanosensors in macrophage, inflammatory response of cells to nanosensors was studied. This was done by exposing macrophage to polyacrylamide nanosensors in presence and absence of conjugated Pt porphyrin. In this experiment LPS treated macrophage was used as positive control and pH nanosensors was used as a positive nanosensors without conjugated porphyrin. The reason for using pH nanosensors in this study is to confirm the effect of Pt porphyrin conjugated to polyacrylamide surface on phenotype modulation of macrophage.

Cytokine production (TNF-α and IL-10) of pro-inflammatory and anti-inflammatory phenotypes, respectively were determined. Initial observations suggest that there may be a link between surface chemistry and modulation of macrophage. The result in Figure 4-9 shows modulating of naïve macrophage to pro-inflammatory phenotype by significant production of TNF-α with oxygen nanosensors was comparable to control untreated macrophage, which had an insignificant anti-inflammatory effect. Interestingly, production of TNF-α has not significant changed with cells treated pH nanosensors. This response of macrophage is most likely as result of cationic influence of pro-inflammatory cytokines. Furthermore, no significant production of IL-10 was produced from either from oxygen nanosensors or pH nanosensors. Indicating that the overall effect of nanosensors are mostly towards a pro-inflammatory effect.

Although extensive research has been carried out on modulation of macrophage by nanoparticles, the experimental data are rather mixed [214, 215], There is no general consensus about the effect of chemistry on driving naïve macrophage to other phenotype. However, most studies of metallic nanoparticles have noted that macrophages express high pro-inflammatory cytokines such as those related to Ag, Al and Au nanoparticles [216]. In addition, Pt porphyrin could have ROS production effect which could modulate macrophage to pro-inflammatory phenotype.

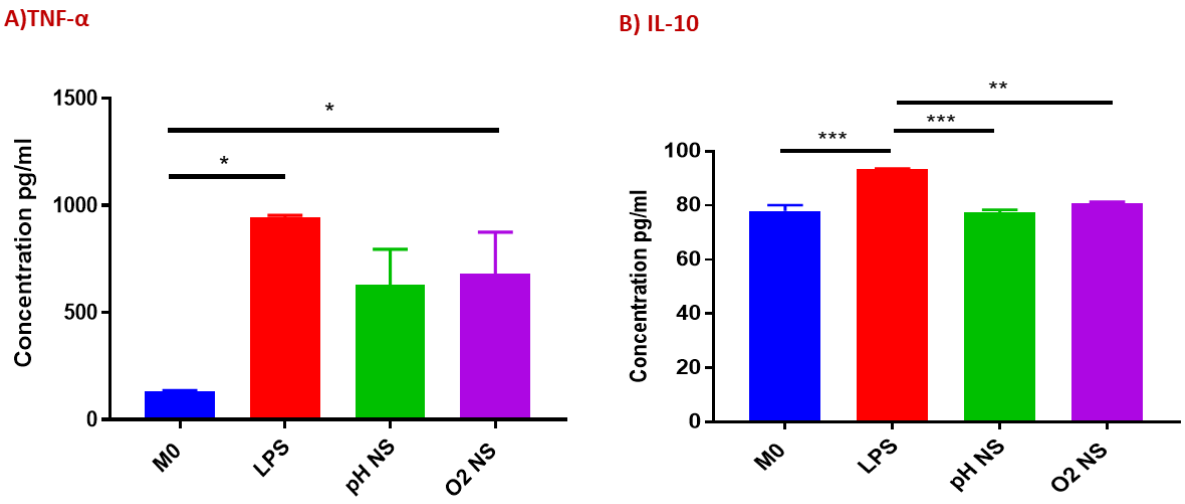


Figure 4-9: Cytokines in the supernatants of THP-1 differentiated macrophages cultured with 100ng/ml LPS, 100 µg/ml oxygen and 250 µg/ml pH nanosensor were measured by means of ELISA for (A)TNF-α and B) IL-10. Data presented are the mean ± SD of at 3 independent experiments, each experiment with one passage number (9-11), n=4, = ±SD (level of significant ****p<0.0001, ***p<0.001, **p<0.01, *p<0.05)

4.2.7 ROS detection with oxygen and pH nanosensors using 2',7'-dichlorodihydrofluorescein diacetate (H_2DCFDA)

It was previously noted in Chapter 1 that porphyrins are the dynamic photo-sensitizers and have potential to use in photo-medicines. Insertion of the metal in porphyrin ring can significantly change the chromophore behaviour [217]. Metal ions drive porphyrin to undergo intersystem crossing (ISC) which influences the phosphorescence and lifetimes of the resulting excited triplet state. This affects the behaviour of the oxygen sensor and acts as a sensitizer [218]. Studies in the literature have been shown that interaction of triplet excited state of porphyrin and molecular oxygen leads to induce ROS production and induce cell death [219-221].

To investigate the production of ROS in the cells treated with oxygen nanosensors, 1 mg/mL of nanosensors were mixed with 9,10-anthracenedyl-bis(methylene) di malonic acid (ABMA) which is a probe used for detection of ROS using spectroflurometer, see Appendix 2 Figure B-1. It has been shown remarkable decrease in fluorescence APMA as result of generating ROS with Pt porphyrin nanosensors. An assay of cellular ROS detection were performed using H_2DCFDA. Menadione, which is activated cytochrome c release from mitochondrial membrane, was used as positive control for generating H_2O_2. The result shows in Figure 4-10 A the H_2DCFDA expressed significantly higher intensity with oxygen compared to pH nanosensors and control. The result reflects the ability of Pt porphyrin to generate H_2O_2. Additionally, the result suggested that ROS was produced as a result of conversion of oxygen to ROS within mitochondrial membrane, Figure 4-10 B. These results are comparable to the previous result which shows that porphyrin produce H_2O_2 [222, 223]. The suggested mechanism of producing H_2O_2 is that the reaction was carried out by transferring electrons from the triplet excited porphyrin state to oxygen

molecules to produce O_2^- leading to generation of H_2O_2 [222]. These results highlighted the advantage of Pt porphyrin use in photodynamic therapy as ROS generator. Specifically this allows for Pt Porphyrin to modulate and mirror macrophages of additional phenotypes by generating H_2O_2. Although the focus is on the ability of Pt porphyrin in sensing oxygen, it would be interesting if future studies expanded this research by investigating production of other ROS types that include singlet oxygen.

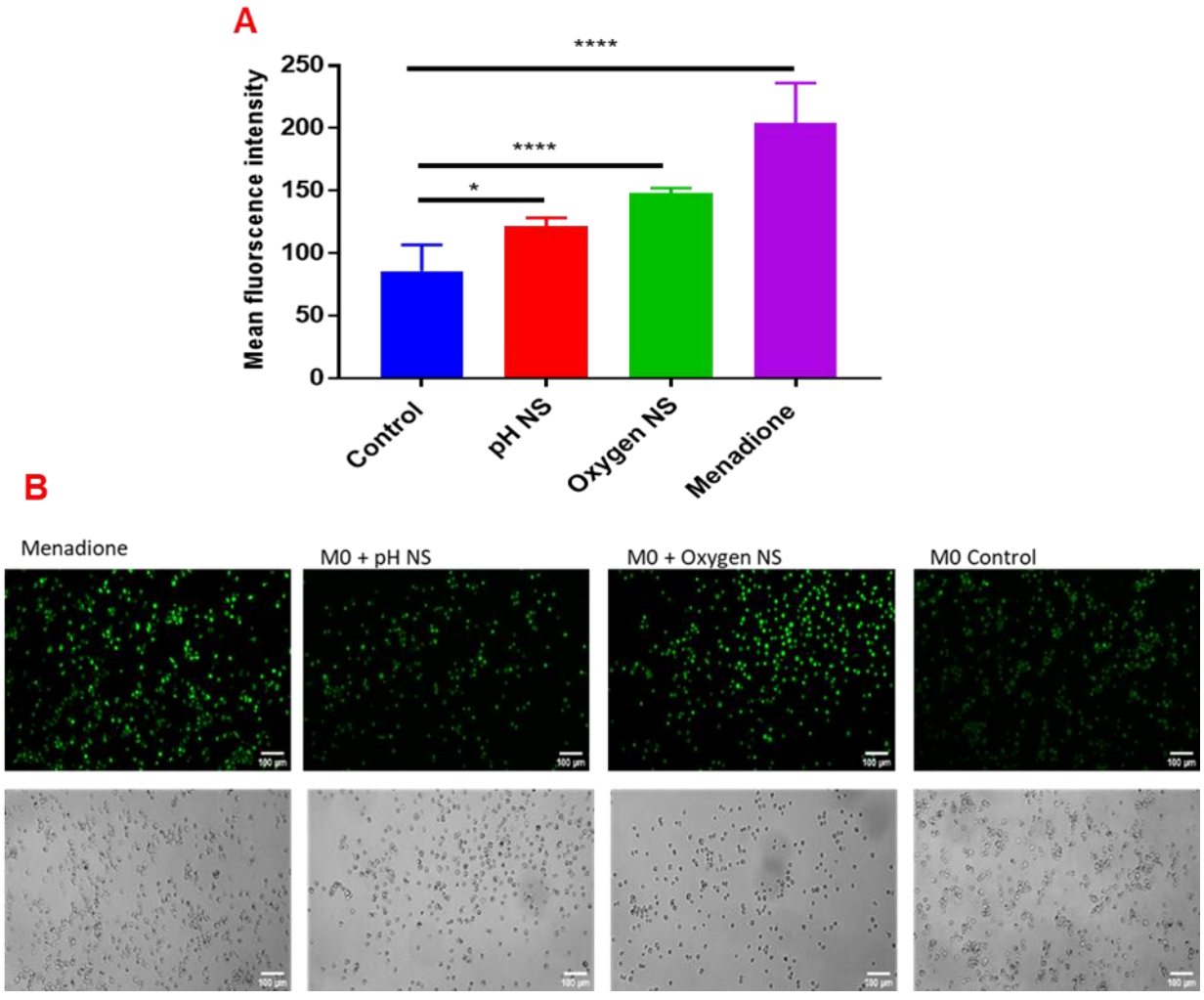


Figure 4-10: A) Detection of ROS by H2DCFDA dyes. Data represent for n=3, (level value of significant ****p<0.0001, ***p<0.001, **p<0.01,*p<0.05). B) Corresponding images of cells that were treated with Menadione, pH NS, oxygen NS compared with control. Scale = 100 µm.

4.2.8 Applying oxygen nanosensors in immune cells

4.2.8.1 Calibration of oxygen nanosensors in fixed cells

In the previous section, it was shown that Pt porphyrin, that can determine dissolved oxygen concentrations, generates ROS that can modulate naïve macrophage to additional phenotypes. Going forward oxygen nanosensors produced as part of this this will be applied to monitor intracellular oxygen macrophage concentration to ambient changes in oxygen concentration.

Calibration of oxygen nanosensors was performed using Ibidi imaging system as described in Chapter 2. Figure 4-11 A shows data linearity of oxyen nanosensors with a Stern-Volmer data transformation (R^2= 0.994). As described in Stern-Volmer equation, $F_0/F = t_0/t = 1 + K_{SV}[O_2]$, increasing of porphyrin fluorescence intensity or life time are inversely proportional to concentration of oxygen. K_{sv} is the quenching constant which expresses the sensitivity of nanosensors. It can be determined by applying the equation of $K_{sv} = K_q * t_0$ where K_q = quenching constant of porphyrin and t_0 = porphyrin lifetime. Another method is to determine K_{sv} is graphically by calculating the Stern –Volmer slope. Sensitivity of our oxygen nanosensors K_{sv} was determined from Stern –Volmer equation. By demonstrating Stern-Volmer equation Figure 4-1 B, K_{sv} was calculated to be 0.2097 ± 0.07 $\%^{-1}$ which is comparable to K_{sv} measured for porphyrins mentioned by Giuntini *et al.* [45].

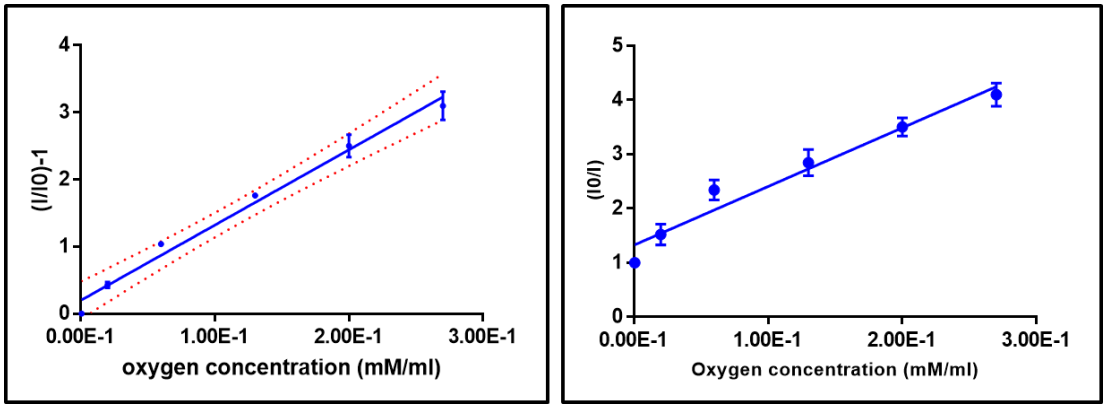


Figure 4-11: A) Calibration of intracellular oxygen nanosensors B) Stern-Vomer calibration (I0/I) where I0 = intensity with absence of oxygen, I = intensity with presence of oxygen versus percent of oxygen concentration.

The application of the calibration curves derived above, permits monitoring of oxygen concentrations that respond to biological change. Therefore, oxygen modulators used for disrupt oxygen by disrupting mitochondrial metabolic pathways in cells. The next section will determine oxygen concentration through the application of imaging algorithms and which visually depicts oxygen concentration as a false colour heat map.

4.2.8.2 Modulation of oxygen concentration in macrophage

Based on sensing capabilities of Pt porphyrin conjugated to polyacrylamide matrix, the fabricated nanosensors were used for measuring intracellular oxygen. In this study, control of input oxygen was studied for two reasons first: to establish use of nanosensors in biological system and secondly to challenge cells to modulate oxygen concentration by using pharmacological compounds that affect cell respiration and measure oxygen using imaging microscopy techniques.

The pharmacological compounds used in this study are bafilomycin and antimycin. They were used as described in Chapter 2. The results in Figure 4-12 shows effect of 0.25 µM bafilomycin and 16 µM antimycin on respiration over one hour post treatment of macrophage cells. Bafilomycin induces sub cellular oxygen changes due to transient disturbance of electron shuttling of mitochondrial membrane, where as antimycin operates as a complex III inhibitor in mitochondrial membrane [194]. Bearing in mind that, bafilomycin is a pharmacological tool in cell physiological research and its mechanism of action is currently being investigated, studies have illustrated extensively that bafilomycin has V-ATPase inhibition activity which has an impact on cellular pH [207]. Additionally, it was evidenced that antimycin has its effect on cellular apoptosis through measurement of respiration [194]. Oxygen respiration have been reported by a variety of methods that include electrochemical and optical sensing [82, 84, 224-226].

The fluorescence based nanosensors which target oxygen measurement in this study have an advantage of providing cell statues however imaging is limited by ROS production and dye photo-bleaching causing cell toxicity.

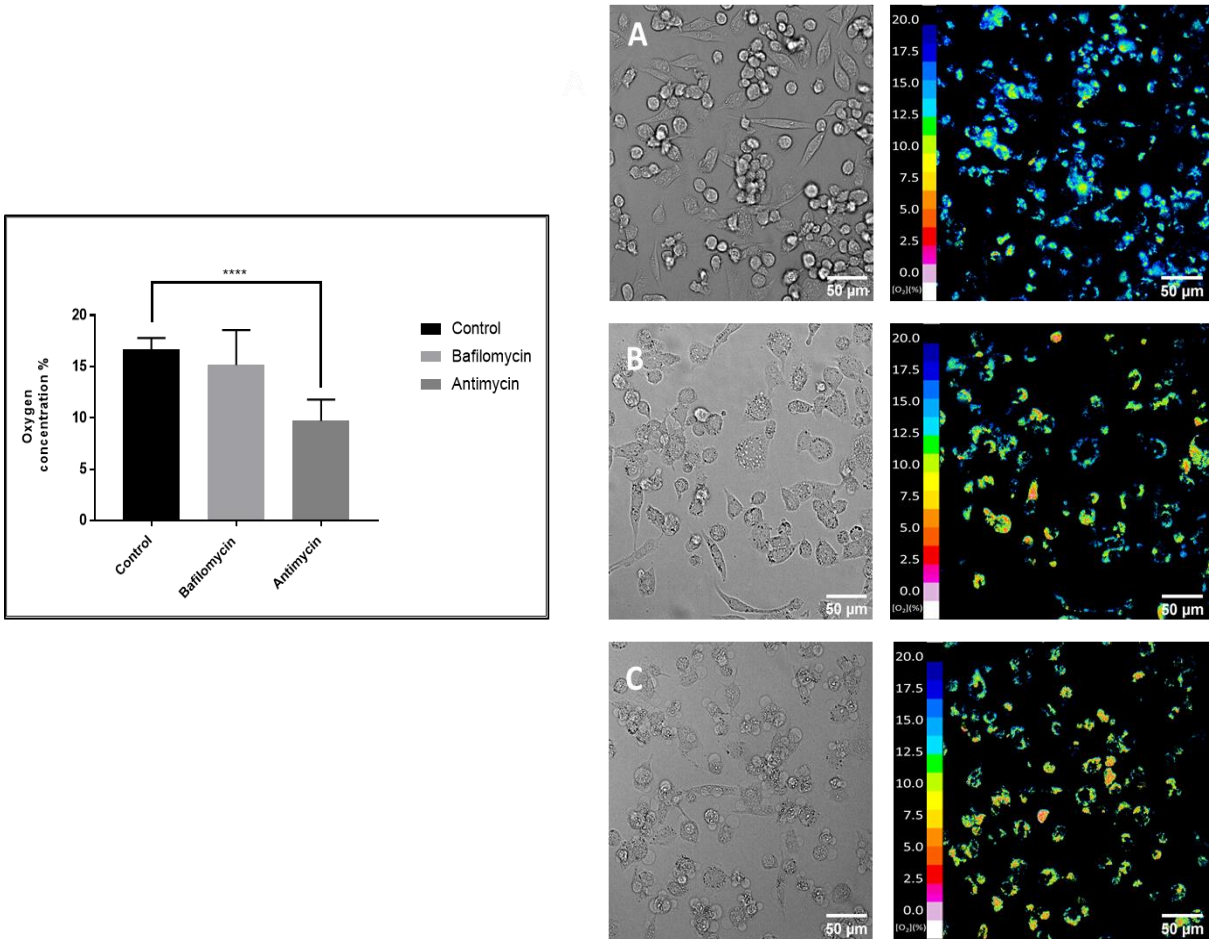


Figure 4-12: Effect of bafilomycin (0.25 µM) and antimycin (5 µM) on macrophage respiration of is attributed to mitochondrial uncoupling after 1 hour treatment. Error bars = SD ($P < 0.05$).

4.2.8.3 Modulation of pH in macrophage

In the previous section, bafilomycin has been shown its effect on oxygen intracellularly. In addition, it was noted in literature that bafilomycin has an effect on H^+ ion flux on mitochondrial membrane. Therefore, following to our interest of using nanosensors, pH nanosensors used for investigating pH change with exposure to bafilomycin. It has been seen in Figure 4-13 that pH has increased significantly with bafilomycin treatment after 30 minutes and one hour from pH 4.5 to 5.0 and 5.2, respectively. The data results were comparable to a previous study by Prill *et al.*[22]. In addition to pH measurements, the pH measured indicated the location of pH nanosensors intracellularly which are most likely found in the cell lysosomes, which typically range from pH 4.5 – 5.0 [227].

The difference between oxygen and pH nanosensors, used in this study, is the presence of Pt porphyrin which alter the surface chemical properties of the nanosensors. Consequently, this affects its interaction with cellular organelles. This may influence nanosensors sub-cellular. These were explored by examining the co-localisation with cell organelles in Chapter 5.

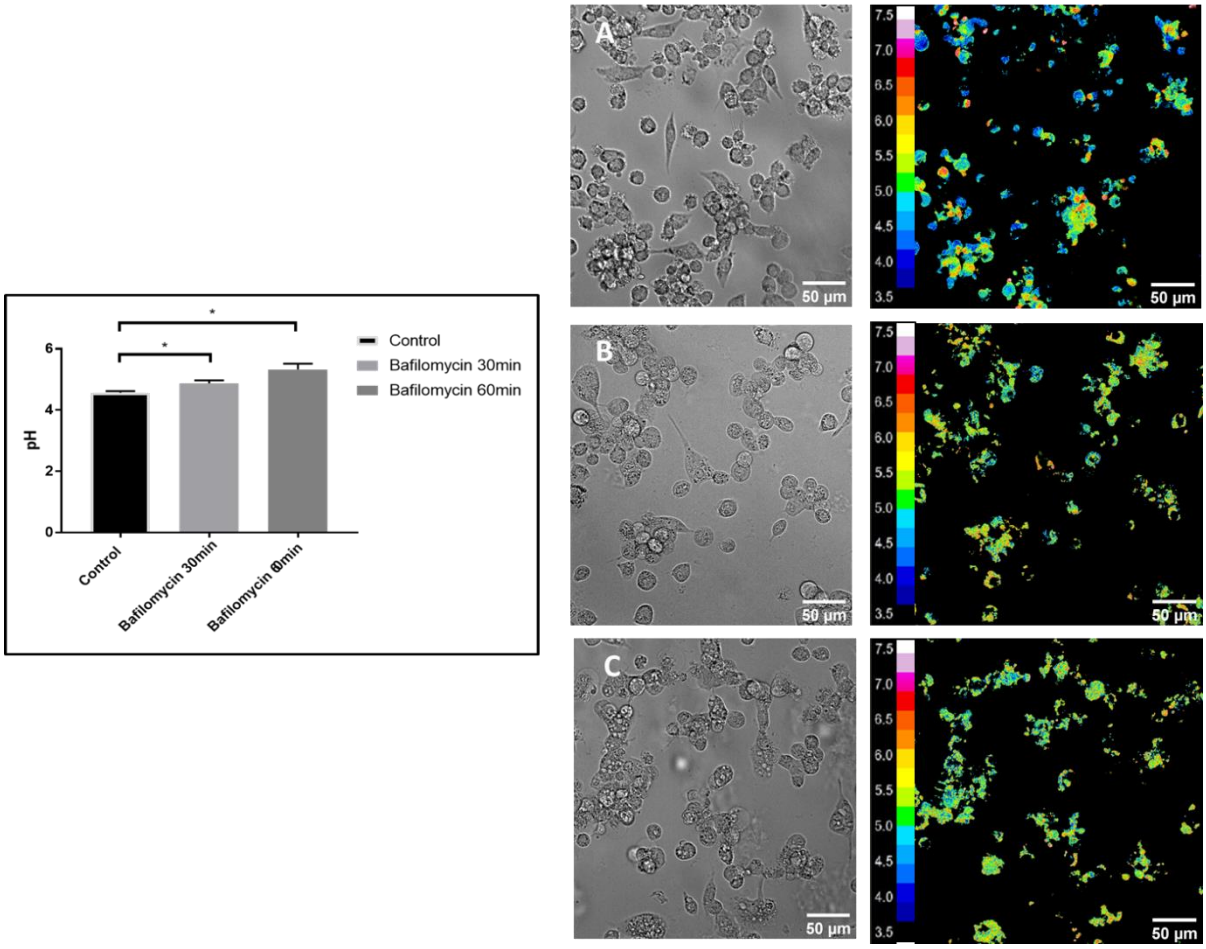


Figure 4-13: (Left) Response of nanosensors to phagosome acidification inhibition. Cells were exposed to nanosensors for 24 hours before being given Bafilomycin A1 (image A). (Inhibitor of phagosome acidification for 30 minutes (image B) and 60 minutes (image C). (n = ~ 200 cells) error bars represent SD. Statistically significance level ($P < 0.05$.)

4.2.9 Heat map of oxygen distribution in macrophage within co-culture model (MRC-5/ macrophage)

Following to the application of oxygen nanosensors in macrophage cells, oxygen nanosensors were used to study oxygen distribution in co-culture model. Co-culture model usually used to simulate wound healing studies [228]. Wound healing is a dynamic process which consists of inflammation, proliferation and tissue remodelling [229]. Through these processes, change the biomarkers such as pH and oxygen cause wound abnormalities [230]. These biomarkers could be monitored by different techniques to manage wound healing pathophysiology such as those based on electrochemical and optical sensors [231].

Fluorescence nanosensors used to study biomarkers involved in wound healing by different representative modalities [232]. In this chapter, study targeted to determine oxygen concentration to differentiate between cell activities. The experimental rational was a potential monitoring of oxygen within wound healing processes using oxygen nanosensors.

Initially, uptake of nanosensors was examined to show nanosensor distribution in MRC-5 cells (fibroblast cells), Figure 4-14. Images of fibroblast cells illustrates an uptake of oxygen nanosensors after treating the cells with nanosensors for 24 hours. The cell continued to proliferate and did not exhibit indicators of stress (blebbing etc.) [233].

Moving to Figure 4-15 which illustrates co-culture of MRC-5 (fibroblast cells) and macrophage treated with oxygen nanosensors. MRC-5 (fibroblast cells) were pre-treated with 5-chloromethylfluorescein diacetate that used for tracking cell proliferation (CMFDA). In addition, cells were treated with oxygen nanosensors to determine the metabolic characteristics of each cell type through oxygen distribution. At first glance to the images, there appears to be a difference in the intensity of nanosensor dyes between macrophage and fibroblast. This difference was illustrated by heat map images to represent the difference in oxygen concentrations.

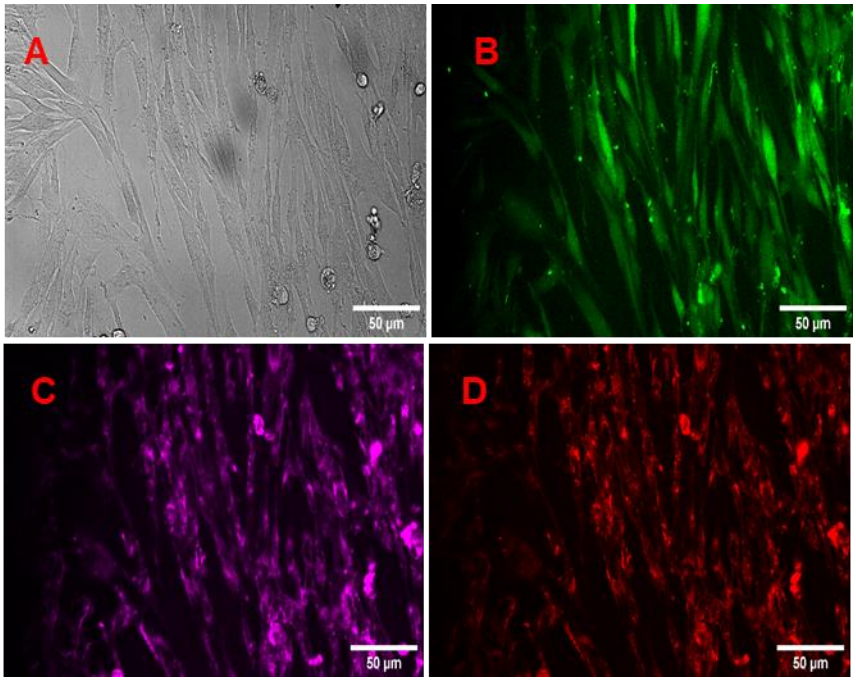


Figure 4-14: Fibroblasts MRC-5 image treated with nanosensors, A) Brightfield, B) Green fluorescent were pre-labelled with CFDA-SE), C) Red fluorescent TAMRA, D) Magenta fluorescent Pt. porphyrin. Imaged by fluorescent wide field microscope. Scale bar= 50µm.

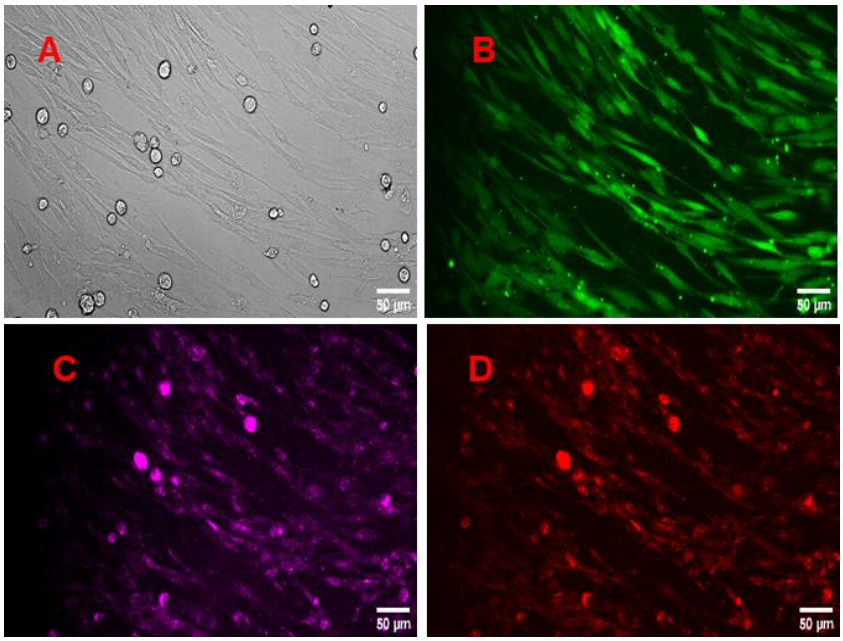


Figure 4-15: Co-culture (fibroblasts MRC-5 + Macrophage) image treated with oxygen nanosensors, A) Brightfield, B) Green fluorescent were pre-labelled with CFDA-SE), C) Red fluorescent TAMRA, D) Magenta fluorescent Pt. porphyrin. Imaged by fluorescent wide field microscope (scale bar= 50µm).Scale bar= 50µm.

Figure 4-16 shows super-resolution microscopy of a macrophage and fibroblast co-culture image that represent intracellular presence of oxygen nanosensors in the cells. The important feature of super-resolution microscopy is providing highest resolution images with minimal invasiveness. Obtaining high spatial resolution images with super-resolution can be generated by optical sectioning. The concept of optical sectioning is practically demonstrated by technical illumination techniques [234].

Figure 4-16 shows the distribution of oxygen nanosensors in both type of cells (macrophages and fibroblast cells) and highlights an aggregation of cells due to a potential photo-toxicity. Despite the high spatial resolution image generated from super –resolution microscopy, the microscopy setup did not provide a viable environment to the cells compared to wide-field fluorescence microscopy which was complimented with an Ibidi controlled stage which provide 5% CO_2 and 37°C. Therefore, wide-field fluorescence microscopy was used to determine oxygen distribution in macrophage and fibroblast co-culture.

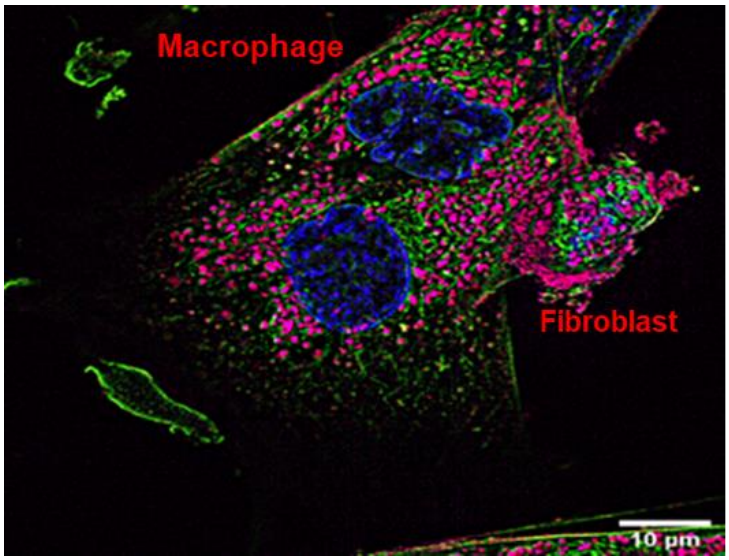


Figure 4-16: Distribution of nanosensors in MRC-5 and macrophage co-culture image intracellularly in both type of cells. Nanosensors (Magenta), nucleus (Blue), cell mask (Green). (Scale bar= 10µm) using super-resolution microscopy.

Images of co-culture in Figure 4-17 have a range of oxygen concentrations exhibited as a false colour heat map. Figure 4-17 A shows a bright field image of co-culture which represent the macrophage and fibroblast cells. Figure 4-17 B shows macrophages that were treated with oxygen nanosensors in the absence of fibroblasts. The oxygen concentration appears to be less than 10 %. Figure 4-17 C shows fibroblast cells treated with oxygen nanosensors and indicates relatively higher oxygen concentration between 15 -17%. Figure 4-17 D, the fibroblast and macrophage co-culture the oxygen consumption is greater in macrophage more than fibroblasts. This could be explained by the cell phenotypes and their modulation of glycolysis dependent metabolism [235].

This study provides the rationale for the potential to investigate cell –cell interactions requiring complex co-cultures. Further research is required to map oxygen concentrations for the wound healing process, that help in cell oxygen monitoring approaches for treatment of inflammation and fibrosis.

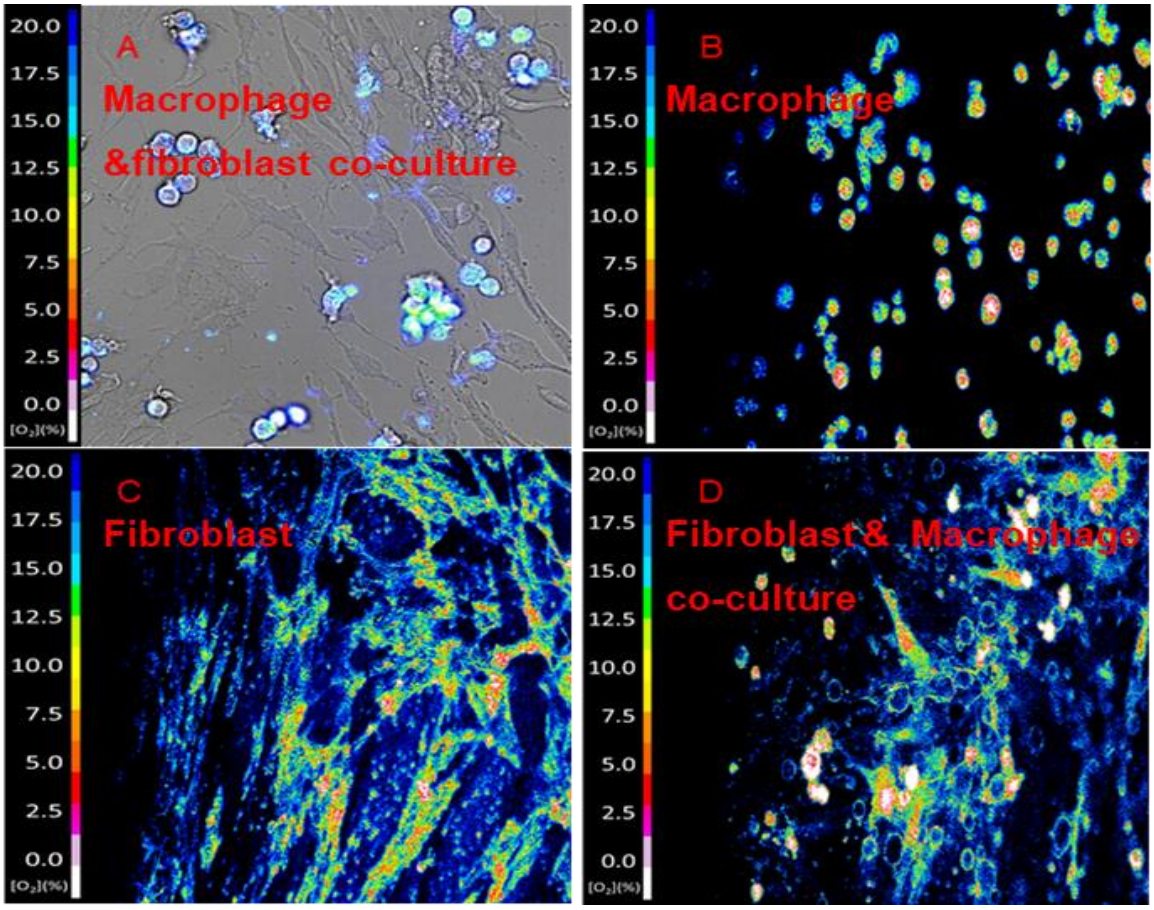


Figure 4-17: Distribution of nanosensors in MRC-5 and macrophage co-culture images A) Heat map of oxygen distribution in macrophage co-cultured with fibroblast, B) oxygen distribution in macrophage, C) shows oxygen distribution in fibroblast, D) oxygen distribution in fibroblast co-cultured with macrophage.

4.3 Conclusion

In summary, THP-1 cell line were differentiated to macrophages and used as an immune of biological model. THP-1 cells were differentiated to macrophages by incubating them with PMA. After differentiation to macrophages, they have been characterised by staining its surface marker. Additionally, characterisation of polarised macrophage was validated by examining cytokine productions and immunofluorescence of M1 and M2.

Oxygen nanosensors were delivered to macrophage cells with minimal effect on metabolic activity. Oxygen nanosensors enhanced pro-inflammatory behaviour by producing TNF-α cytokines compared to pH nanosensors which were characterised as M1 like macrophage. ROS have been generated through exposure of the cells to oxygen nanosensors, when the ROS generating effect of Pt porphyrin is considering. Further studies of the ROS producing effect of Pt porphyrins is required to determine their impact on cell polarisation and viability.

This chapter also examined the spatial co-localisation of the dyes TAMRA (reference dye) and Pt-porphyrin (indicator dye) in the same area which confirm conjugation and absence of leaching of porphyrin and TAMRA from the nanosensor polyacrylamide matrix. The stability of nanosensor fluorescence was also studied over a week. Nanosensors fluorescence peaked at ~ 24 hours was the highest, then decreased after day 4.

Intracellular oxygen measurements were made using fluorescent nanosensors. Macrophages were exposed to bafilomycin and antimycin which have been shown to be influence to oxygen concentrations; via their action on mitochondria. Practically, cell respiration was assessed by measuring oxygen concentration. Based on that macrophage cells were exposed to cell activators such as Lipopolysaccharides (LPS) and Interferon ɣ. The result in Appendix B Figure 2 demonstrates the oxygen consumption can monitored using fluorescence nanosensors in response to IFN-ɣ as a result of its strong effect on metabolic modulation of macrophage, relative to compared to the addition of LPS [236].

Using pH nanosensors, the pH was measured in lysosome. The pH of the lysosomes were characterised to be acidic (pH~4.5) in control macrophage. The modulation of pH was achieved through treatment with bafilomycin at a variety of time points and shown to increase to pH 5.2 at 1 hour post bafilomycin treatment.

False colour heat map were applied to show oxygen concentration variations in co-culture (macrophage and fibroblast). The results highlighted that macrophages consumed oxygen at a greater rate than fibroblasts. This observation was attributed to macrophage plasticity and its phenotype transitions due to metabolic modulation.

Chapter 5 . Studying oxygen flux in hepatic cells

5.1 Introduction

The Hepatocyte model is rich of enzymes which underpin the central role of metabolism [237]. It has been used in studies of drug toxicity, modification and clearance. Specifically, one of the main signs of drug induced liver toxicity is the mitochondrial dysfunction [238]. Assays have been widely used to evaluate mitochondrial function, including the MTT assay [239] which is used to measure metabolic activity and JC1 mitochondrial staining which used to assess membrane potential [240]. Mitochondrial dysfunction is likely to increase the sensitivity to drugs that lead to decrease of cellular repair and viability [241]. An indirect method to assess mitochondrial activity is by measuring oxygen consumption and extracellular pH [242]. Papkovsky *et. al.* demonstrated an approach to monitor metabolic activity using oxygen consumption as an indirect measure using quenchable fluorophores [84].

It is important to choose instrumentation with suitable cellular quantification criteria which is easy to use, does not require laboratory cellular preparations and has sensitive detectors. The most commonly used instrument is the Seahorse bioanalyser coupled with the mitostress assay, which is becoming an industry standard for the quantification of oxygen consumption rate (OCR) and extracellular acidification rate (ECAR) [243] [244].

However, this method has its limitations, for example 1) it requires expensive equipment and consumables, 2) a large number of samples for screening increases the cost and time, 3) the medium used during performing assays should be without bicarbonate which is in the physiological buffer system and important for metabolic regulation of mammalian cells [245].

An alternative approach, optical nanosensor technology is able to spatiotemporally monitor oxygen and pH and their gradients in 2D and 3D biological systems. Oxygen sensitive probes coupled with different detection platforms from time resolved simple phosphorimeters to automated readers and wide-field, confocal, and multiphoton FLIM (fluorescence lifetime imaging microscopy) systems [140, 246, 247]. In addition, fluorescence co-localisation microscopy studies are well established for determining cellular location where the fluorescence signals of labelled objects and subcellular organelles are observed with different fluorophores. Co-localisation can be quantified from images by object overlap in two different fluorophores channels and pixel-by-pixel methods. Then quantification of co-localisation can be described by Pearson's or Manders' correlation coefficient.

Fluorescence microscopy allows visualisation of dynamic and endpoint biological processes in 2D and 3D [248]. As discussed in Chapter 3, microscopy approaches provide several advantages such as high analytical power, versatility of measurement and afford broad application across sample type [22]. However, some challenges remain associated with selection of oxygen probe and imaging modalities, especially when it comes to quantitative imaging [249]. Thus, applying sensible design principles, validating biosensor function and the appropriate fluorescence microscopy imaging technique are key to producing a successful nanosensor for biological measurement [249]. Therefore, in this study, first, it is necessary to identify the cellular positioning of oxygen nanosensors to determine the location of intracellular measurements. Secondly, having defined the spatial location of measurements, hepatocytes (HepaG2 cells) are challenged by pharmacological compounds and the oxygen flux in 2D and 3D models is measured.

5.2 Results and discussion

5.2.1 Toxicity assay

The work started by examining the toxicity of oxygen nanosensors to HepaG2 cells. Different nanosensor concentrations, from 0 to 1000 µg/mL, were incubated with the cells and the response assessed using a Toxilight® kit to detect adenylate kinase from damaged cells. The result in Figure 5-1shows that nanosensors can be used up to 100 µg/mL without significant effect on cell viability. A sample of dead cells was used as a positive control.

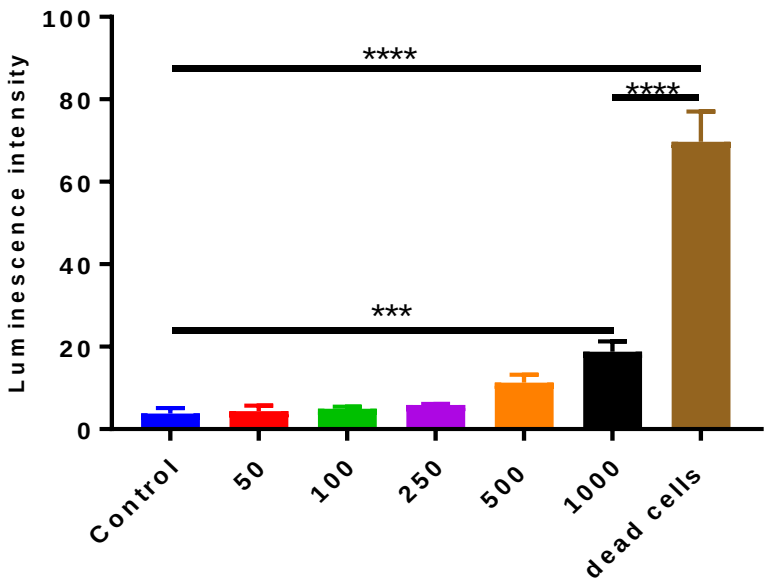


Figure 5-1: Toxicity assay of oxygen nanosensors in HepaG2 cells. Cells were treated with 100 µg/ml of nanosensors. Data showed mean luminescence intensity which representative for n=3, (level value of significant ****p<0.0001, ***p<0.001, **p<0.01).

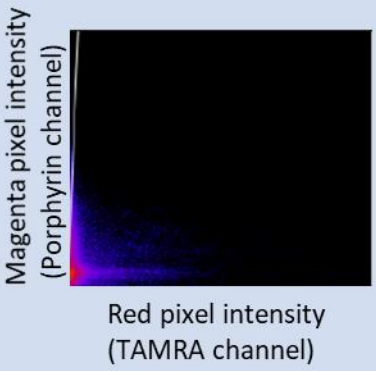
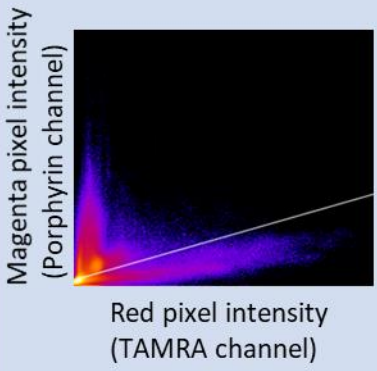
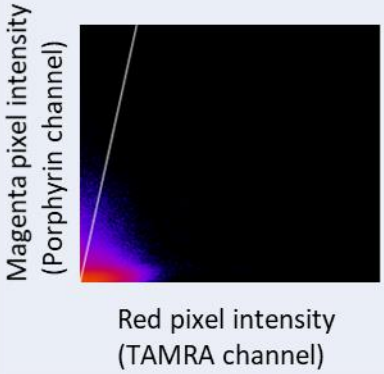
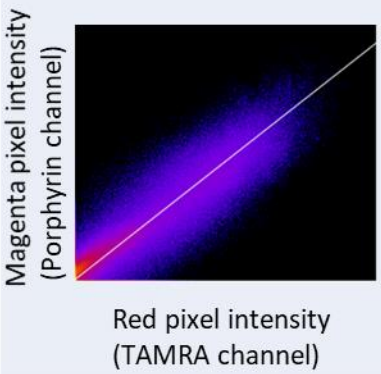
5.2.2 Intracellular fate of nanosensors

Determination of nanosensor location using super-resolution microscopy permits determination of the precise location of nanosensors intracellularly. Images in Figures

5-2 to 5-6 were taken using a super-resolution microscope (ELYRA PS.1 super resolution system on a Zeiss 780 microscope platform), which has the capability of improving the spatial resolution of imaging 10 to 20 nanometres.

To assess the degree of co-localisation of nanosensors with cellular organelles an approach where lysosomes and mitochondria were labelled green (using fluorescent CellLights®) and nanosensors were labelled red. A comparison was made Table 5.1 of the intracellular localisation of pH and oxygen nanosensors. For pH nanosensor mimics the OG and FAM indicator fluorophores were removed, leaving only TAMRA as the fluorophore (TAMRA) in particles to prevent spectral overlap with cell markers. For the oxygen nanosensors the Pt porphyrin dye and the TAMRA did not overlap with the CellLights and so were used without modification. The cells were exposed to oxygen and pH-mimic nanosensors for 24 hours. The localisation of nanosensors, lysosomes and mitochondria were studied and analysed in respect to each other and the degree of co-localisation was calculated from PCC as seen in Table 5.1.

Table 5.1: Co-localisation of Pearson's Correlation Coefficients (PCC) for TAMRA nanoparticles and oxygen nanosensors with mitochondria and lysosomes, calculated from five microscopic images of two experiments.

	Oxygen sensors	TAMRA nanoparticles
Mitochondria	PCC= 0.054 ± 0.04 	PCC= 0.246 ± 0.13 
Lysosomes	PCC = 0.09 ± 0.83 	PCC = 0.83 ± 0.148 

The data from Table 5-1 and images in Figure 5-2 show weak co-localisation of both the oxygen nanosensors and TAMRA particles with mitochondria (PCC = 0.054 and PCC= 0.246), respectively. Comparing to TAMRA particles which strongly co-localised with lysosomes (PCC= 0.83). Whereas TAMRA particles have shown weak co-localization with mitochondria (PCC= 0.09). These findings indicate that pH sensors most likely prefer to locate in lysosomes but not in mitochondria. On the other hand, oxygen sensors are potentially localised in the cytoplasm.

From the data shown in Figure 5-2, it can be suggested that the fate of pH-sensitive polyacrylamide nanosensors is to localise in the lysosomes, whereas presence of Pt porphyrin on the surface of particles would induce an alternative cellular uptake route. The images indicate that the oxygen nanosensors are not localised within the lysosomes or associated with mitochondria, they may be within the cytoplasm.

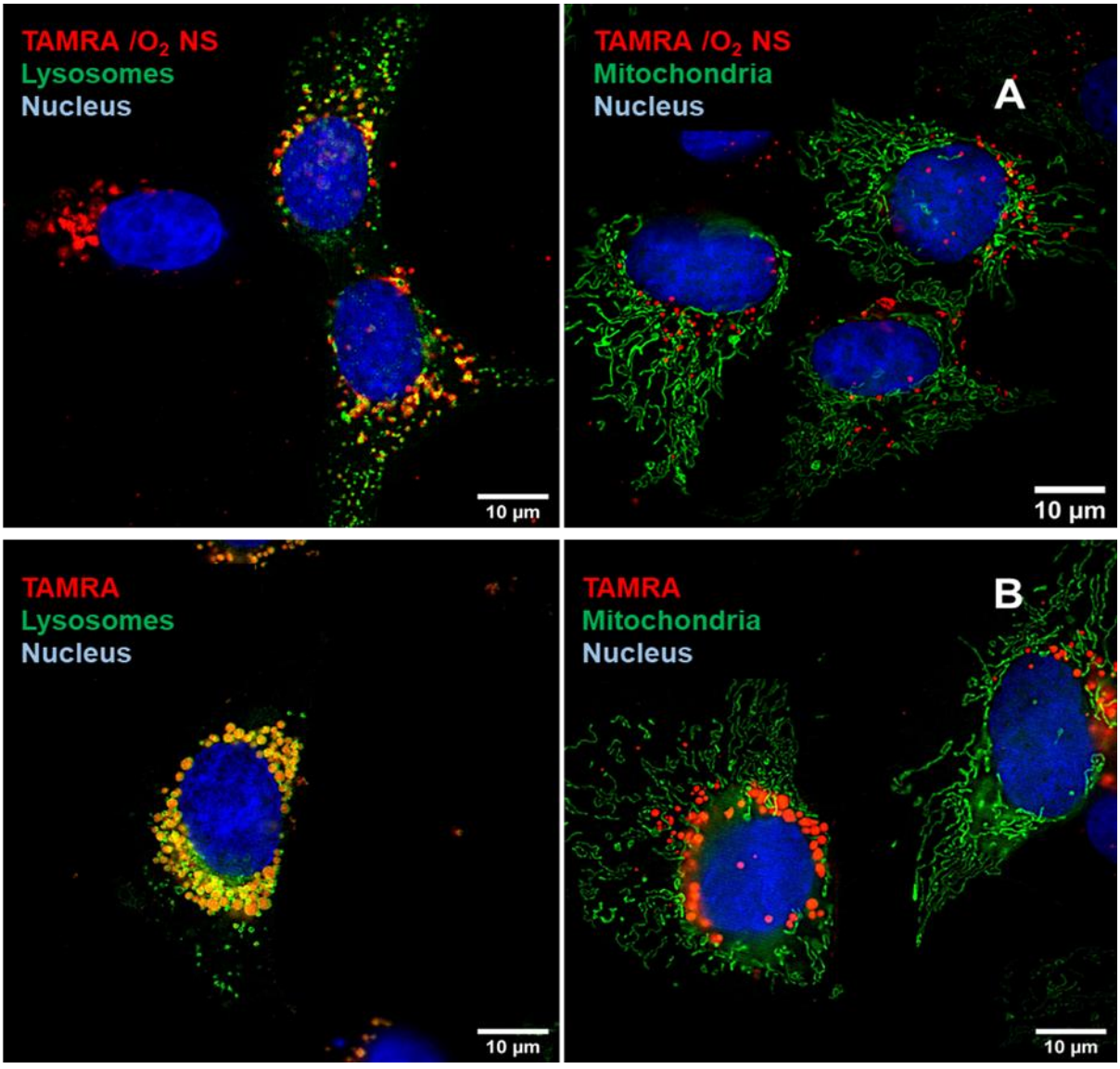


Figure 5-2: Intracellular co-localisation of (A) TAMRA coupled with oxygen and (B) TAMRA nanoparticles with mitochondria and lysosomes. Mitochondria and lysosomes labelled with cellLight® (green), TAMRA/O2 and TAMRA particles (red), nucleus (blue). Co-localisation were determined by super-resolution microscopy by calculation Pearson's Correlation Coefficient (PCC) of images. Scale bar=10 µm.

The escape of nanomaterials from endo-lysosomal compartments within cells has been observed in other studies though the mechanism for this remains under debate [18-21]. It is postulated that a number of factors play a role in oxygen nanosensors not associating with lysosomes. These include nanosensor composition and surface chemistry (amino functionalities), hydrophilicity and osmotic imbalance which could cause rupture of lysosomal membrane [250]. Another possibility is that oxygen nanosensors are directly trafficked to the cytoplasm. However, further studies are needed to confirm this, potentially using a cytoplasm marker and following different time points in order to track nanosensors in cell compartments.

In Figure 5-2 B, TAMRA particles are seen inside the vesicles ring of lysosomes which show yellow colour in merge images of labelled lysosomes and TAMRA particles. Conversely images do not show co-localisation with mitochondria. Interestingly, TAMRA particles are observed to the periphery of the nucleus which display definitely that particles inside the lysosomes. Previous reviews have discussed that lysosomes are present mainly to the nuclear periphery [251, 252].

In this context, if we assume that oxygen and pH measurements indicate the intracellular location of sensors after 24 hours uptake, the design of pH and oxygen nano-diagnostics is a significant insight. As a consequence, these results provide data where the oxygen and pH and gives information when and what the nanomaterials affected by biological environment.

5.2.3 Respiration assay (ratiometric imaging of hypoxia)

Developed oxygen nanosensors were fabricated as described in chapter 2 and tracked in the cells as shown in previous (section 5.2.2) for measuring oxygen concentration intracellularly. Cellular respiration has been quantified previously using nanosensors [253, 254]. It was mentioned that technical measurements of biological oxygen concentration is challenging and difficult to be accurately determined. However, what can be clearly seen is that bio-imaging techniques for measuring oxygen is a trend that is building. In addition, detectable fluorophores can be mixed to acquire more reliable data.

Oxygen bio-imaging is a way to determine the dynamic metabolism. Thus, liver cells which are derived from a highly vascularised organ have been chosen as an exemplar to investigate whether nanosensors can measure biological activity. In this study, we aimed to assess the applicability of an endpoint respiration assay which could eventually form the basis of a cell toxicity testing platform.

To evaluate the response to oxygen in live cells, the cells were treated with different doses of acetaminophen. Additionally, cells were treated with methotrexate 250µM, propranolol 5mM and antimycin 5µM. Each of these drugs has a different toxic mechanism effect on mitochondria. Thus, we hypothesised that exposing cells to these drugs could give different respiration and hence oxygen levels, according to the effect on mitochondria. Cells imaged using *Nikon* wide field microscope and the data was analysed using image J. The analysis steps are explained in methodology (Chapter 2).

The results shown in Figure 5-3 indicates the toxicity mechanism of acetaminophen by using 1, 5 and 25mM dose. The results show a slight shift of the histogram to higher oxygen concentration to 2.3 % (3×10^{-2} mM) with decrease of pixel frequency in 25mM treated cells. The increase in oxygen concentration might be due to failure of oxygen consumption and loss of cell membrane integrity. The noticeable description of decrease in pixel frequency with acetaminophen toxic dose could be due to detachment of dead cells which can be seen in mapping image of cells with 25mM dose. Oxygen mapping of 25mM shows marked reduction in cell number and subsequently decrease in nanosensors which affect the overall measurements.

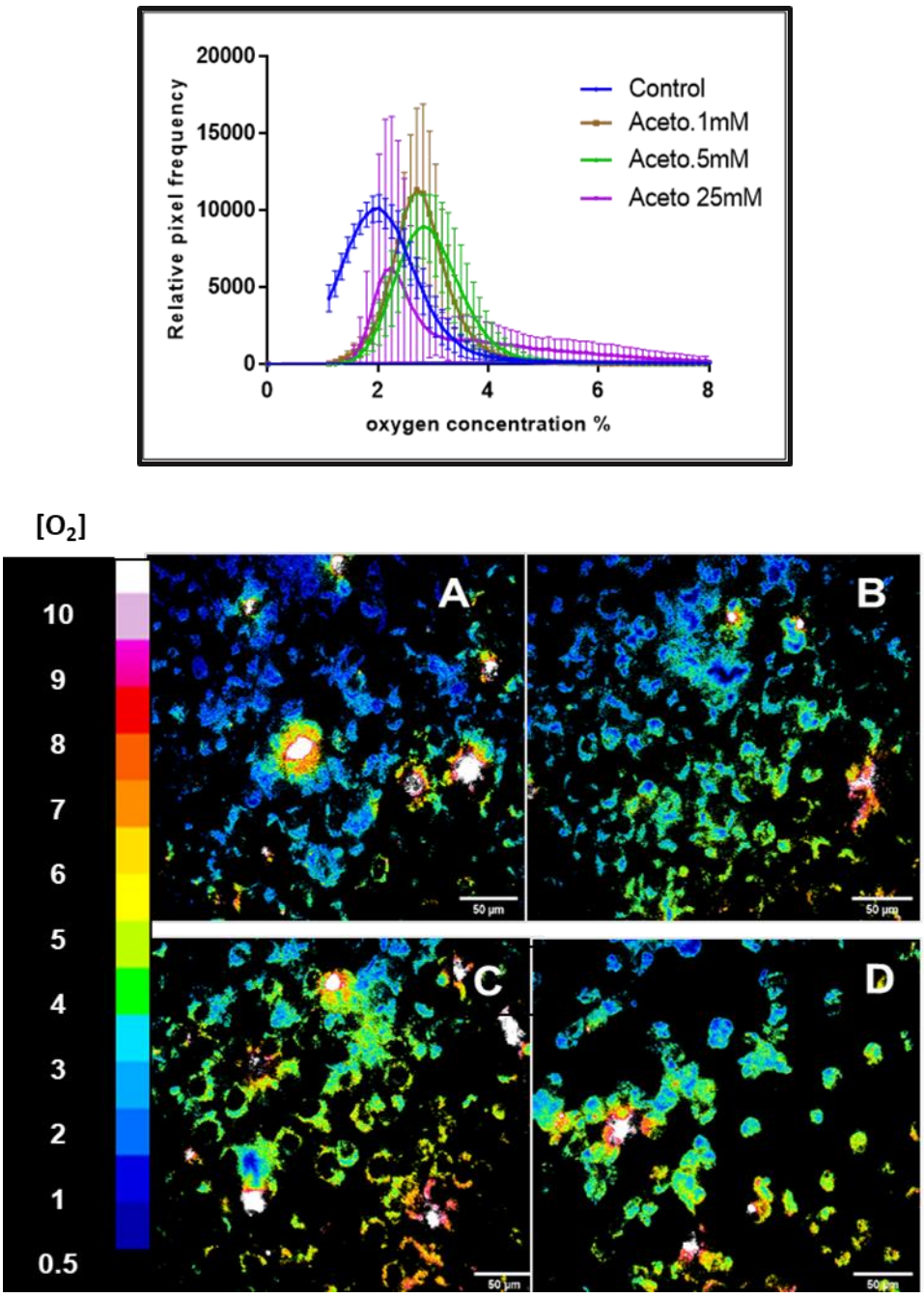


Figure 5-3: Histogram of oxygen distribution in cells. Oxygen concentration in response to 1, 5 and 25µM acetaminophen, statistics based two experimental repeats (n = 5 ROI). Corresponding colour oxygen maps are shown under the histograms.

The mechanism of high dose toxicity of acetaminophen in hepatic cells is explained in a review article by Coen [255]. The main cause of toxicity is production of toxic metabolite (*N*-acetyl benzoquinone imine) (NAPQI) by P450 enzymes, specifically CYP2E1 [255]. Another suggested mechanism of toxicity was reported by Behrends et al [256] found that HepaG2 cells shows overproduction of lactate from glucose as result of ‘’Warburg effect’. In addition, to its toxic mechanism as CIII complex inhibitor as investigated by Prill et al [254] when they studied acetaminophen toxic mechanism on HepaG2 cell spheroids.

Returning to Figure 5-3, the graph shows that histogram of 1 and 5 mM doses of acetaminophen shifted slightly comparing to control to 3% and 3.1%, respectively. This could be attributed to switch of cellular respiration that affect intracellular oxygen concentration, leading to create spatial oxygen gradient. Further, pixel frequency decreased with 5 mM acetaminophen dose.

Study of antimycin, methotrexate and propranolol effect on oxygen concentration shows a significant reduction in oxygen consumption as shown in Figure 5-4. Antimycin has been extensively used in studying mitochondrial functionality compared to other reagents because of its direct inhibition effect on cytochrome C [190, 253, 254, 257]. Cell morphology in oxygen mapping Figure 5-4 D indicates necrotic cells that show as having high oxygen concentration, and therefore are not consuming oxygen, in mapping image of cells treated with antimycin. The effect of antimycin on the cells in our results is comparable to that previously reported which also showed immediate loss of oxygen consumption [254]. This is corroborated by the histogram data showing the cells treated with antimycin have a higher average oxygen concentration, determined as 3.1% (4×10^{-4} mM) In addition, histogram in Figure 5-4 shows a lower

oxygen concentration of approximately 2.2 % (2.9 $x10^{-4}$ mM) for cells treated with methotrexate and propranolol, when compared to antimycin. Though it should be noted that these values are higher than the control that shows oxygen concentration at approximately 1% ($1.3x10^{-4}$ mM), indicating that all the treatments are having some effect on cellular respiration. Further work to explore the response of oxygen over time would prove extremely interesting in understanding cellular metabolism of these pharmacological compounds.

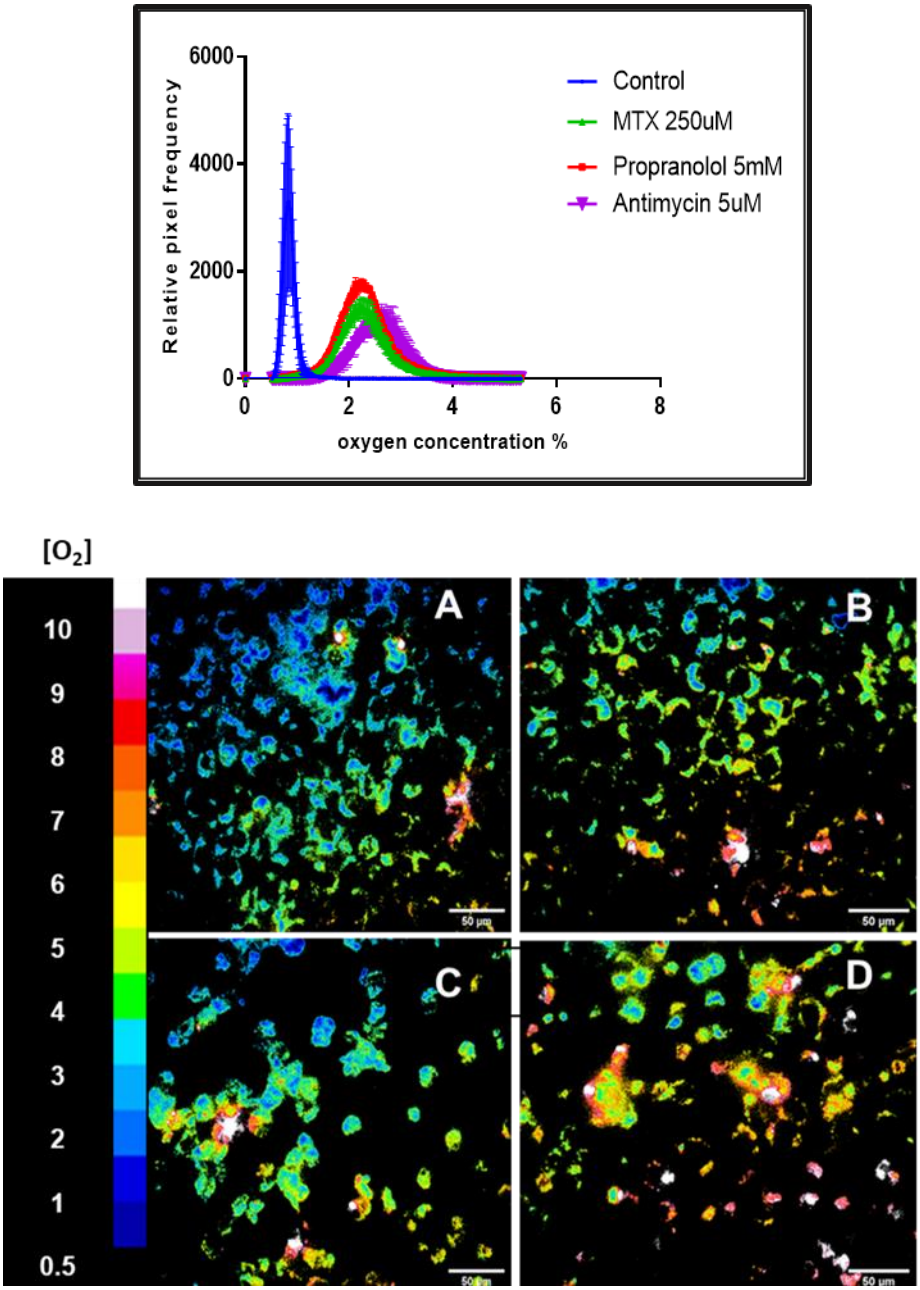


Figure 5-4: Histogram of oxygen distribution in cells A) control in response to B) 5µM propranolol, C) 250µM methotrexate and D) 5µM antimycin, statistics based two experimental repeats (n = 5 ROI). Corresponding colour oxygen maps are shown next to the histograms

Previous studies suggest that methotrexate toxicity mechanism is related to depletion of folate which has been shown that affect proliferation, cell arrest and respiration inhibitory effect [258, 259]. Despite respiration inhibitory effect of methotrexate deduce the effect on ETC was pointed by Behrends et al in the study of methotrexate toxicity, he mentioned lack of measuring oxidative stress which is key of mitochondrial functionality[256]. Moving to propranolol which has been shown an inhibitory effect on CIII complex [260]. Which expect to have direct effect on oxygen. These would be another possible area of future research to investigate the mechanism of toxicity.

More recently, literature has emerged that offers contradictory findings about metabolic bioreactor [254, 256, 261, 262] which is used to monitor oxygen for drug metabolic functionality screening. However, one of the limitations with bioreactor technique is that need cells and sensor to be proximity close to be sensitive to metabolic change that could be affect respiration which require critical preparation setup. It is important to note that it is challenging to make an oxygen measurement in live cells due to the difficulty to maintain health status that might effect respiration. Moreover, continuous imaging may cause photo-toxicity. Because of that in this work, theory has been built on measured oxygen with toxic and treatment doses of drugs within the dynamic oxygen range and show cell apoptotic pattern that result in proliferation arrest.

Having focused attention thus far in this chapter on using nanosensors to measure differences in cellular oxygen concentration in different metabolic states it is appropriate to now consider whether the same conditions induce changes in cellular pH. To do this changes HepG2 cells were incubated with pH nanosensors and then treated with 1mM, 5mM and 25-mM doses of acetaminophen, as well as 5mM

propranolol and 250µM methotrexate. The intracellular pH was monitored using wide field fluorescence microscopy and the images and compiled histograms are shown in Figure 5-5 and 5-6. For the experiments where different doses of acetaminophen were added to the cells there is a slight shift of pH to approximately 5.7 with 1mM and 5mM doses of acetaminophen when compared to pH of 5.5 observed with control cells (Figure 5-5). The 25 mM acetaminophen treatment shifts the pH to 5.8 with lower pixel frequency, likely due to detachment of dead cells from the sample plate. In addition, the data indicates that the fate of pH nanosensors is likely into lysosomes that are characterised by low pH. This is in agreement with previous results from our group and proved in this chapter (section 5.2.2).

Figure 5-6 shows the images obtained after treatment of cells with 5mM propranolol and 250µM methotrexate. Shows small change of pH which reflect minimal effect of these drugs on lysosomes acidity. While post treatment of cells by antimycin shows toxic dose effect which cause cell necrosis. As a result of disturbance of cellular functionality the pH increased which suggest an equilibration effect of nanosensors trafficking through endoplasmic pathway because a toxic dose of different drugs [36]. This theory, could can be explained in detail by exposing the cells to different doses of each drugs with determine nanosensor co-localisation within endoplasmic pathway and the data also may be supported by kinetic information.

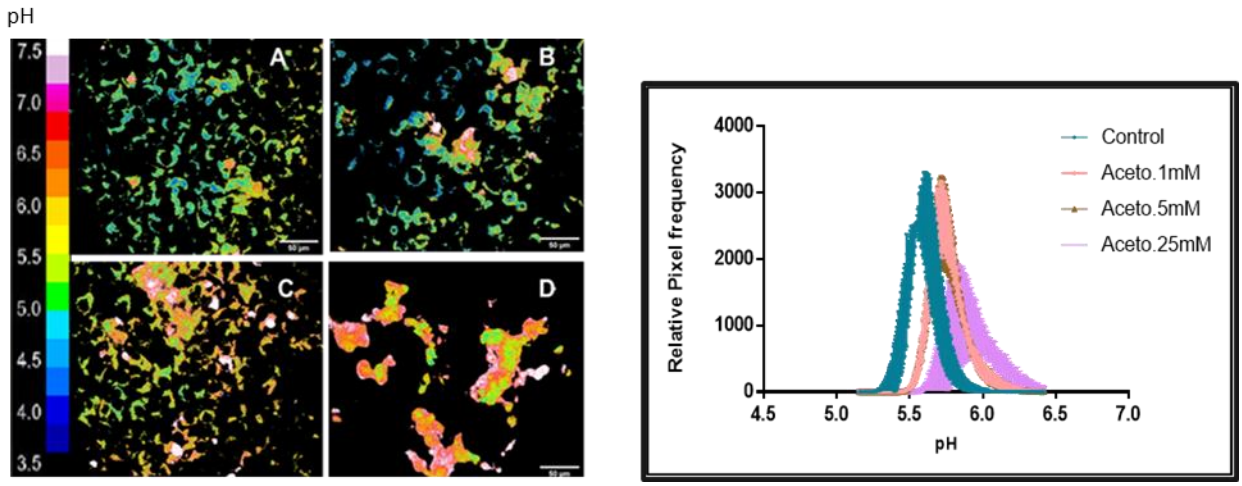


Figure 5-5: Histogram of pH distribution in A) control of $HepG_2$cells in response to B) 1mM, C) 5 mM, D)25 mM acetaminophen. (n=5 ROI).

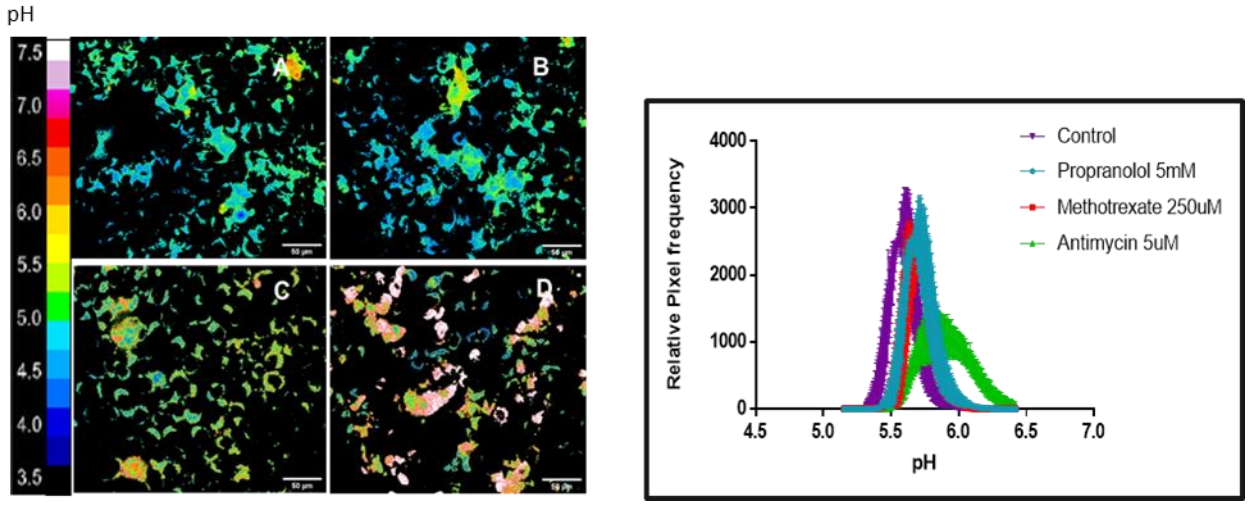


Figure 5-6: Histogram of pH distribution in A) control of HepG2cells in response to 5mM propranolol, 250µM methotrexate, and 5 µM antimycin. (n=5 ROI).

The primary target to investigate drug toxicity mechanism is ETC or uncoupled mitochondrial oxidative phosphorylation by demonstrating oxygen flux. However, there are secondary targets including molecular regulation and protein trafficking [242]. Higher number of mitochondrial assays were published with different mechanism due to complexity of mitochondrial physiology. In this work, apoptotic assay were carried out to study drug effect on apoptotic and necrotic pattern using standard flow cytometry (Annexin V/PI staining). It has been chosen to support our findings with oxygen uptake study.

5.2.4 Apoptosis assay

Apoptosis assays were investigated using Annexin V Alexa Flour® 488, which binds to cell surface markers that are translocated during apoptosis. Whereas, necrosis was determined using the DNA staining of permeable cell membrane using propidium iodide. Data were obtained using flow cytometry and analysed using Kaluza software. The result in Figure 5-7 shows the dot plots of 5 and 25 mM acetaminophen, 250 µM methotrexate and 5 mM propranolol and 5 µM antimycin. A necrotic pattern was observed for with the cells treated with 25 mM acetaminophen and 5 µM antimycin. While, the cells treated with 5 mM acetaminophen, 250 µM methotrexate and 5 mM propranolol have shown an apoptotic when with compared to untreated cells.

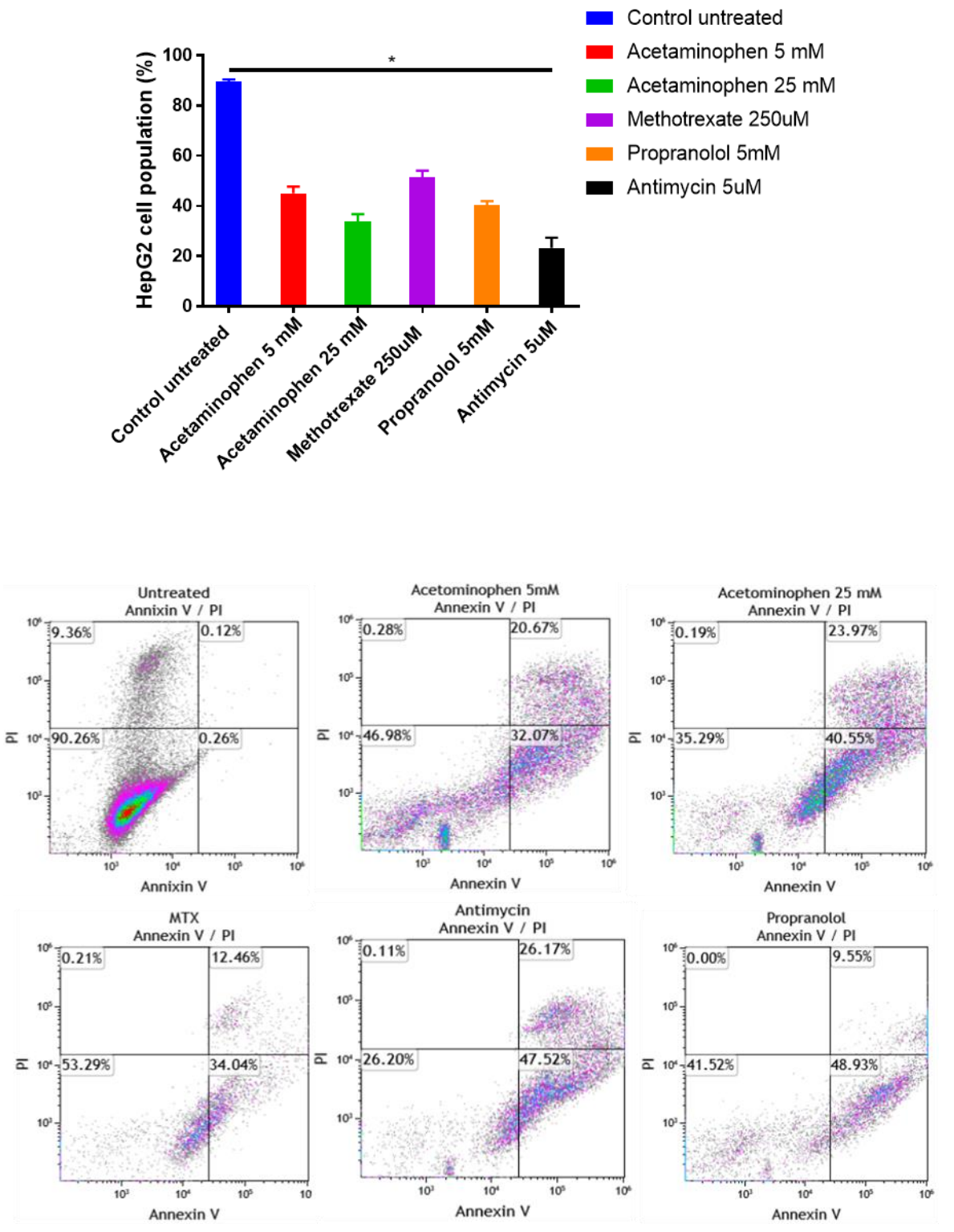


Figure 5-7: Apoptotic assay of HepG2 cells exposed to different drugs, Data showed mean luminescence intensity which representative for n=2, (level value of significant *p<0.05). Representative dot plot apoptotic Annexin V/PI assay from (n= two different biological passage).

The data indicates that there is a link between oxygen consumption and status of cells. Antimycin and a high concentration of acetaminophen cause cell poisoning that occurs through a series of sequential events; mitochondrial oxidative stress, depletion of mitochondrial membrane potential, inability of ATP synthesis, leading to cell necrosis. The cellular oxygen measurement information provides an indirect indicator to predict cellular behaviour.

5.2.5 Use of imaging flow cytometry platform to test change of oxygen intracellularly

There have been continuous developments in flow cytometry instrumentation which have led to a revolution in determining the cell markers and imaging of cells using suitable fluorophores. The results from our oxygen sensors and the apoptotic assay results allied to the developments in flow cytometry instrumentation led us to believe we may be able to use imaging flow cytometry to determine oxygen concentration per cells and showing cell status.

Imaging flow cytometry is an advanced instrumental technique that has high throughput and multi-parametric analysis due to a combination of detecting of single cell properties (traditional flow cytometry) and collecting more informative spatial resolution of the cells [263]. The imaging flow cytometer can measure the fluorescence and light scattering in a high speed manner combined with a camera for imaging which is indispensable for full cellular analysis such as cell morphology, size, distribution or spot of labelled molecules within cells [264]. Successful use of such instrumentation for detecting cells labelled with biomarker tags and oxygen nanosensors is encouraging the hypothesis that this instrument could be used for kinetic monitoring of oxygen [265].

Therefore, experiments were conducted using fixed HepG2 cells which were suspended into PBS deoxygenated with argon gas and PBS oxygenated with oxygen gas, respectively. Cell images in porphyrin channel and TAMRA channel shows spots of nanosensors intracellularly (Figure 5-8, top two panels). Maximum intensities were measured for porphyrin channel and TAMRA channel and ratio was calculated. However, the values of the ratio did not show a difference between the oxygenated and deoxygenated samples. The suggested reason for the lack of change is that the difference in oxygen concentration could not be maintained as the fixed cells passed through the instrument and the oxygen concentration equilibrated to give the same overall oxygen concentration for both sample conditions.

The experiment was changed to test the ratio differences between signals extracted from images of live HepaG2 exposed to different doses of drugs 5 and 25 mM acetaminophen, 5 µm antimycin and 250 µM methotrexate. The result shown in Figure 5-8 indicates a failure of nanosensors to detect any change in oxygen concentration. It is not clear whether this is due to a lack of sensitivity of the nanosensors or the conditions required in the imaging flow cytometry instrumentation.

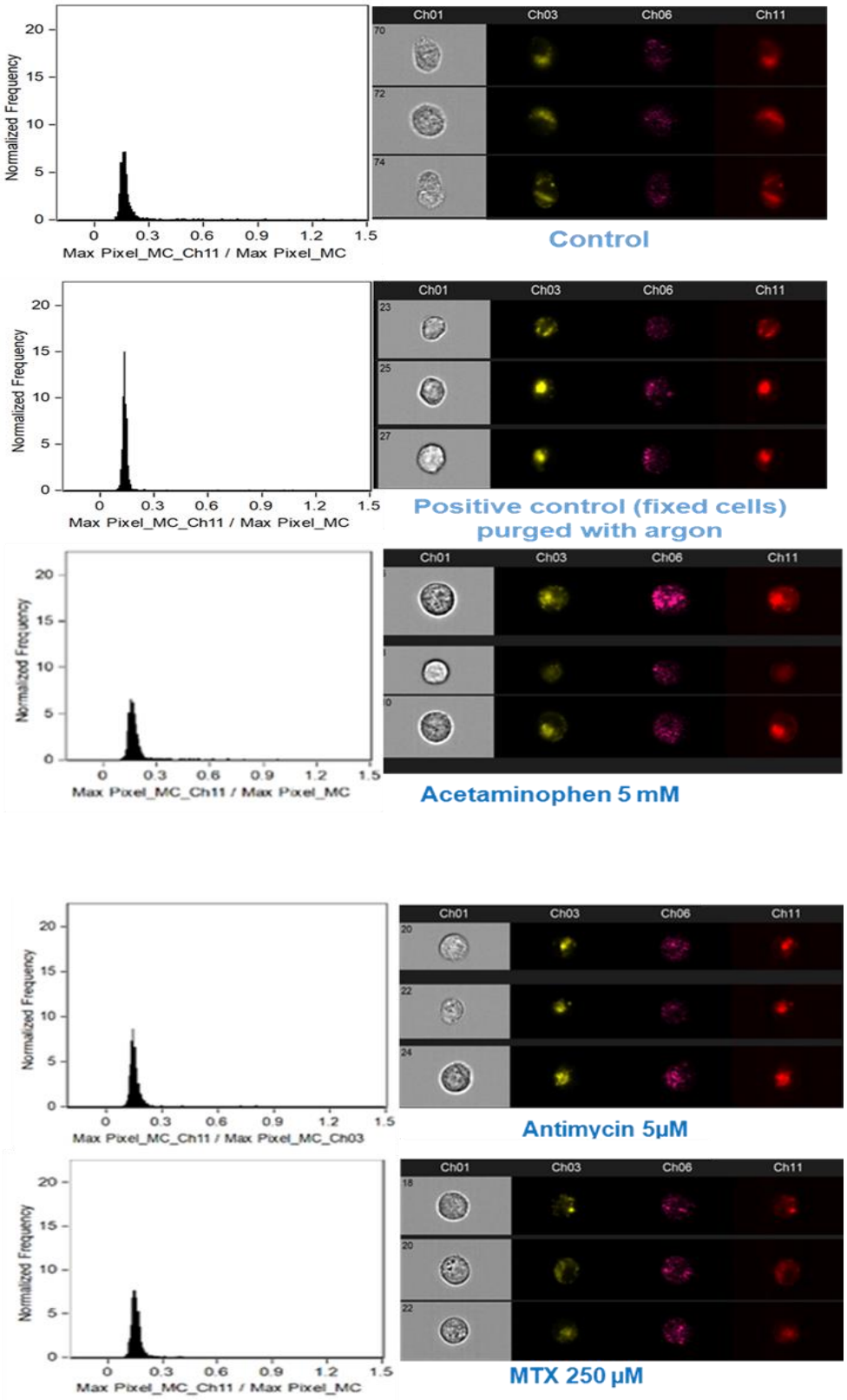


Figure 5-8: Maximum intensity of Ch:11 (porphyrin) and Ch:03 (TAMRA) images of HepaG2 cells using image stream instrument

5.2.6 Study of pH / O_2 flux in 3D hepatic cancer cell models using fluorescent nanosensors

Established methods for determination of pH and oxygen have been performed in two and three-dimensional culture [266], [247], [267]. However, while 2D cell monolayers have provided optimised readouts of cell activity or bio-indicators such as pH and oxygen, 3D cell culture have reported significant differences due to high cell densities. However 3D cell cultures are deemed to be advantageous as they allow the cells to be maintained closer to a physiological environment, enabling the cells communicate with each other across the extracellular matrix [268]. 3D culturing is a platform to enable analysis of biochemical and metabolic activities of living cells in functional tissue and organ contexts while allowing for potential high-resolution real-time imaging and mapping [266].

In this study, the type of cell used is HepaG2 cells which as discussed earlier in this chapter are human cell line derived from hepatocellular carcinoma. HepaG2 cells unlike other cells, preserve liver function and CYPs, nuclear receptors, transporters of membrane, phase II enzymes in the same level of primary liver cells [269]. While, HepG2 monolayers are extensively used to test drug toxicity, 3D HepG2 cells are generally cultured as spheroids and used as tumour models. Usually, tumour models have a limited diffusion of nutrients such as oxygen, which can lead to strikingly different gradients within cellular aggregates [270]. Spheroids are made by methods that enhance cell – cell attachment to keep long-term viability and maintain liver-specific functions in vitro. Indeed, while methods for culturing spheroids is acknowledged [267], there has been less focus on measuring the variation of oxygen levels within the spheroid as opposed to the surrounding medium.

Therefore an investigation of HepaG2 spheroids treated with oxygen and pH nanosensors was undertaken to establish whether pH and/or oxygen profiles could be measured. The size of the cultured spheroids were determined to be approximately 136.29 ± 11.98 μm, Figure 5-9**.**

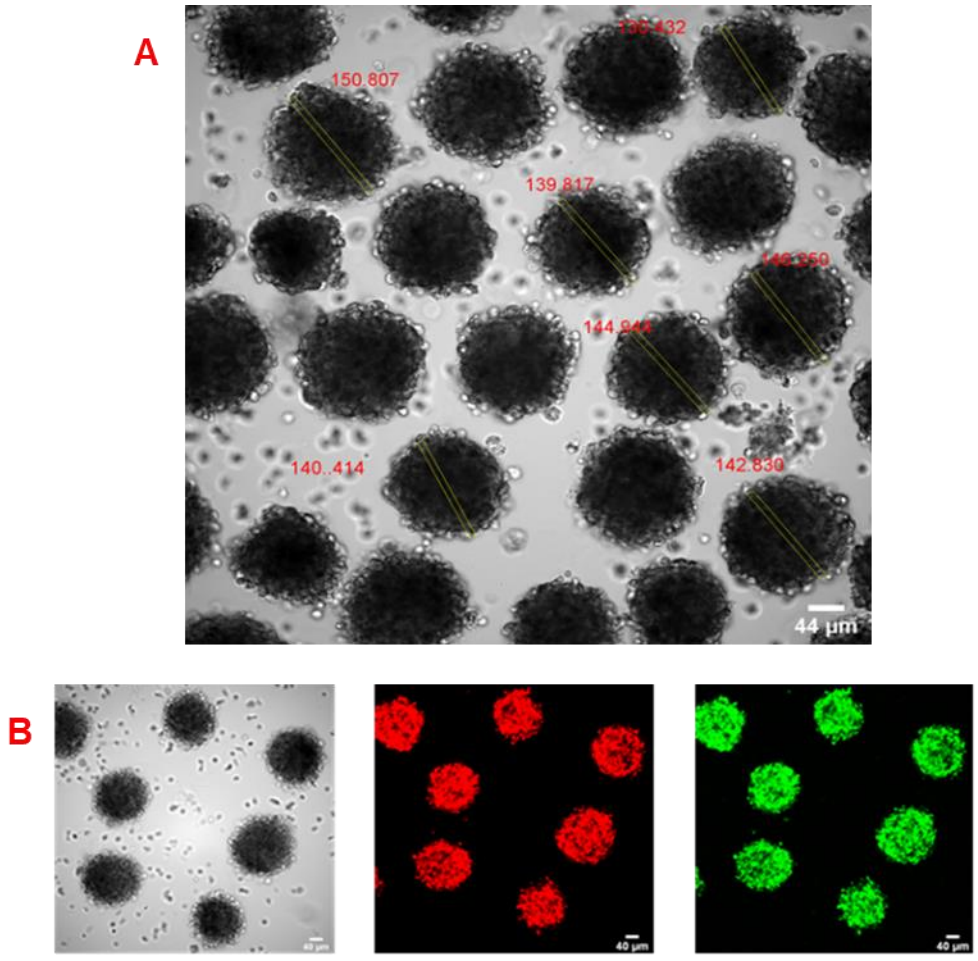


Figure 5-9: A) HepG2 spheroids mean size is 136, B) distribution of nanosensors in spheroid treated with pH nanosensors Brightfield, Red is TAMRA channel, Green is OG&FAM.

Figure 5-9 A shows the excellent uptake of pH nanosensors in HepaG2 spheroids. As in Chapter 4 where macrophages were exposed to pharmacological compounds, the pH nanosensor-loaded spheroids were exposed to medium containing low and high dose acetaminophen (5mM and 25mM, respectively) and 16 μM antimycin.

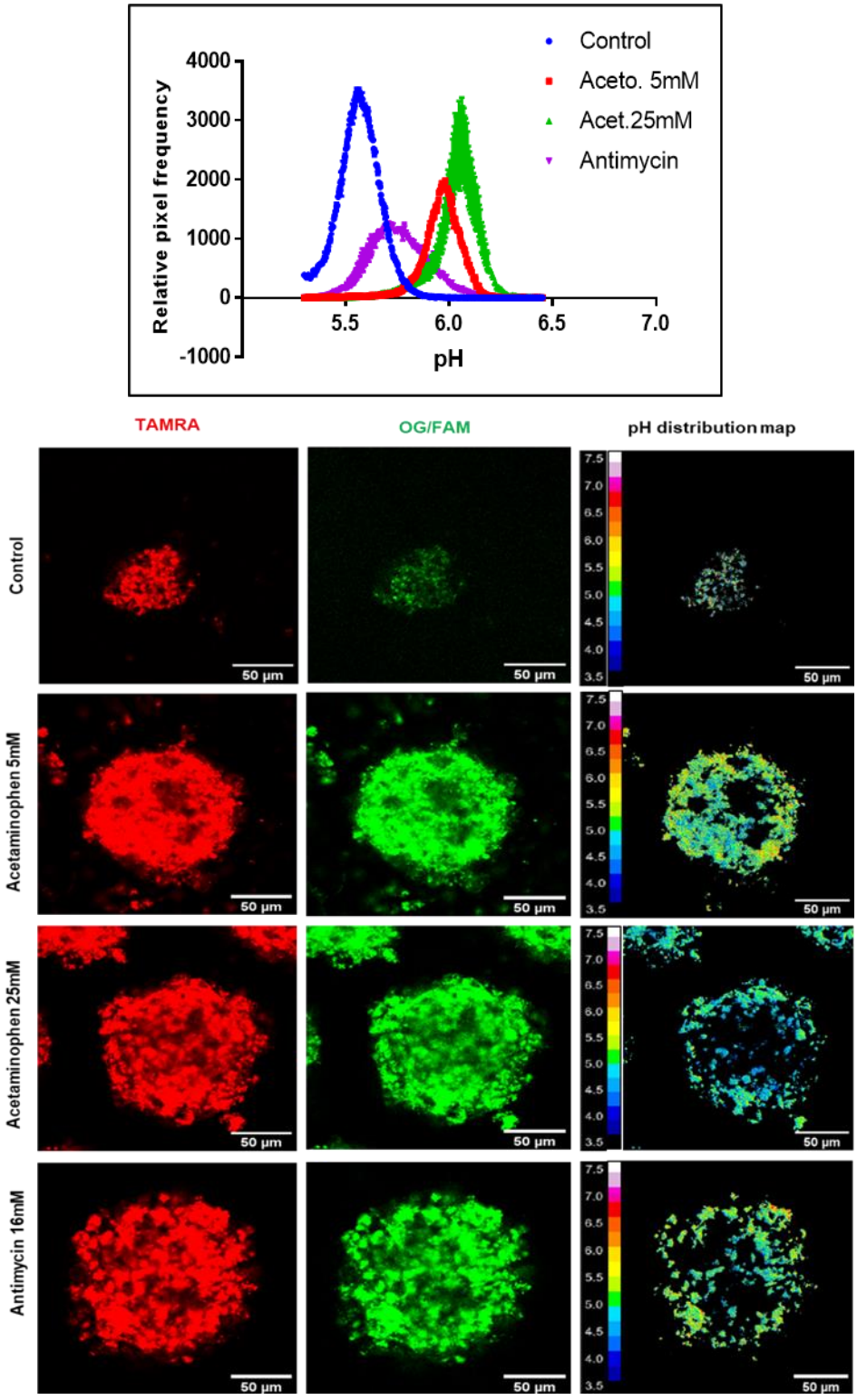


Figure 5-10: Image histogram of average z stack HepG2 cell spheroids treated with pH nanosensors exposed to pharmacological drugs acetaminophen 5mM, acetaminophen 25mM, 16uM antimycin. (± SD = 3 ROI) for above corresponding images

It is critical to determine the methodology of imaging such as magnification, imaging speed and depth to get accurate quantitative results. It should be noted that these images were imaged at magnification of 20X, and image intensities were calculated using average z stacks. The histograms shown in Figure 5-10 were generated from images of cells treated with pharmacological compounds and show a shift of pH from 5.5 for that of the control to higher values of approximately 5.7, 6 and 6.2 which suggest a toxic doses of 16 µM antimycin, acetaminophen 5 and 25 mM, respectively. The reason for increasing pH could be endosome and lysosome rupture as a result of osmotic swelling [271]. The pH sensing nanosensors can be utilized to dynamically monitor spheroid pH. The response of nanosensors to pH was very high compared to pH values showed in Figure 5-6 with monolayer HepaG2 cells and this could be attributed cell – cell contact.

Following our interest to monitor oxygen in spheroids the aim was to expose them to environmental hypoxia. As an initial experiment to assess the performance of the oxygen nanosensors spheroids were fixed using 4% paraformaldehyde then exposed them to an enzymatic reaction of glucose and glucose oxidase to reduce the oxygen concentration over time. The spheroids were imaged using a wide field microscope at different times over a 30 minute period, Figure 5-11.

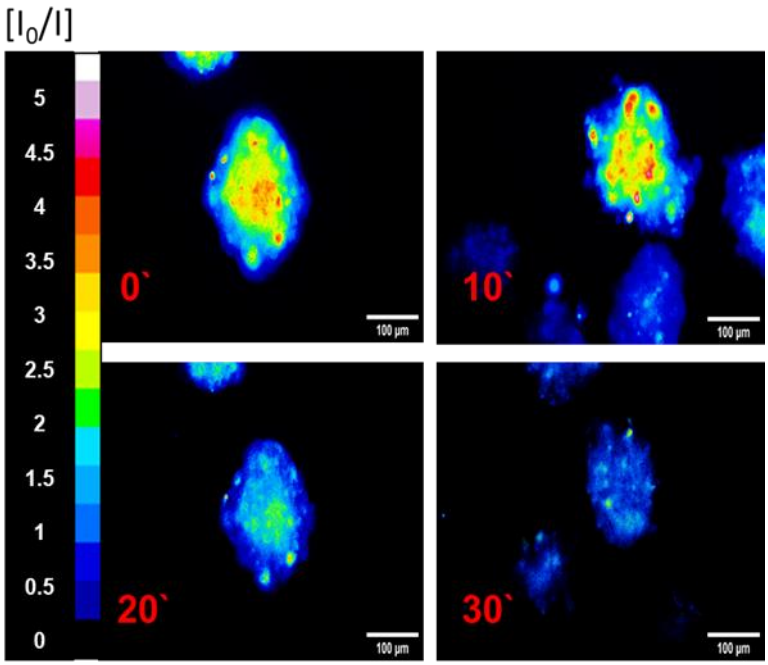


Figure 5-11: Fluorescence intensities distribution heat map of ratiometric spheroid images (fixed spheroid) when exposed to glucose/glucose oxidase at different time point. 0, 10, 20 and 30 minutes. Image J used for map analysis.

Heat maps in this work were represented by ratiometric measurements rather than absolute oxygen concentration. Figure 5-11 demonstrates the ratiometric brightness of nanosensors that shows fixed spheroids containing oxygen nanosensors responding to the environmental decrease in oxygen that is being induced by the glucose/glucose oxidase reaction. It can be seen that the oxygen levels in the spheroid initially start high indicated by the yellow colour and then over time are reduced, as shown by the blue colour. This concept was developed further by applying the methodology to spheroids that consisted of live cells.

Figure 5-12shows the variation of oxygen concentration in the spheroids and the changes over time. From this experiment it is not clear what the effect of the glucose/glucose oxidase is. It is apparent that at time T=0 the spheroid is in a low oxygen state. This may be due to the steady state metabolic activity of the spheroid. It appears that after addition of the glucose/glucose oxidase there is an increase in oxygen detected by the nanosensors, followed by a decrease over time. The reasons for this are not clear and so repeat experiments are required to tease out the subtleties of this process.

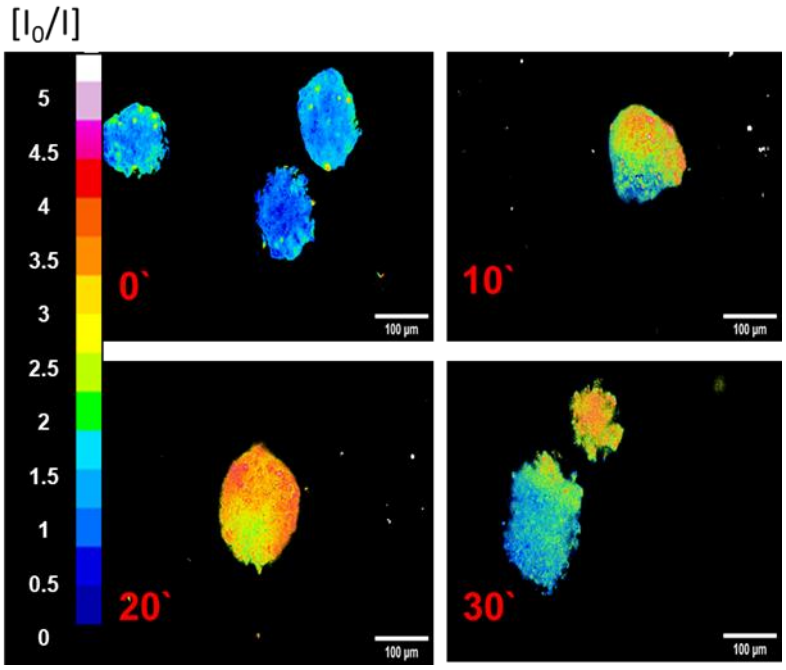


Figure 5-12: Oxygen distribution map of ratiometric spheroid images (live spheroid) when exposed to glucose/glucose oxidase at different time point 0, 10, 20 and 30 minutes

The images shown in Figure 5-11 and 5-12 were taken on a wide-field microscope, whereas imaging using confocal microscopy has advantages of extracting more information from Z-stack images and converting them to 3-D images. For the study to investigate changes of oxygen in different positions within a spheroid a preliminary experiment was carried out using doses of mitochondrial uncouples, antimycin and acetaminophen. Figure 5-13 shows images of Z average of spheroid images exposed to 16 µM antimycin and 25 mM acetaminophen for 30 minutes that show higher brightness of nanosensors compared by control which indicate lower oxygen concentration. By going to deep inside spheroids, nanosensors recognised hypoxic spot inside spheroid through z stack image analysis.

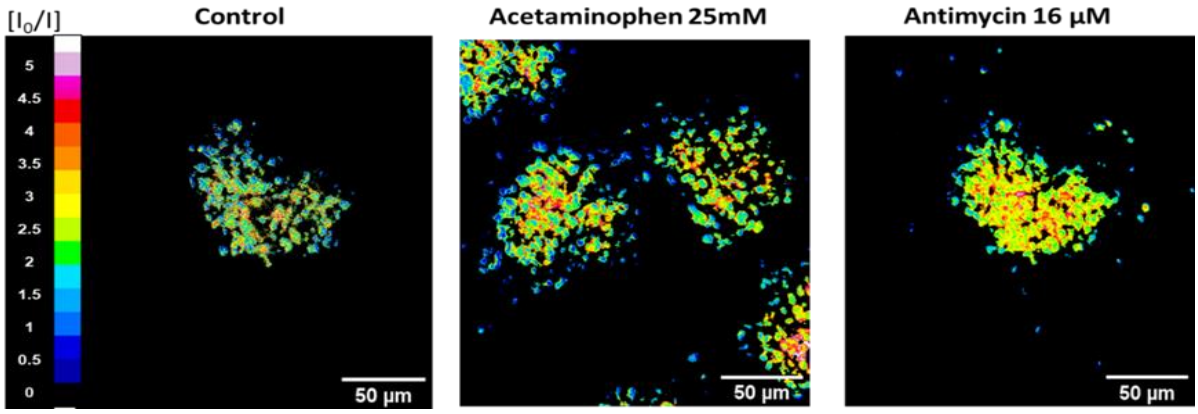


Figure 5-13: Live spheroid images of oxygen mapping, spheroid exposed to 25mM acetaminophen and 16 uM antimycin at different time point 30 minutes.

From Figure 5-14, we can say that using oxygen nanosensors for determination of oxygen gradients is applicable by determining the methodology of analysis. Plot profile in image J was used in this type of analysis for the ratiometric image. The method was reported previously to determine 3D image oxygen concentration in biofilm [245]. It is difficult to generalise the method of analysis and values that generated from the result because a verities of instrumentation specification and properties and the method used for analysis.

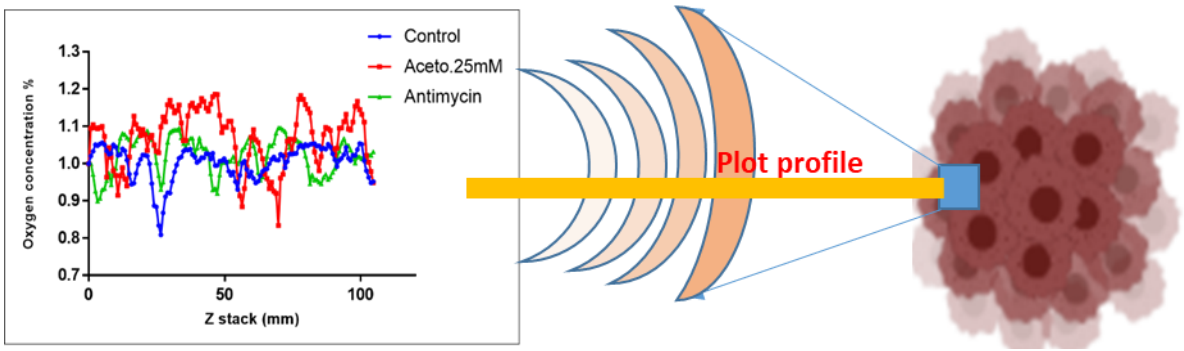


Figure 5-14: Plot profile of oxygen concentration change within different Z stack image of spheroids, Z stack is slice of spheroid in mm.

5.3 Conclusion

The first aim of this chapter was to determine the cellular fate of oxygen nanosensors. This is important because it provides the information of the spatial location from where any nanosensor measurement may originate and that could form part of the explanation of the physiological mechanism of cellular functionality being investigated. Cellular tracking of nanosensors have previously been conducted in our group, Desai *et al.* state that trafficking of polyacrylamide pH nanosensors in cells results in lysosome localisation, an observation that the experiments in this Chapter confirmed (Figure 5-2, 5-3). However, oxygen sensitive nanosensors fabricated using a polyacrylamide matrix were not located in lysosome. The reason for this is that the Pt porphyrin conjugated to the surface of nanoparticles altered surface chemistry and charge of nanosensors.

The second aim was to assess the use of oxygen nanosensors in metabolic pathway detection by evaluating mitochondrial activity. This was done by evaluating oxygen in 2D and 3D systems using HepG2 cell line. Due to metabolic enzymatic activity in hepatic cells, oxygen concentration varied when exposing the cells to different drugs due to different mechanisms of toxicity. The results provided by the nanosensors indicated different micro-environmental oxygen and pH measurements depending on the pharmacological challenge. These results were encouraging to check cell status and differences induced with various doses of pharmacological drugs.

Moving to the application of oxygen nanosensors on the 3D spheroid (tumour model). Previous studies agreed that hypoxic areas in tumours can affect therapeutic efficiency and so the use of nanosensors to detect spatial and temporal distribution of oxygen could be beneficial. Because our focus is assessing nanosensor response, the approach used in these experiments was treatment of cells with nanosensors before making spheroid. Fixed and live spheroid were investigated in response to glucose /glucose oxidase reaction by wide field microscope. Confocal microscope has an advantage of giving more information with Z stack images so more depth. The novelty is the ability of Pt porphyrin oxygen nanosensors to detect the hypoxia spots in the spheroid. Interestingly and successfully, doses of acetaminophen and antimycin have its effect on spheroid area which were demonstrated by plot profile in image J.

However, microscopic analysis using image J was time consuming and process needs to be consistent to generate results that are descriptive of biological oxygen and pH change. There is a strong possibility to improve the method of analysis by using high resolution images that could minimise steps of analysis, as well as further automating the analysis by running Image J scripts.

Chapter 6 . Conclusion

To achieve the thesis aims, nanosensors were fabricated, optimised and characterised in response to changes in molecular oxygen (Chapter 3). Nanosensors were applied intracellularly using THP-1 differentiated macrophages. Oxygen nanosensors were calibrated *in situ* for artificial deoxygenated environment in fixed cells and validated with live cells using imaging technique (Chapter 4). Finally, nanosensors were used to implement biological insights in 2D and 3D cellular system by microscopy mapping technique using HepaG2 cells (Chapter 5).

The conclusion of the studies in each of the chapters are summarised as follows: In Chapter 2, oxygen nanosensors were designed, fabricated and optimised in response to oxygen change. Nanosensors that were fabricated are composed of polyacrylamide nanomaterial decorated by amine groups on the surface to facilitate conjugation of fluorophores. Pt porphyrin (molecular oxygen indicator dye) was conjugated by covalent bond and doped with TAMRA (oxygen concentration independent reference dye). The mass of porphyrin was optimised to 4mg per batch of polyacrylamide nanoparticles produced. This design produced sufficient emission robust sensors to obtain a measurement dynamic range between 0 - 21% of dissolved oxygen concentration. Presence of molecular oxygen quenched fluorescence intensity then the readout was controlled by using oxygen meter.

Fluorescence spectrophotometer was the instrumentation used for characterising nanosensor suspension response to dissolved oxygen concentrations. However, it is difficult to be used for cellular detection due to need of tedious cell preparation that might effect cell normal behaviour. Therefore, using another fluorescence detection instrumentation was a must to represent informative cellular aspects such as fluorescence detection of nanosensor in response to biological change and illustrating cell morphology. Fluorescence microscope was the instrument of choice to provide all of those features.

In Chapter 3, oxygen nanosensors were applied to mammalian cells using ratiometric measurement with external oxygen concentration manipulation. A hypoxia chamber that provide humidity, CO_2 and oxygen was used to culture cells, mimicking features of the growth environment in the human body and importantly environmental hypoxia. The work was started by fixing THP-1 differentiated macrophage to calibrate oxygen nanosensors using the hypoxia chamber. Images were taken in different oxygen concentration to calibrate nanosensors. Image analysis was challenging to yield reliable methodology, however the methodology applied to analyse images with intracellular pH nanosensors as described by Desai *et. al* [22] provided a useful resource.

Some changes of methodology have been made to produce accurate measurements. The detailed of analysis methodology using Fiji® was described in Chapter 2. Detail image interpretation methods were produced based on experimental, instrumental conditions extraction data from images. The result obtained shows the response of Pt-porphyrin intracellularly to different oxygen concentration.

Stern-Volmer calibration curve was performed to demonstrate the response of nanosensor to different concentration of oxygen. As well as, the same equation used for determining the K_{sv} which represents the sensitivity of Pt porphyrin to dissolved oxygen concentrations. Theoretically, the bases of consideration in any ratiometric measurements especially for those used sensor intracellularly. Nevertheless, large variations from image analysis which can result in bias the final measurements.

In order to investigate utilisation of nanosensors for biological application, experiments were performed in immune cell in Chapter 4. Specifically macrophages which are plastic cells could be transformed to additional phenotypes. The rationale for these experiments is that it was thought macrophage phenotype would influence sub cellular oxygen concentration which could be monitored using fluorescent nanosensors. This is because the macrophage phenotype has different metabolic pathways.. The resulted of the chapter highlighted that shows that oxygen nanosensors convert the macrophage phenotype to M1, where as the macrophage treated with pH nanosensors has no significant effect on macrophage phenotype [275].

It has been hypothesised the reason for this phenotypic shift is the Pt porphyrin incorporated into the nanosensor matrix, which has ROS generation properties. Experimentally, it is tested that Pt porphyrin conjugated nanoparticle suspension generate singlet oxygen. In addition, by using H_2DCFDA for measuring H_2O_2 intracellularly when exposed to oxygen nanosensor, H_2O_2 was detected in abundance. These observations may provide the basis for future studies for monitoring intracellular ROS concentration whilst exploring its effect on macrophage phenotype. However the significant modulation in macrophage was detected, oxygen nanosensors have shown a response to mitochondrial uncouplers antimycin and bafilomycin which has

kinetically an effect on respiration. To examine its effect as V-ATPase inhibitors, pH nanosensor was used and have shown to be able to monitor intracellular acidification.

Oxygen heat mapping was used to represent the data and showing the histograms of oxygen transition with hepatic cells (HepaG2) in Chapter 5. The location of nanosensors in HepaG2 cells was investigated in lysosome and mitochondria. Super-resolution was used to determine intracellular location and showed a co-localisation of nanosensors with lysosomes and no localisation with mitochondria. Further studies of intracellular location are required to enhance oxygen nanosensor localisation with mitochondrial targeting.

HepaG2 cells were exposed to different pharmacological compounds to determine change in oxygen. The aim of this study was to show potential insights of monitoring oxygen concentration using oxygen nanosensor and investigate the mechanism of toxicity in mitochondria. In response to acetaminophen at a variety of concentrations, nanosensors were able to successfully map subcellular changes in oxygen. Toxic doses of acetaminophen were shown measure higher concentrations of dissolved, potentiality due to cell membrane permeabilisation. Subcellular oxygen concentrations were also characterised in response to treatment with methotrexate, antimycin and propranolol. It has been seen that these drugs effect the subcellular oxygen concentration and distribution. This is thought to be due to perturbation of the mitochondrial respiration reflects the pattern of apoptosis and necrosis of cells. Further investigation needs to be done for tracking the respiration with time when exposed to the drugs.

Nanosensors were used in 3D spheroids using imaging techniques to investigate the response of oxygen nanosensors to hypoxia. The reason for this to show distribution of response oxygen and detect hypoxic differences in the spheroid microarchitecture. These findings were provided by analysing images with Fiji software using plot profile plugin. The obtained results were encouraging for a potential biological insight to test the penetration of anticancer drugs and examine its action under hypoxic regions.

Future perspective:

Dynamic combinatorial chemistry: Combinatorial chemistry could be used to develop new and improved fluorophores that could be used for biological sensing [276, 277]. Sensitive oxygen nanosensor based nanoparticles. Dynamic combinatorial chemistry, offers utilisation of reversible reactions to produce equilibrating mixture of molecules, known as combinatorial chemistry libraries. This library offers comparing its composition in presence and absence of the target and determining the library members with a high affinity for specific target [278].

The instruments used for biological and potentially clinical application require non-invasiveness and high accurate technique for measurement. In this work, *Nikon* wide field microscope was used for measuring oxygen and pH with good capability of sensing detector. In addition to use confocal microscopy and super-resolution microscope to get higher resolution images for studying the study of oxygen and pH flux in spheroid and *in situ* co-localisation of nanosensors, respectively. New instruments that permit imaging sensors in biological tissue at depth would facilitate clinical translation of nanosensor technologies is safety protocols could be established.

Biomarker and diagnostics: Monitoring of biomarkers in wound healing is necessary especially for antibiotic response to wound inflammation. Experimentally, the idea was started to do co-culture of fibroblast and THP-1 differentiated macrophages as method mentioned [279]. Both types of cells were treated with nanosensors and oxygen was determined by identifying oxygen distribution in fibroblast and macrophage cells. The initial mapping results have shown the potential application of oxygen nanosensor to differentiate between the cell types. As well as explaining metabolic change with effect of wound healing. It would be valuable to do kinetic real time monitoring of oxygen and pH in co-culture and examine the presence of antibiotic as a pharmaceutical application.

In this work, oxygen nanosensors have been used in concept of measuring cellular respiration. Nevertheless, Conjugation of nanoparticles by specific dyes to target mitochondria [280] make nanosensors more specific to mitochondria respiration and enhance sensitivity.

Covid-19 pandemic impact on PhD study

In 2020, COVID-19 lockdown stopped laboratory work for six months. It was a challenging time as a PhD student. Interruption for long period of time, change a planned path of my project. The work in using labs was delayed because the new strategies with COVID-19. Working in our laboratories required to have additional risk assessments and permission to use booking system. The cell work was conducted in life science building, culture hood required to be booked in advanced and this was need a full prepared plan. As well as, a delay in getting training to use confocal and super resolution microscopes because the restriction contact to the trainer.

Because the limited time, the project was focused on sensing properties of Pt porphyrin and was applied in two cell types. Biological assays like HIF detection by ELISA and detection of real time PCR need specific reagents that was difficult to be conducted. Finally, the project was completed by bringing into focus the multiple uses of oxygen nanosensor for biological application.

Chapter 7 . Reference

1. Bayda, S.; M. Adeel; T. Tuccinardi; M. Cordani and F. Rizzolio 2019. The History of Nanoscience and Nanotechnology: From Chemical-Physical Applications to Nanomedicine. *Molecules (Basel, Switzerland),* 25, 112.

2. Strebhardt, K. and A. Ullrich 2008. Paul Ehrlich's magic bullet concept: 100 years of progress. *Nature Reviews Cancer,* 8, 473-480.

3. Munawar, A.; Y. Ong; R. Schirhagl; M.A. Tahir; W.S. Khan and S.Z. Bajwa 2019. Nanosensors for diagnosis with optical, electric and mechanical transducers. *RSC advances,* 9, 6793-6803.

4. Mahesh Mukund, D. 2020. Analytical, Bioanalytical, Stability-Indicating Methods: Key Part of Regulatory Submissions. *In*: ABHAY NANDA, S. (ed.)^(eds.) Analytical Chemistry. ed. Rijeka: IntechOpen.

5. Abdel-Karim, R.; Y. Reda and A. Abdel-Fattah 2020. Review-Nanostructured Materials-Based Nanosensors. *Journal of the Electrochemical Society,* 167, 37554.

6. Javaid, M.; A. Haleem; R.P. Singh; S. Rab and R. Suman 2021. Exploring the potential of nanosensors: A brief overview. *Sensors International,* 2, 100130.

7. Abdel-Karim, R.; Y. Reda and A. Abdel-Fattah 2020. Review-Nanostructured Materials-Based Nanosensors. *Journal of the Electrochemical Society,* 167.

8. Kettler, K.; P. Krystek; C. Giannakou; A.J. Heniks and W.H. de Jong 2016. Exploring the effect of silver nanoparticle size and medium composition on uptake into pulmonary epithelial 16HBE14o-cells. *Journal of nanoparticle research : an interdisciplinary forum for nanoscale science and technology,* 18, 1-11.

9. Hammond, J.L.; N. Formisano; P. Estrela; S. Carrara and J. Tkac 2016. Electrochemical biosensors and nanobiosensors. *Essays in biochemistry,* 60, 69-80.

10. Săndulescu, R. 2015. New Materials for the Construction of Electrochemical Biosensors. *In*: (ed.)^(eds.) ed.: IntechOpen.

11. Hanssen, B.L.; S. Siraj and D.K.Y. Wong 2016. Recent strategies to minimise fouling in electrochemical detection systems. *Reviews in analytical chemistry,* 35, 1-28.

12. Li, Z. and B.H. Graham 2011. Measurement of Mitochondrial Oxygen Consumption Using a Clark Electrode. *Methods in Molecular Biology,* 837, 63-72.

13. Kahn, J.S. 1964. Construction of a simple and sensitive clark-type electrode for measurement of oxygen concentration. *Analytical Biochemistry,* 9, 389-391.

14. Simonnet, H.; A. Vigneron and J. Pouysségur 2014. Chapter Eight - Conventional Techniques to Monitor Mitochondrial Oxygen Consumption. *In*: GALLUZZI, L.& KROEMER, G. (ed.)^(eds.) Methods in Enzymology. ed.: Academic Press.

15. Chauhan, V.M.; F. Giuntini and J.W. Aylott 2016. Quadruple labelled dual oxygen and pH-sensitive ratiometric nanosensors. *Sensing and Bio-Sensing Research,* 8, 36-42.

16. Liu, Y.; X. Li; J. Chen and C. Yuan 2020. Micro/Nano Electrode Array Sensors: Advances in Fabrication and Emerging Applications in Bioanalysis. *Frontiers in chemistry,* 8, 573865-573865.

17. Xia, J. and S. Sonkusale 2021. Flexible thread-based electrochemical sensors for oxygen monitoring. *Analyst (London),* 146, 2983-299.

18. Fritz, J. 2008. *Cantilever biosensors*, CAMBRIDGE, CAMBRIDGE: Royal Soc Chemistry.

19. Meléndrez, D.; T. Jowitt; M. Iliut; A.F. Verre; S. Goodwin and A. Vijayaraghavan 2018. Adsorption and binding dynamics of graphene-supported phospholipid membranes using the QCM-D technique. *Nanoscale,* 1, 2555-2567.

20. Tian, Y.; Y. Liu; Y. Wang; J. Xu and X. Yu 2021. A flexible pi/si/sio2 piezoresistive microcantilever for trace-level detection of aflatoxin b1. *Sensors (Basel, Switzerland),* 21, 1-16.

21. Liu, X.; L. Wang; J. Zhao; Y. Zhu; J. Yang and F. Yang 2019. Enhanced Binding Efficiency of Microcantilever Biosensor for the Detection of Yersinia. *Sensors (Basel),* 19.

22. Desai, A.; V. Chauhan; A. Johnston; T. Esler and J. Aylott 2014. Fluorescent nanosensors for intracellular measurements: synthesis, characterization, calibration, and measurement. *Frontiers in Physiology,* 4.

23. Liu, M.; X. Yu; M. Li; N. Liao; A. Bi; Y. Jiang; S. Liu; Z. Gong and W. Zeng 2018. Fluorescent probes for the detection of magnesium ions (Mg2+): from design to application. *RSC Advances,* 8, 12573-12587.

24. Chauhan, V.M.; G. Orsi; A. Brown; D.I. Pritchard and J.W. Aylott 2013. Mapping the Pharyngeal and Intestinal pH of Caenorhabditis elegans and Real-Time Luminal pH Oscillations Using Extended Dynamic Range pH-Sensitive Nanosensors. *ACS Nano,* 7, 5577-5587.

25. Liu, Y.; Y. Gu; W. Yuan; X. Zhou; X. Qiu; M. Kong; Q. Wang; W. Feng and F. Li 2020. Quantitative Mapping of Liver Hypoxia in Living Mice Using Time-Resolved Wide-Field Phosphorescence Lifetime Imaging. *Advanced science,* 7, 1902929-n/a.

26. Harrison, R.P. and V.M. Chauhan 2018. Enhancing cell and gene therapy manufacture through the application of advanced fluorescent optical sensors (Review). *Biointerphases,* 13, 01A301.

27. Elsutohy, M.M.; V.M. Chauhan; R. Markus; M.A. Kyyaly; S.J.B. Tendler and J.W. Aylott 2017. Real-time measurement of the intracellular pH of yeast cells during glucose metabolism using ratiometric fluorescent nanosensors. *Nanoscale,* 9, 5904-5911.

28. Lakowicz, J.R. and B.R. Masters 2008. *Principles of Fluorescence Spectroscopy, Third Edition*.

29. Guardigli, M. 2012. *Markus Sauer, Johan Hofkens, and Jörg Enderlein: Handbook of fluorescence spectroscopy and imaging: from ensemble to single molecules*, Berlin/Heidelberg, Berlin/Heidelberg: Springer-Verlag.

30. Lakowicz, J.R. and B.R. Masters 2008. Principles of Fluorescence Spectroscopy, Third Edition. *Journal of biomedical optics,* 13, 29901.

31. Sauer, M., Hofkens, J. and Enderlein, J 2011. Basic Principles of Fluorescence Spectroscopy. *In*: (ed.)^(eds.) Handbook of Fluorescence Spectroscopy and Imaging. ed.

32. Berezin, M.Y. and S. Achilefu 2010. Fluorescence lifetime measurements and biological imaging. *Chem Rev,* 110, 2641-84.

33. 2022 Ryosuke University. *Principle of Generating Phosphorescence: Intersystem Crossing and Triplet Excited State* [Online]. Available: https://j-tradition.com/fluorescence.html [Accessed 3rd of Feburary 2022].

34. Würth, C.; D. Geißler; T. Behnke; M. Kaiser and U. Resch-Genger 2014. Critical review of the determination of photoluminescence quantum yields of luminescent reporters. *Analytical and bioanalytical chemistry,* 407, 59-78.

35. Resch-Genger, U. and K. Rurack 2013. Determination of the photoluminescence quantum yield of dilute dye solutions (IUPAC Technical Report). *Pure and applied chemistry,* 85, 2005-2013.

36. Albani, J.R. 2008. *Principles and Applications of Fluorescence Spectroscopy*, Chichester, UNITED KINGDOM, John Wiley & Sons, Incorporated.

37. Vasil'ev, V.V. and S.M. Borisov 2002. Optical oxygen sensors based on phosphorescent water-soluble platinum metals porphyrins immobilized in perfluorinated ion-exchange membrane. *Sensors and Actuators B: Chemical,* 82, 272-276.

38. Ramakrishna, T.-C.L.a.S. 2006. A Conceptual Review of Nanosensors. *Verlag der Zeitschrift f¨ur Naturforschung*.

39. Xu, H.; J.W. Aylott; R. Kopelman; T.J. Miller and M.A. Philbert 2001. A Real-Time Ratiometric Method for the Determination of Molecular Oxygen Inside Living Cells Using Sol−Gel-Based Spherical Optical Nanosensors with Applications to Rat C6 Glioma. *Analytical Chemistry,* 73, 4124-4133.

40. Wolfbeis, O.S. 2005. Materials for fluorescence-based optical chemical sensors. *Journal of Materials Chemistry,* 15, 2657.

41. Fu, J.; C. Ding; A. Zhu and Y. Tian 2016. An efficient core-shell fluorescent silica nanoprobe for ratiometric fluorescence detection of pH in living cells. *Analyst (London),* 141, 4766-4771.

42. Harrison, R.P.; V.M. Chauhan; D. Onion; J.W. Aylott and V. Sottile 2019. Intracellular processing of silica-coated superparamagnetic iron nanoparticles in human mesenchymal stem cells. *RSC Advances,* 9, 3176-3184.

43. Hollmann, B.; M. Perkins; V.M. Chauhan; J.W. Aylott and K.R. Hardie 2021. Fluorescent nanosensors reveal dynamic pH gradients during biofilm formation. *NPJ Biofilms Microbiomes,* 7, 50.

44. Lunov, O.; T. Syrovets; C. Loos; G.U. Nienhaus; V. Mailänder; K. Landfester; M. Rouis and T. Simmet 2011. Amino-Functionalized Polystyrene Nanoparticles Activate the NLRP3 Inflammasome in Human Macrophages. *ACS nano,* 5, 9648-9657.

45. Giuntini, F.; V.M. Chauhan; J.W. Aylott; G.A. Rosser; A. Athanasiadis; A. Beeby; A.J. MacRobert; R.A. Brown and R.W. Boyle 2014. Conjugatable water-soluble Pt(II) and Pd(II) porphyrin complexes: novel nano- and molecular probes for optical oxygen tension measurement in tissue engineering. *Photochem Photobiol Sci,* 13, 1039-51.

46. Chen, G.; I. Roy; C. Yang and P.N. Prasad 2016. Nanochemistry and Nanomedicine for Nanoparticle-based Diagnostics and Therapy. *Chem Rev,* 116, 2826-85.

47. Reisch, A. and A.S. Klymchenko 2016. Fluorescent Polymer Nanoparticles Based on Dyes: Seeking Brighter Tools for Bioimaging. *Small,* 12, 1968-1992.

48. Behnke, T.; C. Würth; K. Hoffmann; M. Hübner; U. Panne and U. Resch-Genger 2010. Encapsulation of Hydrophobic Dyes in Polystyrene Micro- and Nanoparticles via Swelling Procedures. *Journal of fluorescence,* 21, 937-944.

49. Klymchenko, A.S.; E. Roger; N. Anton; H. Anton; I. Shulov; J. Vermot; Y. Mely and T.F. Vandamme 2012. Highly lipophilic fluorescent dyes in nano-emulsions: Towards bright non-leaking nano-droplets. *RSC advances,* 2, 11876-11886.

50. Andreiuk, B.; A. Reisch; E. Bernhardt and A.S. Klymchenko 2019. Fighting Aggregation-Caused Quenching and Leakage of Dyes in Fluorescent Polymer Nanoparticles: Universal Role of Counterion. *Chemistry–An Asian Journal,* 14, 836-846.

51. Margineanu, A.; J. Hofkens; M. Cotlet; S. Habuchi; A. Stefan; J. Qu; C. Kohl; K. Müllen; J. Vercammen; Y. Engelborghs; T. Gensch and F.C. De Schryver 2004. Photophysics of a Water−Soluble Rylene Dye: Comparison with Other Fluorescent Molecules for Biological Applications. *The journal of physical chemistry. B,* 108, 12242-12251.

52. Wolf, D.E.; C. Samarasekera and J.R. Swedlow 2013. Chapter 14 - Quantitative Analysis of Digital Microscope Images. *In*: SLUDER, G.& WOLF, D.E. (ed.)^(eds.) Methods in Cell Biology. ed.: Academic Press.

53. Ripoll, C.; M. Roldan; R. Contreras-Montoya; J.J. Diaz-Mochon; M. Martin; M.J. Ruedas-Rama and A. Orte 2020. Mitochondrial pH Nanosensors for Metabolic Profiling of Breast Cancer Cell Lines. *International Journal of Molecular Sciences,* 21.

54. Piantadosi, C.A. and H.B. Suliman 2012. Transcriptional control of mitochondrial biogenesis and its interface with inflammatory processes. *Biochimica et Biophysica Acta (BBA) - General Subjects,* 1820, 532-541.

55. Swietach, P.; A. Hulikova; S. Patiar; R.D. Vaughan-Jones and A.L. Harris 2012. Importance of intracellular pH in determining the uptake and efficacy of the weakly basic chemotherapeutic drug, doxorubicin. *PloS one,* 7, e35949-e35949.

56. Zhao, X.; S. Campbell; G.Q. Wallace; A. Claing; C.G. Bazuin and J.-F. Masson 2020. Branched Au Nanoparticles on Nanofibers for Surface-Enhanced Raman Scattering Sensing of Intracellular pH and Extracellular pH Gradients. *ACS Sensors,* 5, 2155-2167.

57. Turel, M.; M. Čajlaković; E. Austin; J.P. Dakin; G. Uray and A. Lobnik 2008. Direct UV-LED lifetime pH sensor based on a semi-permeable sol-gel membrane immobilized luminescent Eu3+ chelate complex. *Sensors and actuators. B, Chemical,* 131, 247-253.

58. Dong, S.; M. Luo; G. Peng and W. Cheng 2008. Broad range pH sensor based on sol–gel entrapped indicators on fibre optic. *Sensors and actuators. B, Chemical,* 129, 94-98.

59. Motellier, S.; M.H. Noiré; H. Pitsch and B. Duréault 1995. pH determination of clay interstitial water using a fiber-optic sensor. *Sensors and actuators. B, Chemical,* 29, 345-352.

60. Leung, C.K.Y.; K.T. Wan; D. Inaudi; X. Bao; W. Habel; Z. Zhou; J. Ou; M. Ghandehari; H.C. Wu and M. Imai 2013. Review: optical fiber sensors for civil engineering applications. *Materials and structures,* 48, 871-906.

61. Vo-Dinh, T. 2002. Nanobiosensors: Probing the sanctuary of individual living cells. *Journal of cellular biochemistry,* 87, 154-161.

62. Khan, M.R.R.; A.V. Watekar and S.-W. Kang 2018. Fiber-Optic Biosensor to Detect pH and Glucose. *IEEE Sensors Journal,* 18, 1528-1538.

63. Werner, J.; M. Belz; K.-F. Klein; T. Sun and K.T.V. Grattan 2021. Characterization of a fast response fiber-optic pH sensor and illustration in a biological application. *Analyst (London),* 146, 4811-4821.

64. Khan, M.R.R.; A.V. Watekar and K. Shin-Won 2018. Fiber-Optic Biosensor to Detect pH and Glucose. *IEEE sensors journal,* 18, 1528-1538.

65. Graber, M.L.; D.C. DiLillo; B.L. Friedman and E. Pastoriza-Munoz 1986. Characteristics of fluoroprobes for measuring intracellular pH. *Anal Biochem,* 156, 202-12.

66. Aylott, J.W. 2003. Optical nanosensors—an enabling technology for intracellular measurements. *The Analyst,* 128, 309-312.

67. Zhang, X.F.; J. Zhang and L. Liu 2014. Fluorescence properties of twenty fluorescein derivatives: lifetime, quantum yield, absorption and emission spectra. *J Fluoresc,* 24, 819-26.

68. Le Guern, F.; V. Mussard; A. Gaucher; M. Rottman and D. Prim 2020. Fluorescein derivatives as fluorescent probes for ph monitoring along recent biological applications. *International journal of molecular sciences,* 21, 1-23.

69. Chauhan, V.M.; G.R. Burnett and J.W. Aylott 2011. Dual-fluorophore ratiometric pH nanosensor with tuneable pKa and extended dynamic range. *Analyst,* 136, 1799-1801.

70. Boens, N.; W. Qin; N. Basarić; A. Orte; E.M. Talavera and J.M. Alvarez-Pez 2006. Photophysics of the Fluorescent pH Indicator BCECF. *The journal of physical chemistry. A, Molecules, spectroscopy, kinetics, environment, & general theory,* 110, 9334-9343.

71. Miksa, M.; H. Komura; R. Wu; K.G. Shah and P. Wang 2009. A novel method to determine the engulfment of apoptotic cells by macrophages using pHrodo succinimidyl ester. *Journal of immunological methods,* 342, 71-77.

72. Myochin, T.; K. Kiyose; K. Hanaoka; H. Kojima; T. Terai and T. Nagano 2011. Rational design of ratiometric near-infrared fluorescent pH probes with various pKa values, based on aminocyanine. *Journal of the American Chemical Society,* 133, 3401-3409.

73. Huang, W.; W. Lin and X. Guan 2014. Development of ratiometric fluorescent pH sensors based on chromenoquinoline derivatives with tunable pKa values for bioimaging. *Tetrahedron letters,* 55, 116-119.

74. Beal, M.F.; B.T. Hyman and W. Koroshetz 1993. Do defecs in mitochondrial energy metabolism underlie the pathology of neurodegenerative diseases? *Trends in Neurosciences,* 16, 125-131.

75. Rosas, C.; E. Martinez; G. Gaxiola; R. Brito; A. Sánchez and L.A. Soto 1999. The effect of dissolved oxygen and salinity on oxygen consumption, ammonia excretion and osmotic pressure of Penaeus setiferus (Linnaeus) juveniles. *Journal of Experimental Marine Biology and Ecology,* 234, 41-57.

76. Apel, K. and H. Hirt 2004. REACTIVE OXYGEN SPECIES: Metabolism, Oxidative Stress, and Signal Transduction. 55, 373-399.

77. Parkhill, K.L. and J.S. Gulliver 1997. Indirect measurement of oxygen solubility. *Water Research,* 31, 2564-2572.

78. Golterman, H.L. and A.G. Wisselo 1981. Ceriometry, a combined method for chemical oxygen demand and dissolved oxygen (with a discussion on the precision of the winkler technique). *Hydrobiologia,* 77, 37-42.

79. Gupta, A. and G. Rao 2003. A study of oxygen transfer in shake flasks using a non-invasive oxygen sensor. *Biotechnol Bioeng,* 84, 351-8.

80. Koo, Y.-E.L.; Y. Cao; R. Kopelman; S.M. Koo; M. Brasuel and M.A. Philbert 2004. Real-Time Measurements of Dissolved Oxygen Inside Live Cells by Organically Modified Silicate Fluorescent Nanosensors. *Analytical Chemistry,* 76, 2498-2505.

81. Zhdanov, A.V.; V.I. Ogurtsov; C.T. Taylor and D.B. Papkovsky 2010. Monitoring of cell oxygenation and responses to metabolic stimulation by intracellular oxygen sensing technique. *Integrative Biology,* 2, 443-451.

82. Giuntini, F.; V.M. Chauhan; J.W. Aylott; G.A. Rosser; A. Athanasiadis; A. Beeby; A.J. MacRobert; R.A. Brown and R.W. Boyle 2014. Conjugatable water-soluble Pt(ii) and Pd(ii) porphyrin complexes: novel nano- and molecular probes for optical oxygen tension measurement in tissue engineering. *Photochemical & Photobiological Sciences,* 13, 1039-1051.

83. Ji, S.; W. Wu; W. Wu; P. Song; K. Han; Z. Wang; S. Liu; H. Guo and J. Zhao 2010. Tuning the luminescence lifetimes of ruthenium(ii) polypyridine complexes and its application in luminescent oxygen sensing. *Journal of Materials Chemistry,* 20, 1953-1963.

84. Papkovsky, D.B. and R.I. Dmitriev 2013. Biological detection by optical oxygen sensing. *Chemical Society Reviews,* 42, 8700-8732.

85. Wu, C.; B. Bull; K. Christensen and J. McNeill 2009. Ratiometric Single-Nanoparticle Oxygen Sensors for Biological Imaging. *Angewandte Chemie International Edition,* 48, 2741-2745.

86. Xu, H.; J.W. Aylott and R. Kopelman 2002. Fluorescent nano-PEBBLE sensors designed for intracellular glucose imaging. *Analyst,* 127, 1471-1477.

87. Pandey, G.; R. Chaudhari; B. Joshi; S. Choudhary; J. Kaur and A. Joshi 2019. Fluorescent Biocompatible Platinum-Porphyrin–Doped Polymeric Hybrid Particles for Oxygen and Glucose Biosensing. *Scientific Reports,* 9, 5029.

88. Zhao, H.; L. Zang; L. Wang; F. Qin; Z. Zhang and W. Cao 2015. Luminescence ratiometric oxygen sensor based on gadolinium labeled porphyrin and filter paper. *Sensors and Actuators B: Chemical,* 215, 405-411.

89. Koo Lee, Y.-E.; E.E. Ulbrich; G. Kim; H. Hah; C. Strollo; W. Fan; R. Gurjar; S. Koo and R. Kopelman 2010. Near Infrared Luminescent Oxygen Nanosensors with Nanoparticle Matrix Tailored Sensitivity. *Analytical Chemistry,* 82, 8446-8455.

90. Lin, Y.; H. Xu; B. Dong; X. Sun; C. Li; J. Li; L. Xu; X. Bai and H. Song 2017. Amphiphilic silane modified multifunctional nanoparticles for ratiometric oxygen sensing. *RSC advances,* 7, 34118-34124.

91. Wang, X.D. and O.S. Wolfbeis 2014. Optical methods for sensing and imaging oxygen: materials, spectroscopies and applications. *Chem Soc Rev,* 43, 3666-761.

92. Chen, S.; Q. Ren; K. Zhang; W.E.I. Sha; T. Hao; H. Xu; J. Zhao and Y. Li 2022. A highly sensitive and flexible photonic crystal oxygen sensor. *Sensors and actuators. B, Chemical,* 355, 131326.

93. Smith, C.S.; C.W. Branham; B.J. Marquardt and K.R. Mann 2010. Oxygen Gas Sensing by Luminescence Quenching in Crystals of Cu(xantphos)(phen)+ Complexes. *Journal of the American Chemical Society,* 132, 14079-14085.

94. Papkovsky, D.B. and T.C. O'Riordan 2005. Emerging Applications of Phosphorescent Metalloporphyrins. *Journal of Fluorescence,* 15, 569-584.

95. Changfeng, W.; B. Barbara; C. Kenneth and M. Jason 2009. Ratiometric Single-Nanoparticle Oxygen Sensors for Biological Imaging. *Angewandte Chemie International Edition,* 48, 2741-2745.

96. Lavado, A.S.; V.M. Chauhan; A. Alhaj Zen; F. Giuntini; D.R.E. Jones; R.W. Boyle; A. Beeby; W.C. Chan and J.W. Aylott 2015. Controlled intracellular generation of reactive oxygen species in human mesenchymal stem cells using porphyrin conjugated nanoparticles. *Nanoscale,* 7, 14525-14531.

97. Briñas, R.P.; T. Troxler; R.M. Hochstrasser and S.A. Vinogradov 2005. Phosphorescent Oxygen Sensor with Dendritic Protection and Two-Photon Absorbing Antenna. *Journal of the American Chemical Society,* 127, 11851-11862.

98. Fercher, A.; G.V. Ponomarev; D. Yashunski and D. Papkovsky 2010. Evaluation of the derivates of phosphorescent Pt-coproporphyrin as intracellular oxygen-sensitive probes. *Analytical and Bioanalytical Chemistry,* 396, 1793-1803.

99. Potzkei, J.; M. Kunze; T. Drepper; T. Gensch; K.-E. Jaeger and J. Büchs 2012. Real-time determination of intracellular oxygen in bacteria using a genetically encoded FRET-based biosensor. *BMC biology,* 10, 28-28.

100. Parkin, J. and B. Cohen 2001. An overview of the immune system. *The Lancet,* 357, 1777-1789.

101. Murphy, K. 2017. *Janeway's immunobiology*, New York, New York : Garland Science.

102. Inoue, T. and K. Yasugi 2011. Safety evaluation of biotechnology-derived pharmaceuticals. *Drug delivery system,* 26, 622-627.

103. Bart, V.M.T.; R.J. Pickering; P.R. Taylor and N. Ipseiz 2021. Macrophage reprogramming for therapy. *Immunology,* 163, 128-144.

104. Andrade, R.G.D.; B. Reis; B. Costas; S.A.C. Lima and S. Reis 2020. Modulation of Macrophages M1/M2 Polarization Using Carbohydrate-Functionalized Polymeric Nanoparticles. *Polymers (Basel),* 13.

105. Rostam, H.M.; P.M. Reynolds; M.R. Alexander; N. Gadegaard and A.M. Ghaemmaghami 2017. Image based Machine Learning for identification of macrophage subsets. *Scientific Reports,* 7, 3521.

106. Newman, R.H.; M.D. Fosbrink and J. Zhang 2011. Genetically Encodable Fluorescent Biosensors for Tracking Signaling Dynamics in Living Cells. *Chemical reviews,* 111, 3614-3666.

107. Setiadi, A.F.; N.C. Ray; H.E. Kohrt; A. Kapelner; V. Carcamo-Cavazos; E.B. Levic; S. Yadegarynia; C.M. van der Loos; E.J. Schwartz; S. Holmes and P.P. Lee 2010. Quantitative, architectural analysis of immune cell subsets in tumor-draining lymph nodes from breast cancer patients and healthy lymph nodes. *PloS one,* 5, e12420-e12420.

108. Shang, J.; Q. Yang; W. Fan; Y. Chen; D. Tang; H. Guo; B. Xiong; S. Huang and X.B. Zhang 2021. Probing Dynamic Features of Phagosome Maturation in Macrophage using Au@MnO(x) @SiO(2) Nanoparticles as pH-Sensitive Plasmonic Nanoprobes. *Chem Asian J,* 16, 1150-1156.

109. Zhou, J.; Y.-T. Tsai; H. Weng; D.W. Baker and L. Tang 2011. Real time monitoring of biomaterial-mediated inflammatory responses via macrophage-targeting NIR nanoprobes. *Biomaterials,* 32, 9383-9390.

110. Law, S.M.; S.J. Stanfield; G.R. Hardisty; I. Dransfield; C.J. Campbell and R.D. Gray 2020. Human cystic fibrosis monocyte derived macrophages display no defect in acidification of phagolysosomes when measured by optical nanosensors. *Journal of Cystic Fibrosis,* 19, 203-210.

111. Mulukutla, B.C.; S. Khan; A. Lange and W.-S. Hu 2010. Glucose metabolism in mammalian cell culture: new insights for tweaking vintage pathways. *Trends in Biotechnology,* 28, 476-484.

112. Herst, P.M. and M.V. Berridge 2007. Cell surface oxygen consumption: A major contributor to cellular oxygen consumption in glycolytic cancer cell lines. *Biochimica et Biophysica Acta (BBA) - Bioenergetics,* 1767, 170-177.

113. Sousa Fialho, M.d.L.; A.H. Abd Jamil; G.A. Stannard and L.C. Heather 2019. Hypoxia-inducible factor 1 signalling, metabolism and its therapeutic potential in cardiovascular disease. *Biochimica et biophysica acta. Molecular basis of disease,* 1865, 831-843.

114. DeBerardinis, R.J.; J.J. Lum; G. Hatzivassiliou and C.B. Thompson 2008. The Biology of Cancer: Metabolic Reprogramming Fuels Cell Growth and Proliferation. *Cell Metabolism,* 7, 11-20.

115. Zheng, J.I.E. 2012. Energy metabolism of cancer: Glycolysis versus oxidative phosphorylation (Review). *Oncology letters,* 4, 1151-1157.

116. Walsh, C.T.; B.P. Tu and Y. Tang 2018. Eight Kinetically Stable but Thermodynamically Activated Molecules that Power Cell Metabolism. *Chem Rev,* 118, 1460-1494.

117. Vyas, S.; E. Zaganjor and M.C. Haigis 2016. Mitochondria and Cancer. *Cell,* 166, 555-566.

118. 2018. Focusing on mitochondrial form and function. *Nature Cell Biology,* 20, 735-735.

119. Sazanov, L.A. 2015. A giant molecular proton pump: structure and mechanism of respiratory complex I. *Nat Rev Mol Cell Biol,* 16, 375-88.

120. Lackner, L.L. 2014. Shaping the dynamic mitochondrial network. *BMC Biology,* 12, 35.

121. Li, J.-L.; T.-Y. Lin; P.-L. Chen; T.-N. Guo; S.-Y. Huang; C.-H. Chen; C.-H. Lin and C.-C. Chan 2021. Mitochondrial Function and Parkinson's Disease: From the Perspective of the Electron Transport Chain. *Frontiers in molecular neuroscience,* 14, 797833-797833.

122. Zhao, R.-Z.; S. Jiang; L. Zhang and Z.-B. Yu 2019. Mitochondrial electron transport chain, ROS generation and uncoupling (Review). *International journal of molecular medicine,* 44, 3-15.

123. Ruoß, M.; M. Vosough; A. Königsrainer; S. Nadalin; S. Wagner; S. Sajadian; D. Huber; Z. Heydari; S. Ehnert; J.G. Hengstler and A.K. Nussler 2020. Towards improved hepatocyte cultures: Progress and limitations. *Food and chemical toxicology,* 138, 111188.

124. Weise, F.; U. Fernekorn; J. Hampl; M. Klett and A. Schober 2013. Analysis and comparison of oxygen consumption of HepG2 cells in a monolayer and three-dimensional high density cell culture by use of a matrigrid. *Biotechnology and bioengineering,* 110, 2504-2512.

125. Beckers, S.; F. Noor; U. Müller-Vieira; M. Mayer; A. Strigun and E. Heinzle 2010. High throughput, non-invasive and dynamic toxicity screening on adherent cells using respiratory measurements. *Toxicology in vitro,* 24, 686-694.

126. Mattiazzi Usaj, M.; E.B. Styles; A.J. Verster; H. Friesen; C. Boone and B.J. Andrews 2016. High-Content Screening for Quantitative Cell Biology. *Trends in Cell Biology,* 26, 598-611.

127. Gerets, H.H.J.; K. Tilmant; B. Gerin; H. Chanteux; B.O. Depelchin; S. Dhalluin and F.A. Atienzar 2012. Characterization of primary human hepatocytes, HepG2 cells, and HepaRG cells at the mRNA level and CYP activity in response to inducers and their predictivity for the detection of human hepatotoxins. *Cell biology and toxicology,* 28, 69-87.

128. Pegoraro, G. and T. Misteli 2016. High-throughput Imaging as a versatile and unbiased discovery tool. *Methods (San Diego, Calif.),* 96, 1-2.

129. Feng, Z.; P. Tao; L. Zou; P. Gao; Y. Liu; X. Liu; H. Wang; S. Liu; Q. Dong; J. Li; B. Xu; W. Huang; W.-Y. Wong and Q. Zhao 2017. Hyperbranched Phosphorescent Conjugated Polymer Dots with Iridium(III) Complex as the Core for Hypoxia Imaging and Photodynamic Therapy. *ACS applied materials & interfaces,* 9, 28319-28330.

130. Abuawad, A.; C. Mbadugha; A.M. Ghaemmaghami and D.-H. Kim 2020. Metabolic characterisation of THP-1 macrophage polarisation using LC–MS-based metabolite profiling. *Metabolomics,* 16, 33.

131. Abuawad, A.; C. Mbadugha; A. Ghaemmaghami and D.-H. Kim 2020. Metabolic characterisation of THP-1 macrophage polarisation using LC–MS-based metabolite profiling. *Metabolomics,* 16.

132. *eBioscience™ Annexin V Apoptosis Detection Kits* [Online]. Thermo Fisher Scientific Available: https://www.thermofisher.com/order/catalog/product/BMS500BT-20 [Accessed 23th of March 2022].

133. Dunn, K.W.; M.M. Kamocka and J.H. McDonald 2011. A practical guide to evaluating colocalization in biological microscopy. *American Journal of Physiology - Cell Physiology,* 300, 723-742.

134. Xie, H.; L. Zhang; L. Wu and J. Wang 2017. Polyacrylamide Nanoparticles with Visible and Near-Infrared Autofluorescence. *Particle & Particle Systems Characterization,* 34, 1700222-n/a.

135. Yao, C.; P. Wang; L. Zhou; R. Wang; X. Li; D. Zhao and F. Zhang 2014. Highly biocompatible zwitterionic phospholipids coated upconversion nanoparticles for efficient bioimaging. *Anal Chem,* 86, 9749-57.

136. Sun, H.H.; T.L. Andresen; R.V. Benjaminsen and K. Almdal 2009. Polymeric Nanosensors for Measuring the Full Dynamic pH Range of Endosomes and Lysosomes in Mammalian Cells. *Journal of Biomedical Nanotechnology,* 5, 676-682.

137. McDonagh, C.; C.S. Burke and B.D. MacCraith 2008. Optical Chemical Sensors. *Chemical Reviews,* 108, 400-422.

138. Cao, Y.; Y.-E. Lee Koo and R. Kopelman 2004. Poly(decyl methacrylate)-based fluorescent PEBBLE swarm nanosensors for measuring dissolved oxygen in biosamples. *Analyst,* 129, 745-750.

139. Buck, S.M.; Y.-E.L. Koo; E. Park; H. Xu; M.A. Philbert; M.A. Brasuel and R. Kopelman 2004. Optochemical nanosensor PEBBLEs: photonic explorers for bioanalysis with biologically localized embedding. *Current Opinion in Chemical Biology,* 8, 540-546.

140. Kondrashina, A.V.; R.I. Dmitriev; S.M. Borisov; I. Klimant; I. O' Brien; Y.M. Nolan; A.V. Zhdanov and D.B. Papkovsky 2012. A Phosphorescent Nanoparticle-Based Probe for Sensing and Imaging of (Intra)Cellular Oxygen in Multiple Detection Modalities. *Advanced Functional Materials,* 22, 4931-4939.

141. Fercher, A.; S.M. Borisov; A.V. Zhdanov; I. Klimant and D.B. Papkovsky 2011. Intracellular O2 Sensing Probe Based on Cell-Penetrating Phosphorescent Nanoparticles. *ACS Nano,* 5, 5499-5508.

142. Napp, J.; T. Behnke; L. Fischer; C. Würth; M. Wottawa; D.M. Katschinski; F. Alves; U. Resch-Genger and M. Schäferling 2011. Targeted Luminescent Near-Infrared Polymer-Nanoprobes for In Vivo Imaging of Tumor Hypoxia. *Analytical Chemistry,* 83, 9039-9046.

143. Roussakis, E.; J.A. Spencer; C.P. Lin and S.A. Vinogradov 2014. Two-photon antenna-core oxygen probe with enhanced performance. *Analytical chemistry,* 86, 5937.

144. *Malvern Instruments Dynamic light scattring* [Online]. Malvern Panalytical and spectral company Available: https://www.malvernpanalytical.com/en/learn/knowledge-center/whitepapers/WP120620BasicGuidePartChar [Accessed 4th of April 2021].

145. © 1996-2022 *Dynamic light scattering principle* [Online]. Kyoto, Japan: © 1996-2022 HORIBA, Ltd. All rights reserved. Available: https://www.horiba.com/es/scientific/products/particle-characterization/particle-size-analysis/details/sz-100-7245/ [Accessed 16.02 2022].

146. Pecora, R. 2000. Dynamic light scattering measurement of nanometer particles in liquids. *Journal of Nanoparticle Research,* 2, 123–131.

147. Mohd, T.A.T.; M.Z. Jaafar; A.A.A. Rasol and J. Ali 2017. Review: A new prospect of streaming potential measurement in alkaline-surfactant-polymer flooding. *Chemical engineering transactions,* 56, 1183-1188.

148. Malvern. 2004. *Zetasizer Nano Series* [Online]. united kingdom. Available: http://www.biophysics.bioc.cam.ac.uk/files/Zetasizer_Nano_user_manual_Man0317-1.1.pdf [Accessed 28/6/2018 2018].

149. Khandpur, R.S. 2006. *Handbook of Analytical Instruments*, New York, McGraw-Hill Education.

150. Gomes, A.J.; C.N. Lunardi; F.S. Rocha and G.S. Patience 2019. Experimental methods in chemical engineering: Fluorescence emission spectroscopy. *Canadian journal of chemical engineering,* 97, 2168-2175.

151. Combs, C.A. and H. Shroff 2017. Fluorescence Microscopy: A Concise Guide to Current Imaging Methods. *Curr Protoc Neurosci,* 79, 2.1.1-2.1.25.

152. 2013. Fundamentals of Light Microscopy and Electronic Imaging, Second Edition. *Journal of biomedical optics,* 18, 029901-029901.

153. Choi, N.W.; S.S. Verbridge; R.M. Williams; J. Chen; J.-Y. Kim; R. Schmehl; C.E. Farnum; W.R. Zipfel; C. Fischbach and A.D. Stroock 2012. Phosphorescent nanoparticles for quantitative measurements of oxygen profiles in vitro and in vivo. *Biomaterials,* 33, 2710-2722.

154. Feng, Y.; J. Cheng; L. Zhou; X. Zhou and H. Xiang 2012. Ratiometric optical oxygen sensing: a review in respect of material design. *Analyst,* 137, 4885-4901.

155. Mishra, V.; S. Kumar and N. Shukla 2017. Image Acquisition and Techniques to Perform Image Acquisition. *SAMRIDDHI : A Journal of Physical Sciences, Engineering and Technology,* 9.

156. Carpenter, A. 15 June, 2017. *Quantifying microscopy images: top 10 tips for image acquisition* [Online]. broad Institute

Available: https://carpenter-singh-lab.broadinstitute.org/blog/quantifying-microscopy-images-top-10-tips-for-image-acquisition/ [Accessed 24th Feb 2022].

157. Engelborghs, Y. and A.J.W.G. Visser 2014. *Fluorescence spectroscopy and microscopy : methods and protocols / edited by Yves Engelborghs, Antonie J.W.G. Visser*, New York, New York : Humana Press.

158. Ogama, T. 2020. A beginner's guide to improving image acquisition in fluorescence microscopy. *The Biochemist,* 42, 22-27.

159. Hoebe, R.A.; C.H. Van Oven; T.W.J. Gadella; P.B. Dhonukshe; C.J.F. Van Noorden and E.M.M. Manders 2007. Controlled light-exposure microscopy reduces photobleaching and phototoxicity in fluorescence live-cell imaging. *Nature biotechnology,* 25, 249-253.

160. Otsu, N. 1979. A Threshold Selection Method from Gray-Level Histograms. *IEEE Transactions on Systems, Man, and Cybernetics,* 9, 62-66.

161. Christensen, K.A.; J.T. Myers and J.A. Swanson 2002. pH-dependent regulation of lysosomal calcium in macrophages. *J Cell Sci,* 115, 599-607.

162. Zumaya, A.L.; S. Rimpelová; M. Štějdířová; P. Ulbrich; J. Vilčáková and F. Hassouna. 2022. Antibody Conjugated PLGA Nanocarriers and Superparmagnetic Nanoparticles for Targeted Delivery of Oxaliplatin to Cells from Colorectal Carcinoma. *International Journal of Molecular Sciences* [Online], 23. Available: [Accessed.

163. Gupta, A.; S. Wang; A. Marko; P. Joshi; M. Ethirajan; Y. Chen; R. Yao; M. Sajjad; R. Kopelman and R.K. Pandey 2014. Polyacrylamide-Based Biocompatible Nanoplatform Enhances the Tumor Uptake, PET/fluorescence Imaging and Anticancer Activity of a Chlorophyll Analog. *Theranostics,* 4, 614-628.

164. Tang, W.; H. Xu; R. Kopelman and M.A. Philbert 2005. Photodynamic Characterization and In Vitro Application of Methylene Blue-containing Nanoparticle Platforms ¶. *Photochemistry and Photobiology,* 81, 242-249.

165. Gong, X.; T. Milic; C. Xu; J.D. Batteas and C.M. Drain 2002. Preparation and Characterization of Porphyrin Nanoparticles. *Journal of the American Chemical Society,* 124, 14290-14291.

166. *Stage Top Incubators* [Online]. ibidi, cells in focus. Available: https://ibidi.com/78-stage-top-incubators) [Accessed 28th January 2022].

167. Daigneault, M., Preston, J.A., Marriott, H.M., Whyte, M.K.B. & Dockrell, D.H. 2010. The Identification of Markers of Macrophage Differentiation in PMA-Stimulated THP-1 Cells and Monocyte-Derived Macrophages. *PLoS One,* 5.

168. Wang, D. and K.M. Bratlie 2015. Influence of Polymer Chemistry on Cytokine Secretion from Polarized Macrophages. *ACS biomaterials science & engineering,* 1, 166-174.

169. Zhou, H.; Y. Xue; L. Dong and C. Wang 2021. Biomaterial-based physical regulation of macrophage behaviour. *Journal of materials chemistry. B, Materials for biology and medicine,* 9, 368-3621.

170. Miao, X.; X. Leng and Q. Zhang 2017. The current state of nanoparticle-induced macrophage polarization and reprogramming research. *International journal of molecular sciences,* 18, 336.

171. Moghimi, S.M.; L. Parhamifar; D. Ahmadvand; P.P. Wibroe; T.L. Andresen; Z.S. Farhangrazi and A.C. Hunter 2012. Particulate Systems for Targeting of Macrophages: Basic and Therapeutic Concepts. *Journal of Innate Immunity,* 4, 509-528.

172. Desbordes, S.C.; D.G. Placantonakis; A. Ciro; N.D. Socci; G. Lee; H. Djaballah and L. Studer 2008. High-Throughput Screening Assay for the Identification of Compounds Regulating Self-Renewal and Differentiation in Human Embryonic Stem Cells. *Cell Stem Cell,* 2, 602-612.

173. Syrovets, T.; K. Haas; C. Loos; A. Musyanovych; V. Mailänder; K. Landfester and T. Simmet 2015. Differential Effects of Nanoparticle Surface-Functionalization on the Polarization Profiles of M1 and M2 Macrophages. *The FASEB Journal,* 29, 716.9.

174. McBane, J.E.; L.A. Matheson; S. Sharifpoor; J.P. Santerre and R.S. Labow 2009. Effect of polyurethane chemistry and protein coating on monocyte differentiation towards a wound healing phenotype macrophage. *Biomaterials,* 30, 5497-5504.

175. Qie, Y.; H. Yuan; C.A. Von Roemeling; Y. Chen; X. Liu; K.D. Shih; J.A. Knight; H.W. Tun; R.E. Wharen; W. Jiang and B.Y.S. Kim 2016. Surface modification of nanoparticles enables selective evasion of phagocytic clearance by distinct macrophage phenotypes. *Scientific reports,* 6, 26269-26269.

176. Jones, J.A.; D.T. Chang; H. Meyerson; E. Colton; I.K. Kwon; T. Matsuda and J.M. Anderson 2007. Proteomic analysis and quantification of cytokines and chemokines from biomaterial surface-adherent macrophages and foreign body giant cells. *Journal of Biomedical Materials Research Part A,* 83A, 585-596.

177. Dobrovolskaia, M.A. and S.E. McNeil 2007. Immunological properties of engineered nanomaterials. *Nature Nanotechnology,* 2, 469-78.

178. Chen, H.; P. Li; Y. Yin; X. Cai; Z. Huang; J. Chen; L. Dong and J. Zhang 2010. The promotion of type 1 T helper cell responses to cationic polymers in vivo via toll-like receptor-4 mediated IL-12 secretion. *Biomaterials,* 31, 8172-80.

179. Gao, D.; H. Xu; M.A. Philbert and R. Kopelman 2007. Ultrafine Hydrogel Nanoparticles: Synthetic Approach and Therapeutic Application in Living Cells. *Angewandte Chemie (International ed.),* 46, 2224-2227.

180. Chen, L.; J.D. Simpson; A.V. Fuchs; B.E. Rolfe and K.J. Thurecht 2017. Effects of Surface Charge of Hyperbranched Polymers on Cytotoxicity, Dynamic Cellular Uptake and Localization, Hemotoxicity, and Pharmacokinetics in Mice. *Molecular pharmaceutics,* 14, 4485-4497.

181. Villanueva-Flores, F.; A. Castro-Lugo; O.T. Ramírez and L.A. Palomares 2020. Understanding cellular interactions with nanomaterials: Towards a rational design of medical nanodevices. *Nanotechnology,* 31, 132002.

182. Nienhaus, G.U.; F. Zhang; W.J. Parak; C. Röcker and M. Pötzl 2009. A quantitative fluorescence study of protein monolayer formation on colloidal nanoparticles. *Nature nanotechnology,* 4, 577-580.

183. Martins, C.; V.M. Chauhan; M. Araújo; A. Abouselo; C.C. Barrias; J.W. Aylott and B. Sarmento 2020. Advanced polymeric nanotechnology to augment therapeutic delivery and disease diagnosis. *Nanomedicine (London, England),* 15, 2287-2309.

184. Corbo, C.; R. Molinaro; A. Parodi; N.E. Toledano Furman; F. Salvatore and E. Tasciotti 2016. The impact of nanoparticle protein corona on cytotoxicity, immunotoxicity and target drug delivery. *Nanomedicine (London, England),* 11, 81-100.

185. Sarkar, S.; B.F. Leo; C. Carranza; S. Chen; C. Rivas-Santiago; A.E. Porter; M.P. Ryan; A. Gow; K.F. Chung; T.D. Tetley; J.J. Zhang; P.G. Georgopoulos; P.A. Ohman-Strickland and S. Schwander 2015. Modulation of human macrophage responses to mycobacterium tuberculosis by silver nanoparticles of different size and surface modification. *PloS one,* 10, e0143077.

186. Yue, H.; W. Wei; Z. Yue; P. Lv; L. Wang; G. Ma and Z. Su 2010. Particle size affects the cellular response in macrophages. *European journal of pharmaceutical sciences,* 41, 650-657.

187. Kusaka, T.; M. Nakayama; K. Nakamura; M. Ishimiya; E. Furusawa and K. Ogasawara 2014. Effect of silica particle size on macrophage inflammatory responses. *PloS one,* 9, e92634-e92634.

188. Henderson, J.R.; D.A. Fulton; C.J. McNeil and P. Manning 2009. The development and in vitro characterisation of an intracellular nanosensor responsive to reactive oxygen species. *Biosensors and Bioelectronics,* 24, 3608-3614.

189. Wang, X.-d.; J.A. Stolwijk; T. Lang; M. Sperber; R.J. Meier; J. Wegener and O.S. Wolfbeis 2012. Ultra-Small, Highly Stable, and Sensitive Dual Nanosensors for Imaging Intracellular Oxygen and pH in Cytosol. *Journal of the American Chemical Society,* 134, 17011-17014.

190. Wang, X.H.; H.S. Peng; L. Yang; F.T. You; F. Teng; L.L. Hou and O.S. Wolfbeis 2014. Targetable Phosphorescent Oxygen Nanosensors for the Assessment of Tumor Mitochondrial Dysfunction By Monitoring the Respiratory Activity. *Angewandte Chemie (International ed.),* 53, 12471-12475.

191. Rostam, H.M.; S. Singh; N.E. Vrana; M.R. Alexander and A.M. Ghaemmaghami 2015. Impact of surface chemistry and topography on the function of antigen presenting cells. *Biomaterials Science,* 3, 424-441.

192. Xu, H.; Y. Sun; Y. Zhang; W. Wang; J. Dan; J. Yao; H. Chen; F. Tian; X. Sun; S. Guo; Z. Tian and Y. Tian 2014. Protoporphyrin IX Induces a Necrotic Cell Death in Human THP-1 Macrophages through Activation of Reactive Oxygen Species/c-Jun N-Terminal Protein Kinase Pathway and Opening of Mitochondrial Permeability Transition Pore. *Cellular Physiology and Biochemistry,* 34, 1835-1848.

193. Düssmann, H.; S. Perez-Alvarez; U. Anilkumar; D.B. Papkovsky and J.H. Prehn 2017. Single-cell time-lapse imaging of intracellular O(2) in response to metabolic inhibition and mitochondrial cytochrome-c release. *Cell Death Dis,* 8, e2853.

194. Zhdanov, A.V.; R.I. Dmitriev and D.B. Papkovsky 2011. Bafilomycin A1 activates respiration of neuronal cells via uncoupling associated with flickering depolarization of mitochondria. *Cellular and molecular life sciences : CMLS,* 68, 903-917.

195. Kondrashina, A.V.; D.B. Papkovsky and R.I. Dmitriev 2013. Measurement of cell respiration and oxygenation in standard multichannel biochips using phosphorescent O2-sensitive probes. *Analyst,* 138, 4915-4921.

196. Lian, Y.; Z. Lin; Z. Zhang and X.-d. Wang 2021. Active-Targeting Polymeric Dual Nanosensor for Ratiometrically Measuring Proton and Oxygen Concentrations in Mitochondria. *Analytical chemistry (Washington),* 93, 8291-8299.

197. Kalbácová, M.; M. Vrbacký; Z. Drahota and Z. Melková 2003. Comparison of the effect of mitochondrial inhibitors on mitochondrial membrane potential in two different cell lines using flow cytometry and spectrofluorometry. *Cytometry A,* 52, 110-6.

198. Düssmann, H.; S. Perez-Alvarez; U. Anilkumar; D.B. Papkovsky and J.H.M. Prehn 2017. Single-cell time-lapse imaging of intracellular O2 in response to metabolic inhibition and mitochondrial cytochrome-c release. *Cell Death & Disease,* 8, e2853-e2853.

199. Dmitriev, R.I. and D.B. Papkovsky 2012. Optical probes and techniques for O2 measurement in live cells and tissue. *Cellular and molecular life sciences : CMLS,* 69, 2025-2039.

200. Heinz, S.; A. Freyberger; B. Lawrenz; L. Schladt; G. Schmuck and H. Ellinger-Ziegelbauer 2017. Mechanistic Investigations of the Mitochondrial Complex i Inhibitor Rotenone in the Context of Pharmacological and Safety Evaluation. *Scientific reports,* 7, 45465.

201. Giorgi-Coll, S.; A.I. Amaral; P.J.A. Hutchinson; M.R. Kotter and K.L.H. Carpenter 2017. Succinate supplementation improves metabolic performance of mixed glial cell cultures with mitochondrial dysfunction. *Scientific Reports,* 7, 1003.

202. Lewis, W.; W.C. Copeland and B.J. Day 2003. Mitochondrial toxicity of nrti antiviral drugs: an integrated cellular perspective. *Nature reviews. Drug discovery,* 2, 812-822.

203. Li, N.; K. Ragheb; G. Lawler; J. Sturgis; B. Rajwa; J.A. Melendez and J.P. Robinson 2003. Mitochondrial Complex I Inhibitor Rotenone Induces Apoptosis through Enhancing Mitochondrial Reactive Oxygen Species Production. *The Journal of biological chemistry,* 278, 8516-8525.

204. Moreno-Sánchez, R.; C. Bravo; C. Vásquez; G. Ayala; L.H. Silveira and M. Martínez-Lavín 1999. Inhibition and uncoupling of oxidative phosphorylation by nonsteroidal anti-inflammatory drugs: Study in mitochondria, submitochondrial particles, cells, and whole heart. *Biochemical pharmacology,* 57, 743-752.

205. Zholobenko, A.V.; A. Mouithys-Mickalad; Z. Dostal; D. Serteyn and M. Modriansky 2017. On the causes and consequences of the uncoupler-like effects of quercetin and dehydrosilybin in H9c2 cells. *PLOS ONE,* 12, e0185691.

206. Smolina, N.; J. Bruton; A. Kostareva and T. Sejersen 2017. Assaying Mitochondrial Respiration as an Indicator of Cellular Metabolism and Fitness. *In*: GILBERT, D.F.& FRIEDRICH, O. (ed.)^(eds.) Cell Viability Assays: Methods and Protocols. ed. New York, NY: Springer New York.

207. Teplova, V.; A. Tonshin; P. Grigoriev; N.-E. Saris and M. Salkinoja-Salonen 2007. Bafilomycin A1 is a potassium ionophore that impairs mitochondrial functions. *Journal of Bioenergetics and Biomembranes,* 39, 321-329.

208. Hytti, M.; E. Korhonen; J.M.T. Hyttinen; H. Roehrich; K. Kaarniranta; D.A. Ferrington and A. Kauppinen 2019. Antimycin A-Induced Mitochondrial Damage Causes Human RPE Cell Death despite Activation of Autophagy. *Oxid Med Cell Longev,* 2019, 1583656.

209. Chanput, W.; J.J. Mes; H.F.J. Savelkoul and H.J. Wichers 2013. Characterization of polarized THP-1 macrophages and polarizing ability of LPS and food compounds. *Food & Function,* 4, 266-276.

210. Lin, J.; Y. Jiang; Y. Luo; H. Guo; C. Huang; J. Peng and Y. Cao 2020. Multi-walled carbon nanotubes (MWCNTs) transformed THP-1 macrophages into foam cells: Impact of pulmonary surfactant component dipalmitoylphosphatidylcholine. *Journal of Hazardous Materials,* 392, 122286.

211. Alvarez, M.M.; J.C. Liu; G. Trujillo-de Santiago; B.H. Cha; A. Vishwakarma; A.M. Ghaemmaghami and A. Khademhosseini 2016. Delivery strategies to control inflammatory response: Modulating M1-M2 polarization in tissue engineering applications. *J Control Release,* 240, 349-363.

212. Gordon, S. and A. Plüddemann 2017. Tissue macrophages: heterogeneity and functions. *BMC Biology,* 15, 53.

213. Josefsen, L.B.; J.W. Aylott; A. Beeby; P. Warburton; J.P. Boyle; C. Peers and R.W. Boyle 2010. Porphyrin-nanosensor conjugates. New tools for the measurement of intracellular response to reactive oxygen species. *Photochemical & photobiological sciences,* 9, 801-811.

214. Kwon, D.; B.G. Cha; Y. Cho; J. Min; E.B. Park; S.J. Kang and J. Kim 2017. Extra-Large Pore Mesoporous Silica Nanoparticles for Directing in Vivo M2 Macrophage Polarization by Delivering IL-4. *Nano Lett,* 17, 2747-2756.

215. Bancos, S.; D.L. Stevens and K.M. Tyner 2015. Effect of silica and gold nanoparticles on macrophage proliferation, activation markers, cytokine production, and phagocytosis in vitro. *International journal of nanomedicine,* 10, 183-206.

216. Nishanth, R.P.; R.G. Jyotsna; J.J. Schlager; S.M. Hussain and P. Reddanna 2011. Inflammatory responses of RAW 264.7 macrophages upon exposure to nanoparticles: role of ROS-NFκB signaling pathway. *Nanotoxicology,* 5, 502-16.

217. Giuntini, F.; F. Foglietta; A.M. Marucco; A. Troia; N.V. Dezhkunov; A. Pozzoli; G. Durando; I. Fenoglio; L. Serpe and R. Canaparo 2018. Insight into ultrasound-mediated reactive oxygen species generation by various metal-porphyrin complexes. *Free radical biology & medicine,* 121, 190-201.

218. Ohse, T.; S. Nagaoka; Y. Arakawa; H. Kawakami and K. Nakamura 2001. Cell death by reactive oxygen species generated from water-soluble cationic metalloporphyrins as superoxide dismutase mimics. *Journal of Inorganic Biochemistry,* 85, 201-208.

219. Kolarova, H.; P. Nevrelova; K. Tomankova; P. Kolar; R. Bajgar and J. Mosinger 2008. Production of reactive oxygen species after photodynamic therapy by porphyrin sensitizers. *Gen Physiol Biophys,* 27, 101-5.

220. Wong, H.S.; P.A. Dighe; V. Mezera; P.A. Monternier and M.D. Brand 2017. Production of superoxide and hydrogen peroxide from specific mitochondrial sites under different bioenergetic conditions. *J Biol Chem,* 292, 16804-16809.

221. Fagadar-Cosma, E.; N. Plesu; A. Lascu; D. Anghel; M. Cazacu; C. Ianasi; G. Fagadar-Cosma; I. Fratilescu and C. Epuran 2020. Novel platinum-porphyrin as sensing compound for efficient fluorescent and electrochemical detection of H2O2. *Chemosensors,* 8, 29.

222. Komagoe, K. and T. Katsu 2006. Porphyrin-Induced Photogeneration of Hydrogen Peroxide Determined Using the Luminol Chemiluminescence Method in Aqueous Solution: A Structure-Activity Relationship Study Related to the Aggregation of Porphyrin. *Analytical Sciences,* 22, 255-258.

223. Wu, J.; Z. Chu; Z. Ruan; X. Wang; T. Dai and X. Hu 2018. Changes of Intracellular Porphyrin, Reactive Oxygen Species, and Fatty Acids Profiles During Inactivation of Methicillin-Resistant Staphylococcus aureus by Antimicrobial Blue Light. *Frontiers in Physiology,* 9.

224. Pan, T.; C. Yang; J. Shi; C. Hao; Y. Qiao; J. Li; M. Deng; Y. Tian and M. Chen 2019. Dual pH and oxygen luminescent nanoprobes based on graft polymers for extracellular metabolism monitoring and intracellular imaging. *Sensors & Actuators: B. Chemical,* 291, 306-318.

225. Khan, D.H.; S.A. Roberts; J.R. Cressman and N. Agrawal 2017. Rapid Generation and Detection of Biomimetic Oxygen Concentration Gradients In Vitro. *Scientific Reports,* 7, 13487.

226. Lloyd, D.; C.F. Williams; K. Vijayalakshmi; M. Kombrabail; N. White; A.J. Hayes; M.A. Aon and G. Krishnamoorthy 2014. Intracellular oxygen: Similar results from two methods of measurement using phosphorescent nanoparticles. *Journal of innovative optical health science,* 7, 1350041-1350041-14.

227. Zeng, J.; O.S. Shirihai and M.W. Grinstaff 2020. Modulating lysosomal pH: a molecular and nanoscale materials design perspective. *J Life Sci (Westlake Village),* 2, 25-37.

228. Dohle, E.; A. Scherrieble; M. Doser; S. Al-Maawi; M. Hoss; M. Dauner; R. Sader; C.J. Kirkpatrick and S. Ghanaati 2020. Co-culture Model for Cutaneous Wound Healing to Assess a Porous Fiber-Based Drug Delivery System. *Tissue Eng Part C Methods,* 26, 475-484.

229. Gonzalez, A.C.D.O.; Z.D.A. Andrade; T.F. Costa and A.R.A.P. Medrado 2016. Wound healing - A literature review. *Anais brasileiros de dermatología,* 91, 614-620.

230. Kwon, D.; E.M. Genden; R. de Bree; J.P. Rodrigo; A. Rinaldo; A. Sanabria; A.D. Rapidis; R.P. Takes and A. Ferlito 2018. Overcoming wound complications in head and neck salvage surgery. *Auris, nasus, larynx,* 45, 1135-1142.

231. Tang, N.; Y. Zheng; H. Haick; X. Jiang; C. Zhou; H. Jin; K. Jin and W. Wu 2021. Wearable sensors and systems for wound healing-related ph and temperature detection. *Micromachines (Basel),* 12, 430.

232. Anderson, K. and R.L. Hamm 2012. Factors That Impair Wound Healing. *Journal of the American College of Clinical Wound Specialists,* 4, 84-91.

233. Chen, N.Y.; P. Kim; T.A. Weston; L. Edillo; Y. Tu; L.G. Fong and S.G. Young 2018. Fibroblasts lacking nuclear lamins do not have nuclear blebs or protrusions but nevertheless have frequent nuclear membrane ruptures. *Proc Natl Acad Sci U S A,* 115, 10100-10105.

234. Schermelleh, L.; R. Heintzmann and H. Leonhardt 2010. A guide to super-resolution fluorescence microscopy. *Journal of Cell Biology,* 190, 165-175.

235. Palmieri, E.M.; M. Gonzalez-Cotto; W.A. Baseler; L.C. Davies; B. Ghesquière; N. Maio; C.M. Rice; T.A. Rouault; T. Cassel; R.M. Higashi; A.N. Lane; T.W.M. Fan; D.A. Wink and D.W. McVicar 2020. Nitric oxide orchestrates metabolic rewiring in M1 macrophages by targeting aconitase 2 and pyruvate dehydrogenase. *Nature communications,* 11, 698-17.

236. Viola, A.; F. Munari; R. Sánchez-Rodríguez; T. Scolaro and A. Castegna 2019. The Metabolic Signature of Macrophage Responses. *Frontiers in Immunology,* 10.

237. Kaplowitz, N. 2004. Drug-Induced Liver Injury. *Clinical Infectious Diseases,* 38, S44-S48.

238. Han, D.; L. Dara; S. Win; T.A. Than; L. Yuan; S.Q. Abbasi; Z.-X. Liu and N. Kaplowitz 2013. Regulation of drug-induced liver injury by signal transduction pathways: critical role of mitochondria. *Trends in pharmacological sciences (Regular ed.),* 34, 243-253.

239. Ahamed, M.; M.J. Akhtar; H.A. Alhadlaq; M.A.M. Khan and S.A. Alrokayan 2015. Comparative cytotoxic response of nickel ferrite nanoparticles in human liver HepG2 and breast MFC-7 cancer cells. *Chemosphere,* 135, 278-288.

240. Elefantova, K.; B. Lakatos; J. Kubickova; Z. Sulova and A. Breier 2018. Detection of the mitochondrial membrane potential by the cationic dye JC-1 in l1210 cells with massive overexpression of the plasma membrane ABCB1 drug transporter. *International journal of molecular sciences,* 19, 1985.

241. Will, Y.; J.E. Shields and K.B. Wallace 2019. Drug-Induced Mitochondrial Toxicity in the Geriatric Population: Challenges and Future Directions. *Biology,* 8, 32.

242. van der Stel, W.; G. Carta; J. Eakins; S. Darici; J. Delp; A. Forsby; S.H. Bennekou; I. Gardner; M. Leist; E.H.J. Danen; P. Walker; B. van de Water and P. Jennings 2020. Multiparametric assessment of mitochondrial respiratory inhibition in HepG2 and RPTEC/TERT1 cells using a panel of mitochondrial targeting agrochemicals. *Archives of Toxicology,* 94, 2707-2729.

243. Eakins, J.; C. Bauch; H. Woodhouse; B. Park; S. Bevan; C. Dilworth and P. Walker 2016. A combined in vitro approach to improve the prediction of mitochondrial toxicants. *Toxicology in Vitro,* 34, 161-170.

244. Tilmant, K.; H. Gerets; P. De Ron; E. Hanon; C. Bento-Pereira and F.A. Atienzar 2018. In vitro screening of cell bioenergetics to assess mitochondrial dysfunction in drug development. *Toxicology in Vitro,* 52, 374-383.

245. Jewell, M.P.; A.A. Galyean; J. Kirk Harris; E.T. Zemanick and K.J. Cash 2019. Luminescent Nanosensors for Ratiometric Monitoring of Three-Dimensional Oxygen Gradients in Laboratory and Clinical Pseudomonas aeruginosa Biofilms. *Applied and Environmental Microbiology,* 85, e01116-19.

246. Rexius-Hall, M.L.; G. Mauleon; A.B. Malik; J. Rehman and D.T. Eddington 2014. Microfluidic platform generates oxygen landscapes for localized hypoxic activation. *Lab on a chip,* 14, 4688-4695.

247. Takahashi, R.; Y. Zhou; Y. Horiguchi; H. Shiku; H. Sonoda; N. Itabashi; J. Yamamoto; T. Saito; T. Matsue and A. Hisada 2014. Noninvasively measuring respiratory activity of rat primary hepatocyte spheroids by scanning electrochemical microscopy. *Journal of bioscience and bioengineering,* 117, 113-121.

248. Schnell, U.; F. Dijk; K.A. Sjollema and B.N.G. Giepmans 2012. Immunolabeling artifacts and the need for live-cell imaging. *Nature methods,* 9, 152-158.

249. Papkovsky, D.B. and R.I. Dmitriev 2018. Imaging of oxygen and hypoxia in cell and tissue samples. *Cellular and molecular life sciences : CMLS,* 75, 2963-2980.

250. Bus, T.; A. Traeger and U.S. Schubert 2018. The great escape: how cationic polyplexes overcome the endosomal barrier. *Journal of materials chemistry. B, Materials for biology and medicine,* 6, 694-6918.

251. Pu, J.; C.M. Guardia; T. Keren-Kaplan and J.S. Bonifacino 2016. Mechanisms and functions of lysosome positioning. *Journal of cell science,* 129, 4329-4339.

252. Oyarzún, J.E.; J. Lagos; M.C. Vázquez; C. Valls; C. De la Fuente; M.I. Yuseff; A.R. Alvarez and S. Zanlungo 2019. Lysosome motility and distribution: Relevance in health and disease. *Biochimica et biophysica acta. Molecular basis of disease,* 1865, 1076-1087.

253. Danny, B.; P. Sebastian; E. Elishai; L. Gahl; C. Merav; V. Mathieu; V. Jan; J. Magnus and N. Yaakov 2016. Real-time monitoring of metabolic function in liver-on-chip microdevices tracks the dynamics of mitochondrial dysfunction. *Proceedings of the National Academy of Sciences - PNAS,* 113, E2231-E2240.

254. Prill, S.; D. Bavli; G. Levy; E. Ezra; E. Schmälzlin; M.S. Jaeger; M. Schwarz; C. Duschl; M. Cohen and Y. Nahmias 2016. Real-time monitoring of oxygen uptake in hepatic bioreactor shows CYP450-independent mitochondrial toxicity of acetaminophen and amiodarone. *Archives of Toxicology,* 90, 1181-1191.

255. Coen, M. 2015. Metabolic phenotyping applied to pre-clinical and clinical studies of acetaminophen metabolism and hepatotoxicity. *Drug Metabolism Reviews,* 47, 29-44.

256. Behrends, V.; G.F. Giskeødegård; N. Bravo-Santano; M. Letek and H.C. Keun 2019. Acetaminophen cytotoxicity in HepG2 cells is associated with a decoupling of glycolysis from the TCA cycle, loss of NADPH production, and suppression of anabolism. *Archives of toxicology,* 93, 341-353.

257. Kurokawa, H.; H. Ito; M. Inoue; K. Tabata; Y. Sato; K. Yamagata; S. Kizaka-Kondoh; T. Kadonosono; S. Yano; M. Inoue and T. Kamachi 2015. High resolution imaging of intracellular oxygen concentration by phosphorescence lifetime. *Scientific Reports,* 5, 10657.

258. Friedman, B. and B. Cronstein 2019. Methotrexate mechanism in treatment of rheumatoid arthritis. *Joint, bone, spine : revue du rhumatisme,* 86, 301-307.

259. Mikkelsen, T.S.; C.F. Thorn; J.J. Yang; C.M. Ulrich; D. French; G. Zaza; H.M. Dunnenberger; S. Marsh; H.L. McLeod; K. Giacomini; M.L. Becker; R. Gaedigk; J.S. Leeder; L. Kager; M.V. Relling; W. Evans; T.E. Klein and R.B. Altman 2011. PharmGKB summary: methotrexate pathway. *Pharmacogenetics and genomics,* 21, 679-686.

260. Wang, F.; H. Liu; F. Wang; R. Xu; P. Wang; F. Tang; X. Zhang; Z. Zhu; H. Lv and T. Han 2018. Propranolol suppresses the proliferation and induces the apoptosis of liver cancer cells. *Molecular medicine reports,* 17, 5213-5221.

261. Stine, J.M.; L.A. Beardslee; R.M. Sathyam; W.E. Bentley and R. Ghodssi 2020. Electrochemical Dissolved Oxygen Sensor-Integrated Platform for Wireless In Situ Bioprocess Monitoring. *Sensors and Actuators B: Chemical,* 320, 128381.

262. Stine, J.M.; L.A. Beardslee; S. Chu; S. Liu; D. Motabar; W.E. Bentley and R. Ghodssi 2020. Wireless Sensor-Integrated Platform for Localized Dissolved Oxygen Sensing in Bioreactors. *Journal of Microelectromechanical Systems,* 29, 713-719.

263. Lugli, E.; M. Roederer and A. Cossarizza 2010. Data analysis in flow cytometry: The future just started. *Cytometry. Part A,* 77A, 705-713.

264. Samsel, L.; P.K. Dagur; N. Raghavachari; C. Seamon; G.J. Kato and J.P. McCoy 2013. Imaging Flow Cytometry for Morphologic and Phenotypic Characterization of Rare Circulating Endothelial Cells: Samsel

Imaging Flow Cytometry of CECs. *Cytometry. Part B, Clinical cytometry,* 84.

265. Han, Y.; Y. Gu; A.C. Zhang and Y.-H. Lo 2016. Review: imaging technologies for flow cytometry. *Lab on a chip,* 16, 4639-4647.

266. Achilli, T.-M.; S. McCalla; J. Meyer; A. Tripathi and J.R. Morgan 2014. Multilayer spheroids to quantify drug uptake and diffusion in 3D. *Molecular pharmaceutics,* 11, 2071-2081.

267. Lesher-Pérez, S.C.; G.-A. Kim; C.-H. Kuo; B.M. Leung; S. Mong; T. Kojima; C. Moraes; M.D. Thouless; G.D. Luker and S. Takayama 2017. Dispersible oxygen microsensors map oxygen gradients in three-dimensional cell cultures. *Biomaterials science,* 5, 2106-2113.

268. Leary, E.; C. Rhee; B.T. Wilks and J.R. Morgan 2018. Quantitative Live-Cell Confocal Imaging of 3D Spheroids in a High-Throughput Format. *SLAS technology,* 23, 231-242.

269. Guillouzo, A.; A. Corlu; C. Aninat; D. Glaise; F. Morel and C. Guguen-Guillouzo 2007. The human hepatoma HepaRG cells: A highly differentiated model for studies of liver metabolism and toxicity of xenobiotics. *Chemico-biological interactions,* 168, 66-73.

270. Hirschhaeuser, F.; H. Menne; C. Dittfeld; J. West; W. Mueller-Klieser and L.A. Kunz-Schughart 2010. Multicellular tumor spheroids: An underestimated tool is catching up again. *Journal of biotechnology,* 148, 3-15.

271. Saric, A. and S.A. Freeman 2021. Endomembrane Tension and Trafficking. *Frontiers in Cell and Developmental Biology,* 8.

Chapter 8 . Appendices

8.1 Appendix A

Chapter 3 Figures:

- **Preliminary concentration of porphyrin used in oxygen nanosensors (0.05µg/mL):**

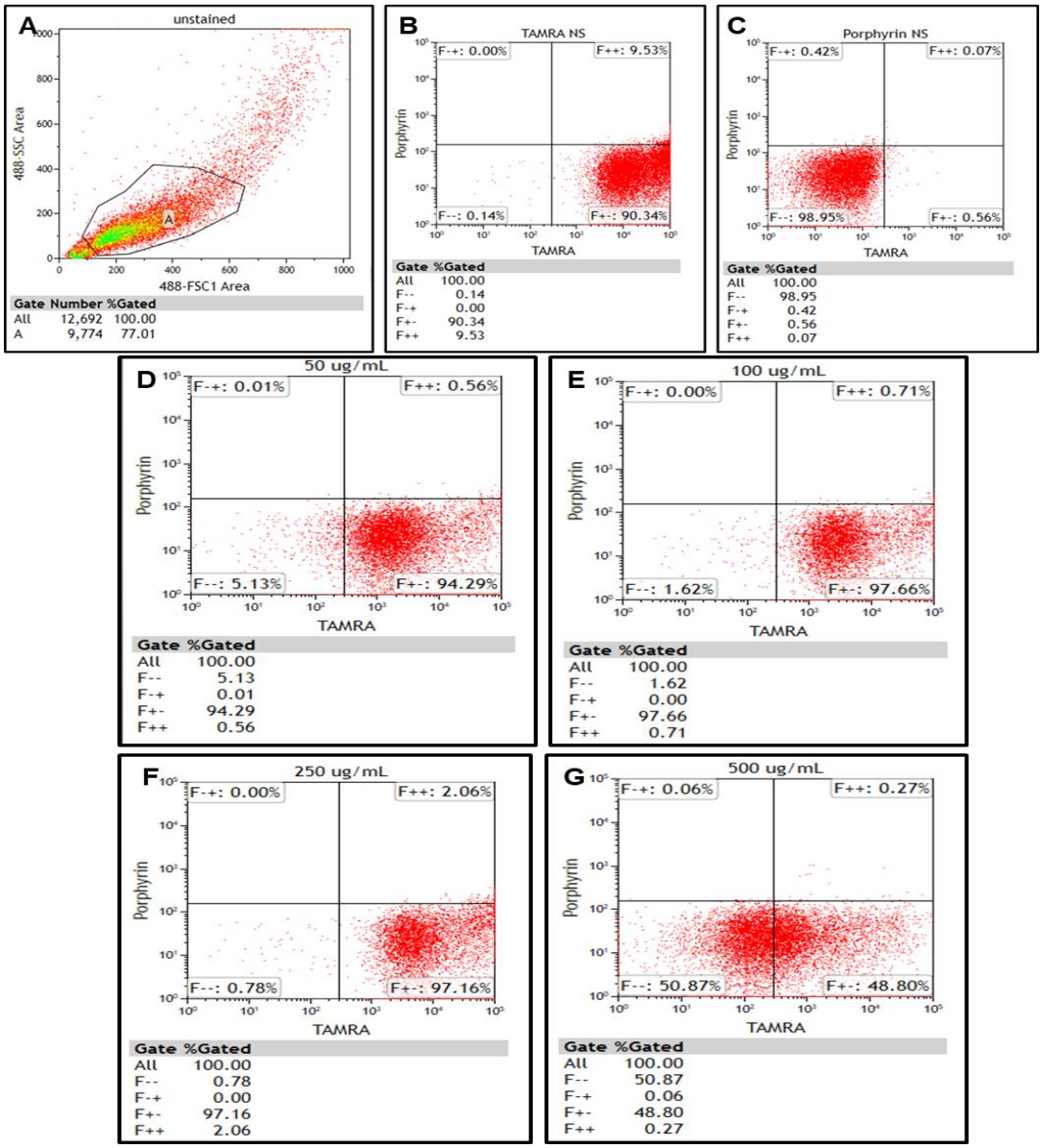


Figure A.1: A) Flow cytometry dot plot of untreated cells, B) treated cells with absolute TAMRA dye, C) treated cells with absolute porphyrin dye D,E ,F, G) 50, 100, 250, 500 µg/mL oxygen nanosensors.

- **Effect of background removal from images which enhances the intensity:**

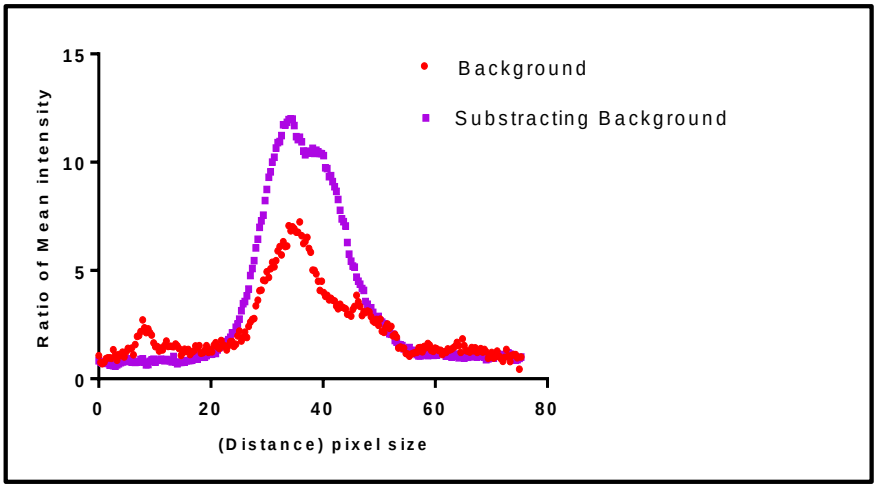


Figure A-2: Example of signal enhancement after removing background in image analysis.

8.2 Appendix B

Chapter 4 Figures:

- **Examining Pt. porphyrin capability to generate ROS by using ABMA:**

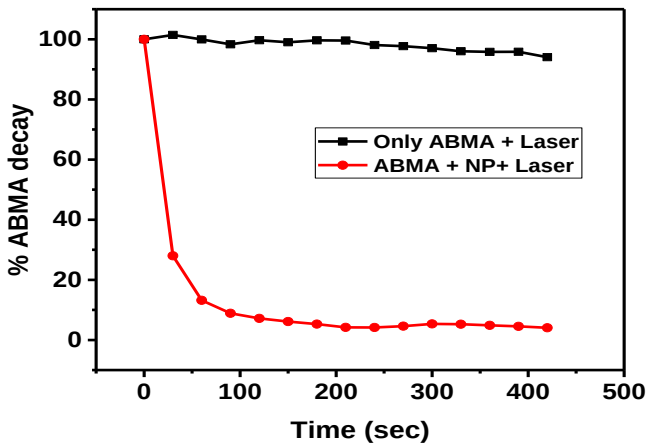


Figure B-1: Reduction of ABMA intensity with presence of porphyrin nanosensors which indicate H2O2 production.

- **Monitoring oxygen consumption by using fluorescence plate reader: challenging macrophage cells with LPS and IFN-ɣ**

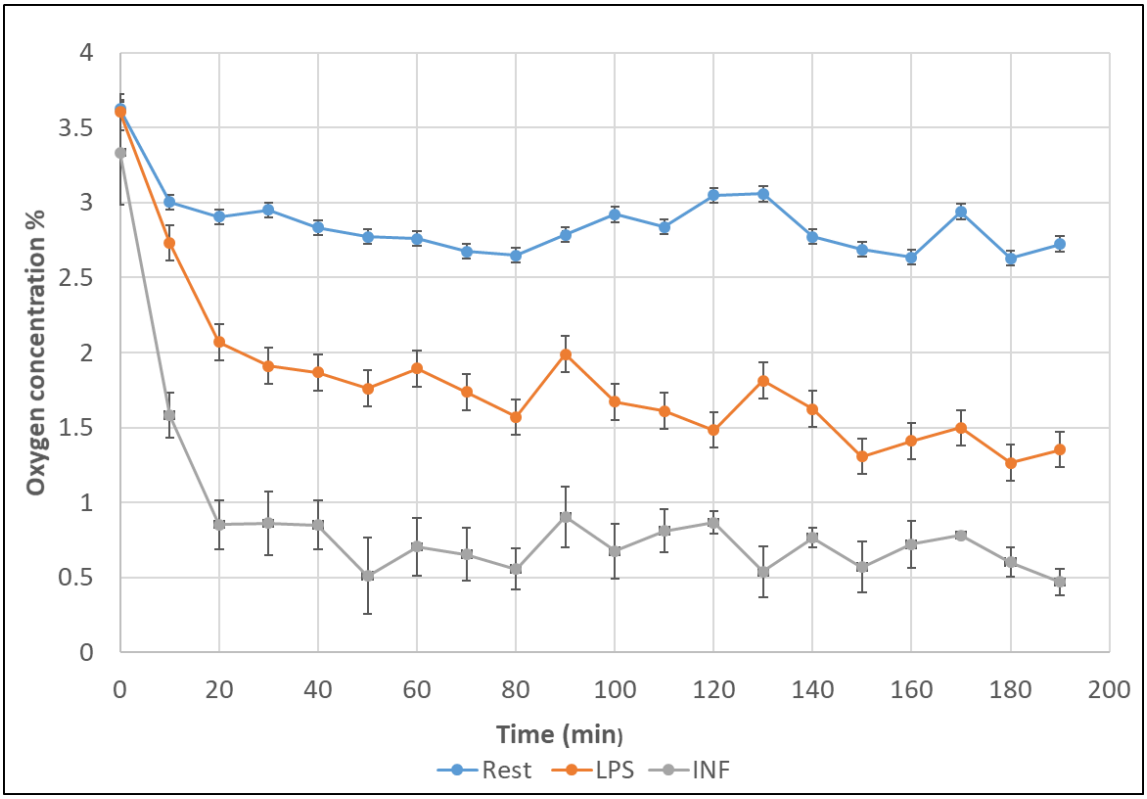


Figure B-2: Monitoring effect of LPS and interferon ɣ on oxygen consumption in macrophage cells Data represents n =3 repeat and error bars =SD.

- **Characterisation of pH nanosensors**

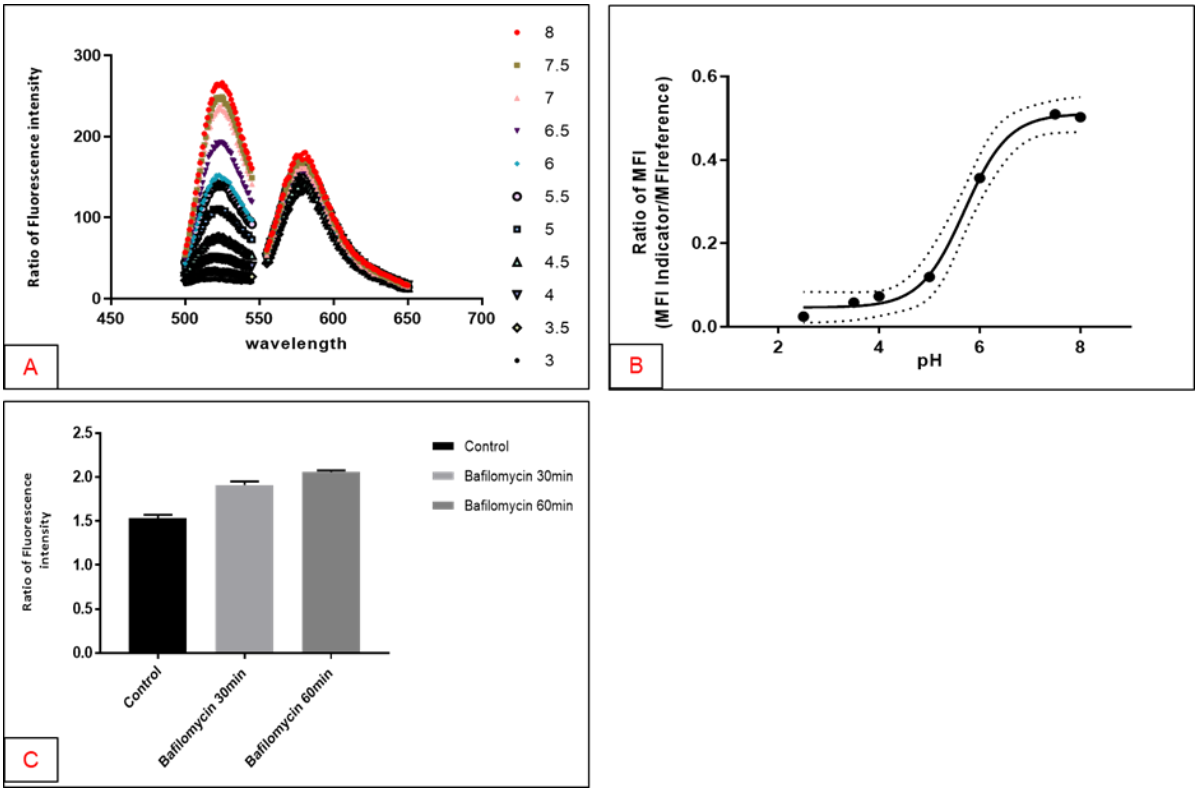


Figure B-3: A) Spectrum of pH nanosensors response to different pH ranging between 3 - 8 which represents physiological pH. B) pH nanosesnsors calibration curve. C) Nanosensor response to inhibition of phagosome acidification. Cells were treated with nanosensors for 24 h and treated with Bafilomycin A1 (inhibitor of phagosome acidification for 30 minutes and 60 minutes). (n = ~ 20 cells) error bars represent SD. Statistically significant ($P < 0.05$).

- **Effect of continuous imaging on morphology of macrophage cells**

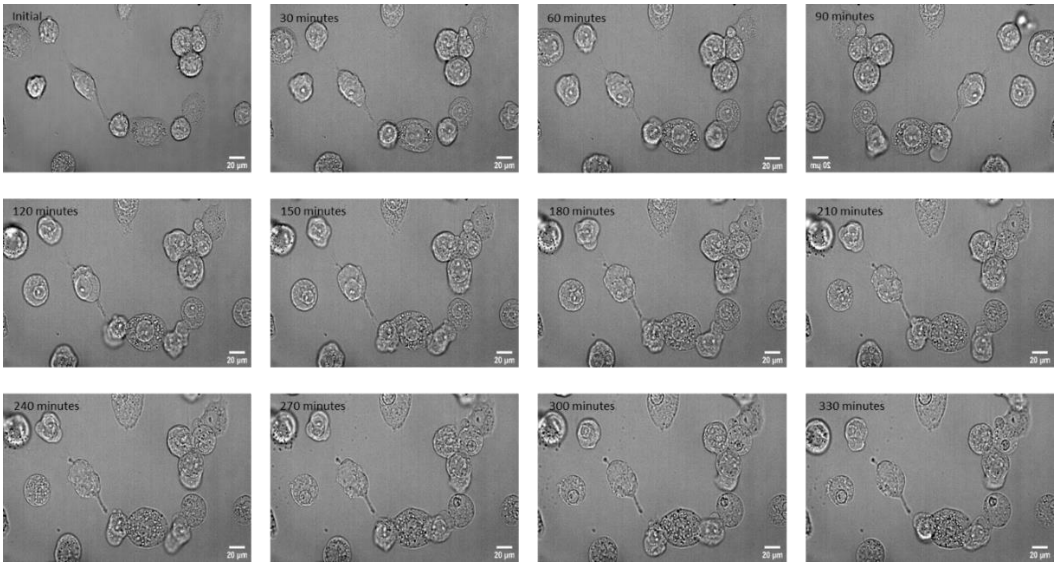


Figure B-4: Morphological change of macrophage as a result of continuous imaging of nanosensors that prove Pt porphyrin generation of ROS.

- **Dual pH and oxygen nanosensors**

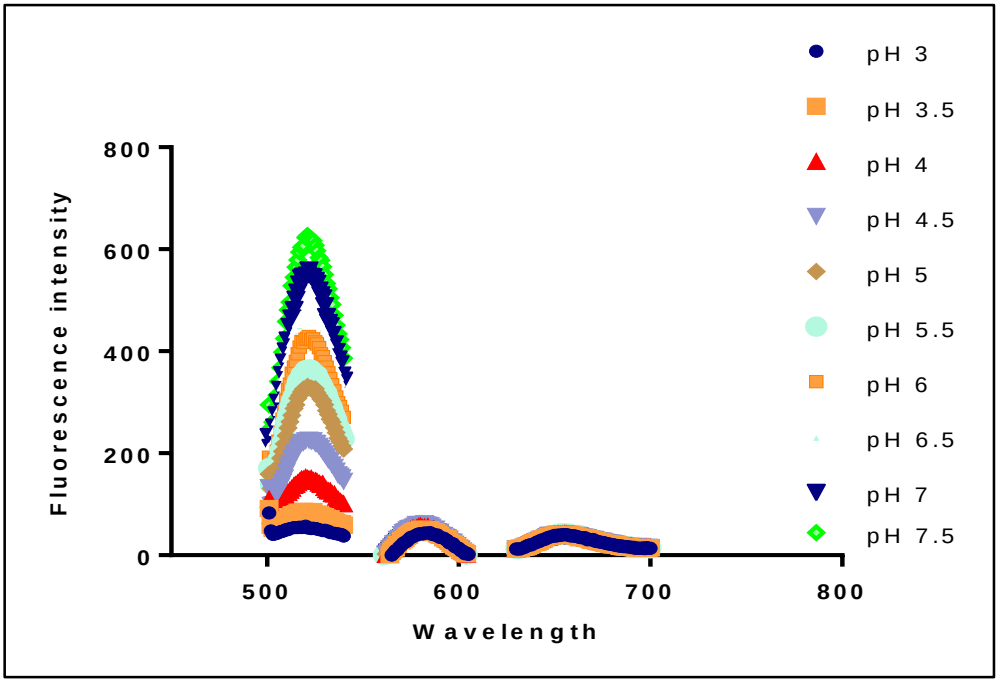


Figure B-5: Effect of different pH range (3 - 7.5) on the intensity of porphyrin (used for sensing oxygen) in dual oxygen and pH nanosensors